Numerical Simulation of the Internal Structure of Sand Dunes

Student: Yukun Liu

Supervisors: Professor Giles Wiggs

& Professor Richard Bailey

A thesis submitted for the degree of Doctor of Philosophy

at the University of Oxford





St Hilda's College

UNIVERSITY OF OXFORD

Abstract

The internal sedimentary structure of aeolian sand dunes has long been considered as an indicator of the paleo environment evolution. Traditional methods (e.g. digging, radar) for studying the internal structure have been restricted by the time and space coverage and data continuity. This thesis deploys a cellular automaton (CA) approach to investigate wind regime controls on the dune dynamic and the corresponding internal stratigraphy. The sand dune CA selected is coupled with a lattice gas (LG) --- a discrete Computing Fluid Dynamic (CFD) model to 'generate' the wind flow instantaneously adapted to the dune topography. In the dune CA, each sand grain cell is enabled with a activation time property to construct the full set of chronology records. The two 'simplest' wind regimes (i.e. unimodal and bimodal) are investigated.

For unimodal winds, scenarios are run on transverse dunes to identify controls of wind speeds and directions. High wind speeds or more crest-normal angles tend to trigger high grain flow magnitude and bury thicker strata whilst the preservation time within the dune body is short.

For bimodal regimes, firstly the fundamental dune evolution pattern and the stratigraphy are identified. With extension of a slip face from the dune crest to the lee slope plinth, the previous stoss slope gets buried, separating two sequences of grain flow strata and forming chronology gaps in age-depth profiles. Secondly the linear dune lateral migration potentials and elongation dynamics are investigated under bimodal winds. For established linear dunes, the lateral migration speeds, directions and the deposition pattern are highly sensitive to tiny (smaller than one degree) changes of wind directions. The sideways moving stratigraphy is either formed by avalanche in the lee or by accumulation of sand on the windward surface. For elongating linear dunes, the stratigraphy is featured by bidirectional strata buried as a core beneath active sand layers. Growth of the core and the whole dune both are influenced by geometries of the bimodal wind regimes, including wind cycle durations, wind directionality and asymmetry of the wind regime.

Acknowledgement

First and foremost, I would like to thank my supervisors Professor Giles Wiggs and Professor Richard Bailey for giving professional support throughout the DPhil research. They both are kind, fun and humorous. It has been important for me that I learnt from them about critical and independent thinking for building my own DPhil research. Giles has huge expertise in field and experimental work and it is great experience to have a chance to take fieldwork (and dish washing) and learn aeolian processes on site in Namibia. Richard is super enthusiastic and has strong logic on computer models and gave constructive suggestions on algorithm making. For the DPhil project I took, Giles and Richard are the best supervision team one could wish for.

The research would not have been possible without the funding support from the Charterhouse European Bursary, St Hilda's College research grants and Santander Travel grants based at Oxford, as well as the research funding paid by IPGP, Paris.

I would like to thank the ReSCAL modelling team at IPGP, Paris. A great amount of computing work has been undertaken with the Linux servers based at IPGP. Olivier Rozier has been extremely patient on explaining any details about algorithms and limitations of ReSCAL. Clément Narteau has been giving insights into data interpretation and offering research funding for the past two years. I especially thank Andreas Baas for teaching me the most fundamental knowledge about sand dune models which led to starting the DPhil and also, developing the MSc thesis into a published paper. I would also like to thank Heather Viles, David Thomas and Simon Dadson for providing constructive comments and advice for my Transfer of status and Confirmation of status. For a modelling based DPhil research, I want to

particularly thank the IT teams of the Oxford department (David Ford, Peter Archer and everyone else who helped me) and IPGP (Pierrick Chanteux, Johan Boudot) for offering the computing equipment and guidance on running simulations. Also, I am grateful to the support from Lorraine Wild, Ruth Saxton (Oxford) and Lydie Guillerot (IPGP) relating to administrations of the DPhil procedure.

I would like to thank Thomas Baird and Zhenyu Zhang for proofreading and making comments on the thesis. I appreciate help received from Jerome Mayaud on clarifying all details of ViSTA model, and discussion with Jo Nield and Matt Baddock in the field of Namibia. I would like to thank Mona Edward and Hong Zhang for offering the part time work in the lab, which largely solved my financial issue in early months. Also, I would like to thank Nicky Charles, Yuxuan Zhang, Baoli Liu and Andre Python for helping with logistic issues when I took international travels.

This thesis is dedicated to my parents Guilian Li and Wenguang Liu who have been unconditionally supporting me throughout the DPhil and all decision makings in my life

Table of Contents

Abstract 2
Acknowledgement 3
Glossaries 8
List of Figures 11
List of Tables 24
Chapter 1 Aim and objectives 25
1.1 Aim and background 25
1.1.1 Aim 25
1.1.2 Background 25
1.2 Objectives 29
1.3 Thesis structure 32
Chapter 2 Introduction to flow patterns and stratigraphy in aeolian sand dunes under unimodal and bimodal wind regimes 35
2.1 Wind patterns, dune dynamics, and stratigraphy with crest-normal and unidirectional winds 35
2.1.1 Literature review 35
2.1.2 Knowledge gaps 43
2.2 Wind flow pattern and stratigraphy under non-crest-normal wind 44
2.2.1 Literature review 44
2.2.2 Research gaps 49
2.3 Evolution and sedimentary structure of linear dunes 50
2.3.1 Literature review 50
2.3.2 Knowledge gaps 57
Chapter 3 Models and methods 59
3.1 Review of numerical simulation of sand dunes 59
3.1.1 Modelling morphology of dunes 59
3.1.2 Possibilities of mapping the stratigraphy 62
3.1.3 Initial model selection 63
3.2 Types of Cellular Automaton (CA) sand dune models 63
3.3 Comparison and selection of CAs 69
3.3.1 Comparison and selection criteria 69
3.3.2 Specification of the selected CA 73

Chapter 4 Wind speed and angle impact on transverse dune dynamics under unimodal winds 76
4.1 Flow pattern, sand movement and sedimentary structure of a transverse dune (crest-normal wind at a fixed speed) 77
4.1.1 Flow pattern and sand movement on the surface 78
4.1.2 Internal sedimentary structure 85
4.1.3 Summary of 4.1 87
4.2 Flow pattern, sand movement and sedimentary structure of a transverse dune with respect to varying (crest-normal) wind speeds 88
4.2.1 Flow pattern and sand movement on the surface 89
4.2.2 Internal sedimentary structure 96
4.2.3 Summary of Section 4.2 101
4.3 Flow pattern, sand movement and sedimentary structure of a transverse dune with respect to (speed-fixed) varying wind-incident angles 102
4.3.1 Flow pattern and sand movement on the surface 102
4.3.2 Internal sedimentary structure 112
4.3.3 Summary of Section 4.3 118
4.4 Summary of Chapter 4 118
Chapter 5 Bimodal wind regime controls on dynamics and internal stratigraphy of established linear dunes 120
5.1 Flow pattern, sand movement and sedimentary structure of a transverse dune with respect to a reversing wind (wind speed and angle fixed) 122
5.1.1 Flow pattern and sand movement on the surface 123
5.1.2 Internal sedimentary structure 133
5.1.3 Summary of Section 5.1 136
5.2 Lateral migration of individual linear dunes 137
5.2.1 Lateral migration cases in response to varying wind angles 137
5.2.2 Internal structure in response to the lateral migration cases 145
5.2.3 Summary of Section 5.2 152
5.3 Lateral migration of multiple linear dunes 152
5.4 Summary of Chapter 5 160
Chapter 6 Bimodal wind regime controls on initiation and elongation of linear dunes 163
6.1 Elongation dynamics of linear dunes 164
6.1.1 Simulation settings 164
6.1.2 Evolution of a cross section 167
6.1.3 Stratigraphy and chronology of the whole dune 176

6.1.4 Key findings from Section 6.1 180
6.2 Wind condition control on linear dune formation 181
6.2.1 Wind angle 182
6.2.2 Wind duration length 187
6.2.3 Wind asymmetry (duration ratio between two winds) 192
6.2.4 Key findings of Section 6.2 198
6.3 Summary of Chapter 6 199
Chapter 7 Conclusion 201
7.1 Key findings 201
7.1.1 Investigation and key findings for Objective 1 202
7.1.2 Investigation and key findings for Objective 2 205
7.2 Overall conclusion 212
7.3 Future work 213
Reference List 216

Glossaries

Parameter	Description	Unit
h	Height of a sand dune (take the crest)	cell
θ_1	For unidirectional wind, angle between the wind and the dune crest. For bidirectional wind, wind-crest angle of the longer duration wind	degree
θ_2	In bidirectional wind, wind-crest angle of the shorter duration wind	degree
θ	Angle between the two winds in bimodal wind regimes	degree
α	Gradient of the lee slope of a 3D dune or 2D transect	degree
α'	Gradient of the lee slope path interacting with the wind incidence at an oblique angle	degree
l_0	Width and length of a squared cell, minimal length unit in ReSCAL model	-
t_0	Minimal time unit (a step for executing a simulation) in ReSCAL model	-
t	Time duration of a simulation run from the initial condition	t_0
t_r	Realistic time duration required for causing the same sand flux in ReSCAL	Second, minute
l_0	Minimal length unit of a cell in squared-grid based model domains	-
τ_0	Unit for wind shear stress	particle number/l_0
τ_s	Wind shear stress	τ_0
τ_{min}	Minimum wind shear stress threshold for occurrence of erosion process	τ_0
τ_{max}	Maximum wind shear stress threshold for applying the linear relationship to determine erosion rate	τ_0

τ_{flat}	Shear stress of the environmental wind over the flat surface	τ_0
δ_s	Change of wind shear stress from the flat surface τ_{flat}	-
R_0	Erosion rate coefficient	R_0
R_e	Surface erosion rate of a given cell in CAs	-
$\vec{V}$	Wind velocity modelled with LG	flow particle number
$\vec{n}$	Vector normal to the local topography	-
Q_{we}	Sand flux from west to east over a local cell	/(cell*t_0) or for a specified time duration
Q_{ns}	Sand flux from north to south over a local cell	/(cell*t_0) or for a specified time duration specified
T_1	In bimodal winds, duration of the long duration wind, at angle θ_1 with the dune crest	t_0
T_2	In bimodal winds, duration of the short duration wind, at angle θ_2 with the dune crest	t_0
T	Total duration of a wind cycle of a bimodal wind regime	t_0
N	Duration ratio between the two winds in a bimodal wind regime T_1/T_2	-
Q_{dune}	Sand flux over the dune surface, crest-parallel	/(cell*t_0)
Q_{out}	Overall sand flux over inter-dune surface	/(cell*t_0)
$Q_{out\|\|}$	Crest-parallel sand flux over inter-dune surface	/(cell*t_0)
$Q_{out\perp}$	Crest-normal sand flux over inter-dune surface	/(cell*t_0)
$Q_{mean\|\|}$	Crest-parallel sand flux over the dune width	/(cell*t_0)
$Q_{\mathrm{mean}\perp}$	Crest-normal sand flux over the dune width	/(cell*t_0)
$Q_{crest\perp}$	Crest-normal sand flux at the dune crest	/(cell*t_0)

W_{dune}	Dune width (cross section) in 3D or transect width in 2D	cell
W_{out}	Width of the inter-dune in linear dune fields, width of the model domain deducted by W_{dune}	cell
r	Radius of the upwind sand source in a circular shape	cell
R_{in}	Sand influx rate from the upwind sand source in a circular shape	cell/(l_0*t_0)

List of Figures

Chapter 1

Figure 1-1. Schematic of the structure of the whole thesis, surrounding the aims, key scientific questions and objectives.

Chapter 2

Figure 2-1. Schematic of wind flow structure over a transverse dune transect with the lee slope fully dominated by the angle of repose.

Figure 2-2. Examples of wind profiles measured on barchans and transverse dunes (with crest-normal wind) in previous work, taking one example of each methods involved in Table 2-1. (A) Field measured data by Baddock, et al., 2007. (B) CFD modelled data by Parsons, et al., 2004. (C) Wind tunnel data by Walker and Nickling, 2003

Figure 2-3. Origins of wind pattern complexity over linear dune surfaces (lee slope gradient α and wind-crest angle $\theta_1 < 90°$). (A) The wind-surface interacting path on the environmental wind direction (interacting path gradient is α', rather than the steepest slope α). (B) Flow deflection to the crest-parallel direction (sourced from Livingstone, 1986).

Figure 2-4. Wind profiles measured on linear dunes (with oblique incidence angle to the crest) in previous work (A) Tsoar, 1983, Sinai Desert, small linear dunes between 5 m and 15 m high. (B) Livingstone, 1986, Namib Desert, big linear dune around 80 m high with static base. (C) Wiggs, et al., 1996b, Kalahari Desert, small vegetated linear dune around 5 m high.

Figure 2-5. In ternal sedimentary structure of linear dunes mapped with GPR. The two dunes surveyed are located in one dune field. (A) Cross sections at varying

locations of one dune (Bristow, et al., 2000) (B) Cross section with identified cross strata and bounding surfaces (Bristow, et al., 2005).

Figure 2-6. Sedimentary structure of linear dunes modelled with the Werner 1995 CA (sourced from Liu and Baas, 2020), under the same wind regime at varying development histories (A) Time sequence of a bedform interaction before a steady state has been reached, involving temporary lateral migration of the earlier dune and a low angle bounding surface. (B) Stratigraphy at two steady states, built by the existing dune that has sufficiently adjusted to the (symmetrical) ongoing wind regime (i.e. dune interaction stratigraphy excluded). Steady state 2 is 20 model years later than Steady state 1

Chapter 3

Figure 3-1. Schematic of simplified aerodynamic rules in Werner, 1995 model (Baas, 2002): erosion, transport, deposition of the environmental wind and shadow zone for the secondary flow in the lee (flow recirculation of four dune heights horizontal distance).

Figure 3-2. Schematic of a Real Space Cellular Automaton (ReSCAL) model (Narteau, et al. 2009). (A) Configuration of doublets and their transition types including sand grain cells and air cells (B) Lattice Gas (LG) Boltzmann theoretical wind including a propagation phase and a collision phase maintaining the momentum of the airflow particles. (C) Coupling rules of the sand movement model in (A) and LG model in (B): the local erosion rate R_e is determined by the shear stress τ_s.

Figure 3-3. Wind speedup stoss slope effect on geometries of transverse dune (including barchans) transects. (A) Barchan dune shown in Mayaud, et al., 2017

using Werner model without wind speedup (B) Sand dune 2D transects presented in Momiji, et al., 2000 with varying speedup coefficient enforced on Werner model. (C) Barchan dune example presented in Narteau, et al., 2009 with LG wind coupled.

Chapter 4

Figure 4-1. Wind shear stress modelled with lattice gas (LG) over a transverse dune 26 cells in height with the wind perpendicular to dune crest at the highest strength ($\tau_{min} = 0$) and lee slope fully covered by the slip face. (A) Topography image of the whole model domain (B) Shear stress τ_s (fractional speedup ratio δ_s labelled together) over the 2D crest-normal transect (topography vertically exaggerated). The shear stress and the topography both take the average of the 200 transects between the two white lines labelled in image (A).

Figure 4-2. Magnitude of sand moving processes modelled with ReSCAL over a transverse dune cross section in response to the wind shear stress of Figure 4-1 over the same topography, under the highest wind speed ($\tau_{,min} = 0$). The magnitude is described by the occurrence times per minimum time step t_0 of each specified transition (Figure 3-2), averaging an instantaneous duration of 5 t_0. (A) Erosion (with wind direction labelled) (B) Transport (C) (non-avalanche) Deposition (D) Avalanche.

Figure 4-3. Sand flux over a crest-normal transverse dune transect resulted from the wind shear stress of Figure 4-1 and sand moving magnitude of Figure 4-2 over the same topography, under the highest wind speed ($\tau_{,min} = 0$).

Figure 4-4. Internal structure of the transverse dune (A) Cross strata pictured with buried surfaces of each 2000 t_0(B) Age-depth profile through the dune crest, drilling location labelled on (A) with a dark blue strait line. (C) Age-downwind distance

profile of the dune bottom sand. (A), (B) and (C) all take the average of the 200 transects labelled in Figure 4-1 (A))

Figure 4-5. Magnitude of sand moving processes modelled with ReSCAL over a transverse dune (shown in Figure 4-1 (A)) enforced with a crest-normal wind at varying speeds implemented by setting the minimum erosion threshold τ_{min} under the same shear stress profile of Figure 4-1 (B), lower $\tau_{,min}$, higher wind erosivity (i.e. higher wind strength). The magnitude is described by the occurrence time of each type of transition (Figure 3-2) for an instantaneous duration of 5 t_0. (A) Erosion (B) Transport (C) Deposition (D) Avalanche. Both the topography and process magnitude profiles take the average of the 200 transects labelled in Figure 4-1 (A).

Figure 4-6. Avalanche magnitude with respect to wind speeds (implemented by setting the shear stress threshold τ_{min} to make erosion occur, higher τ_{min}, lower wind speed). A crest-normal wind is enforced on the transverse dune shown in Figure 4-1 (A). The avalanche magnitude takes the maximum of each set of avalanche transition times shown in Figure 4-5 (D)), taking the average over the instantaneous duration of 5 t_0

Figure 4-7. Sand flux computed with ReSCAL over a crest-normal transverse dune enforced with crest-normal wind under varying wind speeds as a result of the wind shear stress of Figure 4-1 and sand moving magnitude of Figure 4-4 over the same fixed topography, for the same duration of 5 t_0. Varying wind speeds are implemented by setting varying minimum threshold for erosion τ_{min}. (A) Crest-normal (W-E) flux (B) Crest-parallel (N-S) flux.

Figure 4-8. Internal sedimentary structure of a transverse dune at varying (crest-normal) wind speeds, implemented by varying τ_{min}. (A) Bedding pattern pictured

with buried surface lines for every 2000 t_0. (B) Age-depth profile through the dune crest. (C) Age-downwind distance profile of the dune bottom sand.

Figure 4-9. Wind shear stress profiles over the crest-normal topography of the transverse dune show, modelled with lattice gas (LG) at varying wind-crest angles θ_1. The transverse dune is 26 cells in height, with the lee slope at the angle of repose. The 200 transects labelled in Figure 4-1 (A) are taken to average the topography and shear stress profiles.

Figure 4-10. Magnitude of sand moving processes at varying wind-crest angles θ_1 (4 examples) modelled with ReSCAL over a transverse dune cross section in response to the wind shear stress of Figure 4-7 over the same topography, under the highest wind speed. The magnitude is described by the occurrence time of each type of transition in Figure 3-2 for an instantaneous duration of 5 t_0. (A) Erosion (B) Transport (C) Deposition (D) Avalanche.

Figure 4-11 Avalanche magnitude with respect to the wind-crest angle θ_1, as schematized in Figure 4-9 enforced on the transverse dune at the highest wind speed ($\tau_{min} = 0$). The avalanche magnitude is described by avalanche transition times per t_0 averaged over an instantaneous duration of 5 t_0.

Figure 4-12. Sand flux computed with ReSCAL over a crest-normal transverse dune transect enforced with varying wind-crest angle θ_1 (presenting the same 4 θ_1 examples as in Figure 4-8) (A) Crest-normal (W-E) flux (B) Crest-parallel (N-S) flux.

Figure 4-13. Sand outflux resulted from sand erosion and transport on the lee slope with respect wind-crest angle, presenting 4 wind speed sets $\tau_{,min} = 0$, $\tau_{,min} = 100$, $\tau_{,min} = 200$ and $\tau_{,min} = 300$

Figure 4-14. Topography images after 2000 t_0 from the initial transverse dune shown in Figure 4-1 (A) enforced with varying wind-crest angles θ_1 at the highest wind speed ($\tau_{min} = 0$).

Figure 4-15. Internal sedimentary structure of a transverse dune at wind-crest angles θ_1, at the highest wind speed ($\tau_{,min} = 0$). In ReScAL (A) Bedding patterns visualized with buried surfaces of each 2000 t_0. (B) Age-depth profile through the dune crest. (C) Age-downwind distance profile of the dune bottom sand.

Chapter 5

Figure 5-1. Evolution of a transverse dune enforced with a reversed wind (i.e. originally W-E reversed to E-W). The initial condition deploys the topography and domain settings specified in Figure 4-1: a 26 cells high transverse dune with the east slope fully occupied by the slip face, located in a 400-cell (N-S) by 600-cell domain. (A) Topography images at time steps with varying degrees of the slip face downwind (i.e. towards the west) extension. (B) Wind shear stress τ_s (labelled with change from the flat surface δ_s) profiles modelled with LG corresponding to (A), both the 2D topography and τ_s taking the average of the 200 transects labelled in (A) $t = 500\ t_0$.

Figure 5-2. Schematic of wind shear stress τ_s profile (based on Figure 5-1 (B)) over the dune topography where the slip face in the lee has not reached the plinth, but lower base of the lee slope remains low gradients and gets steeper to the plinth (D and E). The six stages of the τ_s evolution with respect to dune topography are labelled.

Figure 5-3. Magnitude of sand moving process (described by doublets transition times for an instantaneous duration of 5 t_0) modelled with ReSCAL in the evolution of a transverse dune enforced with the wind opposing to the original direction (i.e. reversed from W-E to E-W), in response to the wind shear stress profiles presented in Figure 5-1 (B). (A) Erosion (B) Transport (C) (non-avalanche) Deposition (D) Avalanche

Figure 5-4. Sand E-W flux computed at a distance (white dashed line labelled in the second image of Figure 5-1 (A)) from the lee (west) slope plinth. The magnitude of sand outflux is shown to decrease over time as the dune re-orientates to the E-W wind.

Figure 5-5. Evolution of the internal sedimentary structure of the dune enforced with a reversed wind. (A) Beddings visualized with buried dune surfaces with an interval of 1000 t_0 (B) Age-depth profiles through the dune crest.

Figure 5-6. Lateral migration of the linear dune (by tracking dune crest locations) at varying combination of wind-crest angles θ_1 and θ_2, with the wind-wind angle fixed to $\theta = 120°$ ($\theta_1 + \theta_2 = \theta$ fixed with varying combinations of θ_1 and θ_2), wind cycle duration fixed T=2400 t_0 and durations of the two winds fixed where $T_1 = 1600\ t_0$ and $T_2 = 800\ t_0$. The 200-cell (N-S) by 400-cell (E-W) domain is enforced with periodical boundaries. (A) Topography image of the linear dune at initial condition. (B) Crest-normal (N-S) distance of the dune crest location with respect to time, taking four lateral migration examples. (C) Southward lateral migration rate (cells/t_0) with respect to a set of combination of θ_1 and θ_2. In (C), positive rates mean the dune has a net migration to the south and negative rates mean the dune migrates to the north.

Figure 5-7. Crest-normal (N to S) sand flux (averaging a full wind cycle T=2400 t_0) from north to south measured at the dune crest (Q_{crest}) and over a distance (Q_{out}) from the primary wind (duration T_1, angle θ_1) lee slope base (measurement location is labelled with a white dashed line in the topography image of Figure 5-6 (A)) with respect to the wind angles θ_1 and θ_2 ($\theta_2 = 120° - \theta_1$) for the set of angles shown in Figure 5-6. (A) Schematic of locations of the flux measurement (B) Flux-θ_1 profiles. Positive values mean the resultant flux is to the south and negative values mean the resultant flux is to the north.

Figure 5-8. Accumulative distribution of deposition time of preserved sand within a wind cycle duration T=2400 t_0 ($T_1 + T_2$). The four stages of preserved deposition are labelled on the plot: Stage 1---beginning of the primary wind period T_1 at angle θ_1, Stage 2---end of the primary wind period T_1 at angle θ_1, Stage 3---beginning of the secondary wind period T_2 at angle θ_2, Stage 4---end of the secondary wind period T_2 at angle θ_2.

Figure 5-9. Distribution of the four sand deposition stages (labelled in Figure 5-8) within a wind cycle over dune topography, under fixed wind cycle duration T=2400 t_0 ($T_1 + T_2 = T$), fixed $T_1 = 1600\ t_0$ and $T_2 = 800\ t_0$, fixed wind-wind angle $\theta = \theta_1 + \theta_2 = 120°$ with varying combinations θ_1 and θ_2, The distribution is described by the cell number deposited in a wind cycle and remains preserved after the subsequent cycle. The topography at the end of T_1 and T_2 are labelled (black curves) on each diagram and their interacting area is the preserved part.

Figure 5-10. Bedding patterns of linear sand dunes under varying lateral migration scenarios indicated by Figure 5-6 (C), visualized with buried surface lines with the time interval of per 5 T.

Figure 5-11. Lateral migration of multiple closely spaced linear dunes under symmetrical bimodal wind regimes where wind cycle duration T=2400 t_0, within which each of the wind period $T_1 = T_2 = 1200\ t_0$ and the angle (with dune crest) of the two wind $\theta_1 = \theta_2 = 60^{\circ}$. The initial distance between adjacent dunes is 40 cells and all dunes have the same size 10 cells high. (A) Topography images and wind shear stress (modelled with LG) profiles. Time steps from the initial condition are labelled on each topography image. (B) Dune migration with respect to time described by taking the total mass of sand per cross section of the whole domain,

Figure 5-12. Bedding patterns of the dune separation scenarios shown in Figure 5-11, mapped with buried surface lines per 100 T. (A) Two dune separation (B) Four dune separation

Chapter 6

Figure 6-1. Topographic evolution of an elongating linear dune modelled with ReSCAL from the early stage to a steady state (i.e. all cross sections have finished growing) applying a circular sand source from the upwind (location labelled with the red dot in (a)). The wind condition is schematized in the first image: T=2400t_0, θ=120° and N=2 (T_1 =1600t_0, T_2 =800t_0, $\theta_1 = 41^{\circ}$, $\theta_2 = 79^{\circ}$). N-S domain boundaries are periodical boundaries. Four images are the snapshot at the end of the wind cycle at t=3 T, 20 T, 30 T and 408 T from the initial condition.

Figure 6-2. Dynamics of a linear dune cross section (labelled with a white line in Figure 6-1) modelled with ReSCAL under the bimodal wind regime T=2400t_0, θ=120° and N=2 (T_1 =1600t_0, T_2 =800t_0, $\theta_1 = 41^{\circ}$, $\theta_2 = 79^{\circ}$) enforced with N-S periodical boundaries (A) 2D topography transects at the specified time steps (a) stratigraphy preservation not started (b) a preserved core started growing (c) steady state. (B)

Dune width and core width evolution with time from beginning of the simulation to the steady state, associated with tracks of dune crest and north (N1&N2) and south (S1&S2) plinths at ends of two wind periods, see points labelled in (A), core initiating time labelled with a vertical black line.

Figure 6-3. Sand flux profiles driving the dune cross section (labelled in Figure 6-1) reaching a steady state, taking sum of flux data of a full wind cycle (A) Crest-parallel (W-E) sand flux evolution with time, including the flux over the whole dune surface and outflux measured at the inter-dune surface (north domain boundary). The influx supplied by the upwind circular source and the dune width evolution with time both are labelled. (B) Dune surface W-E flux with respect to the cross section width up to the maximum width reached.

Figure 6-4. Beddings of an elongating dune cross section (labelled in Figure 6-5) under a bimodal wind regime, visualized by topography surfaces after each wind period.

Figure 6-5. Chronology profiles of the preserved core (visualized with coloured images) of the cross section labelled in Figure 6-1, sampled when the cross section is at the steady state (i.e. has reached the maximum width and stopped widening further). The chronology is described by the absolute deposition time (since the initial condition of a simulation run). (A) Chronology with respect to vertical distance (from the highest elevation of the preserved core) sampled at varying transverse (N-S) locations labelled. (B) Chronology with respect to transverse (N-S) distance sampled at varying elevations as labelled.

Figure 6-6. Chronological profiles of the preserved core (visualized with coloured images) of the elongating linear dune shown in Figure 6-1, sampled when the whole

dune within the model domain has reached the steady state (i.e. each cross section has reached the steady width). The chronology is described by the absolute deposition time since the initial condition. (A) Chronology with respect to vertical distance sampled at varying longitudinal (W-E) locations labelled. (B) Chronology with respect to transverse (N-S) distance sampled at same W-E locations of (A), labelled (C) Chronology with respect to W-E distance sampled at varying N-S locations labelled.

Figure 6-7. Bimodal wind regime and sand supply settings schematized on an elongating dune. The upwind sand supply source is labelled with a red dot, a 10 cells diameter circle installed on the ceiling of the 3D domain, enforced with an injection rate of 0.05 (i.e. probability of injecting a grain on the surface per t_0), dropping sand on the land surface directly under it.

Figure 6-8. Topographic images of dunes under symmetrical (N=1) bimodal wind regimes influenced by the wind-wind angle θ, taking snapshots at the ends of the two wind periods at steady state. (A) T=2400t_0 (B) T=100t_0. The two wind cycle durations T are set to cover a full range of θ from 50° to 120°, identifying the full linear dune initiation potentials driven by wind directionality, as previously raised (Parteli, et al., 2009 and 2014).

Figure 6-9. Cross section (same location as labelled in Figure 6.1) width evolution with time, including whole dune width (dashed line) and preserved core (solid line), at varying wind-wind angles, θ, in bimodal wind regimes. Symmetrical bimodal wind regimes are enforced with a consistent wind cycle duration, T=2400 t_0 with a constant upwind sand supply.

Figure 6-10. Linear dune longitudinal extension (described with downwind dune termination location in W-E distance) with time of the whole dune (dashed line) and the preserved core (solid line), at varying wind-wind angle θ in bimodal wind regimes. Symmetrical bimodal wind regimes are enforced with wind cycle duration T=2400 t_0 with a constant upwind sand supply.

Figure 6-11. Topographic images of dunes under symmetrical bimodal wind regimes influenced by the wind cycle duration, T. Snapshots are at the end of the two wind periods at steady state. (A) θ=120°, to show the T impact on linear dune dimension (B) θ=70°, to show the T impact on linear dune formation.

Figure 6-12. Linear dune longitudinal extension (described with downwind dune termination location in W-E distance) with time of the whole dune (dashed line) and the preserved core (solid line), at varying wind cycle durations T in symmetrical wind regimes where the wind-wind angle θ=120° with a constant sand supply from the upwind.

Figure 6-13. Width evolution with time of the elongating linear dune cross section labelled, including the whole dune (dashed line) and the preserved core (solid line), at varying wind cycle durations T in symmetrical wind regimes where the wind-wind angle θ=120° with a constant sand supply from the upwind

Figure 6-14. Topographic images of dunes under simulated using asymmetrical bimodal wind regimes described by the duration ratios $N = T_1/T_2$, with a constant sand supply from the upwind.

Figure 6-15. Linear dune longitudinal extension (described with downwind dune termination location in W-E distance) with time of the whole dune (dashed line) and

the preserved core (solid line), at varying duration ratios of the two winds $N = T_1/T_2$ in bimodal wind regimes with a constant sand supply from the upwind.

Figure 6-16. Width evolution with time of the elongating linear dune cross section labelled, including the whole dune (dashed line) and the preserved core (solid line), at varying duration ratios of the two winds $N = T_1/T_2$ in bimodal wind regimes. In the bimodal wind enforced, duration of a full wind cycle T=$2400\ t_0$, wind-wind angle $\theta = 120°$ with constant sand supply from the upwind.

List of Tables

Table 2-1. Summary of previous work that involves measurements of wind profiles over barchans and transverse dunes (under crest-normal wind) with identified flow reattachment zone (horizontal distance from the dune crest to downwind).

Table 3-1. Comparison between the two sand dune dynamic CAs: Werner model and ReSCAL.

Table 6-1. Summary of quantified features of linear dunes with simulations at steady state, infinite elongation and constant upwind sand supply. The dune width and height data are measured at the end of each wind cycle. (A) At varying wind-wind angle, θ (B) At varying wind cycle duration ratio, T (C) At varying bimodal wind asymmetry, duration ratio N=T_1/T_2.

Chapter 1 Aim and objectives

1.1 Aim and background

1.1.1 Aim

The aim of this DPhil research is to use a numerical modelling approach to investigate the internal sedimentary structures associated with chronological patterns of aeolian sand dunes. The project has a goal to elucidate the controls on the development of dune sedimentary structures. The study incorporates modelling over long time scales (years to millennia) spanning the dune accumulation history, associated with modelling aeolian structure and sediment transport processes over a short time scale (seconds to minutes), and leading to an understanding of the sand deposition, erosion, and sediment preservation behaviour of differing dune types.

1.1.2 Background

Wind-blown environments and corresponding aeolian dune landscapes are distributed across global hot deserts (e.g. Bagnold, 1941; Wilson, 1972; Fryberger and Dean, 1979; Lancaster, 1995; Pye and Tsoar, 2008; Kocurek, 2009; Pye and Tsoar, 2009; Wiggs, 2021) and cold deserts (Webb and McKelvey, 1959; Bourke, et al., 2009; Bristow, et al., 2010a and b) at varying scales of coverage. Dunes also exist on other planetary bodies and have been increasingly investigated on Mars (e.g. Sagan and Bagnold, 1975; Breed, 1979; Greeley & Iverson, 1985; Edgett, K.S. and Blumberg, 1994; Fenton, 2005; Jackson, et al., 2015; Davis, et al., 2020) and Titan (e.g. Greeley & Iverson, 1985; Rubin and Hesp, 2009; Lucas, et al., 2014; Day and Kocurek, 2018). Owing to the high sensitivity of aeolian processes to environmental changes, the internal stratigraphy of aeolian dunes has often been used as a source of information to deduce past environmental conditions (Fryberger, 1979; Livingstone and Thomas, 1993; Warren and Allison, 1998; Tsoar, 2005; Thomas, et al., 2005; Yizhaq, et al., 2009; Ashkenazy, et al., 2012; Bailey and

Thomas, 2014; Winter and Ruessink, 2017), and also an indicator of the dynamics of bedform evolution (e.g. Tanner, 1965; Parrish and Peterson, 1988; Petit-Maire, 1989; Lancaster, 1990; Mountney and Jagger, 2004; Kocurek, 2009; Bristow, et al., 2010a; Eastwood, et al., 2012; Brothers and Kocurek, 2016; Day and Kocurek, 2017).

Traditional approaches for investigating the sedimentary structure of sand dunes have included trench digging (e.g. Tsoar, et al. 1982), and observations of exposed stratigraphy (e.g. McKee and Tibbitts, 1964; Hanna, 1969; Clemensen, et al., 2001). Since the study of Schenk (1993) ground penetrating radar (GPR) has also been increasingly employed to image buried cross-beds, including in Antarctica (e.g. Bristow, et al., 2010a,b), in alpine blowouts (e.g. Baird, et al., 2019), coastal dunes (e.g. Hugenholtz, et al., 2007) and parabolic dunes, as well as desert barchan (Bristow, 2019) transverse dunes (e.g. Brothers and Kocurek, 2016) and linear dunes (e.g. Bristow, et al., 2000, 2005 and 2007). Sonic radar has also occasionally been deployed to survey sand dune architecture (Vriend, et al., 2007). In addition to radar imaging techniques, Optically Stimulated Luminescence (OSL) dating has been utilised to offer information on sand dune chronology and rates of dune growth and development (e.g. Stokes and Gaylord, 1993; Duller and Augustinus, 1997; Stokes, et al., 1997; Thomas, et al., 1997; Lancaster, 2008; Telfer et al., 2017; Craddock, et al., 2010 and 2015; Buckland, et al., 2019; Srivastava, et al., 2020). In the absence of other chronological information or long-term data on dune geomorphological changes, OSL dating of dune sediments has proved to be a particularly valuable source of information for reconstructing palaeo-dune environments. Furthermore, GPR and OSL have been combined in several studies such that GPR data have been used to direct and focus OSL sampling, thus

elucidating chronologies of dune strata in preserved sediments (e.g. Bristow, et al. 2005 and 2007; Bristow, et al., 2010a and b).

There are, however, limitations in using some of these traditional approaches to furthering our understanding of the internal structure of dunes. Trench digging (e.g. Tsoar, 1982; Schenk, 1993) can damage the surveyed dunes and the preserved sedimentary architectures. More importantly, trench digging and non-invasive techniques including GPR, result in only very limited data coverage across both temporal and spatial scales. For example, whilst GPR surveys can reach to depths of 20-30 m, far further into a dune body than possible with trench digging, such surveys rarely reach the internal base of dunes (e.g. Bristow, et al., 2007; Bristow, et al., 2010b). Also, there is a lack of spatial continuity with GPR surveys (e.g. Bristow and Jol, 2003; Bristow, 2008) as they are only capable of collecting data at discrete points of manual selection. Further, these techniques can only capture a snapshot of the structure as it is preserved at present. The manual interpretation of the dune dynamics that result in the final observed and preserved architecture involves many uncertainties (e.g. McKee and Tibbitt, 1964; Rubin and Hunter 1985; Bristow, 2019) and the reconstruction process using such data may be completely different from the instantaneous activities that have occurred (e.g. note the variation regarding the interpretation of low angle surfaces near barchan dune crests, Bristow, 2019).

Without an understanding of the temporal dynamics of dune building, it is difficult to recognise the corresponding sedimentary structures from geological records. An example is offered by linear dunes, of which the stratigraphy has been rarely recognized in buried records (e.g. Rubin and Hunter, 1985; Livingstone, et al., 2007). It has been proposed that the internal sedimentary architecture of linear dunes is

not sufficiently known to allow identification of such dunes in the geological record (e.g. Rubin and Hunter, 1985; Bristow, et al., 2000). Also, there are likely to be sedimentary processes that occur which do not leave a persistent internal structure within the emplaced dune. In this case it is impossible to discern these processes from the preserved stratigraphy because the records have been lost. This issue is related to the idea of preservation being dependent on environmental signal frequency. It has been proposed by Jerolmack and Paola (2007, 2010) and Tolby et al., (2019) that the preserved sedimentary structure in aeolian dunes is indicative of low frequency climatic signals, whilst high frequency changes are shredded and not preserved in sedimentary records (e.g. annual rather than daily wind cycles are preserved).

A further example of the non-preservation of processes is offered by dune interaction dynamics. In the case of transverse dune field evolution, multiple interaction types have been identified from topography (e.g. Ewing and Kocurek, 2007; Kocurek and Ewing, 2010; Eastwoods, et al., 2011), including coalescence and repulsion between dunes. However, only repulsion cases have been recognized in the stratigraphy (e.g. Brothers and Kocurek, et al 2016; Day and Kocurek 2017). This may be a result of the short preservation time of coalescence cases (Liu and Baas, 2020). For these processes that cannot be observed in field studies of internal dune structure, computer modelling enables the tracking of any point in a dune body throughout the full history of dune evolution toward the final preserved internal sedimentary structure.

Therefore, in this thesis a numerical modelling approach is used to investigate the internal stratigraphy of aeolian dunes. To fulfil the main aim of the research, investigations are directed towards answering two key questions:

(1) What is the internal sedimentary structure of sand dunes of different types and in differing environmental conditions?

(2) What are the controlling processes that lead to the development and preservation of such internal sedimentary structures?

1.2 Objectives

The internal structure of aeolian dunes is determined by a number of major drivers; an external driver can be defined as environmental wind conditions, and the internal drivers include bedform interaction (e.g. Ewing and Kocuek, 2006; Kocurek, 2009; Day and Kocurek, 2017; Bristow, 2019) as well as geomorphological dynamics and secondary flows, for example, flow deceleration in the lee (e.g. Sweet and Kocure, 1990; Kocurek, 2009; Bristow, 2008; Nield, et al., 2017). This thesis has a focus on elucidating how the development of aeolian dune stratigraphy is driven by the wind dynamic, including the internal geomorphological flow dynamic and the external environmental wind in ‘simple’ unidirectional and bidirectional regimes. To resolve the two research questions and two objectives, a series of corresponding experimental steps are proposed, as described in detail below. The simulations that are carried out investigate both the dynamics and resulting stratigraphy of contemporary dunes, but also explore the longer-term formation processes leading to the contemporary geomorphology and internal structure. An important design feature of the simulations is to enact experimental control to simplify outcomes and test specific hypotheses. Scenarios are presented in order of ascending complexity, starting from the simplest to allow validation with previous work. Figure 1-1 schematizes the structure of the objectives and their distribution in chapters.

Objective 1. To identify the impact of unidirectional wind regimes on aeolian dune evolution and sedimentary structure

Simulations start with the simplest unidirectional wind regime, taking into account the direction and speed of the wind. Stratigraphy of aeolian dunes is driven by the airflow pattern in the lee (Kocurek, 2009; Bristow, 2008; Sutton, et al., 2013a and b, Nield, et al., 2017). Sand is deposited during leeside flow deceleration and becomes incorporated into dune stratigraphy via the process of avalanching (e.g. Bristow, 2008; Kocurek, 2009; Nield et al., 2017). Although the flow recirculation pattern of a crest-normal wind is commonly agreed for barchan and transverse dunes (e.g. Walker and Nickling, 2002; Parsons, et al., 2004; Baddock, et al., 2007), the aerodynamic patterns and corresponding deposition dynamics remain incompletely understood where the wind is incident at an angle to the brink. A more detailed and thorough understanding of the controls on the preservation of sediment in a variety of simple wind regimes would allow improved interpretations of controlling wind regimes and better reconstructions of palaeo wind patterns from stratigraphic evidence (e.g. Tanner, 1965; Mountney and Jagger, 2004; Eastwood, et al*., 2012).*

Two steps are implemented to fulfil Objective 1 and clarify dune evolution with respect to simple variability in wind incident angle and wind speed:

***Step 1.1**---Test the impact of wind speed variability on transverse dune dynamics and sediment preservation.*

***Step 1.2**---Test the impact of wind angle variability on dune dynamics and sediment preservation.*

Objective 2. To identify the impact of bimodal wind regimes on the geomorphological dynamics and sedimentary structure of aeolian dunes

Based on the improved understanding of the impact of wind incidence angle on dune sedimentary structures explored in Objective 1, this objective progresses to bimodal wind regimes and their role in driving existing linear dunes, including their initiation and elongation dynamics. The simulation firstly investigates dune dynamics driven by wind reversal, a fundamental aspect of linear dune evolution (Tsoar, 1983; Livingstone, 1986; Wiggs, et al, 1996b; Bristow, et al., 2000, 2005 and 2007), and progresses to exploration of the environmental controls on sediment preservation and resulting stratigraphy (e.g. Bristow, et al., 2010a).

Three steps are implemented to fulfil Objective 2 and clarify dune evolution with respect to wind bi-modality:

***Step 2.1**-- Identify the fundamental controlling process of wind reversal on established transverse dunes by enforcing an opposing wind to the initial unidirectional wind.*

***Step 2.2**-- Investigate the controlling process of bimodal wind regimes on established linear dunes by testing the geomorphological impact of different combinations of wind incident angles (Step 2.2.1) and the wind flow impact for closely spaced dunes (Step 2.2.2). This series of simulations explore the potential for lateral migration where crest-perpendicular net displacement occurs to the whole linear dune over extended time scales (i.e. rather than periodical oscillation).*

***Step 2.3**--- Test the influence of bimodal wind regimes on linear dune initiation and elongation. This step on the one hand has a goal to investigate the evolution of a given elongating linear dune (Step 2.3.1), on the other hand,*

explores controls (Step 2.3.2) of the wind regime geometries on the dune developing process.

1.3 Thesis structure

The thesis takes advantage of a state-of-the-art numerical modelling approach with full manual control of the wind environment. Investigations in each chapter start with the simplest scenario and experimental control is invoked at each stage. For example, in Steps 2.2 and 2.3, for the two key dynamic features of linear dunes (i.e. lateral migration and elongation), when one variable is investigated, the other is controlled and prevented from influencing the modelled system. The structure of the thesis is schematized in Figure 1-1 and described below.

--- Chapter 2 introduces the airflow structure over aeolian dunes documented by previous field and experimental work. The chapter reviews current understanding of relationships between dune dynamics, sediment preservation, and internal sedimentary structure. The influence on dune geomorphology of the two 'simplest' wind conditions, unimodal and bimodal winds, are included in the introduction associated with representative dune types. Research gaps and priorities are identified in Chapter 2.

--- Chapter 3 introduces and critically reviews a variety of available numerical models that have the capability of simulating sand dune evolution and internal stratigraphy. The selection criteria that justify the model capabilities required to fulfil the thesis objectives are fully discussed.

--- The numerical simulation steps required to fulfil the thesis objectives are implemented in Chapters 4, 5, and 6:

--- Chapter 4 begins with an analysis of the simplest experimental scenario where a unimodal wind is enforced on a transverse dune morphology. This is followed by an investigation of the influence of wind speed and wind direction on dune surface processes and sedimentation patterns. This chapter fulfils the two steps of Objective 1.

---Chapter 5 begins with identification of the airflow structure and stratigraphic features resulting from wind reversal which is fundamental in bimodal winds, fulfilling Step 2.1, Objective 2. Following is exploration on the influence of bimodal wind regimes on established linear dunes, with a particular focus on controls on lateral migration of individual dunes (Step 2.1.1) and closely spaced multiple dunes (Step 2.1.2). This chapter fulfils the requirements of Step 2.2, Objective 2.

---Chapter 6 explores the wind regime controls on linear dune initiation and elongation. This chapter fulfils the requirements Step 2.3 Objective 2.

The thesis is concluded in Chapter 7 where key findings are presented, the extent to which the thesis aims have been met is discussed and potentials for future investigations are proposed.

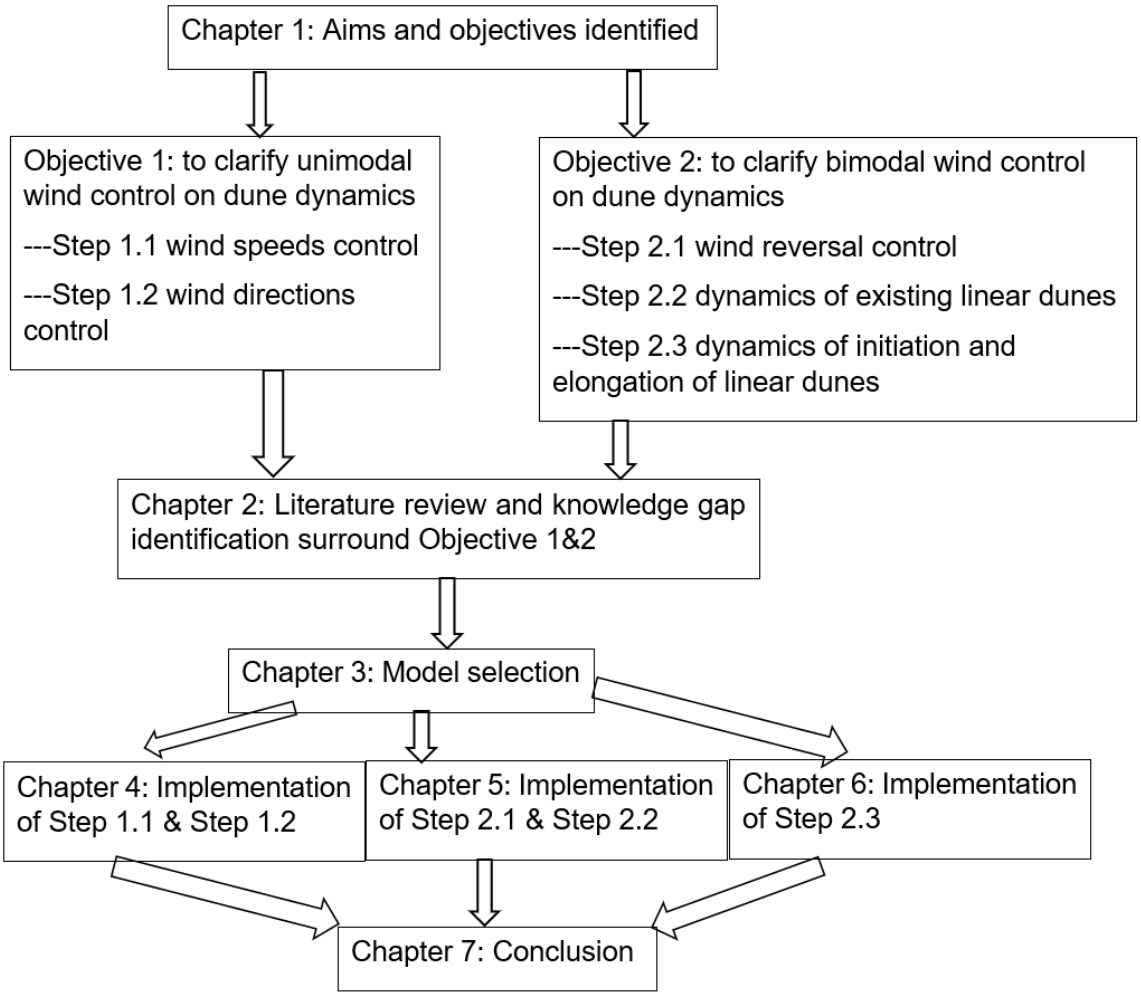


Figure 1-1. Schematic of the structure of the whole thesis, surrounding the aims, key scientific questions and objectives.

Chapter 2 Introduction to flow patterns and stratigraphy in aeolian sand dunes under unimodal and bimodal wind regimes

Regarding the external driver (wind condition) of sand dune stratigraphy, this thesis has a goal to elucidate how the stratigraphy is controlled by unidirectional and bidirectional wind regimes. This chapter reviews the wind-dune surface interaction pattern of the two major types of wind regimes as well as the corresponding sedimentary structure. Firstly, Section 2.1 starts with the simplest case: crest-normal and unidirectional wind as found in areas where barchan and transverse dunes dominate. Secondly, Section 2.2 progresses to approach winds with a non-perpendicular incidence angle. As oblique winds usually occur on linear dunes associated with bidirectional wind regimes, the formation of which have long been under debate, Section 2.3 gives an overall review of the dynamic and the sedimentary structure of linear dunes driven by this wind condition.

2.1 Wind patterns, dune dynamics, and stratigraphy with crest-normal and unidirectional winds

2.1.1 Literature review

Overall wind flow pattern over transverse dunes

The overall structure of the wind flow that interacts with a dune as an obstruction has been well studied by previous work, particularly for transverse dunes, including barchans under the ‘simplest’ unimodal wind. Several features have commonly

found by previous fieldwork, laboratory and numerical surveys, as schematized in Figure 2-1 associated with brief explanation below.

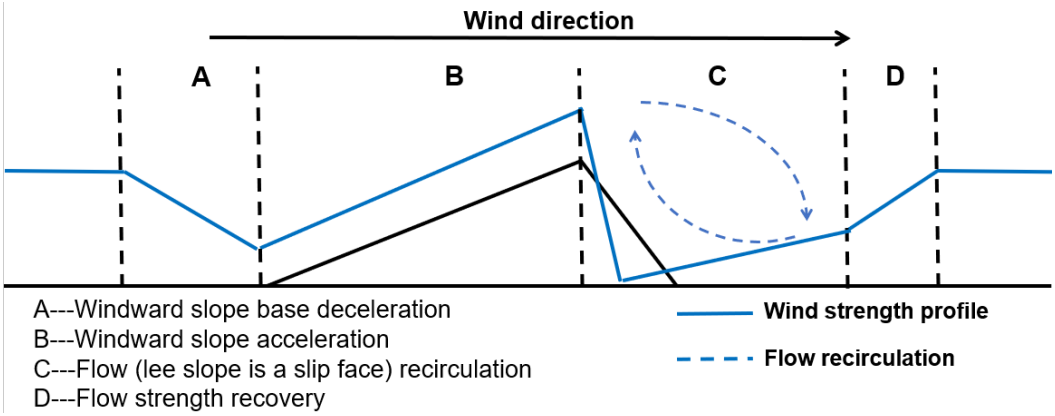


Figure 2-1. Schematic of wind flow structure over a transverse dune transect with the lee slope fully dominated by the angle of repose.

---Zone A: The wind flow decelerates when approaching the base of the windward slope, demonstrated by some field surveys and numerical models (e.g. Howard, 1978; Walmsley and Salmon, 1984; Jensen and Zeman, 1985; by Wiggs, et al., 1996(b); Claudin, et al., 2003; Zhang, et al., 2010; Baddock et al., 2011).

---Zone B: The wind flow accelerates along the stoss slope. This wind speedup and the corresponding increase in sand flux have been widely studied (e.g. Mulligan, 1988; Lancaster, et al., 1996; Wiggs, et al., 1996 a; Neuman, et al., 2000; Claudin, et al., 2003; Baddock, et al., 2011; e.g. Bo and Zheng, et al., 2013; Parsons, et al., 2004; Schatz and Herrmann, 2010), including qualitatively regarding the general wind structure and investigations focusing on the quantitative accuracy.

---Zone C: The wind flow abruptly decelerates in the lee of the dune crest, forming a recirculation with reversed flow. This is the driving process of sand deposition and stratigraphy formation in the lee, introduced with full details in the next section.

---Zone D: The wind flow recovers to the strength of the environmental wind over the flat surface, usually considered together with the flow recirculation in Zone C, as discussed in the next section.

In general, the Zone B speedup and Zone C deceleration are the two flow features leading to sand erosion, transport and deposition when considering dune dynamics (e.g. Lancaster, et al., 1996; Wiggs, 2021). Sand deposition might be expected to occur in the flow deceleration of Zone A. However, previous field measurements (e.g. Wiggs, et al., 1996b; Baddock, et al., 2011; Weaver and Wiggs, 2011) did not find significant deposition at the dune toe. This is attributed to the increased turbulence that is capable of maintaining the local sand transport.

Geomorphological wind flow building the stratigraphy

The sedimentary structure of aeolian dunes is largely determined by the lee side process due to the wind deceleration (e.g., Kocurek, 2009; Bristow, 2008; Pye and Tsoar, 2008), see Zone C schematized in Figure 2-1. The decelerated wind weakens its sand carrying capability and grainfall occurs on the dune lee-downwind of the crest (e.g., Bristow and Jol, 2003; Kocurek, 2009; Bristow, 2008; Sutton, et al., 2013 a and b; Nield, et al., 2017; Cornwall, et al., 2018). For wind regimes that can be approximated to unidirectional and crest-normal, barchans and transverse dunes are the major dune types (e.g. Wasson and Hyde, 1983; Pye and Tsoar, 2008; Wiggs, 2021). For the schematized flow profile of Figure 2-1, in previous fieldwork (e.g. Howard et al; Sweet and Kocurek, 1990; Frank and Kocurek, 1996a; Walker, 1999; Walker and Nickling, 2002; Baddock, et al., 2007; Nield et al., 2017), wind tunnel (e.g. Walker and Nickling, 2003; Dong, et al., 2007 and 2009) and Computing Fluid Dynamic (CFD) models (Schatz and Herrmann, 2007; Parsons, et al., 2004)

measurements, the horizontal distance of the flow recirculation (Zone C, Figure 2-1) has been widely investigated and commonly agreed as four dune heights. The previous work is summarized in Table 2-1 and for each method involved (i.e. fieldwork, wind tunnel and CFD) a wind profile example is presented in Figure 2-2.

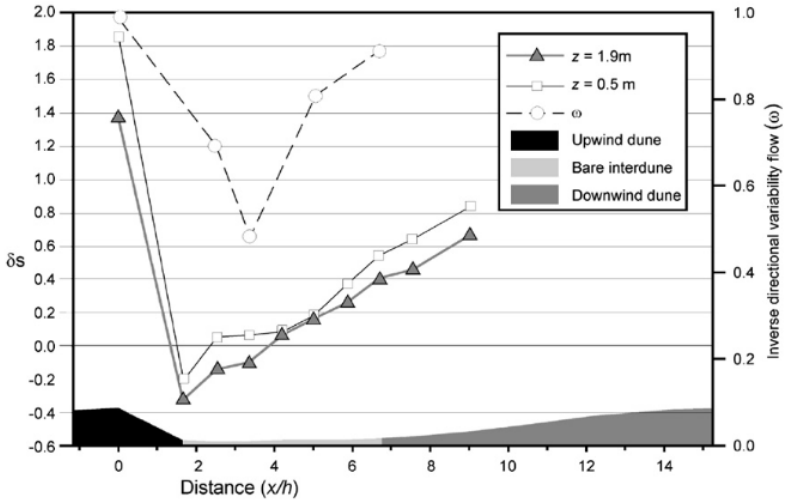
Table 2-1. Summary of previous work that involves measurements of wind profiles over barchans and transverse dunes (under crest-normal wind) with identified flow reattachment zone (horizontal distance from the dune crest to downwind).

Literature	Method	Dune height h	Flow reattachment distance (from crest)
Sweet and Kocurek, 1990	Field measurements	60 m in Algodone	2 h or 3 h, a bit attached to the lee slope edge
		2 m to 4 m in Padre Island	Around 1 h starting on the slope
		5 m in White Sand	Around 5 h or 6 h
Frank and Kocurek, 1996	Field measurements with cup anemometers	Around 3 m to 5 m	3 h to 4 h
Baddock, et al., 2007	Field measurement with cup anemometers	3.87 m, with closely spaced interdune	Around 4 h

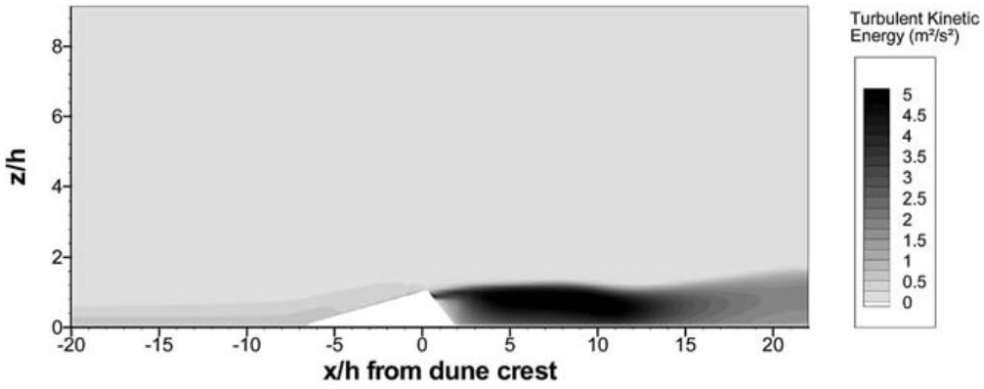
	Field measurement with cup anemometers	5.39 m, with extended interdune	4 h to 5 h
Walker and Nickling, 2002	Conceptual model		4 h to 8 h
Walker, 1999 reversing dune	Field measurement	Around 1.5 m or 2 m	Around 7 m (3.3 h to 4.2 h)
Walker and Nickling, 2003, isolated	Wind tunnel	8 cm	Depending on freestream velocity u (m/s) settings: 6.5 h, u=8; 8.0 h, u=13; 7.5 h, u=18
Walker and Nickling, 2003, closely spaced	Wind tunnel	8 cm	Depending on freestream velocity u (m/s) settings: 3.7 h, u=8; 5.0 h, u=13; 4.4 h, u=18
Dong, et al., 2007	Wind tunnel	Ranging from 3 m to 8 m, lowest for 1 m	Typically 11 h to 12 h
Dong, et al., 2009	Wind tunnel	25 mm	2.5 h to 4 h
Schatz and Hermann, 2006	CFD modelling	Around 10 m or lower, simulated in 30 m high domain	Roughly 3 h to 9 h (from brink) depending on the

			brink angle (dune shape)
Parsons et al., 2004	CFD modelling	0.08 m	3 h to 4 h

(A)



(B)



(C)

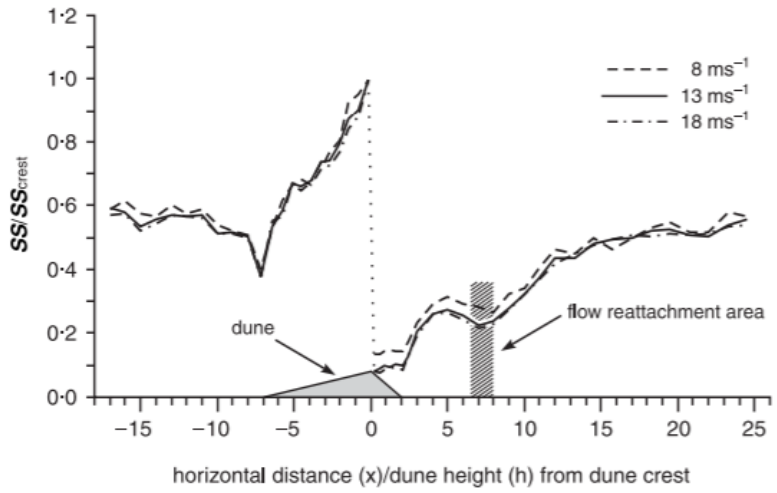


Figure 2-2. Examples of wind profiles measured on barchans and transverse dunes (with crest-normal wind) in previous work, taking one example of each methods involved in Table 2-1. (A) Field measured data by Baddock, et al., 2007. (B) CFD modelled data by Parsons, et al., 2004. (C) Wind tunnel data by Walker and Nickling, 2003

At the reattachment point, the wind reattaches to the environmental wind direction. For example, the wind profile of Baddock, et al., 2007 (Figure 2-2 (A)) indicates that within the horizontal distance of 0 to 4-5 h, the wind speeds are negative (e.g. see the curves measured at 0.5 m and 1.9 m vertical distance from the surface), being opposite to the environmental wind. This is due to recirculation of the flow in the lee. The reversed flow keeps weakening (absolute value of the δ_0 decreasing) until 0 at the 4 h-5 h distance shown where the ω (normalised directional variability of the wind) curve also reaches the minimum. Beyond this distance to downwind, the δ_0 increases, indicating strength recovery of the reattached wind

In addition to the reattachment distance, some of the work summarized in Table 2-1 also identify the flow recovery distance (Zone D of Figure 2-1) from the crest. At this point and going further downwind, the wind has recovered to the environmental

wind in speed, whilst the length of this recovery structure varies between scenarios. For example, in Baddock, et al., 2007 (Figure 2-1 (A)), the distance tends to be (where δ_0 has increased to 1) 10 h, whilst in the CFD of Parsons et al, 2004 (Figure 2-1 (B)) and in wind tunnel (Figure 2-1 (C)) approach of Walker and Nickling, 2003, the wind speed recovery occurs beyond 20 dune heights from the crest. Compared to the commonly confirmed approximately 4 h distance of flow re-attachment, the precise recovery of the flow speed is less constrained by previous studies. However, for individual dunes, the impact of the flow recovery zone on the lee side deposition is less important.

Sand deposition process resulting from the flow pattern

In the flow pattern introduced above, sand is eroded and transported by the accelerated wind along the stoss slope (e.g. Wiggs, 2021). It moves over the crest and deposits by the decelerated wind, accumulating until the grainfall slope over-steepens at a threshold of around 35° (e.g. Kocurek, 2009; Bristow, 2008), then avalanche initiates and terminates until the slope yields an angle of repose of around 32° (Kocurek, 2009; Maske, et al., 2008), forming a slip face. In this avalanche event, the initiating angle is a few degrees larger than the repose angle (e.g. Kocurek, 2009). This deposition process occurs in Zone C of Figure 2-1.

Under the wind and the corresponding sand deposition process described above, the dune shaped by a unidirectional and crest-normal wind is characterized by a lee slope with the slip face reaching the plinth. The slip face is subsequently preserved as the cross strata (i.e. dips, strikes) of the dune (e.g. Kocurek 2006; Bristow, 2008; Bristow, 2019). Regarding deposition of the strata previous investigation has been undertaken on the dune surface by measuring the grainfall (e.g. Nickling, et al., 2002)

and grain flow magnitude (e.g. Sutton, et al., 2013a and 2013b; Nield, et al., 2017; Cornwall, et al., 2018), suggesting that stronger wind produces greater avalanche magnitude. This relationship measured over dune surfaces is in good agreement with the sedimentology view beneath the surfaces: higher wind speeds produce thicker strata for a specified duration (Eastwood, et al., 2012).

As the general forming process of the main strata is well known and agreed, when studying stratigraphy of barchans and transverse dunes, the discussion is more focused on stratigraphy feature (e.g. Brothers, et al., 2016; Bristow, 2019) resulted from dune interaction (e.g. Kocurek, 1981; Kocurek and Ewing, 2005 and 2012; Kocurek, 2010; Day and Kocurek, 2017), as an internal driver in addition to the wind flow structure (i.e. environmental wind as the external driver and geomorphological wind as the internal driver, Chapter 1).

2.1.2 Knowledge gaps

For barchans and transverse dunes, previous work has reached good qualitative agreement regarding a general pattern of wind, sand movement, morphology, and stratigraphic evolution. However, their combined quantitative measures still need to be further investigated. For example, in some geology fieldwork, the orientation of cross strata (i.e. dips/strikes) was considered to result directly from the wind direction at the time of sand burial (Tanner, 1965; Parrish and Peterson, 1988; Mountney and Jagger, 2004; Rowe et al., 2007), whilst others consider this interpretation an oversimplification (e.g. Eastwood, et al., 2012). The similar limitation may be encountered for the wind speed reconstruction based on the thickness of the cross strata, as the wind direction and speed may both determine the thickness (to be resolved in Chapter 4).

For both limitations, an example is offered by presence of longitudinal orientation of dunes under unimodal sand transporting wind (e.g. Fryberger and Dean, 1979; Hesp, 1981; Schatz, et al., 2006; Herrmann, et al., 2008; Rubin and Hesp, 2009; Craddock, et al., 2015) where dune sand transport is prevented, such as by vegetation (e.g. Tsoar, 1989), oil (e.g. Kerr and Nigra, 1951), frozen (e.g. Shatz, et al., 2006; Herrmann, et al., 2008) and so forth. In this type of scenarios, the dipping direction of the grain flow strata (if it still forms) is perpendicular to the crest orientation and at an oblique angle with the wind direction. The grain flow magnitude and the subsequent strata preservation, therefore, are possibly affected by the wind angle (of which the surface flow structure is reviewed in 2.2) because it determines the crest-normal strength of the wind. These limitations identified here are shared with the wind angle issue detailed in Section 2.2 below.

2.2 Wind flow pattern and stratigraphy under non-crest-normal wind

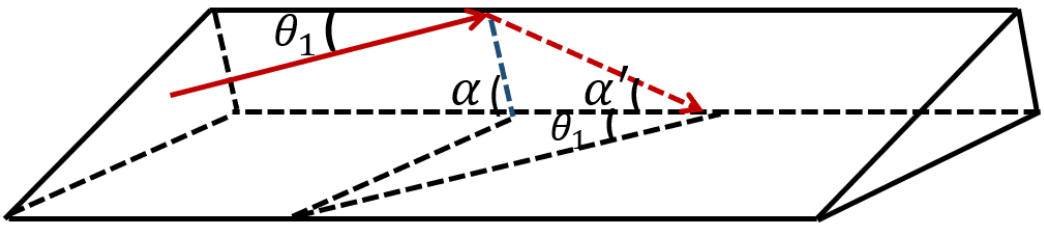
2.2.1 Literature review

In the scenario of transverse dunes discussed in 2.1, the (idealized) wind is perpendicular to the dune crest, while the lee slope is at the angle of repose and the wind interacts with this steepest gradient. If the wind is not completely crest-normal, but approaches the dune crest at an obtuse angle, the two conditions are not satisfied. In the first place, on the path of the environmental wind, the wind-crest angle gets narrower and the morphology of the wind-interacting path has lower gradients. Figure 2-3 (A) shows the schematic of wind-dune interaction when the wind incomes at angle θ_1 and the lee slope gradient is α, whilst it is the lower gradient α' path that is passed through by the oblique wind, where $\tan\alpha' = \sin\theta_1 \tan\alpha$. In addition to this original wind path, when the wind passes the dune crest, the flow is partially deflected to crest-parallel and may carry sand

longitudinally along the length of the dune (e.g. Tsoar, et al., 1983; Lancaster, 1985; Livingstone, 1989; Sweet and Kocurek, 1990), see the conceptual model of Figure 2-3 (B). Even if the wind incident angle was not large, the flow deflected to the crest-parallel direction could be significant. An example is provided by previous field observations in transverse dunes (Walker and Shugar, 2013). The flow surveyed was relatively transverse (i.e. wind-crest angle θ_1 is 70-degree or nearly 90-degree) to the dune crest, while superimposing bedform was displayed near the lee slope base. It was proposed by Walker and Shugar (2013) that the secondary ridges aligned perpendicular to the main dune crest was a result of the deflected flow parallel to the dune crest.

To summarize, comparing to wind profiles reviewed in Section 2.1, the complexity of an oblique incoming wind comes from: (1) the wind interacts with a lower gradient lee slope (Figure 2-3 (A)), thus the 4 dune heights flow reattachment, associated with the deposition become uncertain; (2) the deflected flow in the lee (Figure 2-3 (B)) further complicates the sand transport potentials.

(A)



(B)

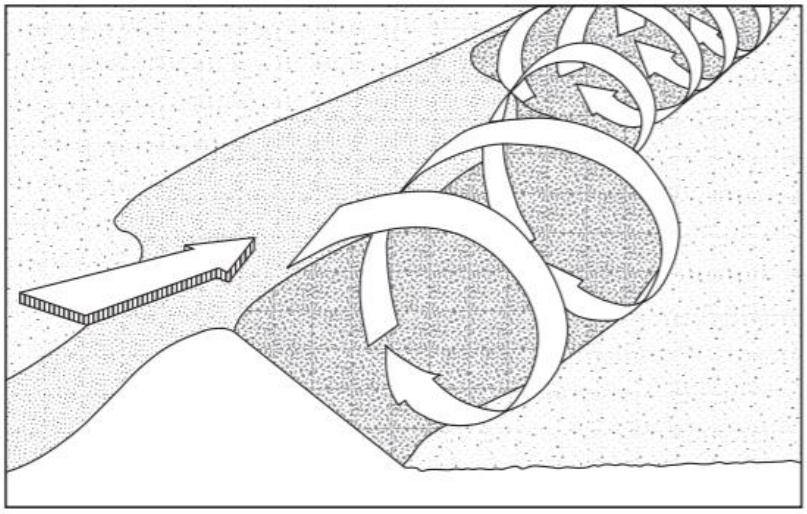
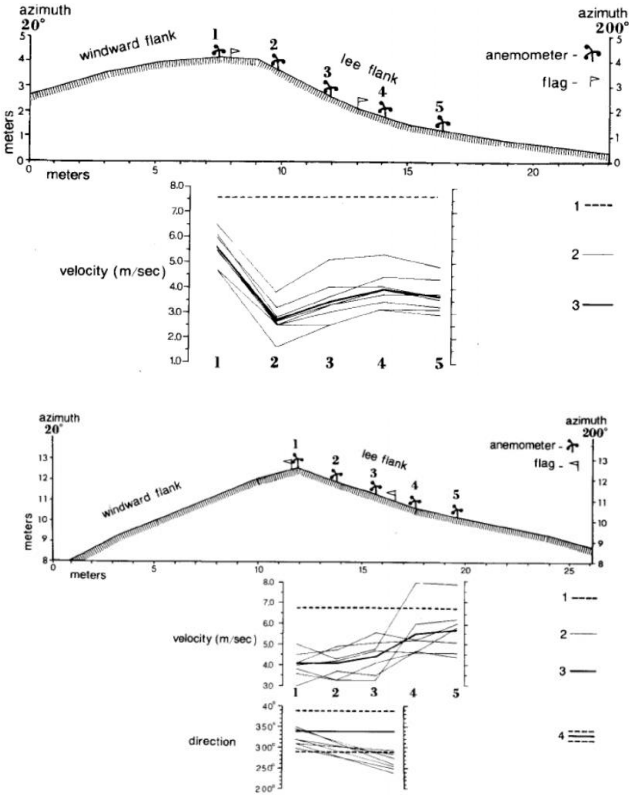


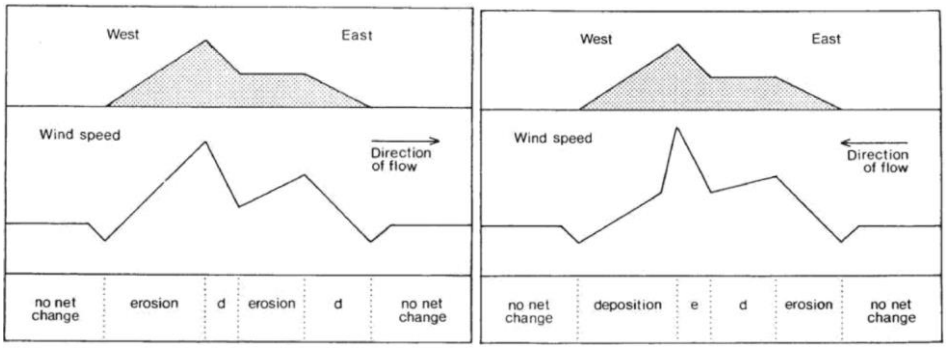
Figure 2-3. Origins of wind pattern complexity over linear dune surfaces (lee slope gradient α and wind-crest angle $\theta_1 < 90°$). (A) The wind-surface interacting path on the environmental wind direction (interacting path gradient is α', rather than the steepest slope α). (B) Flow deflection to the crest-parallel direction (sourced from Livingstone, 1986).

In addition to the measurements undertaken by Walker and Shugar (2013) over transverse dunes, oblique winds were more often surveyed on linear dunes, either under unimodal (e.g. Fryberger and Dean, 1979; Rubin and Hesp, 2009; Craddock, et al., 2015) or bimodal wind regimes (e.g. Bagnold, 1941; Hanna, 1969; McKee and Tibbitt, 1964; Tsoar, 1983; Rubin and Hunter, 1985; Livingstone, 1986; Bristow, et al., 2000, 2005 and 2007) and measurements of the wind profile have been taken on several sites (e.g. Tsoar, 1983; Livingstone, 1986; Sweet and Kocurek, 1990; Wiggs, et al., 1996b). Figure 2-4 provides three representative examples of the wind profile over linear dunes measured in fieldwork.

(A)


azimuth 20°
azimuth 200°
windward flank
lee flank
anemometer -
flag -
meters
velocity (m/sec)
direction

(B)


West
East
Wind speed
Direction of flow
no net change
erosion
d
erosion
d
no net change
West
East
Wind speed
Direction of flow
no net change
deposition
e
d
erosion
no net change

(C)

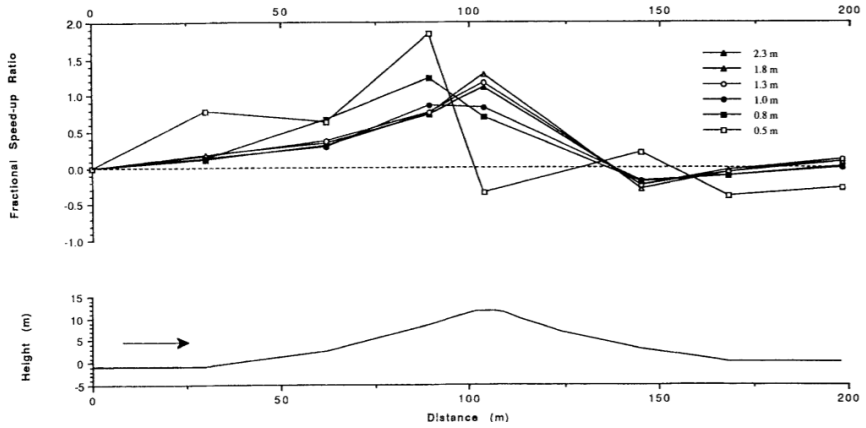


Figure 2-4. Wind profiles measured on linear dunes (with oblique incidence angle to the crest) in previous work (A) Tsoar, 1983, Sinai Desert, small linear dunes between 5 m and 15 m high. (B) Livingstone, 1986, Namib Desert, big linear dune around 80 m high with static base. (C) Wiggs, et al., 1996b, Kalahari Desert, small vegetated linear dune around 5 m high.

The field measured wind profiles of Figure 2-4 well reflect a dependence on the dune morphology: the wind is stronger (deceleration is weaker) in the lee when the lee side gradient is lower. In the wind profiles measured by Livingstone (1986) shown in Figure 2-4 (B), the comparison is directly clear between the two opposite winds over the same topography. When the wind is westerly, the east side becomes the lee side. After passing the crest, the wind still significantly weakens near the crest, but reaccelerates when reaching a lower and flatter portion of the lee side topography. In Wiggs et al., 1996b (Figure 2-4 (C)), the 2D profile is approximately symmetrical. The reduced wind starts to re-accelerate from the middle of the dune lee, between 150 m and 200 m downwind distance. Similarly, in Tsoar, 1983 (Figure 2-4 (A)), the flow reacceleration starts on the lee side of the dune instead of from a downwind distance beyond the downwind plinth of the dune (like in barchans and transverse dunes of Table 2-1 and Figure 2-2). All scenarios presented in Figure 2-

2 have a common feature where the lee side topography has lower gradients than slip faces and the wind deceleration in the lee is gradual with the local topography.

In the three wind profiles shown in Figure 2-4, the wind weakens after passing the crest, whilst it may still carry sand on the lee slope. On the one hand, the weakening may not be sufficient to fully prevent sand from erosion and transport. On the other hand, the sand carrying capability may be recovered with reacceleration in the middle of the slope. Further, sand moved by the longitudinal deflection (Figure 2-3 (B)) also affects deposition in the lee. As a result, the flow pattern of a linear dune complicates the resulting dune dynamic and sedimentary structure, which have been heavily contested. The linear dune dynamic and the sedimentary structure are discussed with full details in Section 2.3.

2.2.2 Research gaps

In comparison to research on transverse dunes, there has been very little research undertaken focusing on the dynamics of sand transport in the lee of linear dunes. Wind patterns have been simply surveyed in fieldwork (e.g. Tsoar, 1983; Lancaster, 1985; Livingstone, 1986; Wiggs, et al., 1996b), including sand movement tracing with fluorescent dye (Tsoar and Yaalon, 1983) whilst numerical methods or wind tunnel experiments have not been employed. The wind flow structure on a 3D basis is not matured in numerical simulations and edge effects are encountered in wind tunnel measurements. Additionally, there is a lack of quantitative analysis regarding the capability of sand movement (by the wind) on the lee slope in response to incoming wind properties (i.e. angle and speed) or to morphology of the slope. For the wind incidence angle, they were only qualitatively classified into transverse (70°-

90°), oblique (10°-70°) and longitudinal (0°-10°) (Sweet and Kocurek, 1990). For the resultant sand movement, there were only descriptive statements that winds with incidence angles greater than 50-degree (e.g. Lancaster, 1986 and 1989; Tsoar, et al., 1985 and 2004) can erode the lee slope.

Giving further considerations to the internal sedimentary structure, scenarios have been reported where linear dunes have a longitudinal or oblique orientation in unidirectional environmental winds (e.g. e.g. Bagnold, 1941; Fryberger and Dean, 1979; Hesp, 1981; Schatz, et al., 2006; Herrmann, et al., 2008; Rubin and Hesp, 2009; Craddock, et al., 2015). For these linear dunes, in addition to the wind strength, wind direction is the other controlling factor on grain flow processes and the long-term impact on stratigraphy. However, comparing to wind speeds surveys on transverse dunes (Sutton, et al., 2013a and 2013b, Nield, et al., 2017; Cornwall, et al., 2018), the grain flow investigation has been absent for these linear dunes regarding the wind directionality. The stratigraphy surveys were also rare in previous work with only some OSL dating work (e.g. Craddock, et al., 2015).

2.3 Evolution and sedimentary structure of linear dunes

2.3.1 Literature review

Linear dunes are commonly considered as the most widely distributed desert dune type on Earth (Lancaster, 1982; Bristow, et al., 2000; Rubin and Hesp, 2009; Telfer, et al., 2020) and they also exist on other planetary bodies such as Mars and Titan (e.g. Lorenz et al., 2006; Rubin & Hesp, 2009; Radebaugh et al., 2010). They were previously referred as longitudinal dunes orientated less than 15 degrees from the resultant wind direction (e.g. Rubin Hunter, et al., 1985; Rubin and Ikeda, 1990; Hesp, et al., 2009), whilst some oblique dunes are also linear in morphology (Hunter, et al., 1983; Rubin and Hunter, 1985; Lv, et al., 2014). Bimodal wind regimes are

usually linked with the evolution of linear dunes with evidence garnered from both field surveys (e.g. Mckee and Tibbitt, 1964; Hanna, 1969; Fryberger, 1979; Tsoar et al., 1983; Lancaster, 1985; Rubin and Hunter, 1964; Livingstone, 1988; Livingstone, 1993; Bristow, et al., 2007), subaqueous experiments (Rubin and Ikeda, 1991) and numerical models (e.g. Werner, 1995; Parteli, et al., 2009; Gao, et al., 2015; Liu and Baas, et al., 2020). Although linear dunes are abundant and have long been studied in morphological field measurements (e.g. Tsoar 1983; Livingstone and Nickling, 1986; Livingstone, 1989, 1993 and 2003; Bullard, et al., 1995; Wiggs, et al., 1995; Bullard and Nash, 1998), understanding about the dune dynamic remains incomplete. On the one hand, linear dunes are subject to seasonally alternating winds that approach the dune alignment at an obtuse (non-perpendicular) incident angle (e.g. Lancaster, 1989; Sweet and Kocurek, 1990). The dune to some extent prevented from net sideways displacement in the wind alternation and the previously buried stratigraphy is prevented from exposure. On the other hand, realistic linear dunes are usually not perfectly linear, but display sinuosity (Rubin and Hunter, 1985; Tsoar, et al., 2004) associated with secondary topographic features like saddles and peaks along the main linear ridge. These factors complicate linear dune dynamics and the internal sedimentary structure.

Longitudinal extension of linear dunes

In the crest-parallel direction, linear dunes have a longitudinal extension and migration manner (e.g. Lancaster, 1982; Tsoar, 1983 and 2001; Tsoar, et al., 2004; Reffet, et al., 2010; Telfer, 2011), which differentiates them from transverse dunes driven by perpendicular winds. On the one hand, a longitudinal component is included by the environmental wind. On the other hand, the deflected lee-side secondary flow (e.g. Livingstone, 1986; Tsoar, et al., 2004, see section 2.2.1) results

in more sand transport along the crest and less in the crest-normal direction. Morphological observations (e.g. Tsoar et al., 1983; Livingstone, 1989), OSL analysis (e.g. Hollands et al., 2006; Telfer, 2011), stratigraphic surveys (e.g. Rubin and Hunter, 1985; Bristow, et la., 2000) and numerical experiments (e.g. Lucas, et al., 2015; Rozier, et al., 2019) have been involved in demonstrating the longitudinal and crest-parallel dynamic of linear dunes. In the resultant direction of sand transport, there is deposition at the dune tip (e.g. Tsoar et al., 1982; Telfer, 2011; Lucas, et al., 2015), leading to crest-parallel elongation. This longitudinal dynamic has been illustrated to take place where sand availability is limited (e.g. Reffet, et al., 2010; Correch du Pont, et al., 2014) and termed as a 'fingering mode' (Correch du Pont, et al., 2014).

Lateral migration of linear dunes

Some research has intimated that lateral migration is key to the sedimentary structure built by a linear sand dune (e.g. McKee and Tibbitts, 1964; Tsoar and Yaalon, 1983; Rubin and Hunter, 1985; Hesp, et al., 1989; Rubin, 1990; Tsoar, et al., 2004; Bristow, 2008). Like in transverse dunes, the lateral movement of the whole dune builds unidirectional strata (Bristow, et al., 2000, 2005 and 2007). Others suggest that, whilst the crest of linear dunes readily migrate by avalanching in response to changing seasonal winds, the dune base remains static where the avalanche slip face does not extend to the plinth (e.g. Livingstone, 1986, 1988; Tsoar et al., 2004). The lee-side flow deflected in a crest-parallel direction reduces the crest-normal transport and crest migration. The wind profile shown in Figure 2-4 (B) was measured on a linear dune with a base less able to move (Livingstone, 1986). In this case the whole dune is disabled from a net sideways movement and the cross strata is built and exposed seasonally by the oscillating part of the dune.

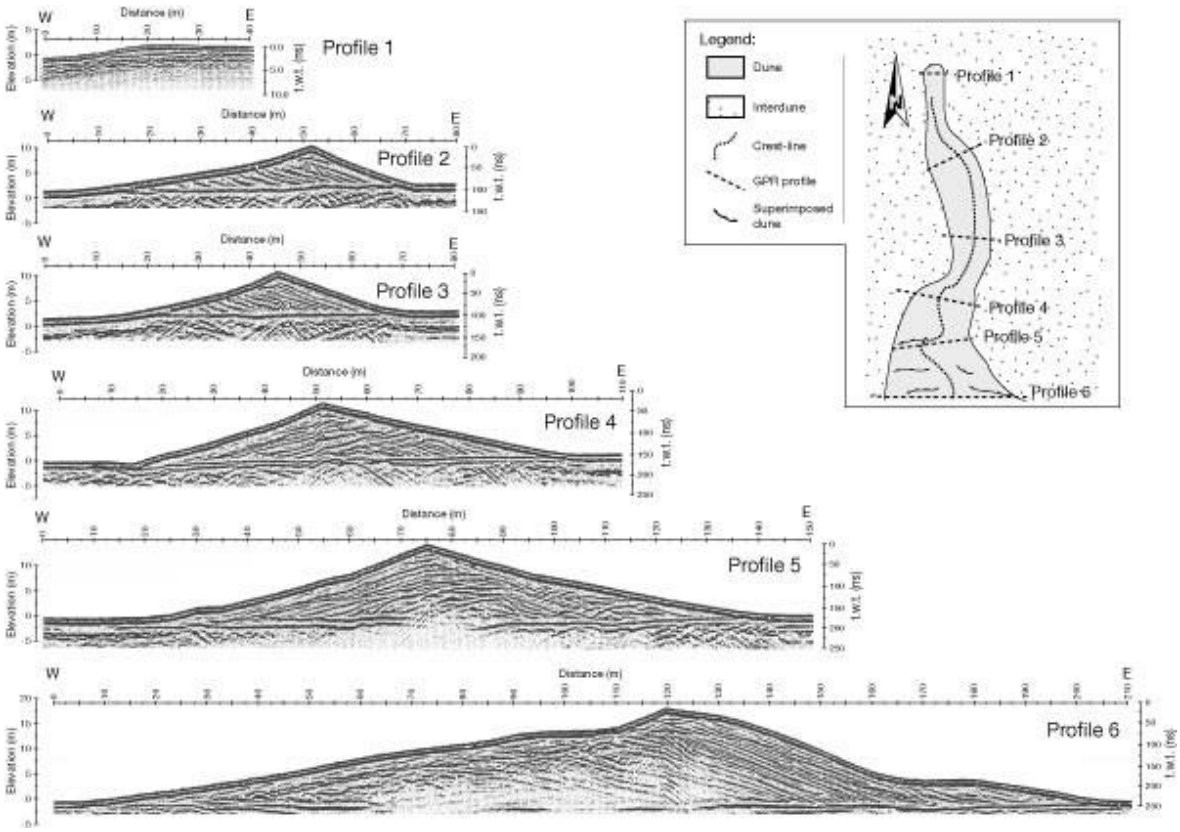
Generally speaking, regarding a linear dune, the occurrence of the lateral migration is driven by (1) to what extent the wind and corresponding sand transport are deflected to the longitudinal direction. Previous study has been descriptive (e.g. Tsoar and Yaalon, 1983; Lancaster, 1985). (2) to what extent the dune crest migrates and whether it makes the slip face reach plinth. In field surveys by Bristow, et al. (2000), the GPR profiles (Figure 2-5 (A)) collected on the same dune show varying degrees of one sequence of cross strata dominating the opposite sequence (e.g. Profile 1).

Internal structure resulted from the lateral and longitudinal dynamics

In the crest-normal direction, the alternating winds cause the oscillation of the dune and restrict the linear ridge from a net sideways movement. Due to the lack of lateral migration (in comparison with barchans and transverse dunes), the buried architecture within the dune body is prevented from exposure. Therefore, linear dunes are recognized as having the potential to preserve a longer sedimentary history. This is the reason why their chronological records are frequently surveyed with OSL techniques to explore depositional ages in relation to paleoclimatic conditions in drylands (e.g. Munyikwa, 2005; Duller and Augustinus, 2006; Fitzsimmons et al., 2007; Telfer and Thomas 2007; Stone and Thomas, 2008; Bristow et al., 2005 and 2007; Srivastava et al., 2019). In recent years OSL techniques have been increasingly combined with GPR surveys (Bristow et al. 2005, 2007a, and 2007b) in linear dune field surveys (see the example shown in Figure 2-5). The vertical chronology of linear dunes has also been simulated numerically (Telfer 2010; Bailey and Thomas, 2014; Leighton, et al., 2014).

Similarly to transverse dunes (e.g. Brothers et al., 2016; Day and Kocurek, 2017), the internal stratigraphy seen is not only driven by the ongoing wind regime, but also by historical wind conditions and bedform evolution. An example is offered by the opposite strata dipping directions between Profile 2 and Profile 4, Figure 2-5 (A)). In these scenarios, a linear dune may originate from reshaping of other dune types (Lucas, et al., 2015). In addition to the historical bedform type evolution, the GPR image provided in Figure 2-5 (B) demonstrates combination of the main strata resulted from sideways moving associated with bounding surfaces truncating the strata. The truncations are reflective of either the reactivation of the strata by a reversed wind or superposition between dunes (Bristow, et al., 2005; Bristow, 2008). For a linear dune, the lack of net lateral migration, on the one hand, preserves longer historical records for OSL surveys as described above, on the other hand, it complicates interpretation of the internal structure.

(A)



(B)

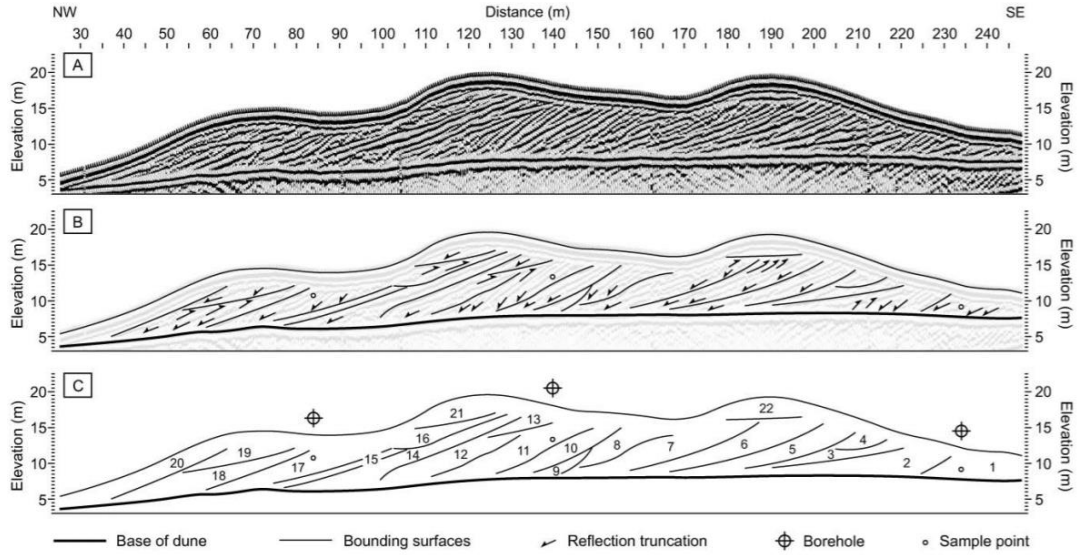
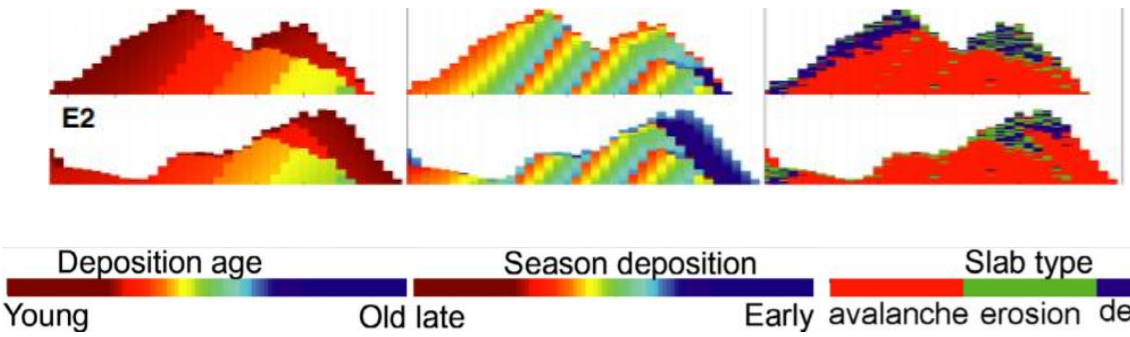


Figure 2-5. Internal sedimentary structure of linear dunes mapped with GPR. The two dunes surveyed are located in one dune field. (A) Cross sections at varying locations of one dune (Bristow, et al., 2000) (B) Cross section with identified cross strata and bounding surfaces (Bristow, et al., 2005).

Generally speaking, the internal stratigraphy of linear dunes is built not only by the established dune, but also by the memory (e.g. Warren and Kay, 1987; Wiggs, 2021) of bedform development history. This has been demonstrated by some recent numerical simulations (e.g. Liu and Baas, 2020), presented in Figure 2-6. Figure 2-6 (A) shows unidirectional dips with superposition surfaces are buried beneath the linear dune, while at the time when they were preserved, the bedform was actually a transverse dune because the 'annual' oscillation distance does not exceed the dune width. Similarly, in GPR profiles (Figure 2-5 (A), Bristow, et al., 2000), the strata was also interpreted (Livingstone, 2007) as partially occurring to the dune termination. Further, even after a linear dune has adequately adapted to the wind with the historical records (e.g. transverse dune strata and collisional surfaces) removed, the stratigraphy may still change phases. For example, Figure 2-6 (A) indicates an increase of the strata symmetry at two steady stages (i.e. without superposition surfaces fully removed).

To summarize, the internal sedimentary structure of established linear dunes is not a unified pattern, but depends on temporally the data collection time and spatially the survey locations on the dune ridge.

(A)



(B)

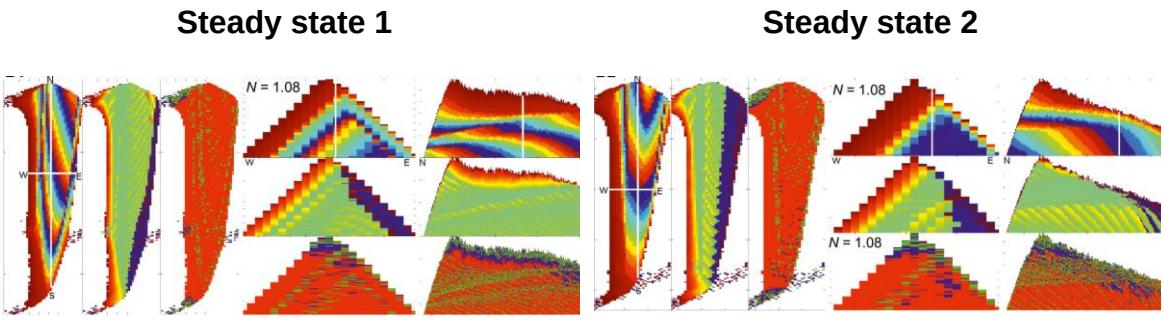


Figure 2-6. Sedimentary structure of linear dunes modelled with the Werner 1995 CA (sourced from Liu and Baas, 2020), under the same wind regime at varying development histories (A) Time sequence of a bedform interaction before a steady state has been reached, involving temporary lateral migration of the earlier dune and a low angle bounding surface. (B) Stratigraphy at two steady states, built by the existing dune that has sufficiently adjusted to the (symmetrical) ongoing wind regime (i.e. dune interaction stratigraphy excluded). Steady state 2 is 20 model years later than Steady state 1

2.3.2 Knowledge gaps

To summarize issues surrounding linear dunes, the complexity of the sedimentary structure originates from variations depending on time and space. A linear dune has varying internal stratigraphy at varying evolution stages and varying portions through the dune. The structure may be recorded by dune interaction or change of wind regime, both of which highly depends on manual interpretation (e.g. Bristow, et al., 2007; Bristow, 2008). Further, due to crest oscillation, the lack of net lateral migration of linear dunes enables better preservation of the stratigraphy built by the earlier dune activities, whilst dynamic of the established dune may not be sufficiently reflected in the sedimentary records. Correspondingly subsequent chapters involve the dynamic of an existing linear dune (based on wind angle and speed effect in Chapter 4 to investigate lateral migration potentials in Chapter 5) as well as

the building process of the linear dune (with a focus on elongation in Chapter 6).

Chapter 3 Models and methods

As noted in Chapter 1, the aim of this thesis is to deploy a numerical model to investigate the wind flow controls on the internal sedimentary structure of sand dunes. This chapter on the one hand reviews previous modelling work surrounding dynamics of sand dunes, on the other hand, outlines detailed considerations for model requirements to fulfil the aims of the thesis model. To start, Section 3.1 introduces numerical simulation of aeolian dunes in previous work and justifies the use of discrete models rather than continuous models for the purposes of the thesis. Section 3.2 discusses the details of discrete model types and explores how they can be developed to fill in research gaps identified in Chapter 2.

3.1 Review of numerical simulation of sand dunes

3.1.1 Modelling morphology of dunes

Both continuous numerical models (e.g. Howard, et al., 1978; Wippermann and Gross, 1986; Sauermann, et al., 2001; Kroy, et al., 2002 Hersen, 2004; Parteli et al., 2012) and discrete models (cellular automaton, CA, Nishimori and Ouchi, 1993; Werner, et al., 1995; Nishimori, et al., 1998; Momiji, et al., 2000; Bishop, et al., 2001; Narteau, et al., 2009; Rozier, et al., 2014) have been developed to simulate the dynamics of sand dunes. For the continuous approach (also termed as ‘analytical models’, e.g. Wiggs, 2021), the dune is treated as a continuous surface controlled by sets of aerodynamic equations, seeking for quantitative accuracies. In comparison, in CAs, the dune is treated as individually controlled cells (or slabs, in Werner model work), mimicking the quantitative patterns of the bedform evolution. Behind the CA approach is the complexity theory where the aeolian bedform at varying hierarchies with pattern similarities has long been studied (e.g. Allen, 1968; Anderson, 1990; Forrest and Haff, 1992; Werner and Gillespie, 1993; Anderson and

Bunas, 1993; Haff, 1994; Landry and Werner, 1994; Werner and Kocurek, 1997 and 1999; Baas, 2002 and 2007; Day and Kocurek, 2018).

Simulating sand dunes using a numerical model usually starts with unidirectional wind scenarios where barchans or transverse dunes occur, (e.g. Howard, et al., 1978; Werner, 1995; Sauermann, et al., 2001; Kroy, et al., 2002; Hersen, 2004; Narteau, et al., 2009; Mayaud, et al., 2017) because the environmental wind condition is simple and unidirectional. Wind rotation in a modelling system (to enable simulation of a bi- or multi-modal wind regime) is expensive in time (e.g. Nield and Baas, 2007; Narteau et al., 2009; Mayaud, et al., 2017) and encounters difficulties of resampling as the dune is processed based on squared cells in a Cartesian coordinate system (e.g. Nishimori, et al., 1998; Baas and Nield, 2007; Mayaud, et al., 2017). In comparison, a constant unidirectional wind is the simpler regime to mimic. Also, for barchan simulation, there are sufficient field measured data surrounding the dune geometry (e.g. Finkel, 1959; Long and Sharp, 1964; Wiggs, et al., 1996a; Hesp and Hasting, 1998; Sauermann, et al. 2000; Hersen, et al., 2002; Bourke and Goudie, 2009) that may be compared with modelled simulations to allow model validation.

Surrounding barchans and transverse dunes, in addition to the geometric features, numerical modelling work had a focus on bedform interaction---the internal driver of dune stratigraphy (as specified in Chapter 1). Transverse dune field patterns have been identified with continuous models (e.g. Parteli, et al., 2006) and CAs combined with remote sensing images (e.g. Kocurek, et al 2007; Ewing and Kocurek, 2010a and 2010b; Eastwood, et al., 2012; Day and Kocurek, 2018). Numerical models were also employed for identification of barchan interaction cases (e.g. Schwämmle and Herrmann, 2003; Katsuki, et al., 2005; Durán et al., 2007; Elbelrhiti, et al., 2008;

Nishimori, et al., 2009; Durán et al., 2009), particularly for demonstration of the long discussed solitons and solitary wave pattern (e.g. Besler, 2002; Endo, et al., 2004 and 2005; Durán et al., 2005; Schwämmle and Herrmann., 2005; Livingstone., et al, 2005; Vermeesch, 2011; Hulgenholtz and Barchyn, 2012; Assis and Franklin, 2020). Additionally, previous work focused on barchan dune size sorting (e.g. Andreotti, et al., 2002; Hersen and Douady, 2005; Durán et al., 2011) as a result of inter-dune collisions. Also, numerical models were deployed to explain the rarity of transverse dune distribution in realistic dune fields (Parteli, et al., 2011; Yizhaq, et al., 2012; Niiya, et al., 2012 and 2013). Here the term 'transverse instability' is proposed, referring to the scenario where a transverse ridge (transversely) breaks into barchans under long term unidirectional wind periods. In addition to dunes based on bare sand, ecology components have been coupled by both continuous (Lima et al., 2004) and CA (Baas, 2002 and 2007; Baas and Nield, 2008; Nield, 2010; Yan and Baas, 2017 and 2019; Mayaud, et al., 2017) models.

For bimodal wind regimes, continuous models and CAs have both been deployed to simulate linear dunes. Parteli, et al. (2009 and 2014) investigated linear dune formation in response to the directionality of bimodal wind regimes. In earlier work, Werner (1995) and Nishimori, et al. (1998) had an initial attempt at linear dune simulation when presenting the early versions of their models. More recently, linear dunes have been increasingly investigated with CAs surrounding multiple purposes, such as the longitudinal extension (Gao et al., 2016; Rozier, et al., 2019), dune field periodicity (Gadal et al., 2020) and dune field patterning process (Liu and Baas, 2020). In general, comparing with continuous models, CAs were more extensively applied in linear dune simulations. This is partially due to the time expenses of

running continuous models and wind rotation (with sacrificing aerodynamic accuracies to some extent).

3.1.2 Possibilities of mapping the stratigraphy

Mapping the stratigraphy may be implemented using both continuous models and CAs. Throughout the entire evolution history of the dune, stacking up the instantaneous morphological surfaces (elevation) eventually can map the preserved cross beds.

A key advantage of CAs over continuous models is that they are capable of tracking properties of interest of each individual cell. For example, they are able to store the full set of sediment age data at the minimal time unit (i.e. a much shorter scale than calendar seasons) and minimal spatial unit (i.e. usually within one meter). This has been implemented in CAs developed from Werner (1995) and Narteau, et al. (2009) by attaching a time marker to each individual cell (i.e. Zhang, et al., 2012; Liu and Baas, 2020). The time marker is refreshed whenever the sand is moved either by wind or in avalanche. Also, the grain sorting and segregation were studied in aeolian ripples (Anderson and Bunas, 1993) and dunes (Gao et al., 2016).

In addition to the two types of dune dynamic model, the chronology was previously modelled with other approaches. Telfer, et al. (2010) attempted to monitor the vertical accumulation of a linear dune, and Bailey and Thomas (2014) further developed the chronology model and identified forcing of dune growth. They both were implemented on a 1D column basis. There are also other numerical approaches to aeolian dune stratigraphy, like geometric visualization (Rubin, 1987) and stratigraphy replication with a 2D transect model (Swanson, et al., 2017 and 2019). Comparing to the continuous / analytical dune dynamic simulations and CAs,

these stratigraphy based models focus on visually replicate the stratigraphy, rather than generating it with aerodynamic controls.

3.1.3 Initial model selection

The knowledge gaps identified in Chapter 2 include questions involving components of wind in bi- directions and linear dunes, of which accurate representation of the chronology of the internal sedimentary structure is particularly important with regards to palaeo-environmental reconstruction (e.g. e.g. Duller and Augustinus, 2006; Fitzsimmons et al., 2007; Telfer and Thomas, 2007; Stone and Thomas, 2008; Bristow et al., 2005 and 2007; Srivastava et al., 2019). Considering the capability of sand age tracking, here firstly CA is prioritized rather than a continuous model. In addition to the data abundance, the computing time of CAs is much shorter than continuous models. For example, a 20 m high barchan takes a few minutes to model in a CA, but over ten hours in a continuous model (Nishimori, et al., 1998; Katsuki, et al., 2005). When running linear dune building scenarios, the computing time becomes even more significant due to the long time required for elongation.

3.2 Types of Cellular Automaton (CA) sand dune models

Wind-blown landscapes over sand, including ripples and dunes, have long been analysed and numerically simulated with discrete approaches (e.g. Forrest and Haff, 1992; Anderson and Bunas, 1993). There are two base models currently available for simulating sand dunes using CA.

Werner (arguably) model

---(1) Sand dune simulation using CA was first published by Nishimori and Ouchi (1993a), followed by revised versions (e.g. Nishimori, and Ouchi, 1993b; Nishimori, et al., 1995; Katsuki, et al., 2005 and 2012). Werner (1995) also introduced a set of CA algorithms to simulate aeolian dunes. The two models share very similar base

algorithms in terms of aerodynamics and dune generation with slight (trivial) difference in parameter settings. Although the Nishimori and Ouchi (1993a) CA was the earliest introduced in CA history for aeolian dune study, this model has been much less known and developed by subsequent users than Werner (1995) (Google Scholar shows 37 citations for Nishimori and Ouchi, 1993a and 399 citations for Werner, 1995). As Werner 1995 CA has been referred and deployed by a wider range of users and for more multiple purpose (e.g Momiji, et al., 2001; Kocurek and Ewing, 2005; Nield and Baas, 2008; Eastwood, et al., 2012; Liu and Coulthard, 2015 and 2017; Mayaud, et al., 2017), here in the thesis it is referred as 'Werner model'. In the CAs, sand is considered as square (2D) or cubic (3D) cells under rules manually defined by simplifying wind flow dynamic. Figure 3-1 below presents the fundamental algorithms involved in the Werner model. Aerodynamic rules include defined probabilities for erosion, transport and deposition. The three probabilities are indicative of strength of the environmental wind. For secondary flows, a 'shadow zone' is enforced to simulate the flow recirculation in the lee (e.g. Baas and Nield, 2008; Nield, 2010). The setting applies the commonly found 4 dune heights (see details in Chapter 2.1) horizontal distance from the crest to downwind. Within the shadow zone, sand erosion and transport are disabled and deposition is enforced with certainty. Additionally, an avalanche event is initiated whenever the elevation gradient between neighbouring cells exceeds the threshold of 30 degrees.

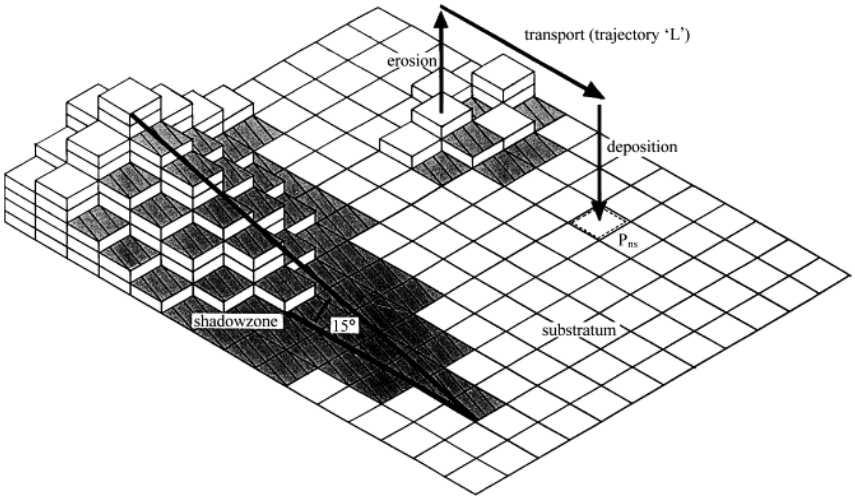


Figure 3-1. Schematic of simplified aerodynamic rules in Werner, 1995 model (Baas, 2002): erosion, transport, deposition of the environmental wind and shadow zone for the secondary flow in the lee (flow recirculation of four dune heights horizontal distance).

The original Werner (1995) CA has been applied and revised to fit a wide range of needs, such as modelling vegetated dunes (e.g. Nield and Baas, 2007; Yan and Baas 2016 and 2018; Mayaud et al., 2017), dune field patterns (e.g. Ewing, et al., 2006; Eastwood, et al., 2011), wind speed up (Momiji, et al., 2000), dune-river interaction (Liu and Coulthard, 2015 and 2017). All these revised versions do not radically change the basic algorithms shown in Figure 3-1.

ReSCAL

---(2) A Real Space Cellular Automaton (ReSCAL) model was first presented by Narteau (2006) using a CA to mimic sand movement. This version has the same fundamental nature as the Nishimori and Ouchi (1993) and Werner (1995) model. Elements including 'air' and 'sand grain' are implemented by defining the type of each pair of neighbouring cells termed as 'doublet'. Following the initial version, ReSCAL was revised to include a Lattice Gas (LG) element that generates a

theoretical wind flow field, first presented by Narteau, et al., (2009). The general algorithms of ReSCAL are schematized in Figure 3-2 and explained with more details below.

Lattice Gas

The LG wind is implemented by a propagation phase and a collision phase between airflow particles (e.g. Narteau, et al., 2009; Zhang, et al., 2012; Rozier, et al., 2014), while the momentum of a LG system is maintained during each propagation and collision (Figure 3-2) process and the wind strength is expressed by the number of particles on each node. Traditional LG simulations are based on hexagonal systems (e.g. Hardy, et al., 1976; Frisch, et al., 1986; Chopard and Droz, 1988; Wolf-Gladrow, 2004). In ReSCAL, the coupled LG wind is revised from these previous versions to rectangular coordinate systems so that it can be coupled with the grids of the sand dune CA.

Sand/Dune CA

In the fundamental structure, there are three types of cells: airflow (wind) cells, immobile grain cells (sand forming the dune body) and mobile cells (sand being transported, not forming the dune body). A ‘doublet’ means a pair of cells combined with two types of cells, aligned either horizontally or vertically (Figure 3-2), forming the configuration ready to go through the transitions. Doublet transitions include the three wind driven processes (i.e. erosion, transport and deposition), the gravity driven process (i.e. avalanche or grain flow), as well as a random lateral (to the wind direction) sand movement. Here the topography within a model domain is described with the number of immobile grain cells stacked up on each specified location. This sand/dune CA can run without the LG, leading to similar outputs to Werner model.

The key difference of ReSCAL from Werner model is coupling of the LG wind. The wind strength and direction are instantaneously adjusted to the topography in the sand/dune CA, as detailed below.

Coupling of lattice gas (LG) wind to sand movement in ReSCAL

The theoretical wind modelled with LG is incorporated into ReSCAL to determine the local erosion rate R_e at the topography. For each node (i.e. each cell location) in the Cartesian coordinate system, firstly the local shear stress is jointly determined by the LG wind velocity $\vec{V}$ and the local topography in the relationship

$$\tau_s = \tau_0 \frac{\partial \vec{V}}{\partial \vec{n}} \qquad \text{Equation 3.1}$$

where τ_0 is a stress scale of the model and $\vec{n}$ is the normal topography of the local cell. Further, the erosion rate R_e is determined by Equation 3.2 when $\tau_{min} < \tau_s < \tau_{max}$. For $\tau_s < \tau_{min}$, the wind is too weak to erode, for $\tau_s > \tau_{max}$, the erosion rate is R_0, as clarified in Figure 3-2 (C).

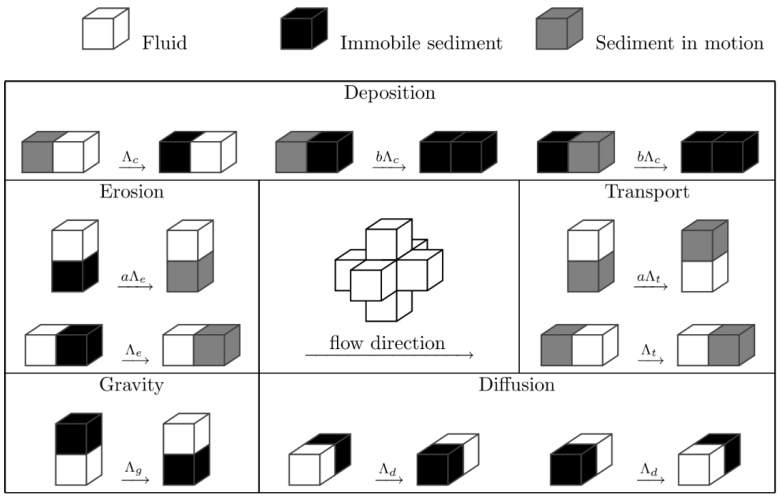
$$R_e = R_0 \frac{\tau_s - \tau_{min}}{\tau_{max} - \tau_{min}} \qquad \text{Equation 3.2}$$

In this equation, R_0 is a constant rate, τ_{min} is the minimum shear stress threshold to enable erosion events, and τ_{max} is the maximum threshold to apply the linear relationship (1) with τ_s (smaller than τ_{max}). The R_e is computed at each minimum time unit t_0 and enforced on the local coordinate point (i.e. cell location) to describe the wind erosivity over the cell surface.

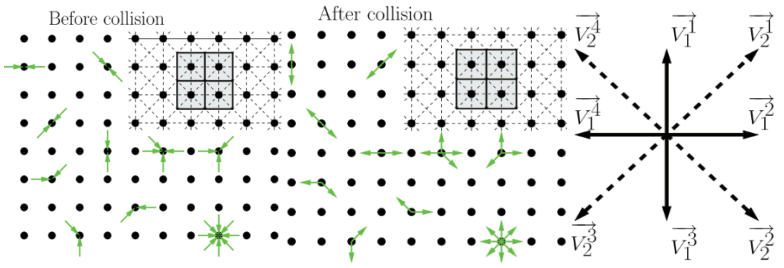
The ReSCAL model has been employed to explore multiple aeolian bedform types, such as star dunes (Zhang, et al., 2012), superimposed bedforms (Zhang, et al.,

2012), elongating dunes (e.g. Gao, et al. 2016; Rozier, et al., 2020; Gadal, et al. 2019) and reversing dunes (Gao, et al., 2021)

(A) Doublets transition types



(B) 8 vectors of fluid(air) particle and their collision rules



(C) Erosion rate R_e with respect to shear stress τ_s

$$\tau_s < \tau_{min}, R_e = 0$$

$$\tau_{min} < \tau_s < \tau_{max}, R_e = R_0 \frac{\tau_s - \tau_{min}}{\tau_{max} - \tau_{min}}$$

$$\tau_s > \tau_{max}, R_e = R_0$$

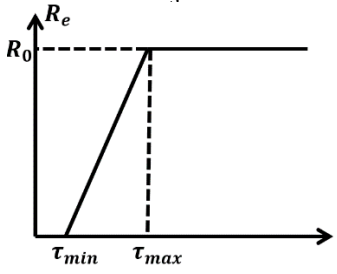


Figure 3-2. Schematic of a Real Space Cellular Automaton (ReSCAL) model (Narteau, et al. 2009). (A) Configuration of doublets and their transition types including sand grain cells and air cells (B) Lattice Gas (LG) Boltzmann

theoretical wind including a propagation phase and a collision phase maintaining the momentum of the airflow particles. (C) Coupling rules of the sand movement model in (A) and LG model in (B): the local erosion rate R_e is determined by the shear stress τ_s.

3.3 Comparison and selection of CAs

3.3.1 Comparison and selection criteria

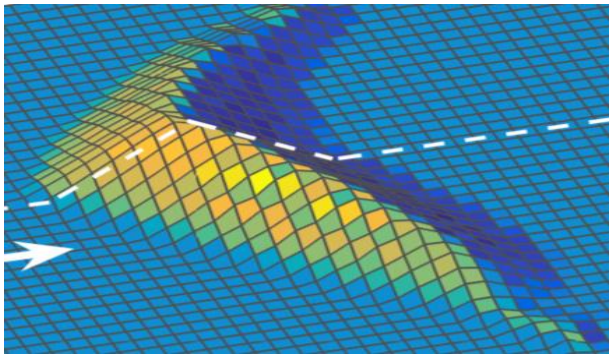
Table 3-1 provides a brief comparison between Werner (1995) model and ReSCAL (Narteau, et al., 2009). As specified in Section 3.2, the nature of sand movement is same for the two types. They both apply probabilities to determine the occurrence of erosion, transport and deposition. They also apply the same avalanche rules, checking the gradients whenever there is a change of elevation. In addition, the initial ReSCAL version of Narteau, et al., 2006 and Werner model both suffer from simulating symmetric cross sections, i.e. the lee slope being equally long to the stoss slope. This is due to the lack of speed up with increase of the elevation. Figure 3-3 (A) presents a barchan dune (Mayaud, et al., 2017) showing this symmetry feature modelled with a recent Werner model version. Figure 3-3 (B) provides a set of transects produced where a range of speedup coefficients is tested by Momiji, et al. (2000) using the Werner model frame.

For ReSCAL, with inclusion of the lattice gas (LG) flow in the ReSCAL model, more realistic asymmetric profiles are simulated (Figure 3-3 (C)). In addition to the dune transect geometry, the overall wind flow modelled with LG (Zhang, et al., 2010) is (qualitatively) in general agreement with the commonly agreed wind profile (see the schematic of Figure 2-1, also validated in the starting section of Chapter 4).

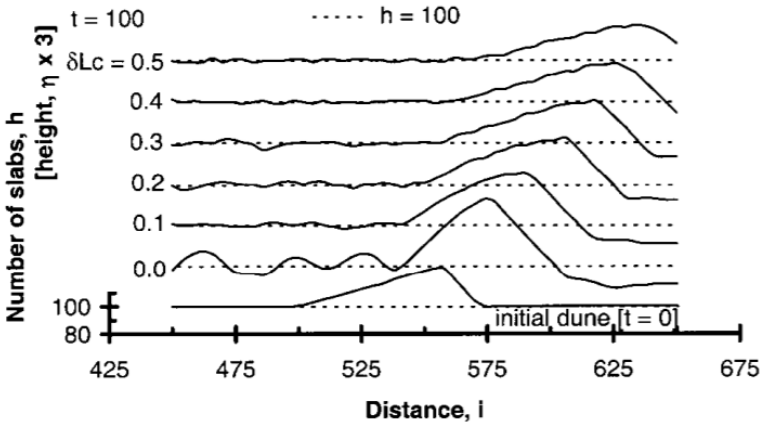
Table 3-2. Comparison between the two sand dune dynamic CAs: Werner model and ReSCAL.

	Werner, 1995 CA	ReSCAL
Literature examples	Nield and Baas, 2007; Eastwood, et al., 2012; Mayaud, et al., 2017	Narteau, et al., 2009; Zhang, et al., 2012; Rozier, et al., 2020; Gadal, et al., 2019
Wind algorithm	Simplified wind dynamic rules, wind not modelled instantaneously	Lattice Gas (LG) Boltzmann wind added, instantaneously adapted to the local topography of each cell, controlling the erosion rate
Sand movement layer	Direct moving cells to monitor the topography	Cell type transition based rules, sand indicated by immobile sediment cells
Flow recirculation	15-degree shadow, 3.72 dune heights long	LG generated, approximately one dune height long.
Users	Wide range of users	Mostly used within the model developing team
Flexibility	Highly flexible to be revised and do simplification testing	Lower flexibility for revision, LG machine not possible to be revised
Clarification of algorithm	All rules matched up to physical process, e.g. shadow zone to flow recirculation	Diffusion transition (random sand movement perpendicular to winds) not clearly explained

(A)



(B)



(C)

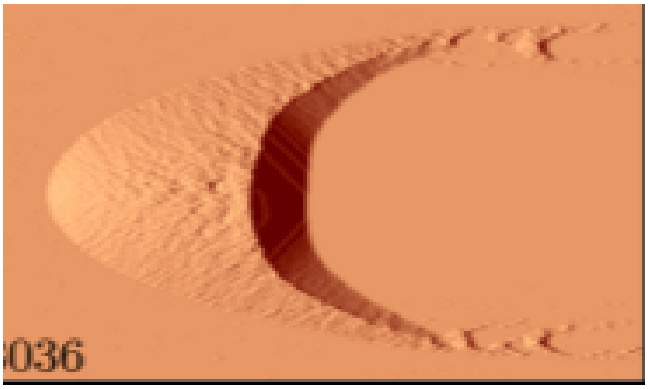


Figure 3-3. Wind speedup stoss slope effect on geometries of transverse dune (including barchans) transects. (A) Barchan dune shown in Mayaud, et al., 2017 using Werner model without wind speedup (B) Sand dune 2D transects

presented in Momiji, et al., 2000 with varying speedup coefficient enforced on Werner model. (C) Barchan dune example presented in Narteau, et al., 2009 with LG wind coupled.

The Werner (1995) CA has been recoded and applied by a wide range of users because the implementation of the rules is simple. The high simplicity of the wind flow algorithm seen in Figure 3-1 leads to a high flexibility of revision for multiple purposes, for example, testing the speedup effect (Momiji, et al., 2000). Further, all parameters are matched to specific environmental parameters so that the probabilities of erosion, transport and deposition reflect wind speeds, the shadow zone is sourced from the flow recirculation of 4 dune heights.

In comparison, the application of ReSCAL has been generally limited to within the research group (e.g. Zhang, et al., 2010; Rozier, et al., 2014; Gao, et al., 2016; Lv., et al., 2017; Gadal, et al., 2020) that developed it. The cell transition based sand movement takes far longer time to compute than directly moving slabs in the Werner model. Additionally, the ‘diffusion’ process (included in Figure 3-2 (A)) of a doublet has not been completely clarified, whilst the model outputs are sensitive to the diffusion rate. The key advantage of ReSCAL however, is the Lattice Gas (LG) component. In effect it is a discrete Computational Fluid Dynamic (CFD) model that generates a fundamental flow pattern around the topography. Comparing with simplifying aerodynamic rules in Werner model, the LG provides more dedicated flow pattern that interacts with the bedform.

For knowledge gaps suggested in Chapter 2, a physical ‘wind’, rather than manually defined aerodynamic rules is needed. Particularly for the issue regarding flow pattern with respect to dune morphology under varying wind angles, previously

measured field or experimental data are not sufficient for making universal algorithms (like the 'shadow zone' mimicking the four dune heights flow recirculation in Werner model) for a sand and dune dynamic CA. Therefore it is determined a computed 'wind' is necessary to solve aerodynamic issues of wind strength and directions control on dune dynamic. Firstly, two options were considered in the first place, one is to separately couple a computing fluid dynamic (CFD) model with Werner model, the other is to deploy ReSCAL. For the first option, there are CFDs that are capable of generating more accurate wind patterns than the LG in ReSCAL, whilst the high accuracy also costs significantly longer computing time and brings extra difficulties of coupling with square (2D) and cube (3D) based sand/dune CAs. Therefore for the considerations (1) needs of a 'wind' (rather than empirically simplified aerodynamics) and coupling with the sand/dune CA (2) reasonable computing time that allows for sufficient simulations to be tested, ReSCAL is selected.

3.3.2 Specification of the selected CA

Below more details are provided surrounding simulating sand dunes and their internal stratigraphy using ReSCAL.

Scaling of time and space in ReSCAL

For the setting of time and length scales in ReSCAL model, so far a rough estimation has been made and first explained with full details by Narteau, et al. (2009). The spatial scaling is based on the assumption (e.g. Elbelrhiti, et al., 2005 and 2008; Claudin and Andreotti, 2006) that the minimum crest-normal (stable) wave length of transverse dunes (including barchans) is approximately 20 m on the Earth. Dunes smaller that this size were thought to be not persistent (e.g. Kocurek, et al., 1991; Elbelrhiti, et al., 2005; Narteau, et al.,

2009), but interact, merge, superimpose each other until the stable wave length is reached. In ReSCAL model (e.g. Narteau, et al., 2009), this minimum wave length is 40-cell width (40 l_0), hence the width of each cubic cell is 0.5 m.

With this fundamental method for setting the space scale, the temporal scales are estimated accordingly (Narteau, et al., 2009): (1) run ReSCAL for a time duration t and compute the total sand flux (on a flat surface) caused, (2) take the realistic time duration needed for the same sand flux (assuming the cell width $l_0 = 0.5\,m$) and calculate how long the minimum time unit t_0 represents. For example, over a given cell surface, if ReSCAL runs for 10 t_0 during which a total sand flux q is caused (practically one transition time between a flow cell and a grain cell) and the realistic time in a natural sandy surface is 60 minutes, hence each t_0 is equivalent to 6 minutes in realistic time.

Implementation of varying environmental wind strength (speed)

In ReSCAL model, varying wind speeds is not implemented by changing the wind profile itself, but by changing the wind erosivity over the local cell surface of the same wind profile modelled in LG. Practically, as detailed in 3.2, a wind shear stress τ_s is computed with LG for the instantaneous topography, there is a minimum shear stress threshold τ_{min} to enable erosion transitions (Figure 3-2 (A)). The surface of the local cell is enforced with the linear relationship (Equation 3.2, Section 3.2) where τ_s is greater than τ_{min}. For example, assuming $\tau_s = 250\,\tau_0$ over a given location, if τ_{min}=300 τ_0, the surface is disabled from erosion, while if $\tau_{min} = 100\,\tau_0$, an erosion rate is enforced based on Equation 3.2.

Visualization of the stratigraphy using time data stored

As specified in Section 3.1 of this chapter, a key advantage of CAs over continuous / analytical dune dynamic models is the capability of storing full sets of chronological data with the highest resolution, spatially for each individual cell and temporally for each minimum time unit t_0. Patterns of the stratigraphic beddings can be visualized using this grain cell property at a given time step. Practically, with the deposition time (absolute time from the initial condition t=0) matrix, for example, for every 2000 t_0, the surface line is taken from the body with grain cells no younger than the specified deposition time. This method is used through the thesis where depositional beddings are visualized.

More detailed limitations and advantages of ReSCAL model will be revealed in explorations of Chapter 4 to Chapter 6 and concluded in Chapter 7.

Chapter 4 Wind speed and angle impact on transverse dune dynamics under unimodal winds

This Chapter explores the flow pattern, corresponding sand movement and the internal sedimentary structure of dunes controlled by the two wind properties (e.g. Sweet and Kocurek, 1990; Eastwood, et al., 2012): wind speeds and wind-incident angles. All simulations are run on a transverse dune. At first place, Section 4.1 presents the simplest scenario of a wind perpendicular to the dune crest at a fixed speed, explaining and validating general wind flow structure modelled with lattice gas (LG) and sand moving processes simulated with ReSCAL. Section 4.2 progresses to explore a set of wind speeds with the perpendicular wind, whilst Section 4.3 investigates a range of wind-incident angles with a fixed wind speed.

Each of the first three sections 4.1, 4.2 and 4.3 includes three sets of explorations: (1) mapping the wind shear stress profiles modelled with the LG over a controlled topography; (2) analysing the instantaneous sand movement over the topography by computing both the magnitude of sand moving processes driven by winds and gravity, and also the overall sand flux; (3) analysing the internal stratigraphy and chronological structure.

The sets (1) and (2) above present instantaneous processes occurring on surfaces of the (controlled) existing dune. Outputs of the two sets are compared with previously measured wind profiles over dunes (e.g. Tsoar, 1983; Livingstone, 1986; Wiggs, et al., 1996(a,b); Schatz and Herrmann 2006; Baddock, et al., 2007 and 2011) as well as lee-side grain flow studies (e.g. Sutton, et al., 2013 (a, b); Nield, et al., 2017; Cornwall, et al., 2018). Set (3) extends the time scale to allow the dune sufficient time to adapt to the enforced wind, investigating how the sedimentary structure is influenced by surface processes of sets (1) and (2). Outputs of Set (3)

are compared with previous sedimentology work regarding properties of cross strata (e.g. Tanner, 1965; Parrish and Peterson, 1988; Mountney and Jagger, 2004; Rowe et al., 2007; Eastwood, et al., 2012). In general. Chapter 4 here has a purpose to fill in knowledge gaps identified in 2.1 and 2.2 in Chapter 2, addressing the wind speeds and wind angles control on dune surface processes and the internal stratigraphy.

4.1 Flow pattern, sand movement and sedimentary structure of a transverse dune (crest-normal wind at a fixed speed)

This section presents the simplest scenario where a transverse dune is enforced with a speed-fixed wind perpendicular to the dune crest. The shape of the transverse dune is idealized: the whole lee slope is at the angle of repose and the dune crest has no sinuosity to ensure a controlled wind-crest angle. The dimension of the domain and the dune topography image are shown in Figure 4-1 (A). The 26-cell high and 60-cell wide (in average of the 200 central slices between the two white lines labelled) transverse dune is located on a 400-cell wide (in N-S direction) and 600-cell long (in W-E direction) field. This initial topography was generated with ReSCL. Firstly the avalanche rule is enforced on a linear bar orientated to N-S, forming a symmetrical dune with both slopes at the repose angle. Secondly a westerly wind ($\tau_{min} = 0$) is enforced for a duration of 200 t_0, flattening the stoss (west) slope and leading to the topography shown in Figure 4-1 (A).

The length of the domain allows adequate distance for the secondary wind recovery to the environmental wind. The N-S boundaries are periodical, connecting the dune at the two boundaries, avoiding formation of dune terminations and keeping the topography the simplest. The crest normal wind is enforced at the highest wind speed where $\tau_{min} = 0$, which means the wind can erode sand as long as the LG

modelled wind shear stress is greater than 0. In this simulation system, there is no extra sand supply from external sources.

4.1.1 Flow pattern and sand movement on the surface

The wind shear stress profile modelled with LG is presented in Figure 4-1 (B). In addition to shear stress τ_s values, a fractional speedup ratio δ_s is also labelled to describe to what extent a τ_s changes from the environmental wind:

$$\delta_s = (\tau_s\text{-}\tau_{flat})/\,\tau_{flat} \qquad \text{Equation 4.1}$$

Where τ_{flat} takes the mean shear stress between downwind distances 80-cell and 150-cell of Figure 4-1 (B). The fractional speedup ratio here has been commonly deployed by previous study for quantifying the wind strength change over a dune topography (e.g. Jackson and Hunt, 1975; Wiggs, 1993; Baddock, et al., 2007). Some general features of the flow shear stress are indicated by Figure 4-1 (B) and they are in good agreement with the documented wind pattern in previous work (schematized in Figure 2-1, Chapter 2):

---Reduction of 2/3 of the flat surface shear stress δ_s at the foot when approaching the dune from 301 τ_0 to the minimum of 103 τ_0, between downwind distances 250-cell to 300-cell. Previous wind flow measurements taken on barchans and transverse dunes have well demonstrated this wind weakening feature (qualitatively), including in field surveys (e.g. Howard, 1978; Baddock et al., 2011) and numerical simulation (e.g. Walmsley and Salmon, 1984; Jensen and Zeman, 1985; Claudin et al., 2003; Zhang, et al., 2010; Michelsen, et al., 2015). Wind flow measured over linear dunes also shows the deceleration when approaching the dune as an obstacle, for example, in wind profiles measured by Wiggs, et al., 1996(b)) in fieldwork.

---Increase of the shear stress along the windward slope from 103 τ_0 to 420 τ_0, over three times higher than the dune foot minimum, between downwind distances 300-cell to 400-cell. This windward speedup has been commonly found by previous work (e.g. Howard 1978; Lancaster, 1985; Livingstone, 1986; Mulligan, 1988; Frank and Kocurek, 1996a; Lancaster, et al., 1996; Wiggs et al., 1996 (a); Neuman, et al., 2000; Baddock, et al., 2011, Araújo, et al., 2013; Walker and Hesp, 2013). Both transverse dunes and linear dunes were involved in the previous work. The acceleration is due to squeezing of the flow streamlines and in a stable flow field (e.g. Wiggs, 2021). Also, in the dune-wind interaction (comparing to dune-flat surface), the same amount of flow needs to travel over a longer distance for the same time duration, hence the speed gets faster than over a flat surface.

---Decrease of the shear stress in the lee after passing the crest from 420 τ_0 to 120 τ_0 between downwind distances 400-cell to 450-cell. This is the key flow feature that forms net deposition and dune stratigraphy and originates from releasing of the streamlines squeezed over the windward slope. As identified in Chapter 2.1, this feature has been adequately demonstrated by previous wind profiles measured on barchans and transverse dunes in field surveys (e.g. Sweet and Kocurek, 1990; e.g. Frank and Kocurek, 1996; Baddock, et al., 2007), numerical simulations (e.g. Schatz and Herrmann, 2010; Parsons et al., 2004) and wind tunnel experiments (e.g. Dong et al., 2003; Walker and Nickling, 2003). Wind profiles measured on linear dunes (detailed in Chapter 2.2) also demonstrate this deceleration (e.g. Tsoar, 1983; Livingstone, et al., 1986; Wiggs, et al., 1996 (b)).

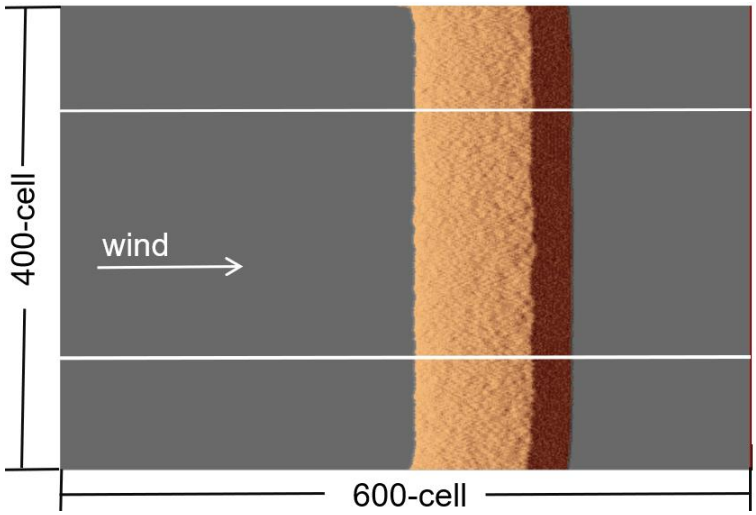
---Recovery of the shear stress starting from the middle of the lee slope at downwind distance 450-cell where the shear stress has reached the minimum of 120 τ_0 on the slope. The shear stress recovers to the strength of the environmental wind at downwind distance of 550-cell, approximately 10 dune heights distance from the crest to downwinds. This recovery distance was also found by previous work by Parsons, et al., 2004, Baddock, et al., 2007 and so forth.

For the shear stress profile given in Figure 4-1 (B), there are two features that tend to be not in agreement with previous work: (1) negative τ_s (reversed wind in flow recirculation) is not indicated (2) recovery of the wind strength starts on the lee slope. Nevertheless, the wind flow pattern modelled with LG generally agrees with the literature. This simplified CFD version does not aim at quantitative accuracies of natural wind measured, but only simulating a qualitative pattern.

Under the shear stress profile of Figure 4-1 (B), at the highest wind speed setting $\tau_{min} = 0$, any surface cells can be eroded with a possibility where the sand-flow doublets  (e.g. the left cube is an airflow cell and the right cube is a sand grain cell) and  (i.e. an airflow cell stacked on a sand grain cell) are available.

In the LG wind of ReSCAL model, on the lee slope, practically the disabled wind carrying sand is not implemented by generating recirculated wind with negative shear stress, but by setting a lack of doublets ready to be eroded. The first type of doublets  mostly exist on the windward slope and occasionally the transition can occur on the lee slope where the slope is not perfectly smooth but with bumps. The second type of doublets  are available for erosion processes throughout the whole dune, at a low possibility of occurrence.

(A)



(B)

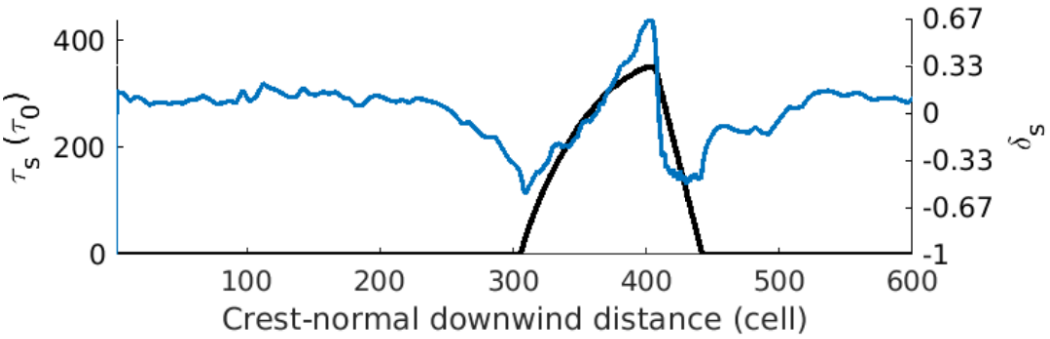


Figure 4-1. Wind shear stress modelled with lattice gas (LG) over a transverse dune 26 cells in height with the wind perpendicular to dune crest at the highest strength ($\tau_{min} = 0$) and lee slope fully covered by the slip face. (A) Topography image of the whole model domain (B) Shear stress τ_s (fractional speedup ratio δ_s labelled together) over the 2D crest-normal transect (topography vertically exaggerated). The shear stress and the topography both take the average of the 200 transects between the two white lines labelled in image (A).

To track the sand moving processes corresponding to shear stress structure of Figure 4-1 (B), magnitudes of erosion (Figure 4-2 (A)), transport (Figure 4-2 (B)),

deposition (Figure 4-2 (C)) and avalanche (Figure 4-2 (D)) are computed. The magnitude of each process on each cell location is described by the frequency of the specified doublet transition type. For each type of transition, the occurrence time is counted for an instantaneous time duration of 5 t_0. The dune can be approximated to a fixed topography during so short time. For Figure 4-2 (C), the deposition process refers to sand directly deposited by the wind, without getting involved in avalanching. Figure 4-2 takes the average of 200 transects (between two white lines labelled in Figure 4-1 (A)) for mapping the topography and magnitude profiles.

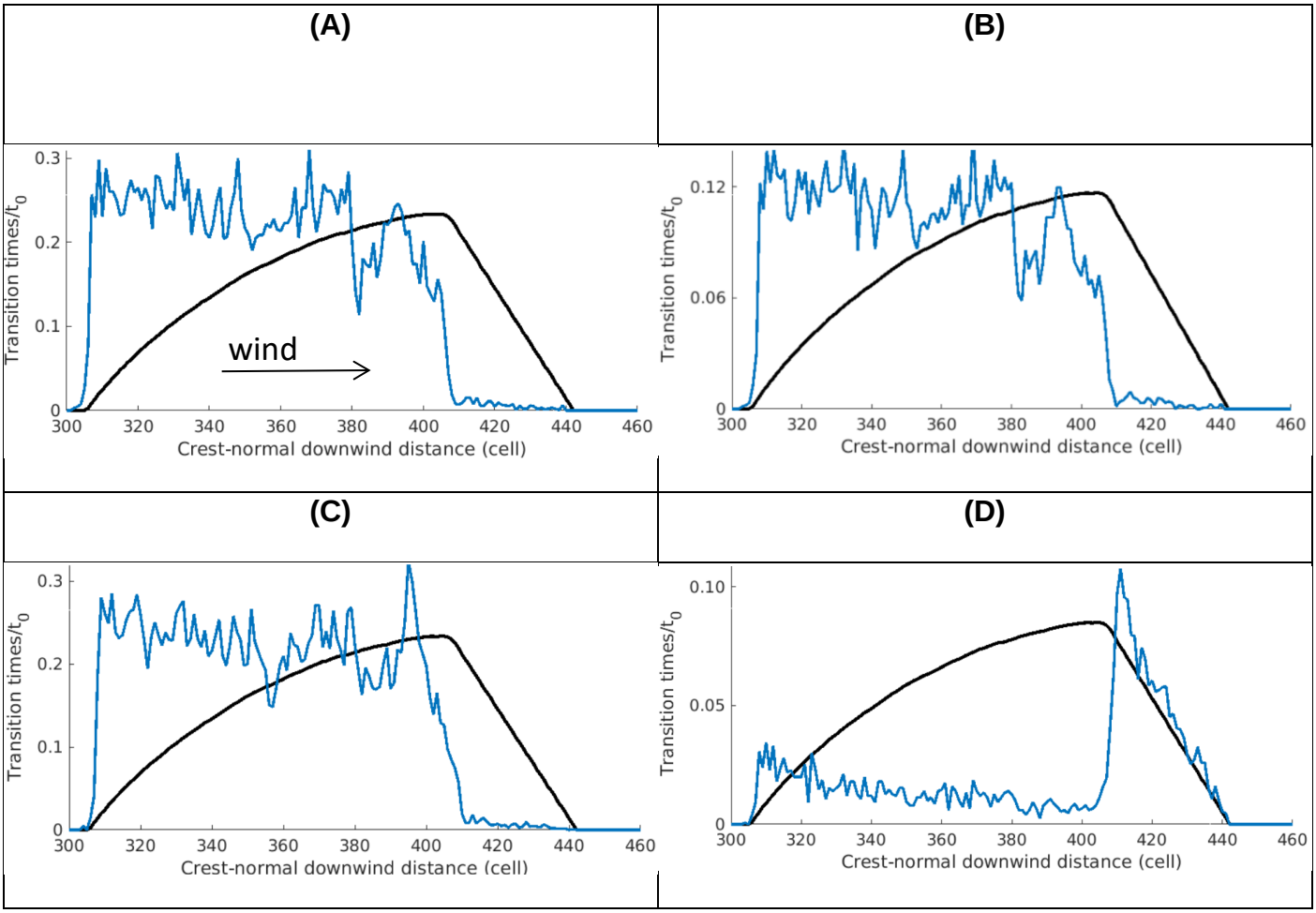


Figure 4-2. Magnitude of sand moving processes modelled with ReSCAL over a transverse dune cross section in response to the wind shear stress of Figure 4-1 over the same topography, under the highest wind speed ($\tau_{,min} = 0$). The

magnitude is described by the frequency (i.e. occurrence times per minimum time step t_0) of each specified transition (Figure 3-2), averaging an instantaneous duration of 5 t_0. (A) Erosion (with wind direction labelled) (B) Transport (C) (non-avalanche) Deposition (D) Avalanche.

In response to the flow pattern of figure 4-1 (B), Figure 4-2 indicate some features of sand movement:

---Erosion, transport and non-avalanche deposition dominate the windward slope. As an erosion transition activates an immobile grain, transport and (non-avalanche) deposition are followed. Therefore, Figure 4-2 (A), (B) and (C) show that erosion, transport and deposition together occur with high magnitudes on the stoss slope, whilst rapidly decrease in the lee side of the crest. In a common recognition (e.g. Pye and Tsoar, 2002; Bristow, 2008; Kocurek, 2009;), sand deposition is supposed to mainly occur in the lee where the wind has largely weakened. This differs from the pattern indicted by Figure 4-2 (C), as the figure separates sand directly deposited by the wind (not involved in avalanche) from sand eventually deposited by avalanche (Figure 4-2 (D)). In Figure 4-2 (C), A rapid increase is shown on the low gradient top of the stoss slope, indicating that the sand accumulates here and eventually triggers the avalanche in the lee around downwind distance of 414-cell of Figure 4-2 (D).

---Avalanching dominates the lee slope and slightly occurs on the stoss slope, as indicated by Figure 4-2 (D). The lee side of the dune crest is where the highest avalanche transition occurs, reaching a peak at downwind distance of 413-cell, around 2 cells away from the crest location in the downwind. This is resulted from the high (wind-driven) deposition in the windward side (Figure 4-2 (C)) around 3

cells from the crest in upwind. From the maximum of avalanche to downwind, there is a gradual reduction of avalanche transition times.

On the stoss slope, the avalanche occurrence corresponds to the gradient of the slope and wind strength. The windward side of the profile (Figure 4-2 (D)) starts with a high magnitude (downwind distance 305-cell) at the steepest slope near the wind deceleration zone. It gradually decreases with the downwind distance with wind speedup and the slope gradient lowering down.

In response to the wind structure of Figure 4-1 (B) associated with the sand moving patterns of Figure 4-2, the resultant sand flux over the dune is computed and shown in Figure 4-3.

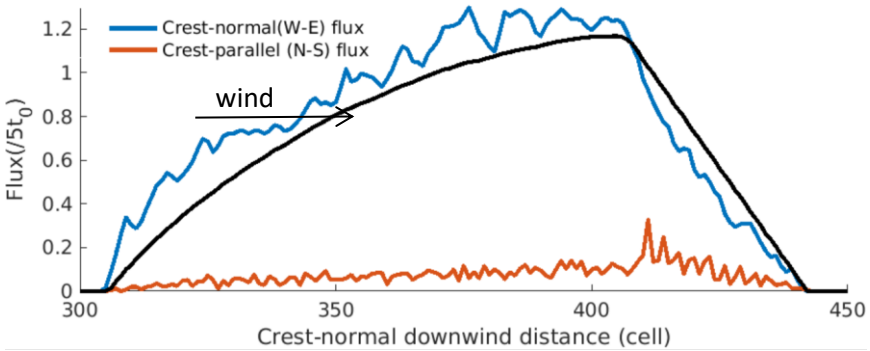


Figure 4-3 Sand flux over a crest-normal transverse dune transect resulted from the wind shear stress of Figure 4-1 and sand moving magnitude of Figure 4-2 over the same topography, under the highest wind speed ($\tau_{,min} = 0$).

Regarding the overall sand flux, the wind-parallel (crest-normal, west to east) flux Q_{we} corresponds to the shear stress profile, as wind is the key driver to move sand. Firstly the flux Q_{we} increases along the windward slope, reaching the maximum near the top where the slope gradient has been flattened. Secondly, due to weakening of the wind, there is a gradual decreasing of Q_{we} on the lee slope. Here the key driver of the flux is gravity and avalanche, instead of the wind. Correspondingly, as grain

flow is the only driver of the lateral (crest-parallel, north to south) flux Q_{ns}, it is high in the lee and reaches a peak at the crest. The structure of Q_{ns} in the lee corresponds to the avalanche transition occurrence of Figure 4-2 (D). However, the windward side of Q_{ns} shows an opposite trend to Figure 4-2 (D), attributed to the stoss slope gradient. At the lower portion, the slope is steeper and smoother, thus less lateral flux is caused in grain flow events. On the contrary, at the lower portion, the slope is flatter with more bumps which produce more possibilities of sand moving laterally.

4.1.2 Internal sedimentary structure

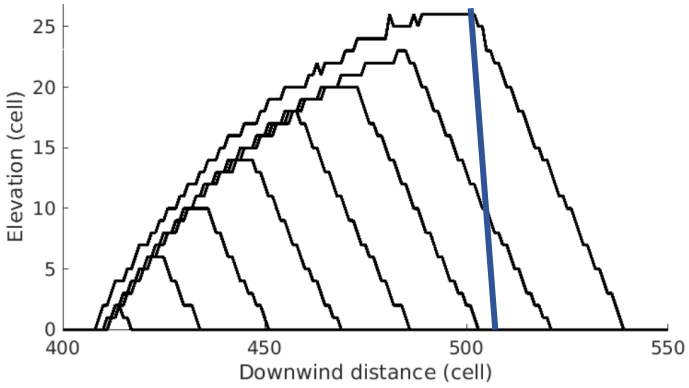
Throughout an extended time scale of dune development, memory (e.g. Warren and Kay, 1987; Wiggs, 2021) of the initial condition topography is gradually removed. All sediments of the initial transverse dune of Figure 4-1 (A) are activated and reburied, thus the internal structure is re-adapted to the ongoing wind condition. Figure 4-4 (A) visualises the stratigraphy of the dune, associated with the age-depth profile of Figure 4-4 (B) collected through the dune crest, and profile of age with respect to downwind distance in Figure 4-4 (C) collected from the bottom layer. They both take the average of 200 transects (between two white lines labelled in Figure 4-1 (A)) for mapping the stratigraphy and chronology profiles. Several cells nearest to dune surfaces are the currently activated sand with the youngest age (see the top 3 cells in Figure 4-4 (B) and most upwind 4 cells in Figure 4-4 (C)). Below this layer of active sand are sediments buried as the stratigraphy.

The sedimentary structure of the transverse dune in Figure 4-4 (A) is characterized by grain flow strata (i.e. strikes, dips) which are the key feature of migrating

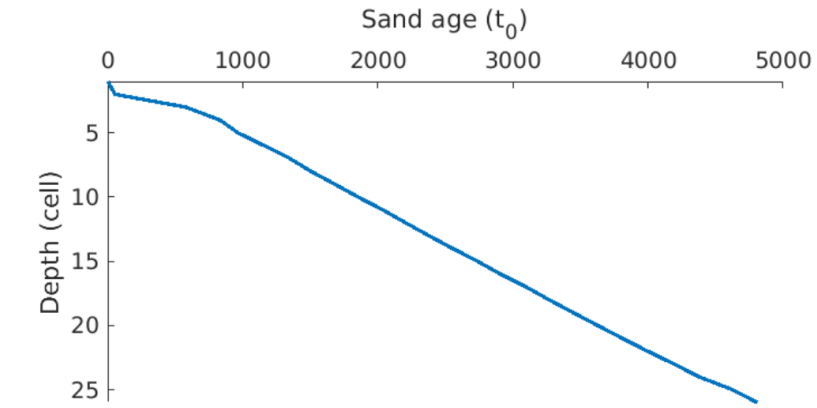
transverse dunes (e.g. Bristow, 2008; Kocurek, 2009; Eastwood, et al., 2012), as introduced in Chapter 3. In Figure 4-4 (A), the time interval (i.e. temporal resolution) between two adjacent surface lines (visualized with the method explained in Section 3.2.2) is 2000 t_0. In Figure 4-4 (B) and (C), the chronological structure is built with the highest spatial resolution by including all cells throughout the distance.

Vertically, through the dune crest (Figure 4-4 (A)), the oldest sand is buried around 5000 t_0 ago and the drilled column spans 2.5 intervals of the strata. This corresponds to the age of the deepest sand indicated by Figure 4-4 (B). Horizontally, a total dune age of approximately 15000 t_0 is indicated by the cross strata (Figure 4-4 (A)), corresponding to the age-downwind distance profile of Figure 4-4 (C) that shows the most upwind bottom sand preserved is around 15000 t_0 old. With respect to time, Figure 4-4 demonstrates a constant rate of formation of the strata, as in (A), the strata thickness preserved during each 2000 t_0 is 18 cells in horizontal and in (C), vertically, 13 cells are preserved for each 2000 t_0.

(A)



(B)



(C)

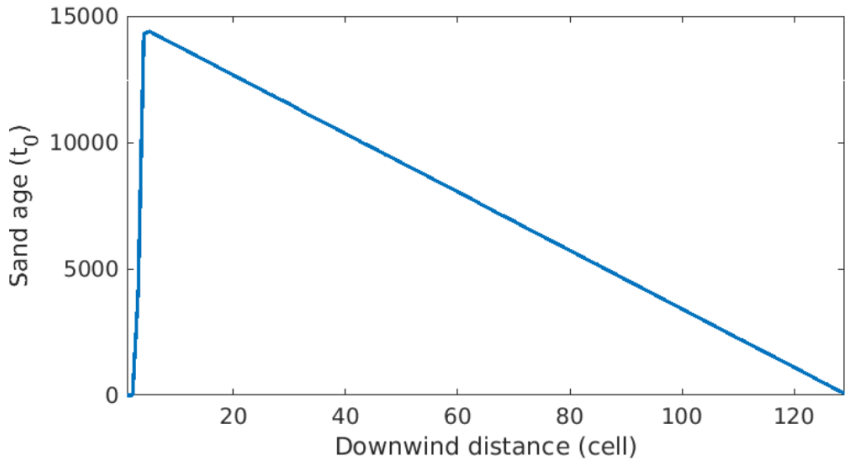


Figure 4-4. Internal structure of the transverse dune (A) Cross strata pictured with buried surfaces of each 2000 t_0(B) Age-depth profile through the dune crest, drilling location labelled on (A) with a dark blue strait line. (C) Age-downwind distance profile of the dune bottom sand. (A), (B) and (C) all take the average of the 200 transects labelled in Figure 4-1 (A))

4.1.3 Summary of 4.1

This section presents a simple scenario with a transverse dune enforced with a constant incoming wind velocity and crest-normal wind angle. The wind shear stress profiles modelled with LG show general features validated by the literature, including wind deceleration when approaching the toe of a dune, acceleration along the

windward slope, deceleration on the lee slope and the subsequent recovery to the environmental wind strength.

By tracking doublet transition times in ReSCAL, magnitudes of sand movements are visualized, showing that the stoss slope accommodates the majority of wind-driven processes involving erosion, transport and (non-avalanche) deposition. The structure of resultant sand flux, therefore, corresponds to these wind driven processes on the crest-normal (i.e. wind parallel) direction. On the contrary, the lee slope is driven by avalanche transitions, whilst significantly less affected by the wind due to its weakened strength. As a result, the crest-parallel flux corresponds to the avalanche process over the lee slope.

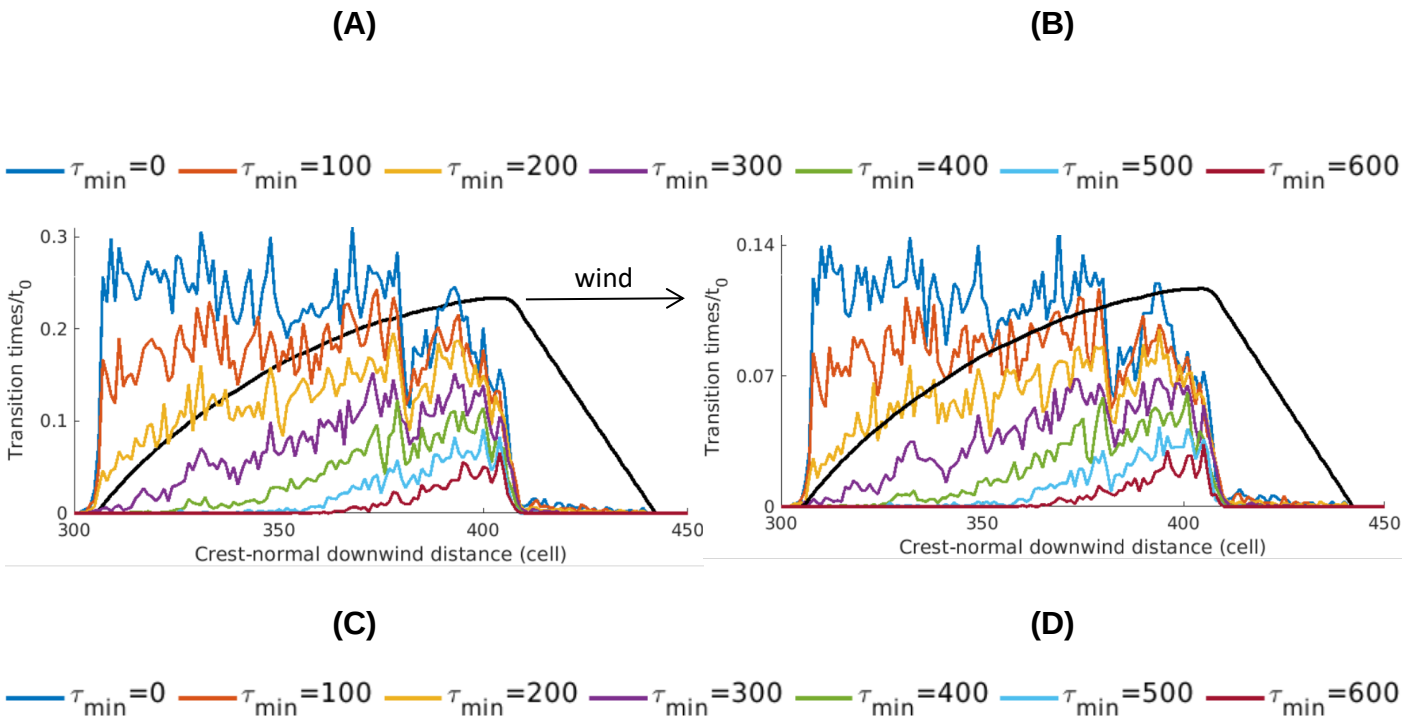
Throughout and extended time scale, the sedimentary architecture of the dune is characterized by cross strata built by grain flow and preserved afterwards by migration. In the scenario run here, the chronology profiles are linear with depth and downwind distance, indicative of constant rate of formation of dips and downwind migration and vertical accumulation of a certain position on the dune.

4.2 Flow pattern, sand movement and sedimentary structure of a transverse dune with respect to varying (crest-normal) wind speeds

This section extends the simplest 4.1 scenario with a crest-normal and speed-fixed wind to a set of varying speeds of the crest-normal wind. As specified in Section 3.3.2, in practical, varying wind speeds is implemented by setting the minimum erosion threshold τ_{min} (see details in Chapter 3), which in fact, varies the wind erosivity to each local cell. The same domain and topography are deployed as in 4.1 with a set of τ_{min} enforced to the transverse dune.

4.2.1 Flow pattern and sand movement on the surface

The wind shear stress profiles are same as Figure 4-1 (B), whilst the wind erosivity towards the slope depends on the τ_{min}. For example, assuming the LG shear stress τ_s on a given cell at a given time step is 280 τ_0, when $\tau_{min} = 300$, this cell is disabled from erosion, whilst under $\tau_{min} = 200$, wind erosivity on this cell is enforced with the linear relationship to $\tau_s - \tau_{min}$ (Equation 3.2, Section 3.2 of Chapter 3)). With this method, increasing τ_{min} makes similar effects to lowering down the wind speed. Figure 4-5 (A) to (D) provide the magnitude profiles of erosion, transport, deposition and avalanche at 6 example wind speeds (i.e. 6 τ_{min} settings as labelled in the legend of Figure 4-5). Same as in Figure 4-2, the doublets transition times are counted within the instantaneous time duration of 5 t_0 and each curve takes the average of the same 200 transects as in 4.1 (between the two white lines in Figure 4-1 (A)).



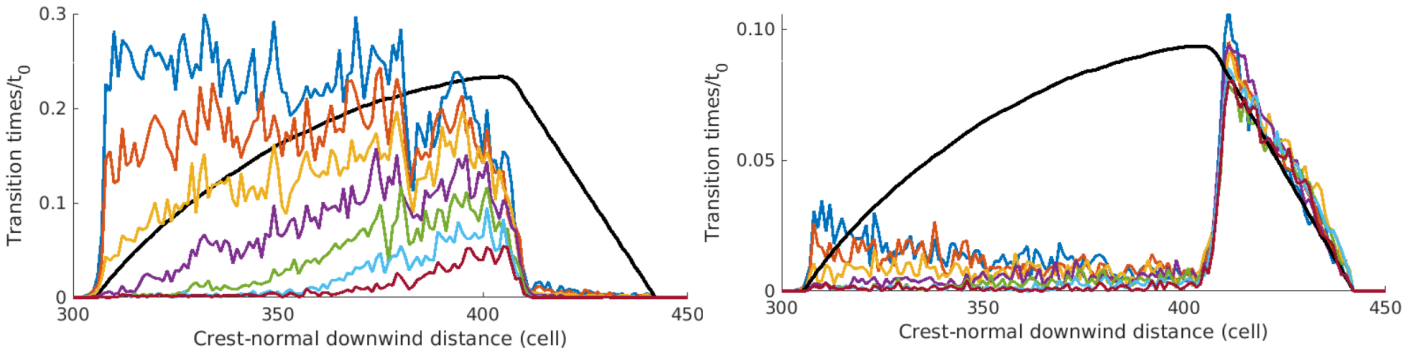


Figure 4-5. Magnitude of sand moving processes modelled with ReSCAL over a transverse dune (shown in Figure 4-1 (A)) enforced with a crest-normal wind at varying speeds implemented by setting the minimum erosion threshold τ_{min} under the same shear stress profile of Figure 4-1 (B), lower $\tau_{,min}$, higher wind erosivity (i.e. higher wind strength). The magnitude is described by the occurrence time of each type of transition (Figure 3-2) for an instantaneous duration of 5 t_0. (A) Erosion (B) Transport (C) Deposition (D) Avalanche. Both the topography and process magnitude profiles take the average of the 200 transects labelled in Figure 4-1 (A).

Figure 4-5 shows that with reduction of wind speeds (increase of τ_{min}), all transition types get less active. This is due to reduced times of erosion which is the initiating process for the subsequent transports and depositions. In addition to this general effect of wind strengths, shapes of the magnitude profiles are different, particularly for the stoss slope of erosion, transport and deposition (Figure 4-5 (A), (B) and (C)), as winds are the key driver of the three processes as well as the stoss slope. Curves of the three lowest wind strengths where τ_{min}=400, 500 and 600 are concave, with the dune base largely prevented from erosion. In comparison, at the three greatest wind strengths where τ_{min}=0, 100 and 200, the curves are convex, indicating that

the dune base is actively eroded. Comparing to dune base, on the upper portion of the stoss slope between 370-cell and 400-cell (dune crest), there is less reduction of the erosion magnitude in response to weakening of the wind (i.e. increase of τ_{min}).

In comparison, the impact of wind strength is less significant on the lee slope, as it is driven by gravity rather than the wind strength and there is a lack of doublets to initiate erosions. For example, on the lower portion of the stoss slope shown in Figure 4-5 (A), between downwind distances 300-cell and 350-cell, the erosion transition time fluctuates around 1.3 when τ_{min}=0, whilst the erosion processes are nearly disabled when τ_{min}=500 and τ_{min}=600. Further, through the lee slope, the erosion processes show little dependency on the wind strength due to the lack of doublets . Similar patterns are indicated by Figure 4-5 (B) and (C).

In general, regarding dependency to winds, the stoss slope base of the dune is the most sensitive part. Changes of τ_{min} make great effects on this lower portion where the shear stress is relatively low, because the change of τ_{min} determines whether or not a local cell can be eroded. In comparison, upper portions of the stoss slope are less affected by τ_{min} setting, as the local shear stress τ_s to a larger extent, exceeds the minimum erosion threshold τ_{min} and has the capability of eroding sand. For avalanche, the decreasing trend with wind weakening is also indicated by Figure 4-5 (D), attributed to stronger wind driven processes (erosion, transport and deposition of Figure 4-5 (A) to (C)) triggering more grain flow as a result. As avalanche/grain flow events are the key formation processes of the internal stratigraphy of dunes (e.g. Bristow, 2008; Kocurek, 2009; Eastwood, et al., 2012; Nield, et al., 2017), below is a more detailed discussion about avalanche magnitude influenced by wind speeds.

Figure 4-6 provides a set of avalanche magnitude with respect to the wind speed (i.e. implemented by setting τ_{min}). Practically, the maximum avalanche magnitude (transition time during the 5 t_0) of each tested wind speed (i.e. each τ_{min} condition) is taken as the magnitude of the specified wind speed. The consideration is that the highest magnitude (like the 7 examples of Figure 4-5) occurs in the lee side of the crest and it is directly triggered by the three wind driven processes on the windwards slope, hence determined by the wind strength. Avalanche events occurring at lower parts of the lee slope are resulted from cascade processes following the avalanche first triggered at the dune crest.

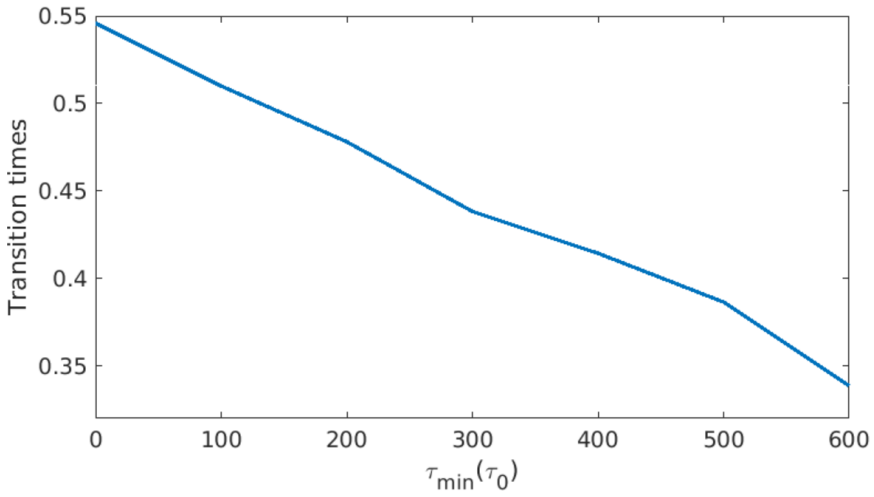


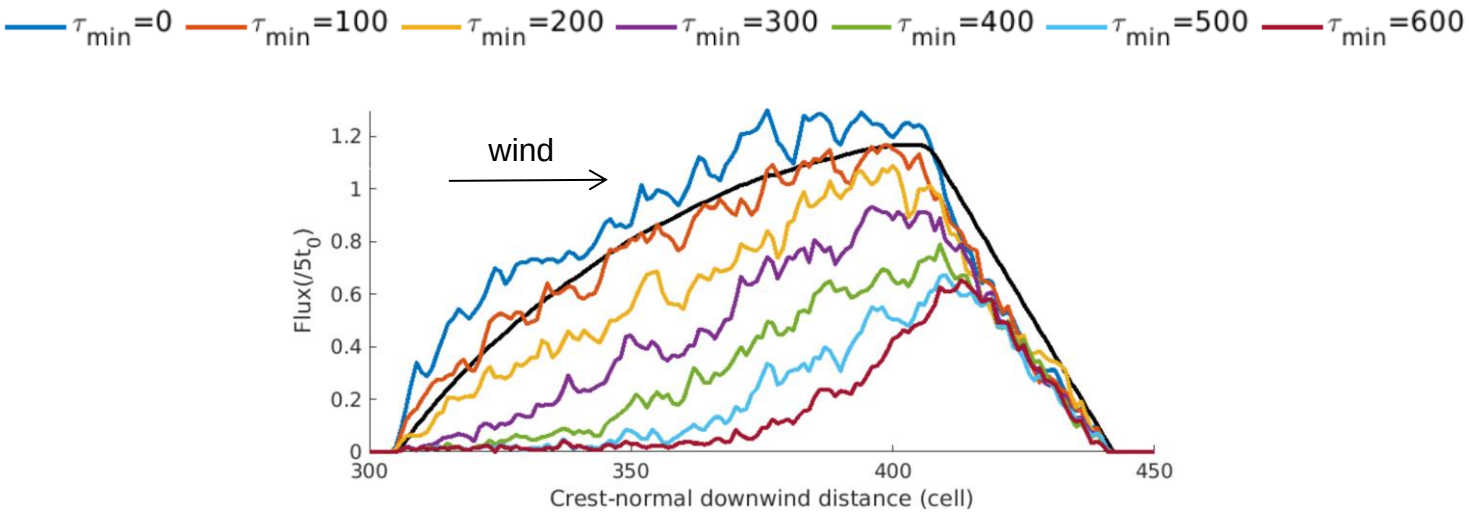
Figure 4-6. Avalanche magnitude with respect to wind speeds (implemented by setting the shear stress threshold τ_{min} to make erosion occur, higher τ_{min}, lower wind speed). A crest-normal wind is enforced on the transverse dune shown in Figure 4-1 (A). The avalanche magnitude takes the maximum of each set of avalanche transition times shown in Figure 4-5 (D)), taking the average over the instantaneous duration of 5 t_0

It is directly clear in Figure 4-6 that the (wind triggered) avalanche magnitude decreases with decreasing of wind strength (increasing of τ_{min}). This trend is in

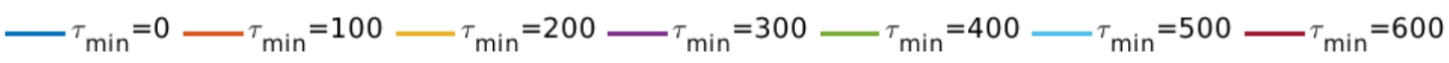
good agreement with previous study (Sutton et al., 2013(a) and (b); Nield, et al., 2017; Cornwall, et al., 2018) demonstrating that higher wind speeds lead to more sand deposited in avalanche. For process magnitude profiles shown in Figure 4-5, the direct driver in ReSCAL model is that under higher wind speeds, the three wind driven processes (i.e. erosion, transport, non-avalanche deposition) occur with higher magnitudes (i.e. higher frequencies of doublet transitions), of which the sensitivity is particularly high at upper stoss slope. Therefore, the subsequent avalanche transition occurs at higher frequency due to the high doublet availability directly comes from the non-avalanche deposition transitions.

Under the sand moving processes of Figure 4-5, the overall crest-normal flux and crest-parallel sand flux over the transverse dune are respectively presented in Figure 4-7 (A) and (B).

(A)



(B)



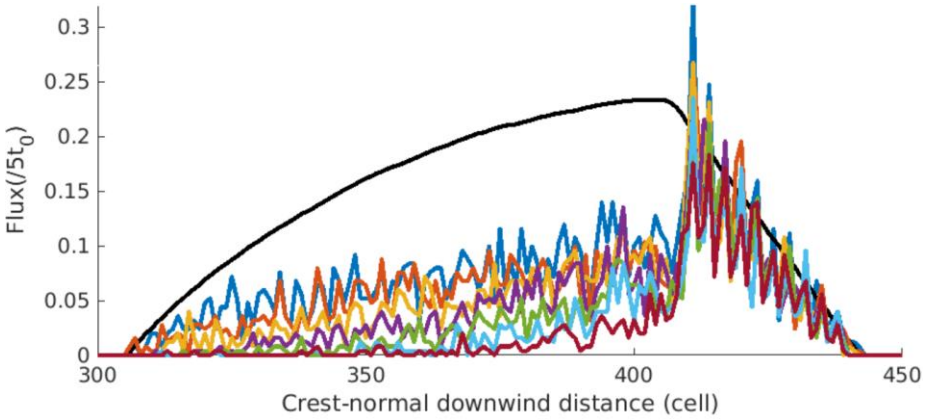


Figure 4-7. Sand flux computed with ReSCAL over a crest-normal transverse dune enforced with crest-normal wind under varying wind speeds as a result of the wind shear stress of Figure 4-1 and sand moving magnitude of Figure 4-4 over the same fixed topography, for the same duration of 5 t_0. Varying wind speeds are implemented by setting varying minimum threshold for erosion τ_{min}. (A) Crest-normal (W-E) flux (B) Crest-parallel (N-S) flux.

As discussed in 4.1.1, the crest-normal flux is mainly driven by the wind and partially by avalanche, while avalanche is the sole origin of the crest-parallel flux. Therefore, the general structure of flux curves shown in Figure 4-7 (A) are in similar structure to the wind driven magnitude of Figure 4-5 (A), (B) and (C). For the crest-normal flux profiles over the topography, lower wind speeds lead to lower sand flux and differing shapes of the flux profiles: the curve is more concave where τ_{min} is higher. When the wind speed is low, resulting in low magnitudes of erosion on the stoss slope base, the overall sand flux is also largely diminished. For example, when $\tau_{min} = 500$ or 600, the flux passing each during the 5 t_0 is less than 0.1 cell between downwind distances 300-cell and 350-cell, which are lower than 1/6 of the flux under the strongest wind where $\tau_{min} = 0$. This general tendency of sand flux profiles of Figure 4-7 (A) is in agreement with some previously field measured data. For example, Lancaster et al. (1996) proposed that under low wind speeds, the flux increases

exponentially up the windward slope, while under high wind speeds, the tendency is linear.

In addition to the general effect of wind strength on crest-normal flux, between the seven τ_{min} conditions, there are slight differences of locations of the maximum fluxes: under higher τ_{min}, the peak of the flux curve of Figure 4-7 (A) occurs at a further downwind distance. For example, the peak is two cells downwind away from the dune crest under the weakest wind τ_{min}=600, whilst the peak is one cell upwind away from the crest under the strongest wind τ_{min}=0. The shift of the sand flux peak has impact on the long term topography evolution (discussed in detail in 4.2.2) as noted by previous work (e.g. Walker and Hesp, et al., 2013; Wiggs, 2021). The dune gets flatter (i.e. horizontally stretched) when the wind-parallel flux peak occurs at the downwind of the crest where τ_{min} is not lower than 300. On the contrary, the dune gets steeper when the flux peaks at the upwind side of the crest.

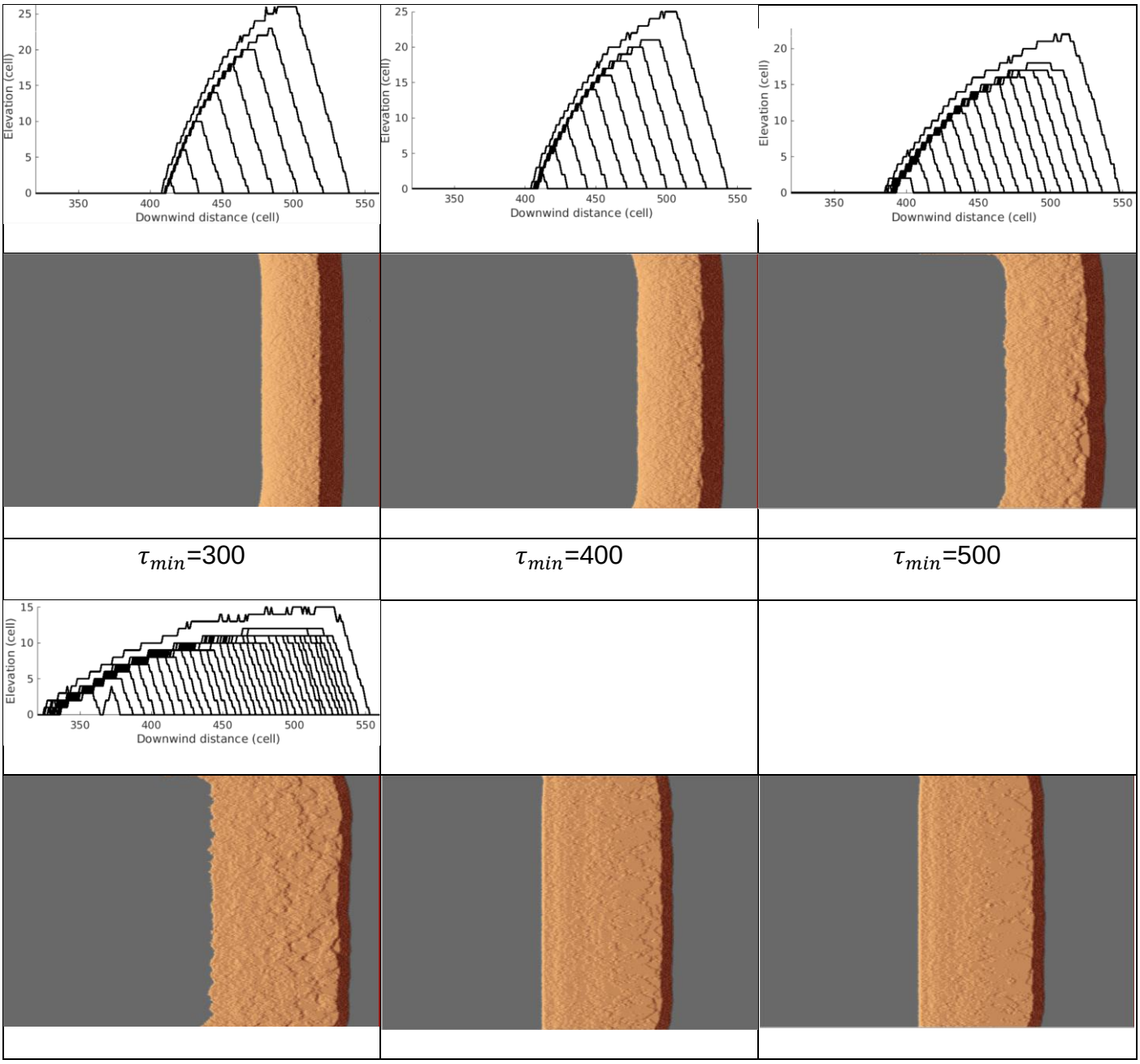
For crest-normal flux shown in Figure 4-7 (B), similarly to the scenario of Figure 4-3, it follows the trend of avalanche transition curve of Figure 4-5 (D), peaking at the crest and gradually decreasing through the lee slope. The stoss slope part of Figure 4-7 (B) shows an increasing trend with the downwind distance and with the slope gradient getting lower, opposing to the structure of Figure 4-5 (D). This indicates that flatter parts of the slope generates more lateral sand movement when avalanche occurs, whilst steeper parts of the slope leads to more sand moving downslope.

4.2.2 Internal sedimentary structure

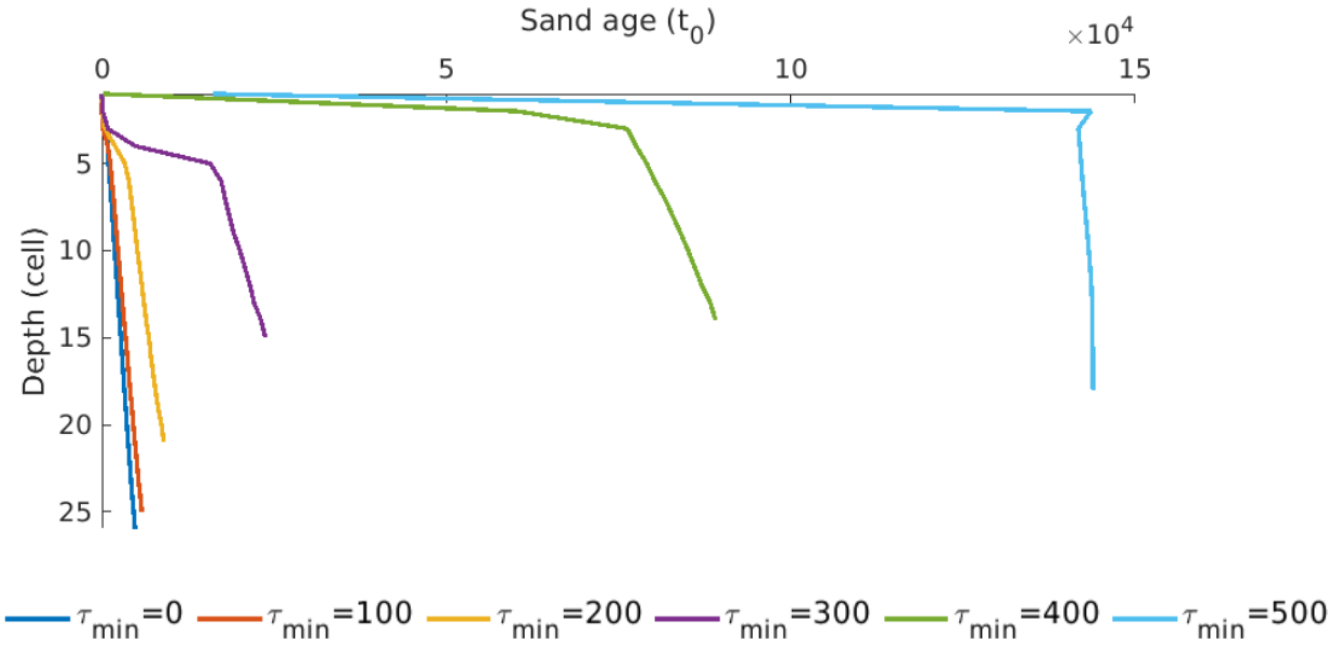
The stratigraphy and chronology features influenced by wind speeds are discussed in this section. Figure 4-8 below presents the internal sedimentary structure of the transverse dune when it has fully adapted to the tested wind condition. This evolution stage refers to: for $\tau_{min} = 0$, $\tau_{min} = 100$, $\tau_{min} = 200$ and $\tau_{min} = 300$, all grain cells at the initial condition have been fully re-activated and redeposited, while for $\tau_{min} = 400$ and $\tau_{min} = 500$, the dune has stopped evolving as the wind has become too weak to carry sand. The bedding pattern together with the corresponding topography are presented in Figure 4-8 (A) using the same methods as in Figure 4-4 (A) by visualizing the buried surface lines at a frequency of every 2000 t_0. Figure 4-8 (B) provides age-depth profiles drilled through dune crests. According to Figure 4-8 (A), when $\tau_{min} = 500$ and $\tau_{min} = 400$, the dune has become inactive due to the low wind erosivity, while sediments provided at the initial condition have not been fully activated and the dune is not reflective of the tested wind. Therefore in Figure 4-8 (C), the age profiles with respect to downwind distances select the four wind scenarios $\tau_{min} = 0$, $\tau_{min} = 100$, $\tau_{min} = 200$ and $\tau_{min} = 300$ where the initial dune memory (Warren and Kay, 1987; Wiggs, 2021) has been renewed and all sediments have been relocated by the ongoing wind regime. The bottom layer of dune sand is sampled for mapping Figure 4-8 (C).

(A)

τ_{min}=0	τ_{min}=100	τ_{min}=200


Elevation (cell)
Downwind distance (cell)
τ_{min}=300
τ_{min}=400
τ_{min}=500

(B)



(C)

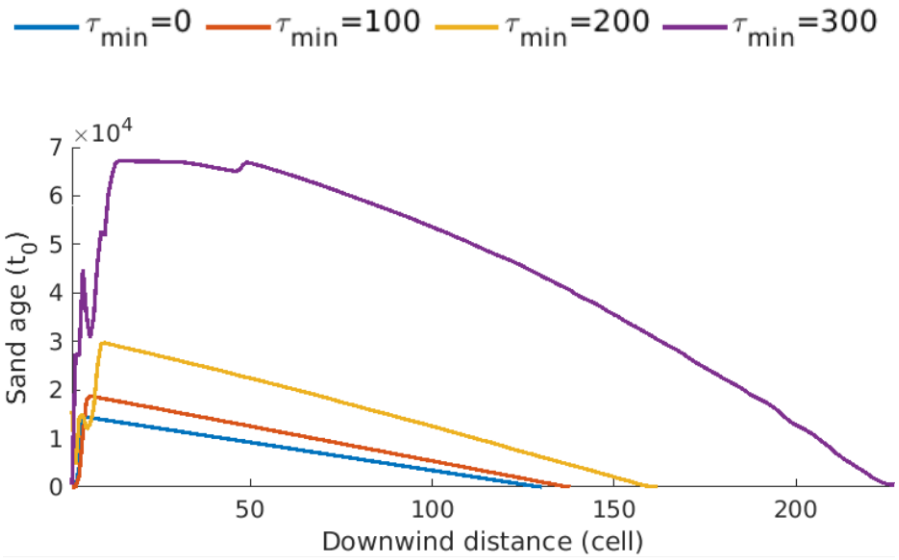


Figure 4-8. Internal sedimentary structure of a transverse dune at varying (crest-normal) wind speeds, implemented by varying τ_{min}. (A) Bedding pattern pictured with buried surface lines for every 2000 t_0. (B) Age-depth profile through the dune crest. (C) Age-downwind distance profile of the dune bottom sand.

In general, the four highest wind speeds $\tau_{min} = 0$, 100, 200 and 300 of Figure 4-8 suggest that when the wind speed is lower, the dune spans longer history in the buried architecture and thinner strata for the fixed duration of time interval. When the wind speed is higher, the strata are thicker, whilst the dune contains shorter history in the internal structure. Figure 4-8 (A) shows that the transverse dune under $\tau_{min} = 0$ has 7.5 sets of strata of 2000 t_0 and the horizontal thickness of each set is 19 cells. In comparison, the density of the cross strata is higher when $\tau_{min} = 200$ approximately doubling that in $\tau_{min} = 0$ and the strata for the fixed duration is thinner.

For these four scenarios, the influence of the wind speed on the stratigraphy and chronology corresponds to the surface process magnitudes controlled in response to the wind speed (Figure 4-6). Stronger winds incorporate larger amount of sand into grain flow, generating more avalanche transition and forming new strata more efficiently. Therefore for the controlled time duration of 2000 t_0, the grain flow strata is thicker. Previous work (e.g. Sutton, et al., 2013 (a) and (b); Nield, et al., 2017; Cornwall, et al., 2018) has commonly found the relationship between dune surface avalanche and wind speeds and it has been suggested (e.g. Nield, et al., 2017) that higher wind speeds preserve more of the deposited sediments. The modelled results here on the one hand, do agree well with this statement regarding the forming process of grain flow strata. On the other hand, considering the whole dune, new strata forms faster means the oldest sediments buried around base of the stoss slope are reactivated faster and less well preserved. Therefore, in terms of formation, higher wind speeds are more effective in generating new strata, whilst in terms of how long sand is buried, lower wind speeds are more effective in long preserving old sediments.

The low wind speed $\tau_{min} = 300$ shows a decreasing thickness of the cross strata (Figure 4-8 (A)), indicating that the dune crest migration slows down. The age-distance curves of Figure 4-8 (C) is also in a concave shape, indicating that preservation of the same strata thickness takes longer period. For example, between downwind distances 15-cell and 50-cell, the strata extends downwind for 3000 t_0 (sand age from 67000 t_0 to 64000 t_0). In comparison, for the same horizontal distance between 160-cell and 200-cell, the sand age spans over 1000 t_0.

For the two lowest wind speeds $\tau_{min} = 400$ and $\tau_{min} = 500$, age-depth views of Figure 4-8 (B) show that the dune is significantly older than those in lower-speed scenarios. This is because their reactivation stops early as soon as the dune activation has stopped to a steady shape due to the low wind erosivity. Additionally, the trend (lower wind speed, slower formation of the stratigraphy) reflected by the three high-speed cases does not apply to the two low wind speed curves. The trend directly clear in Figure 4-8 (B) is that the strata accumulation rate (vertically to time) of the two lowest-speed winds is even higher than the $\tau_{min} = 0$ profile. Here the net vertical deposition rates of $\tau_{min} = 400$ and $\tau_{min} = 500$ are indicative of avalanche that occurs on the initial transverse dune in earlier ages, rather than resulted a dune adapted to the wind.

The varying dune width-τ_{min} pattern of Figure 4-8 (C) shows that for $\tau_{min} = 0$ to 300, with the total volume of sand maintained (i.e. no influx or outflux), the transverse dune gets wider, lower with decrease of the wind erosivity. This tendency has been documented in literature (e.g. Lancaster, 1985; Zhang, et al., 2012) that less steep dunes are engaged with lower wind speeds. Under low wind speeds $\tau_{min} = 300$, the dune base migrates slower than the dune crest and gradually the dune is

horizontally stretched. This mechanism originates from the erosion magnitude profiles provided in Figure 4-5 where the reduced wind erosivity has greater influence (erosion more effectively disabled) on the base than on upper portion of a windward slope.

Previous modelling (e.g. Zhang, et al., 2010) and fieldwork (e.g. Neuman, et al., 2000; Walker and Hesp, 2013; Wiggs, 2021) reported that in barchan scenarios, the dunes are flatter under lower wind speeds, in agreement with the finding here. Additionally, the control of wind speeds on dune shapes may explain the variation of barchan geometric features documented in previous fieldwork throughout multiple dune fields (e.g. Finkel, 1959; Long and Sharp, 1964; Hesp and Hasting, 1998; Bourke and Goudie, 2009).

4.2.3 Summary of Section 4.2

This section resolves the issue of wind speeds control on dynamics of a transverse dune. Practically, the wind shear stress profile is same as in Figure 4-1 (B), whilst the minimum threshold for erosion is varied to change the wind erosivity. For a short time scale, Section 4.2.1 discusses the sand moving magnitudes expressed with occurrence times of doublets transitions (i.e. erosion, transport, deposition and avalanche) involved in ReSCAL. For an extended time scale that allows the dune with adequate adaption to the wind condition, Section 4.2.2 discusses dune evolution and internal stratigraphy. Outputs are in good agreement with literature: (1) Higher wind speeds produce higher avalanche magnitude (e.g. Sutton, et al., 2013 (a) and (b); Nield, et al., 2017; Cornwall, et al., 2018) (2) Higher wind speeds form thicker grain flow strata (e.g. Eastwood, et al., 2012), reactivate oldest sediments faster and leading to younger dunes. (3) If the wind speed is so low that the whole surface is disabled from erosion, the dune stops evolving and the oldest

sediments are preserved. In general, under the condition without external sand influx, high wind speeds are more effective in building new grain flow strata and less preservation of old sediments. Low wind speeds are slower in forming strata and better capable of preserving the oldest records under the wind condition without sand influx (4) High wind speeds maintain steeper dunes and lower wind speeds maintain flatter dunes (e.g. Neuman, et al., 2000;; Zhang, et al., 2010 Walker and Hesp, 2013; Wiggs, 2021)

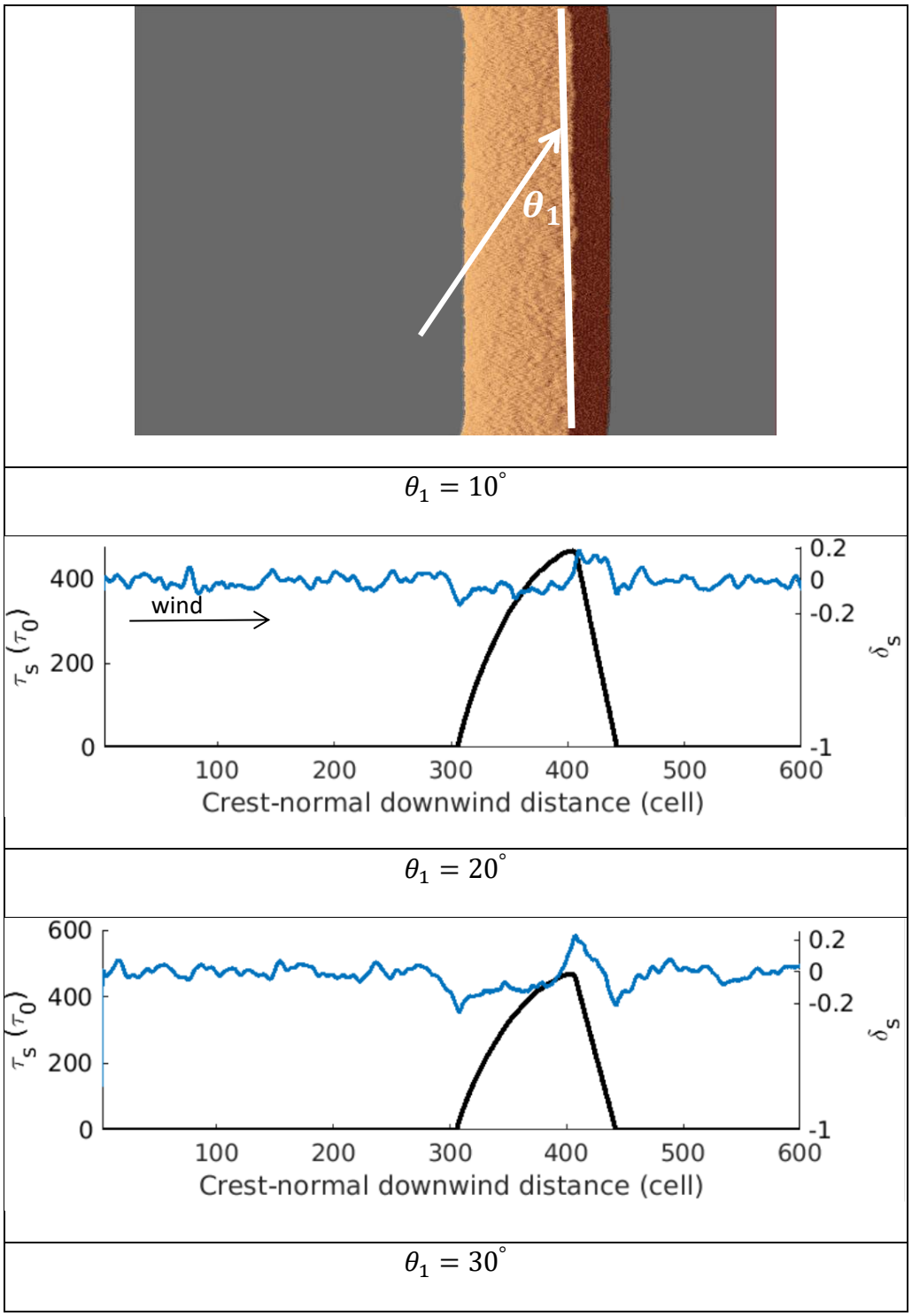
4.3 Flow pattern, sand movement and sedimentary structure of a transverse dune with respect to (speed-fixed) varying wind-incident angles

This section has the goal to elucidate how the wind-crest angle influences the dune dynamic. Section 4.3.1 investigates the wind angle controls on the wind flow structure over the transverse dune, associated with the instantaneous sand movement occurring on dune surfaces. The discussion has a particular focus on the wind-driven sand movement on the lee slope, as this is the process that differentiate the scenarios of 4.3 from crest-normal wind condition of 4.1 and 4.2. Section 4.3.2 explores the dune evolution and internal sedimentary structure built through an extended time scale allowing the dune to adapt to the tested wind condition.

4.3.1 Flow pattern and sand movement on the surface

Wind shear stress τ_s profiles of four wind-crest angle θ_1 examples are given in Figure 4-9 (θ_1 labelled). The change of τ_s from the flat surface τ_{flat} is calculated with equation 4.1 and labelled on each plot, taking the average τ_s between 50-cell and 150-cell crest-normal downwind distances. The shear stress data are based on

2D LG slices rotated to the wind angle (i.e. LG airflow particles cannot move between LG slices on a 3D basis).



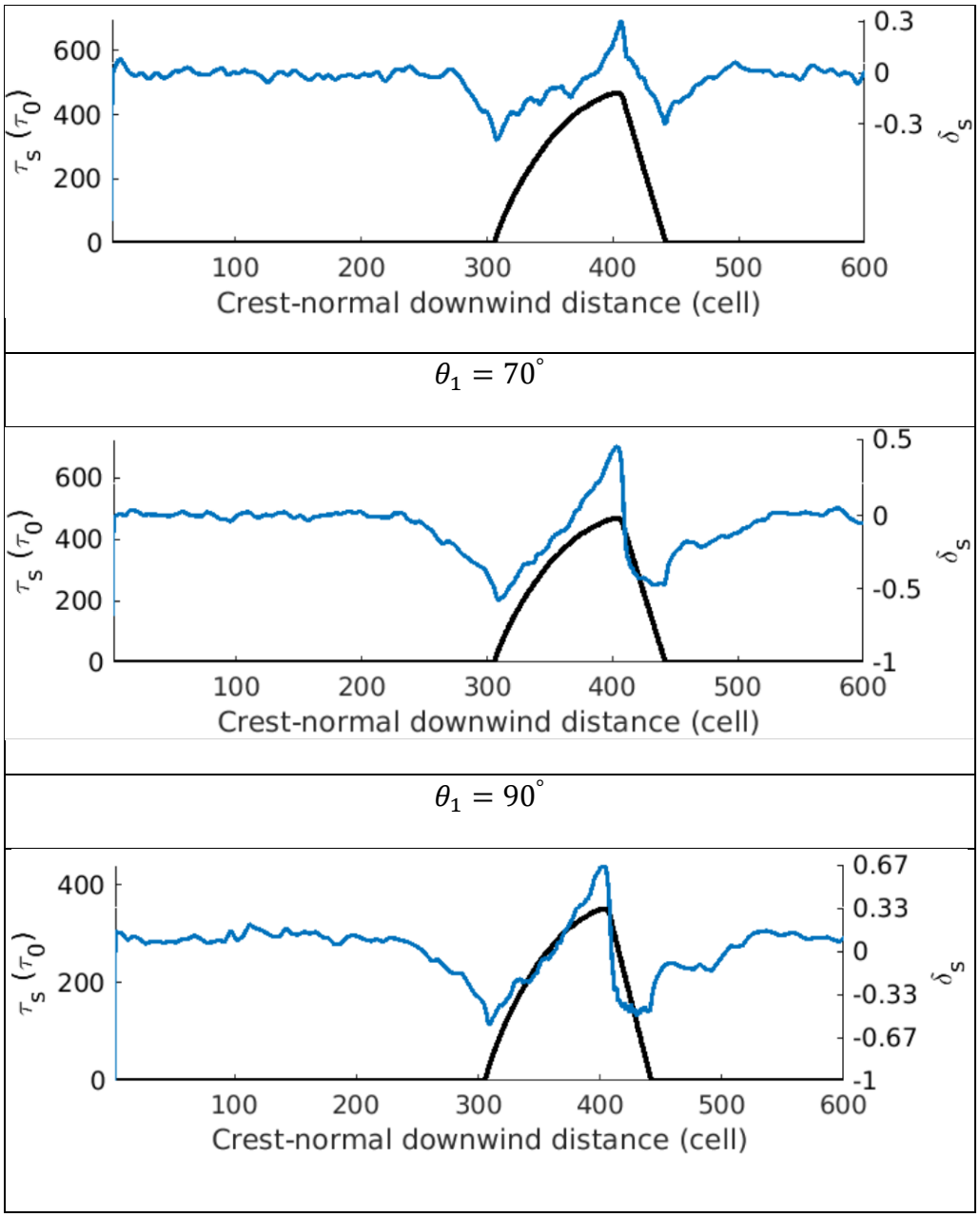


Figure 4-9. Wind shear stress profiles over the crest-normal topography of the transverse dune show, modelled with lattice gas (LG) at varying wind-crest angles θ_1. The transverse dune is 26 cells in height, with the lee slope at the angle of repose. The 200 transects labelled in Figure 4-1 (A) are taken to average the topography and shear stress profiles.

According to Figure 4-9, the general structures discussed in 4.1 are also demonstrated by the set of varying wind-crest angles θ_1, including (1) wind deceleration when approaching windward base, (2) acceleration along the windward

slope, (3) deceleration after passing the crest and (4) reacceleration starting from lee slope base and eventually recovery to the environmental wind strength. However, the wind angle θ_1 has influence on the occurrence degree of these general features. In general, these flow features are stronger under greater wind-crest angle θ_1. For example, when $\theta_1 = 10^{\circ}$, when approaching the windward base (at downwind distance 310-cell), the shear stress τ_s reduction is less than 20% of the environmental wind strength (79 τ_0), from $390\ \tau_0$ to $310\ \tau_0$. To compare, when $\theta_1 = 70^{\circ}$, the deceleration is 57% (280 τ_0) of the environmental wind, from 480 τ_0 to 200 τ_0. Under the two wind-crest angles between ($\theta_1 = 20^{\circ}$ and $\theta_1 = 30^{\circ}$), the same trend is also reflected: the τ_s respectively reduces for 29% and 39%.

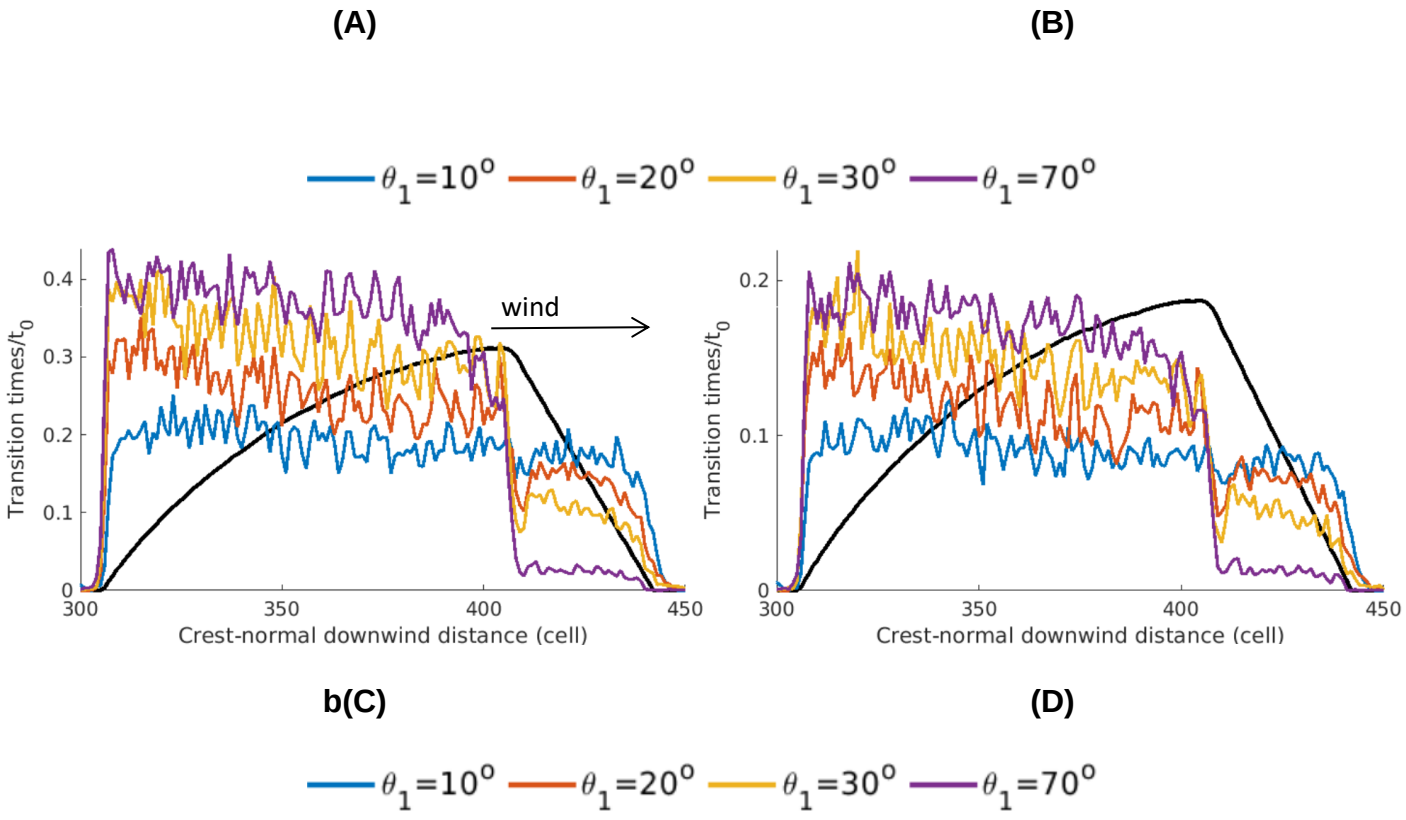
For the wind structure over the stoss slopes, when $\theta_1 = 70^{\circ}$, τ_s reaches 450 τ_0 at the crest, which is the 2.3 times of τ_s at the toe (200 τ_0) of the stoss slope and twice of τ_s at the plinth (210 τ_0) of the lee slope. In comparison, when $\theta_1 = 10^{\circ}$, the change of τ_s of these two portions both are smaller than 20%. The similar tendency with respect to wind directions was demonstrated by some field measured data (e.g. Tsoar, et, al., 1985; Lancaster, 1986)

Based on implementation of the flow field in ReSCAL, practically rotating the wind-crest angle means changing the dune topography that interacts with the LG wind, as detailed in Section 2.2 and in Figure 2-3 of Chapter 2.

Similar wind strength structures are documented in literature. Sweet and Kocurek (1990) measured wind profiles on transverse dunes with varying lee slope gradients. It is indicated that the wind decelerates more over a steeper lee slope. Additionally, in previously surveyed linear dunes (see details of Chapter 2), when the wind incomes at an oblique angle (e.g. Tsoar, 1983; Livingstone, 1986; Wiggs, et al.,

1996 (a)), the flow deceleration tends to be weaker than that in the lee of transverse dunes and reacceleration can occur from the middle of the lee slope (instead of a distance away from the lee slope base).

In response to the shear stress pattern with the four θ_1 scenarios of Figure 4-9, the sand moving (occurrence times of transition) magnitude is provided in Figure 4-10. Figure 4-11 is associated to show the avalanche magnitude with respect to the wind-crest angle.



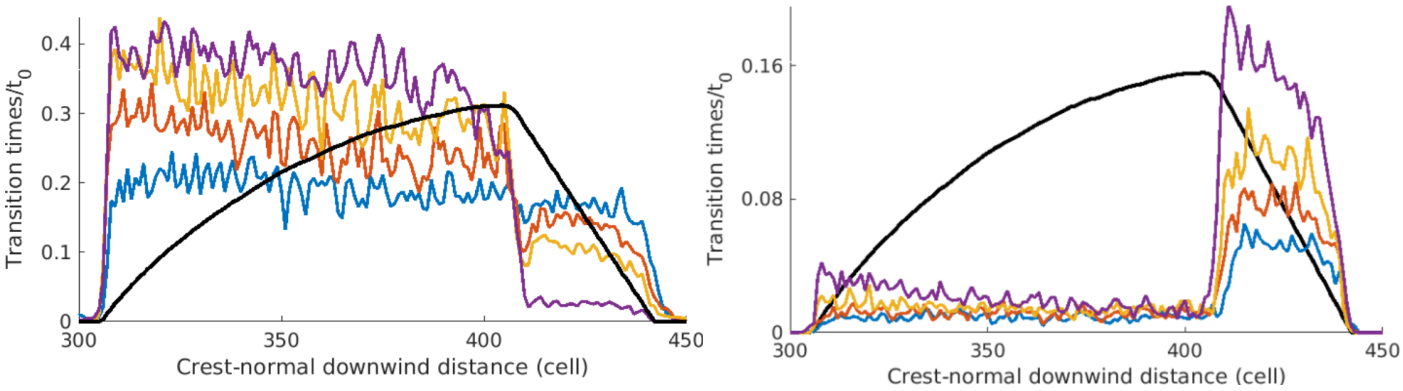


Figure 4-10. Magnitude of sand moving processes at varying wind-crest angles θ_1 (4 examples) modelled with ReSCAL over a transverse dune cross section in response to the wind shear stress of Figure 4-7 over the same topography, under the highest wind speed. The magnitude is described by the occurrence time of each type of transition in Figure 3-2 for an instantaneous duration of 5 t_0. (A) Erosion (B) Transport (C) Deposition (D) Avalanche

For the three processes directly driven by winds: erosion, transport and deposition, the control on the instantaneous sand movement corresponds to the wind strength, as discussed below.

---On the windward slope: With increase of the wind-crest angle θ_1, the wind erosivity gets higher. This trend is reflected by the windward part of erosion, transport and deposition processes presented in Figure 4-10 (A), (B) and (C). Within the downwind distances interval from 310-cell to 405-cell, the three processes occur at lower magnitudes when a narrower angle is applied. For example, under $\theta_1 = 20^{\circ}$, the erosion transition times are approximately 50% less than when $\theta_1 = 70^{\circ}$ on the stoss slope. The control of wind angle on wind strength over the slope is attributed to the speedup ratio Rs = 2h/L (e.g. Jackson and Hunt,

1975), where h is the height and L is the windward slope length in horizontal of the dune. When a smaller θ_1 is enforced, a longer 'dune length' L interacts with the LG flow with the fixed dune height h, hence the speedup is lower.

---On the lee slope: With increase of the wind-crest angle θ_1, the wind erosivity gets lower. This trend is also clear in the three wind driven processes (Figure 4-10 (A), (B) and (C)) between the downwind distances 410-cell and 446-cell. More crest-parallel winds more effectively move sand on the lee slope surface because the wind strength is less reduced (Figure 4-9) and better maintained on the level over the stoss slope, see the discussion above on the shear stress profile.

For the avalanche magnitude the four θ_1 examples presented in Figure 4-10 (D) suggest more avalanche transitions are triggered when θ_1 is larger. Figure 4-11 provides a full range of wind angles to show their control on the avalanche magnitude. The maximum of each avalanche transition curve is taken as the overall magnitude of the specified wind angle, for the same reason as in Figure 4-6, Section 4.2: the magnitude measured at this point is directly driven by the wind, whilst further downwind points are resulted from the cascade triggered by the maximum one. Therefore the peak of avalanche magnitude in each profile is most reflective of the wind condition. Figure 4-11 further demonstrates the trend indicated by Figure 4-10: more crest-normal wind generates larger avalanche magnitude. This relationship is attributed the decreasing crest-normal ($cos\theta_1$) wind component with an increase wind angle θ_1.

The resultant sand flux over the transverse dune is given in Figure 4-12. The flux of the most perpendicular wind $\theta_1 = 70^{\circ}$ under the greatest angle shows a structure corresponding to the shear stress. On the lee slope, particularly for the crest-normal

flux of Figure 4-12 (A), the three low angle ($\theta_1 = 10^\circ$, 20° and 30°)) winds demonstrate a significantly stronger sand carrying flux than on the stoss slope. In general, the flux profiles of these three angle scenarios are wind-driven. However, for the most crest-normal case where $\theta_1 = 70^\circ$, the stoss slope flux is resulted from the wind, whilst the stoss slope is avalanche-driven.

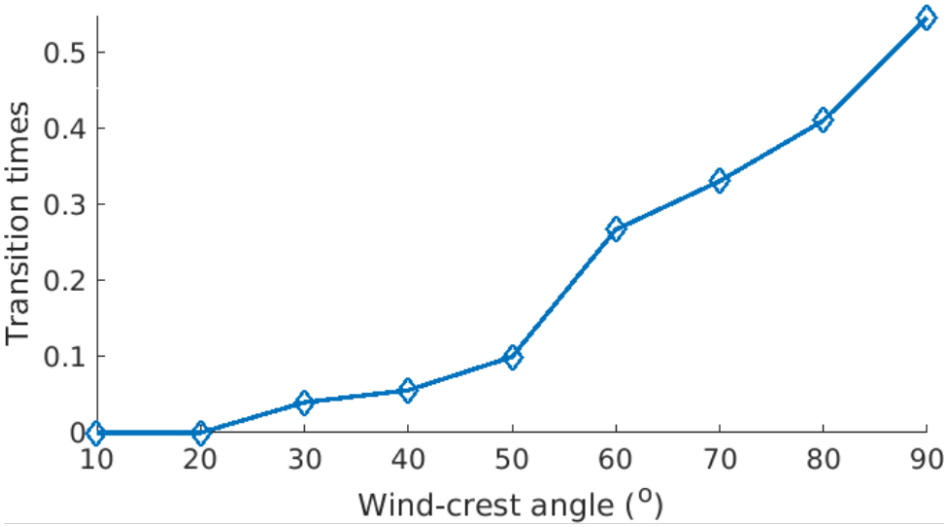
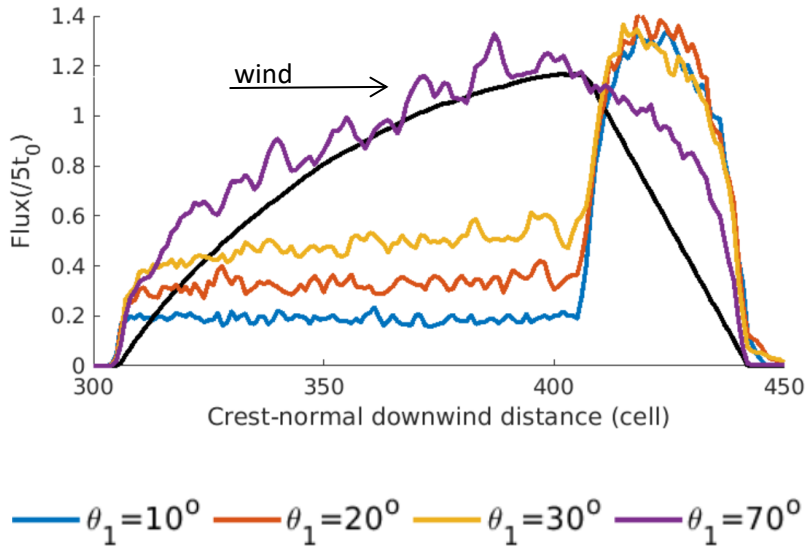


Figure 4-11 Avalanche magnitude with respect to the wind-crest angle θ_1, as schematized in Figure 4-9 enforced on the transverse dune at the highest wind speed ($\tau_{min} = 0$). The avalanche magnitude is described by avalanche transition times per t_0 averaged over an instantaneous duration of 5 t_0.

(A)



(B)

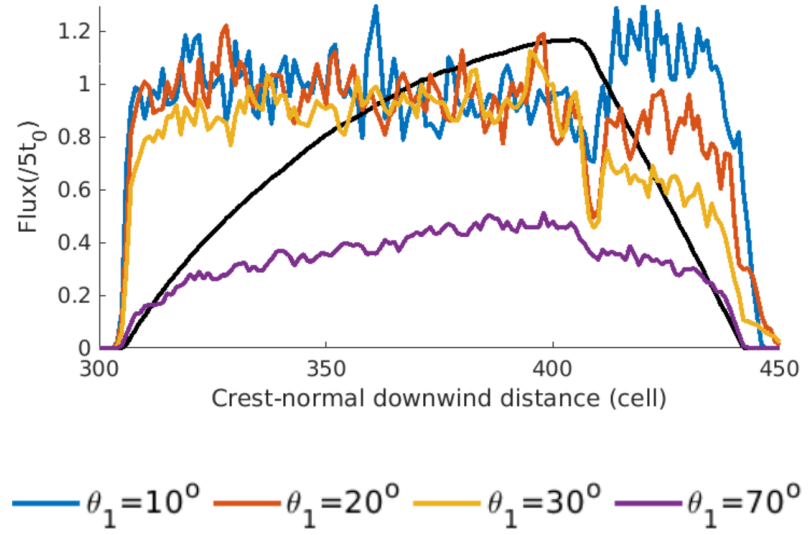


Figure 4-12. Sand flux computed with ReSCAL over a crest-normal transverse dune transect enforced with varying wind-crest angle θ_1 (presenting the same 4 θ_1 examples as in Figure 4-8) (A) Crest-normal (W-E) flux (B) Crest-parallel (N-S) flux.

To further clarify and quantify the sand carrying (by the wind) capability on the lee slope, Figure 4-13 computes the W-E flux Q_{out} (crest-normal flux over inter-dune surfaces, also Q_{we} here) at a distance away (20 cells away from the east domain

boundary) from the lee slope plinth through a set of wind-crest angles θ_1 at four wind speeds (i.e. $\tau_{min} = 0, 100, 200\ and\ 300$). The flux origin is sand not trapped by the dune after moving through the whole dune to the downwind. In other words, the flux is indicative of the capability of wind carrying sand on the lee slope.

The mean of flux measured during the same instantaneous time duration of 5 t_0 is taken for each point and represents the amount of sand 'lost' from the dune in the W-E component. These two outflux-angle trends indicated by Figure 4-13 well corresponds to the dune surface flux shown in Figure 4-12.

It has been demonstrated (Figure 4-9) that the wind strength is better maintained with decreasing θ_1 where the dune slopes are in lower gradients. Where a smaller wind angle θ_1 is enforced, the wind interacts with flatter dune slopes, which lead to stronger sand carrying capability of the wind. For the part of Q_{out} profiles (Figure 4-13) where θ_1 is greater than 20°, although a greater θ_1 has a larger crest-normal wind component ($cos\theta_1$), the wind sufficiently decelerates as the interacting dune slopes are steeper. The θ_1 control on Q_{out}, therefore, is driven by the flatter slopes rather than the crest-normal component $cos\theta_1$. On the contrary, for the other part (Figure 4-13) where Q_{out} shows a positive relationship with θ_1, the driver of the Q_{out} is crest-normal wind vector.

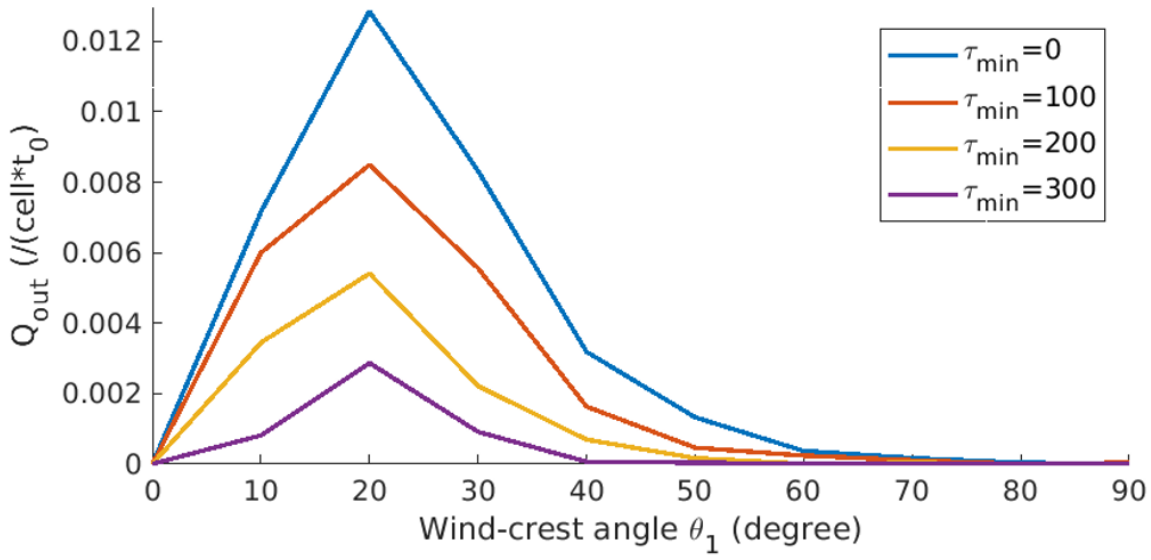


Figure 4-13. Sand outflux resulted from sand erosion and transport on the lee slope with respect wind-crest angle, presenting 4 wind speed sets $\tau_{,min} = 0$, $\tau_{,min} = 100$, $\tau_{,min} = 200$ and $\tau_{,min} = 300$

4.3.2 Internal sedimentary structure

When running the simulation for an extended time, the initial transverse dune may not be maintained, but split into secondary dunes as a result of bed instability (Correch du Pont, et al., 2014). The form of a transverse dune is based on avalanche in the lee associated with crest-normal migration (e.g. Pye and Tsoar, 2008). However, the low wind-crest angle part of the four profiles of Figure 4-13 may indicate that the wind may not be capable of maintaining the transverse dune due to the lack of avalanche control on the dune. To visualize the wind angle effect on dune shapes and clarify the range of angles where the transverse dune can be maintained, Figure 4-14 below

provides the topography images after 2000 t_0 from the initial condition shown in Figure 4-1 (A)

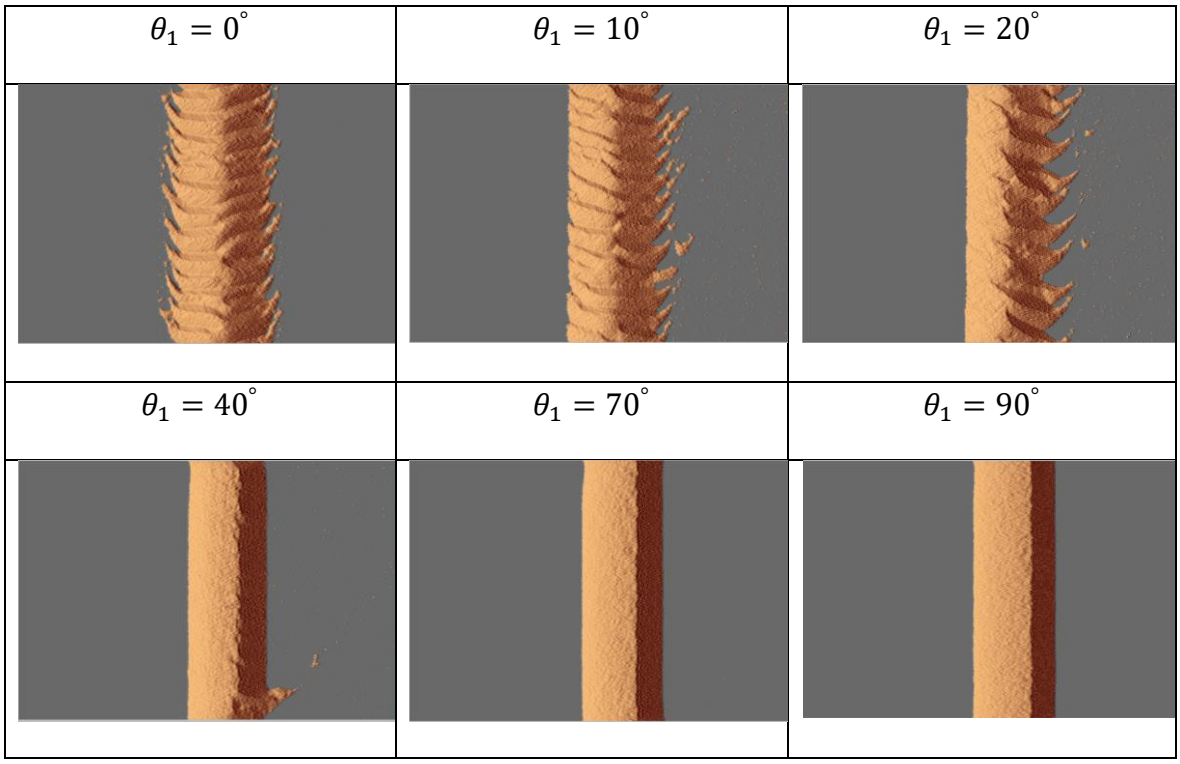


Figure 4-14. Topography images after 2000 t_0 from the initial transverse dune shown in Figure 4-1 (A) enforced with varying wind-crest angles θ_1 at the highest wind speed ($\tau_{min} = 0$).

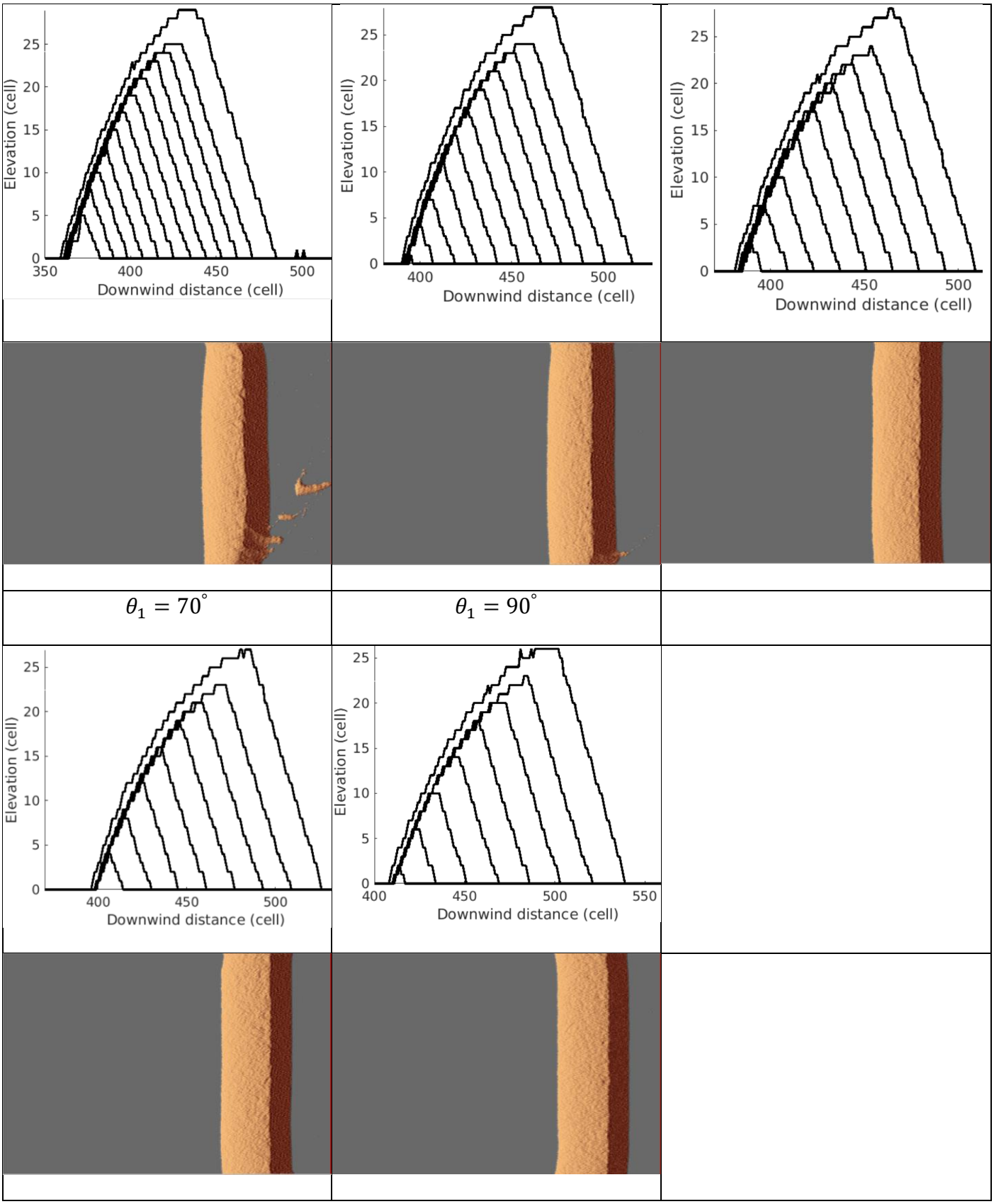
Figure 4-14 directly shows how the transverse dune topography is affected by the incoming wind angle, corresponding to the outflux profile of Figure 4-13. With the wind angle θ_1 getting smaller, the wind gets stronger sand carrying capability over the lee slope, particularly in the crest-parallel direction. Therefore, in Figure 4-14, for $\theta_1 = 20^\circ$ and smaller angles, the crest-parallel wind components are so strong that superimposing dunes arise. With the rapid increase of superimposing dune number, the local bedform gets a finer pattern on the lee slope where wind reacceleration occurs. This change of bedform pattern opposes to the commonly recognized pattern coarsening processes (i.e. Ewing and Kocurek, 2010; Gao, et

al., 2015; Day and Kocurek, 2018) where the dune ridge number reduces, dunes coalesce and get larger. Also, with absence of 3D flow deflection, the 2D modelled flow can produce secondary dune ridges similar to scenarios reported by Walker and Shugar (2013).

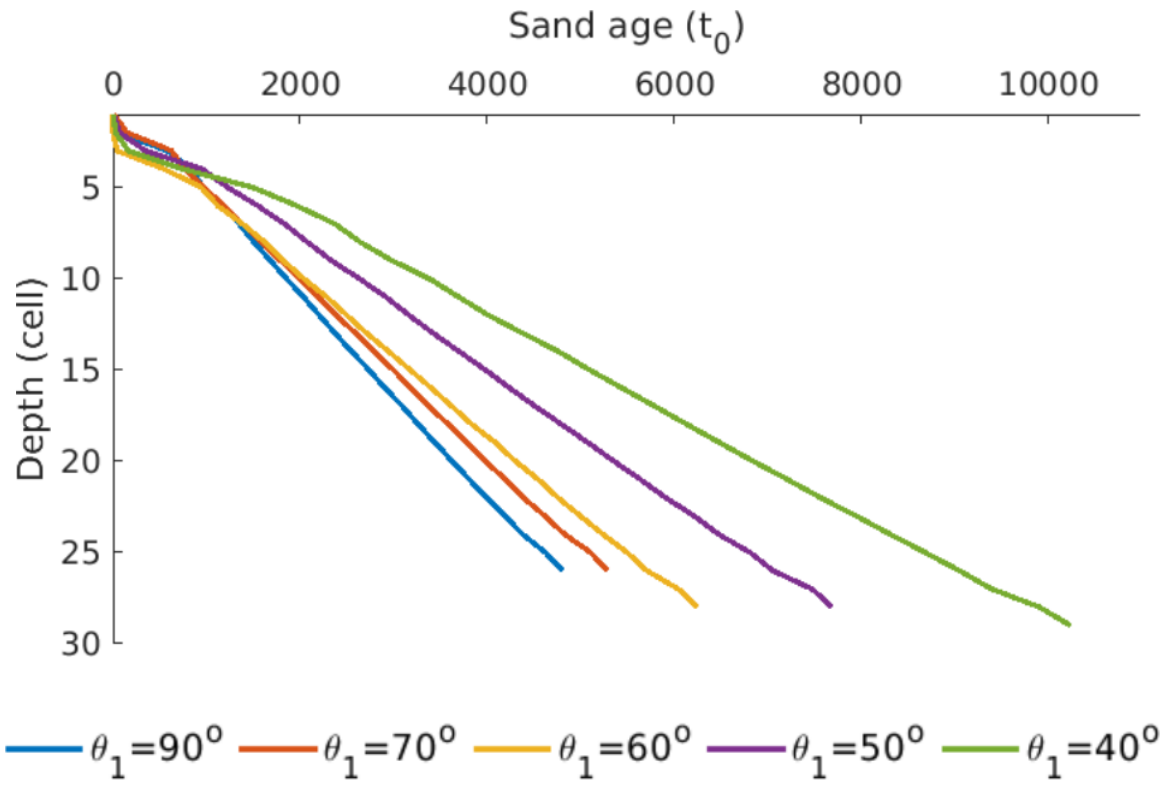
Above this 30-degree angle, the transverse dune is maintained. Figure 4-15 below presents the internal structure of the maintained transverse dune after they are sufficiently adapted to the enforced wind (i.e. all sediments set at the initial condition of Figure 4-1 (A) have been activated in dune migration). Firstly Figure 4-15 (A) visualizes bedding patterns of the dune by mapping buried surfaces with a time interval of 1000 t_0 for the five wind angles $\theta_1 = 40^{\circ}$, 50°, 60°, 70° and 90°. These angles are selected here because the transverse dune is well maintained as a whole after the sand is fully reactivated and reburied. The transverse dune does not exist any longer with lower angles (=<20°) tested. The age-depth profiles drilled through the dune crest are provided in Figure 4-15 (B) and the age-downwind distance profiles of the bottom layer of sand are given in Figure 4-15 (C),

(A)

$\theta_1 = 40^{\circ}$	$\theta_1 = 50^{\circ}$	$\theta_1 = 60^{\circ}$


Elevation (cell)
Downwind distance (cell)
$\theta_1 = 70^\circ$
$\theta_1 = 90^\circ$

(B)



(C)

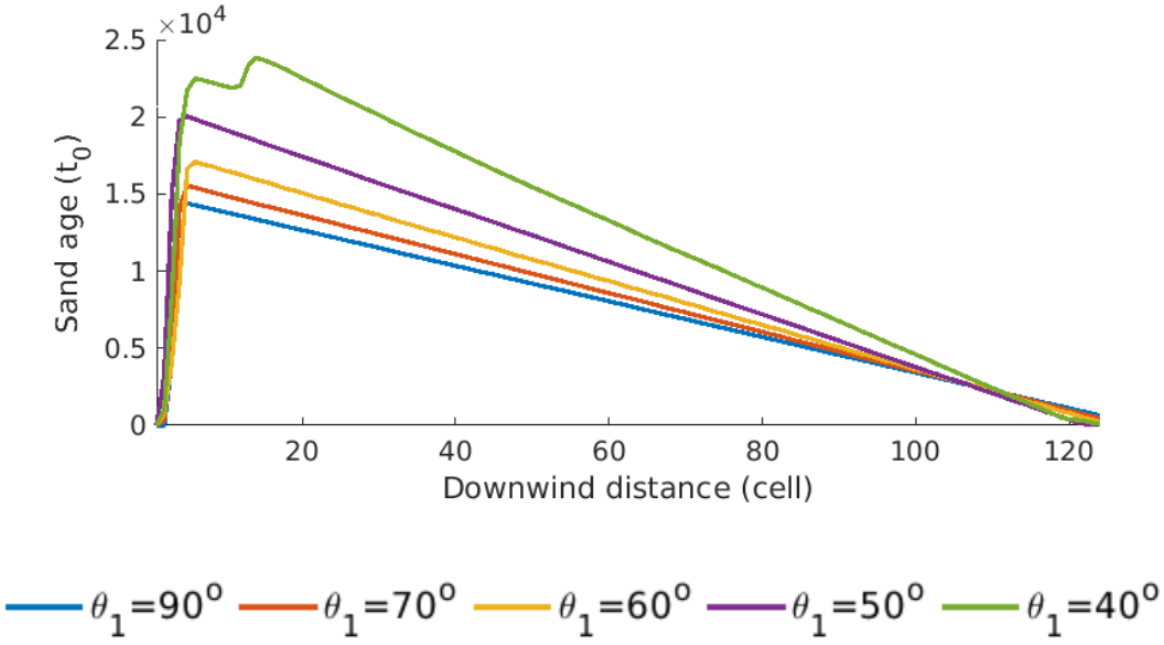


Figure 4-15. Internal sedimentary structure of a transverse dune at wind-crest angles θ_1, at the highest wind speed ($\tau_{,min} = 0$). In ReScAL (A) Bedding patterns visualized with buried surfaces of each 2000 t_0. (B) Age-depth profile

through the dune crest. (C) Age-downwind distance profile of the dune bottom sand.

For the internal stratigraphy shown in Figure 4-15, the shallowest 5 cells (in depth) are the currently active and below are the structure preserved. Figure 4-15 (A) does not indicate a significant trend of dune width with respect to the wind angle θ_1, whilst the density of the cross strata tends to be influenced by θ_1. Greater angle θ_1 builds thicker strata during the same time duration of 1000 t_0. This corresponds to the profile of avalanche magnitude Figure 4-11, indicating that more intense avalanche builds thicker strata under more crest-normal winds. In comparison, smaller θ_1 generates less intense avalanche, thinner cross strata, but the whole dune has longer ages buried. For example, when $\theta_1 = 40^{\circ}$, the dune transect contains 12 surface line intervals with (horizontal) thickness 10 cells in average. When $\theta_1 = 90^{\circ}$, there are 7 sets preserved with an average (horizontal) thickness of 17 cells. The features of the grain flow strata (Figure 4-15 (A)) are more directly indicated by the obliqueness and maximum ages of the age-distance curves of Figure 4-15 (B) and (C).

For stratigraphy, previous studies have been focused on how wind speeds influence the strata thickness (e.g. Tanner, 1965; Parrish and Peterson, 1988; Mountney and Jagger, 2004; Rowe et al., 2007; Eastwood, et al., 2012), while wind angle was mainly concerned with strata orientation (e.g. Eastwood, et al., 2012). The modelled outputs shown here demonstrates that the wind angle has a control on the stratigraphy features without changing orientation of either the dune or the strata preserved beneath. Similarly for dune surfaces processes relating to building up the stratigraphy, wind speeds have also been the key concern (e.g. Sutton, et la., 2013 (a) and (b); Nield, et al., 2017; Cornwall, et al., 2018) in terms of grain flow events,

whilst the Section 4.3 here demonstrates the control of wind angle on the grain flow magnitude.

4.3.3 Summary of Section 4.3

This section firstly investigates how the angle of an incoming wind affects the flow structure as well as sand movement of a transverse dune for a short (i.e. instantaneous) time scale. More crest-parallel winds have stronger sand carrying capability over the lee slope associated with smaller avalanche magnitude. For an extended time scale the dune topography evolution is analysed to identify the range of wind angles that can maintain the form of the transverse dune, instead of generating secondary superposition dunes as a result of strong crest-parallel sand movement. For the range of wind-crest angles (i.e. over 30°) where the transverse dune is maintained, more perpendicular wind builds thicker grain flow strata for a same time duration and eventually the dune contains shorter history. In general, regarding the internal sedimentary structure, more crest-normal winds make similar effect to higher wind speeds: higher avalanche magnitude, thicker cross strata newly builds, younger total age of the transverse dune.

4.4 Summary of Chapter 4

This chapter in the first place explores the wind speeds and wind angles control on the airflow structure modelled with the lattice gas (LG) wind associated with the instantaneous sand movement and dune evolution and internal stratigraphy for an extended time scale. Key findings of the chapter are summarized below:

---The airflow pattern (described with shear stress) modelled with LG over a transverse dune includes deceleration at windward slope foot when approaching the

dune, acceleration through the windwards slope, deceleration through the lee slope and reacceleration afterwards from lower portions of the lee slope.

---The sand moving processes are corresponding to the airflow pattern, including: sand erosion, transport and (directly wind driven, non-avalanche) deposition over the windwards slope and avalanche over the lee slope.

---With respect to wind speeds, higher speeds winds trigger higher avalanche magnitude, forming thicker grain flow strata, whilst activating the oldest sediments sooner and the dune is younger. On the contrary, lower speeds winds trigger lower avalanche magnitude, forming thinner strata, whilst being more preservative on the oldest sediments and the dune is older.

---With respect to wind-crest angles, greater angles make similar effect to higher wind speeds: triggering greater avalanche events and forming thicker strata. Narrower angles make similar effect to lower wind speeds: triggering weaker avalanche and forming thinner strata.

Chapter 5 Bimodal wind regime controls on dynamics and internal stratigraphy of established linear dunes

Following dune dynamics and sedimentary structure controlled by unimodal winds studied in Chapter 4, Chapter 5 progresses to bimodal wind regimes. Regarding the two dynamic features of linear sand dunes (i.e. lateral migration and elongation), experiments designed in this chapter investigate lateral migration, excluding influences of elongation. The subsequent Chapter 6 investigates the elongation dynamics excluding influences of lateral migration.

To start, Section 5.1 presents the simplest scenario where a reversing wind is applied to a transverse dune, investigating the flow structure, surface sand movement and the stratigraphic features resulting from the wind reversal. Regarding the surface processes, outputs of Section 5.1 are compared with documented wind profiles studied over linear dunes, like Tsoar, 1983; Livingstone, 1986; Wiggs, et al., 1996 (b). This comparison is reasonable because a topographic similarity is shared where the dune lee is not purely characterized by a slip face, but the wind interacts with lower-angle topography in the lee. Therefore, these scenarios share similar patterns of the instantaneous sand movement over the dune surface in the wind reversal process. For the stratigraphy features resulting from reversed winds, outputs of this section are compared with ground penetrating radar (GPR) work, including linear dunes surveyed by Bristow, et al. (2000, 2005 and 2007) and reversing transverse dunes by Bristow, et al. (2010 (a)).

From Section 5.2 onwards, this chapter studies dynamics of existing linear dunes controlled by bimodal wind regimes. In particular, the investigation is focused on the lateral migration issue. Firstly Section 5.2 has a purpose to provide a numerical

solution to the lateral migration potential of individual linear dune that has long been under debate (e.g. Hanna, 1969; Tsoar, 1983; Rubin and Hunter, 1985; Tsoar, et al., 2004; Bristow, et al., 2000, 2005 and 2007; Livingstone, et al., 2007; Rubin and Hesp, 2009). Secondly Section 5.3 is extended to study possibilities of the sideways movement of multiple dunes where the interdune spacing is close. The airflow interacts between dunes may influence the lateral displacement of each dune. As discussed in Chapter 2 and Chapter 4, the wind strength recovery to the environmental wind needs around 10 dune heights. Inter-dune spacing shorter than this may result in mass exchange (e.g. Schwämmle and Herrmann, 2003; Liu and Baas, 2020) because the decelerated flow by the upwind dune might preserve erosion of the toe of the downwind dune. Outputs of Section 5.3 are concerned with previous wind flow studies regarding interacting barchans (e.g. Bristow, et al., 2018 and 2019) and wind profiles measured over closely-spaced dunes (e.g. Baddock, et al., 2007 and 2011; Wiggs, et al., 1996 (b)). Additionally, the section may provide possible solutions to several significant aeolian landscape issues, such as controls of width-spacing (e.g. Wasson and Hyde, 1983; Thomas, 1986; Lancaster, 1988) as well as recently raised assumptions surrounding the relationship between the age and coarseness of a dune field pattern (e.g. Telfer, et al., 2017; Day and Kocurek, 2018).

In each set of explorations, the simulation outputs are analysed with the fundamental computing methods shown in Chapter 4, including wind shear stress pattern modelled with lattice gas (LG), surface sand moving processes and the topography associated with the internal sedimentary structure developed throughout an extended model period.

5.1 Flow pattern, sand movement and sedimentary structure of a transverse dune with respect to a reversing wind (wind speed and angle fixed)

Regarding sand dune stratigraphy, the dominant feature is cross strata formed under a stable unidirectional wind and stable dune migration. Concerning capabilities of a CA model, another important stratigraphic feature is low angle surfaces truncating the main strata (e.g. Havholm, and Kocurek, 1994; Kocurek, 2009; Bristow, 2008). One of the key origins (e.g. Bristow, 2008; Bristow, 2019) of the low gradient surface is the dune experiencing winds from opposing directions. After the wind changes back to the original direction and restart to form grain flow strata, the stoss slope of the reversed wind gets buried (e.g. Bristow, et al., 2010 (a)) as a low angle surface intercepting the strata, previously termed as 'reactivation surface' (e.g. Bristow, 2008). This is a commonly seen wind condition in linear dunes under bimodal wind regimes. This section starts with the simplest case, enforcing a reversed wind to the transverse dune shown in Figure 4-1 (A), Chapter 4 and deployed in Sections 4.1 to 4.3. The evolution of the dune due to wind flow structure (e.g. shear stress τ_s), instantaneous sand movement and stratigraphic features built by the reversed wind is investigated.

In this simulation, a crest-normal wind is enforced with the highest wind speed (i.e. lowest shear stress threshold $\tau_{min} = 0$ for erosion occurrence) for a sufficient duration that allows the slip face to reach the lee slope plinth and allows the dune internal structure to adapt to the opposing wind. Practically, the transverse dune shown in Figure 4-1 (A) is deployed as the initial condition (e.g. 400-cell by 600-cell sized domain located with a 26 cells high transverse dune with the east slope fully at the angle of repose), whilst the wind is reversed from W-E to E-W and the

simulation duration ensures the topography has reached a steady shape under this E-W wind.

5.1.1 Flow pattern and sand movement on the surface

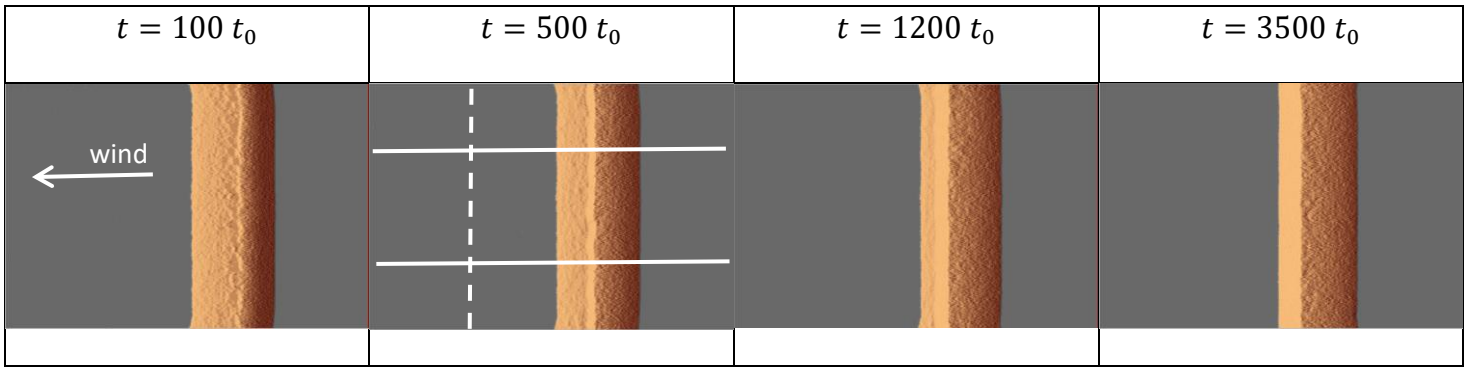
Flow pattern

Four representative time steps are selected and their topography images are presented in Figure 5-1 (A), associated with wind shear stress τ_s profiles presented in Figure 5-1 (B) at each time step. The step t=0 t_0 is the scenario analysed in Section 4.1, with the same topography (east slope at the angle of repose) and wind profiles modelled. Computing of the 2D topography and wind transects of Figure 5-1 (B) takes the average of the 200 transects labelled with two white lines in the $t = 500\ t_0$ image of Figure 5-1 (A). The τ_s plots are labelled with δ_s (computed using Equation 4.1, Chapter 4), the change from the τ_s of environmental wind over flat surfaces, taking the distance between 50-cell and 150-cell.

According to Figure 5-1, at the step $t = 100\ t_0$, the dune crest has just started to migrate towards the west and the slip face has only extended for an 8 cells distance in horizontal. At the following two steps $t = 500\ t_0$ and $t = 1200\ t_0$, the slip face further extends downwind, the crest further migrates, whilst the plinth of the west slope of the dune remains static. Eventually the slip face reaches the plinth and the dune base starts to migrate together with the whole dune. The crest-normal migration of the whole dune is indicated by the last step $t = 3500\ t_0$ of Figure 5-1 (B). At this latest step shown, the plinth of the active (west) lee slope has a net displacement from the upwind (W-E) distance of the initial location 310-cell to 295-cell, while the east slope base has migrated from the W-E distance of 445-cell to

420-cell. The dune gets narrower as the west plinth has a shorter displacement than the east plinth.

(A)



(B)

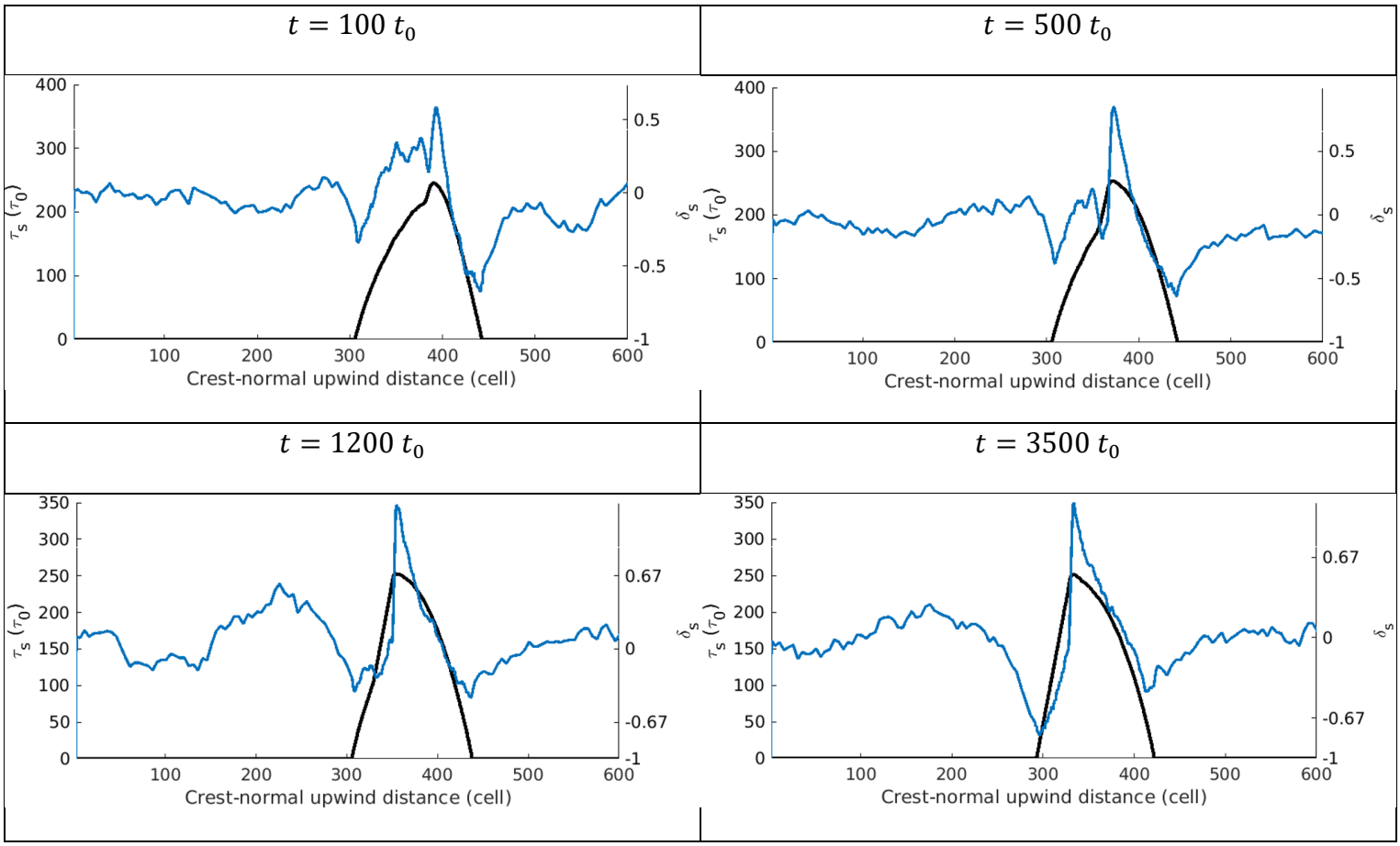


Figure 5-1. Evolution of a transverse dune enforced with a reversed wind (i.e. originally W-E reversed to E-W). The initial condition deploys the topography and domain settings specified in Figure 4-1: a 26 cells high transverse dune

with the east slope fully occupied by the slip face, located in a 400-cell (N-S) by 600-cell domain. (A) Topography images at time steps with varying degrees of the slip face downwind (i.e. westwards) extension. (B) Wind shear stress τ_s (labelled with change from the flat surface δ_s) profiles modelled with LG corresponding to (A), both the 2D topography and τ_s taking the average of the 200 transects labelled in (A) $t = 500\, t_0$.

According to Figure 5-1 (B), when the topography of the active dune lee has not been fully covered under the slip face, but the lower portion is at lower gradients, where $t = 100\, t_0$, $500\, t_0$ and $1200\, t_0$, a common feature is shared between the wind shear stress τ_s profiles. For the three steps, there are two deceleration and reacceleration stages in the lee. The wind structure is schematized in Figure 5-2.

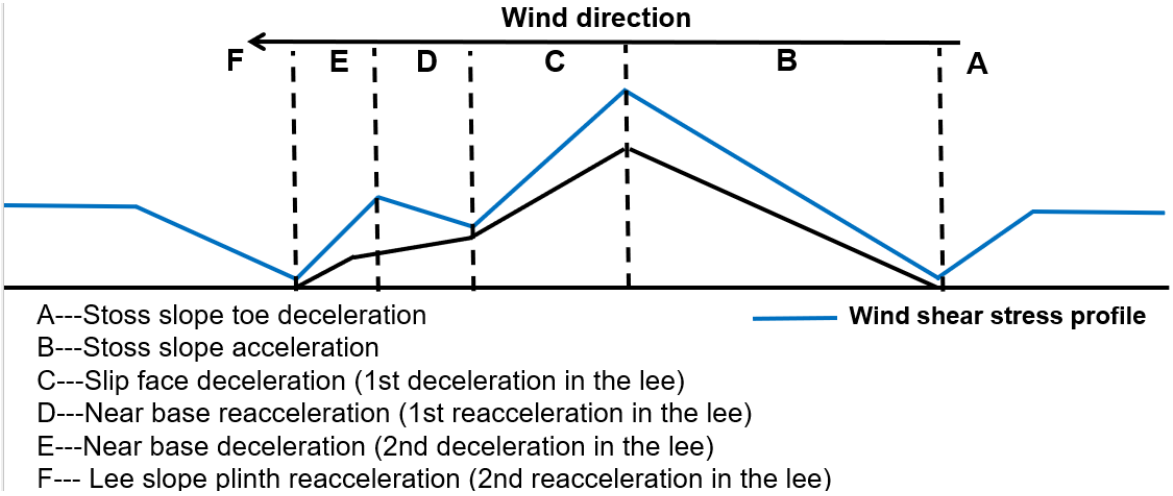


Figure 5-2. Schematic of wind shear stress τ_s profile (based on Figure 5-1 (B)) over the dune topography where the slip face in the lee has not reached the plinth, but lower portion of the lee side topography remains at lower gradients and gets steeper to the plinth (D and E). The six stages of the τ_s evolution with respect to dune topography are labelled.

---The first deceleration initiates from the dune crest, through the slip face until the intercepting point to the low gradient base, see zone C labelled on Figure 5-2. The downwind side of this point is where the first reacceleration occurs. At time $t = 100\ t_0$ (Figure 5-1 (B)), the reacceleration starts around W-E distance of 390-cell and at $t = 500\ t_0$, around 370-cell. For time $t = 1200\ t_0$, it occurs over a very short distance around 330-cell as the slope remaining at the low gradient is short. The zone C deceleration is gradual along the slip face and reaches a minimum at the topography transition point, followed by zone D where the wind reaccelerates to a local maximum in the in the middle of the low gradient portion near dune plinth. For the three time steps $t = 100\ t_0$, $500\ t_0$ and $3500\ t_0$, the partial maximum shear stress τ_s respectively occurs around upwind distance of 370-cell, 350-cell and 305-cell (Figure 5-1 (B)).

---The second deceleration (zone E of Figure 5-2) starts from the local maximum locations (in the middle of the lee slope) described above. The τ_s gradually decreases along the remaining downwind part of the flat dune base and reaches the minimum at the plinth of the active lee slope. This is where the second reacceleration (zone F of Figure 5-2) initiates and the wind starts to recover to the environmental wind strength over the flat non-erodible surface on the downwind side of the whole dune.

Generally speaking, the fluctuation of τ_s in zone D and E (Figure 5-2) is on a smaller magnitude than in zone B and C. Additionally, the τ_s reduction occurring in zone E tends to be the final deceleration regarding the whole dune. In Figure 5-1 (B), for example, when $t = 500\ t_0$, τ_s is reduced approximately half from the dune crest

($\tau_s = 345\ \tau_0$ to $180\ \tau_0$) to the point shifting to zone D. In the subsequent reacceleration, however, τ_s only increases for 40 τ_0. Following is the final reduction of τ_s to 130 τ_0.

This feature differentiates the three steps $t = 100\ t_0, 500\ t_0$ and $1200\ t_0$ from the last time step shown $t = 3500\ t_0$ in Figure 5-1 (B), as well as from wind profiles given in Figure 4-9 of Chapter 4. In these compared scenarios, the slip face fully covers the lee slope, on which deceleration and reacceleration occur once. Therefore, the wind τ_s structure described above (i.e. $t = 100\ t_0, 500\ t_0$ and $1200\ t_0$) is attributed to the change of the local slope gradients. The first reacceleration occurs where gradients lower from the repose angle to the upper and the most flat part of the base (starting point of zone D, Figure 5-2), while with increase of the base gradient, the second deceleration occurs. The overall wind pattern is that the wind has a trend to reaccelerate when starting to interact with a flatter topography, such as the non-erodible flat bed (Figure 2-4 and Figure 4-1 (B)) or lowering of the local slope (three early time steps of Figure 4-1 (B)). Similarly, the wind tends to decelerate when there is an increase (positively to the lee slope) of the slope gradient. After the wind passes over the crest, there is an abrupt change of topography from negative (stoss slope to lee slope) to the steepest positive (slip face), thus the wind weakening is at high magnitude. To compare, the second deceleration (zone E, Figure 5-2) magnitude is lower as the gradient change is smaller.

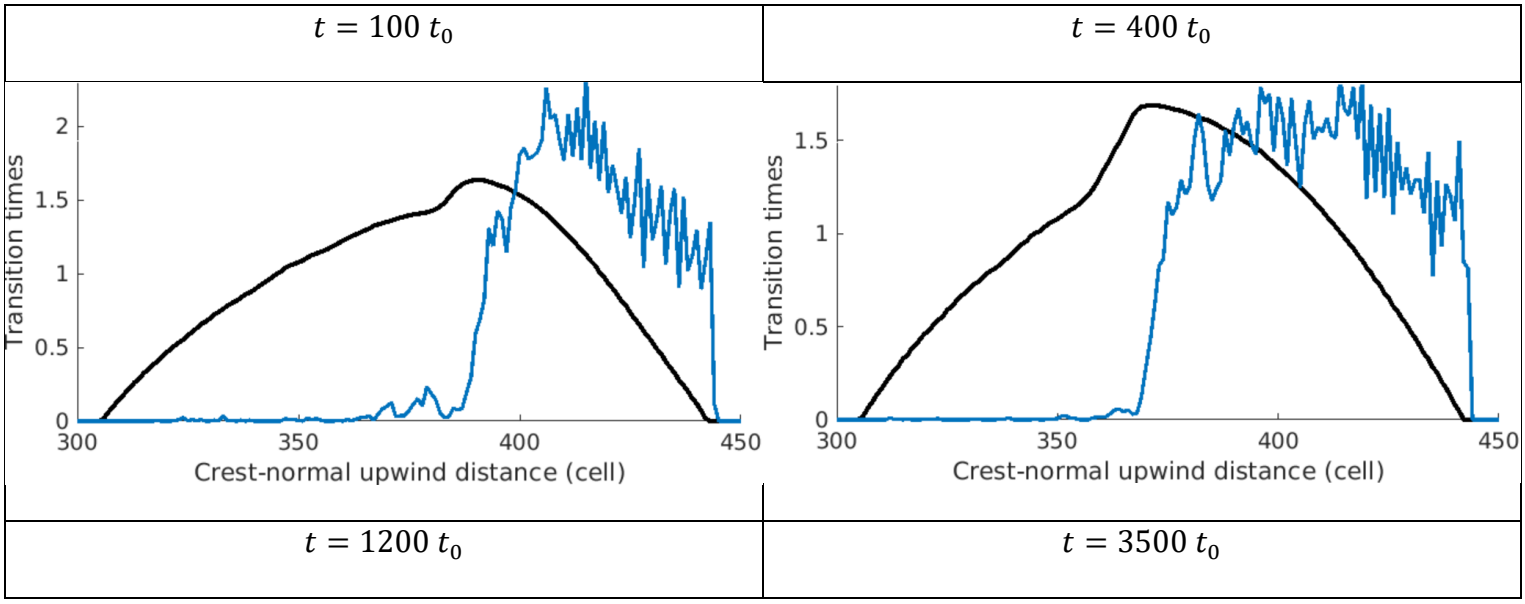
For the three time steps $t = 100\ t_0, 500\ t_0$ and $1200\ t_0$, the shear stress structures given in Figure 5-1 (B) are in agreement with wind profiles measured by Tsoar (1983), Livingstone (1986), Sweet and Kocurek (1990), Wiggs, et al. (1996) and so

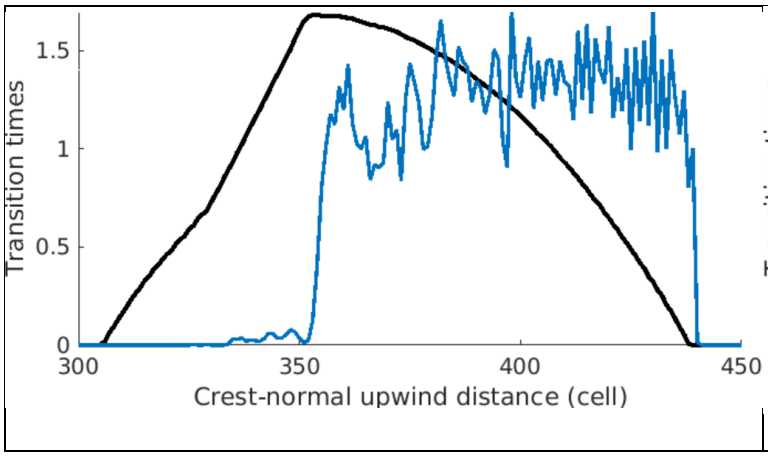
forth, see wind profiles presented in Figure 2-4 of Chapter 2. The dunes are characterized by a lee slope where either there is a static base (Livingstone, 1986, Figure 2-4 (B)) or there is a gradual decrease of the lee slope gradient (Tsoar, 1983, Figure 2-4 (A); Wiggs, et al., 1996 (b), Figure 2-4 (C)). The flow structure schematized in Figure 5-2, therefore is particularly similar to wind profiles measured by Livingstone, 1986, as the topographies have the same feature with a slip face and a low angle plinth. For the last time step $t = 3500\ t_0$, the wind structure is in agreement with regular wind structures measured over transverse dunes (e.g. Sweet and Kocurek, 1990; Walker and Nickling, 2002; Parsons, et al., 2004; Schatz and Herrmann, 2006; Baddock, et al., 2007).

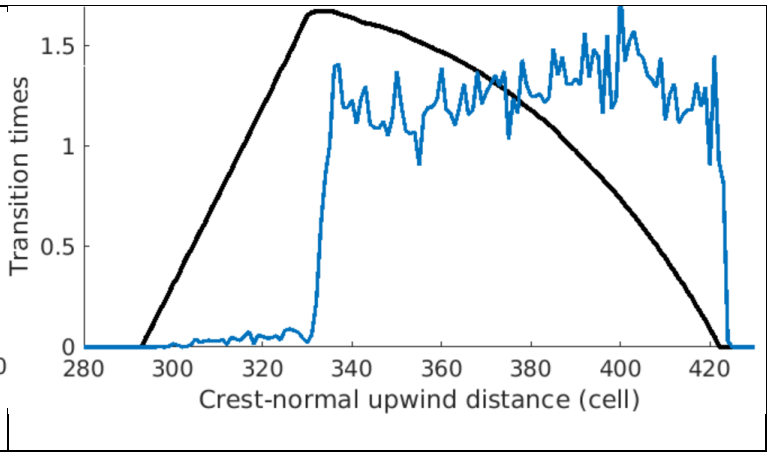
Sand movement

The corresponding sand moving magnitude are presented in Figure 5-3. The magnitudes are expressed with occurrence times of each type of transition for an instantaneous duration of 5 t_0.

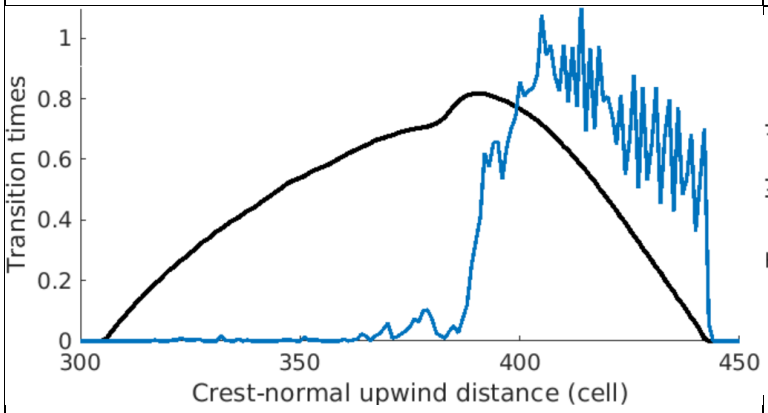
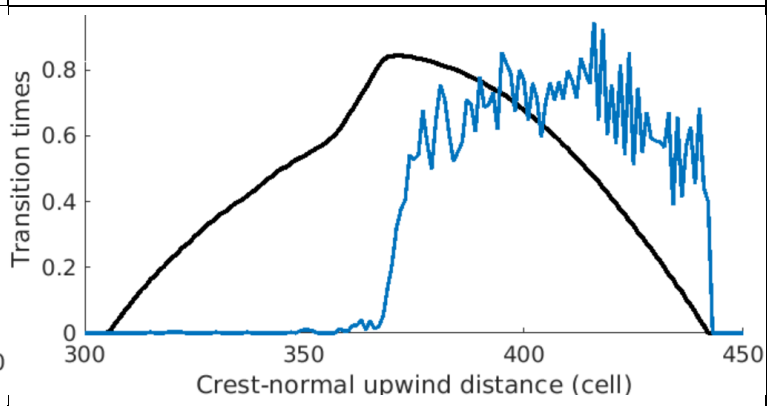
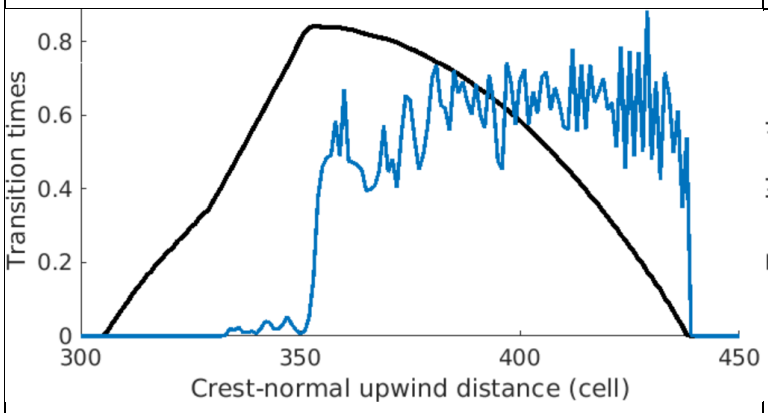
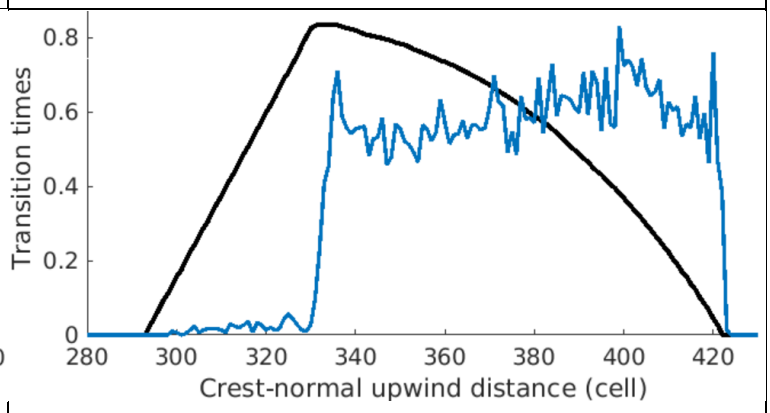
(A)





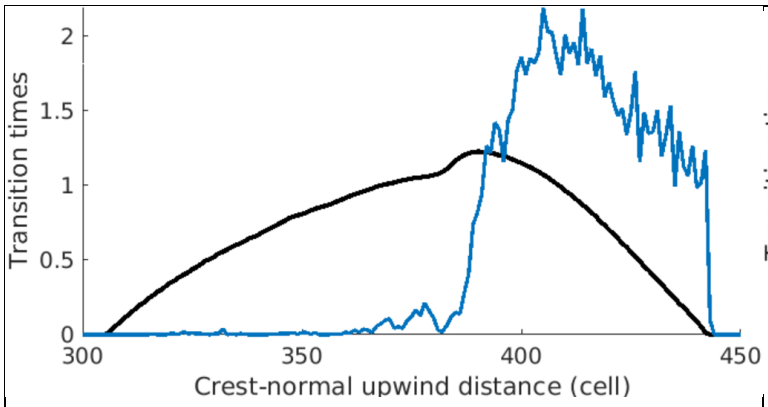


(B)

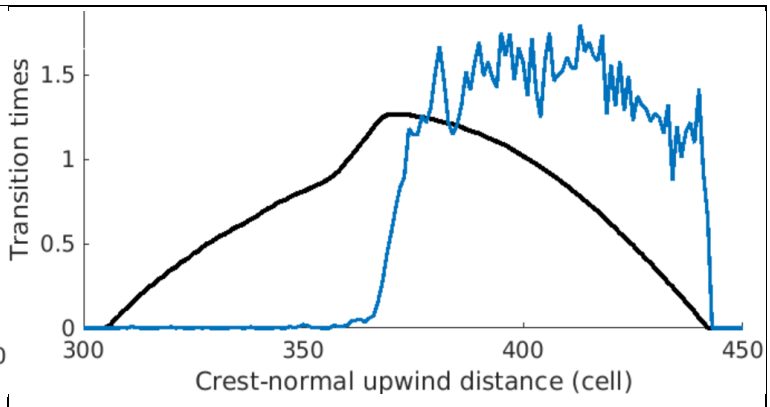
$t = 100\ t_0$	$t = 400\ t_0$
	
$t = 1200\ t_0$	$t = 3500\ t_0$
	

(C)

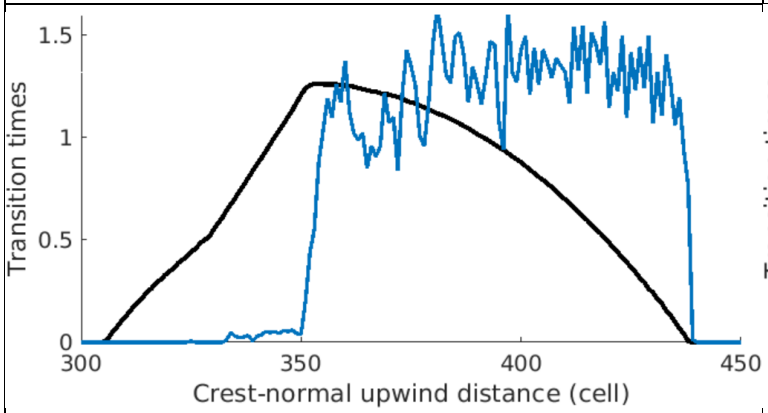
$t = 100\ t_0$	$t = 400\ t_0$

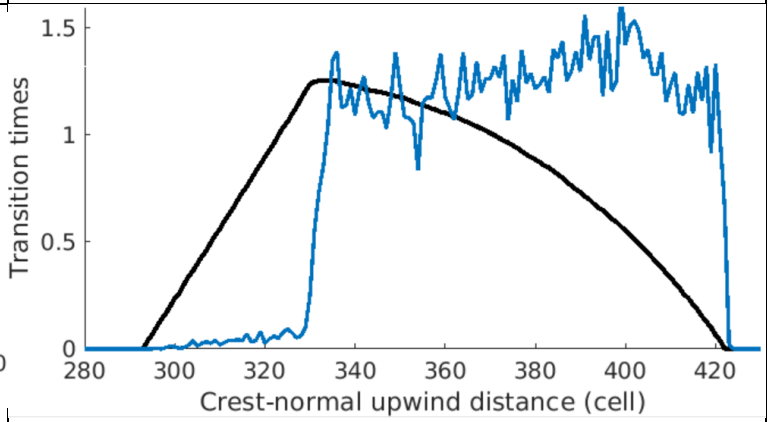


$t = 1200\ t_0$



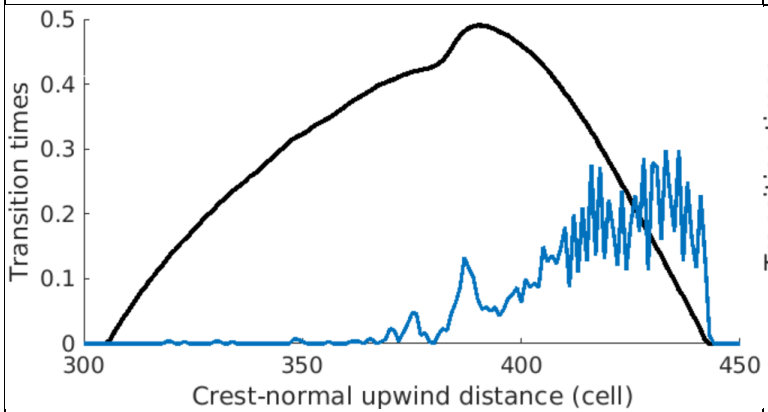
$t = 3500\ t_0$



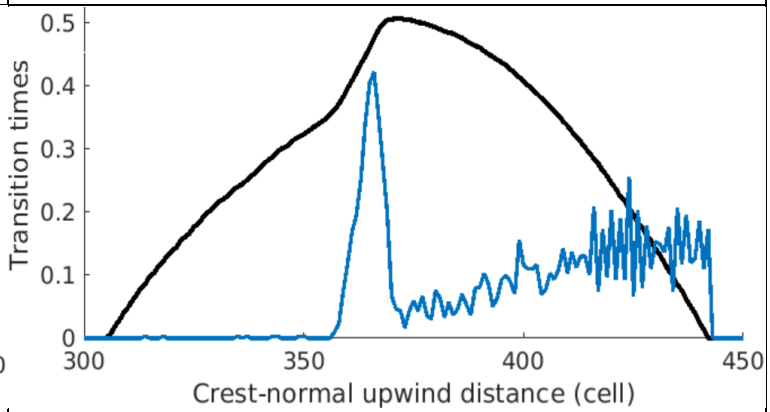


(D)

$t = 100\ t_0$



$t = 400\ t_0$



$t = 1200\ t_0$

$t = 3500\ t_0$

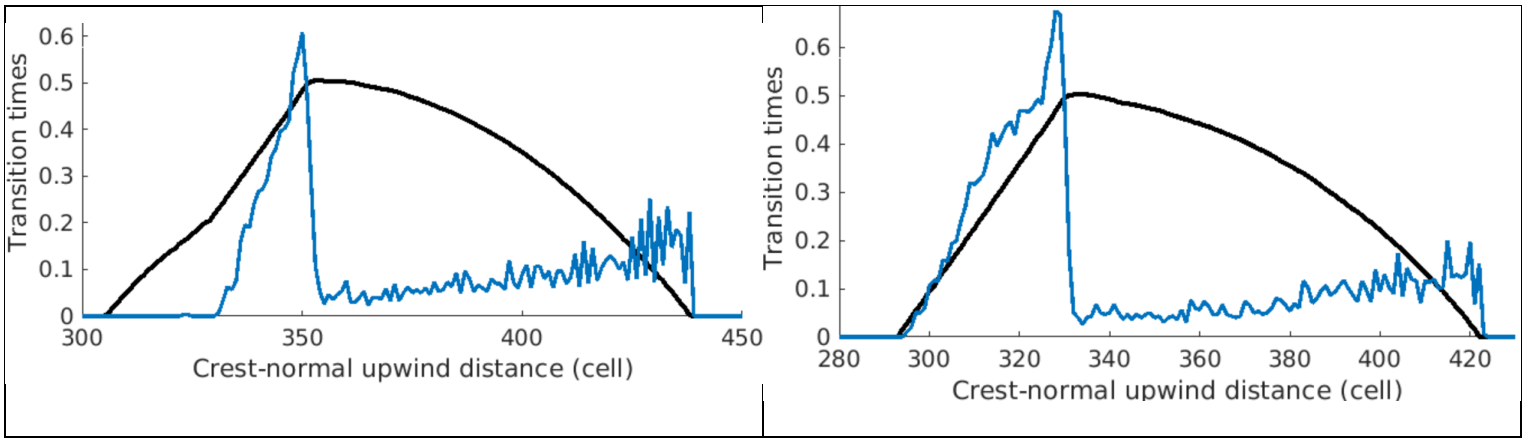


Figure 5-3. Magnitude of sand moving process (described by doublets transition times for an instantaneous duration of 5 t_0) modelled with ReSCAL in the evolution of a transverse dune enforced with the wind opposing to the original direction (i.e. reversed from W-E to E-W), in response to the wind shear stress profiles presented in Figure 5-1 (B). (A) Erosion (B) Transport (C) (non-avalanche) Deposition (D) Avalanche

The key information gained from Figure 5-3 is that sand remains inactive over the lower lee slope where the slip face has reached it. In the three wind driven transitions, erosion, transport and deposition (Figure 5-3 (A) to (C)), wind can carry sand, corresponding to the reaccelerated wind in zone D (Figure 5-2). For example, in the erosion profile (Figure 5-3 (A)) at time step $t = 100t_0$, there is a small increase of the magnitude between 380-cell and 364-cell following the rapid decrease at the short slip face. Also, at time step $t = 1200t_0$, resumption of sand erosion in the lee occurs around the slope changing point from a flip face to a lower gradient at upwind distance of 335-cell. The transport and deposition profiles of Figure 5-3 (B) and (C) show the same pattern as in erosion of Figure 5-3 (A). The three wind driven profiles correspond to the shear stress structure of Figure 5-1 (B) where erosion transitions are initiated in the lee near the first reacceleration zone.

Figure 5-1 (B) shows a gradual reduction of the shear stress through the slip face in the lee. As a result, in Figure 5-3 (A) to (C), the weakening of the three wind driven processes is gradual, instead of immediate disabling. For avalanche magnitude shown in Figure 5-3 (D), the occurrence corresponds to extension of the slip face (zone C of Figure 5-2).

Figure 5-3 (A) to (C) adequately demonstrate that wind is capable of eroding and transporting sand on the lee slope under the E-W wind. To further clarify the strength of this capability, Figure 5-4 below provides the E-W sand outflux evolution with time captured at the crest-normal upwind distance 200-cell, approximately 100 cells away from the lee slope plinth. The flux results either from sand eroded from the lee slope, or from sand directly transported from the stoss slope without deposition. The general pattern indicated by Figure 5-3 and Figure 5-4 is that steepening of the lee slope over time leads to an overall decrease of the outflux. The outflux can be approximated to zero when the slip face has reached the plinth and the whole dune migrates after t=2000 t_0. For ReSCAL algorithms, this is attributed to reduction of doublets  (i.e. less bumps on slip surfaces) and  (i.e. shorter slope length in horizontal).

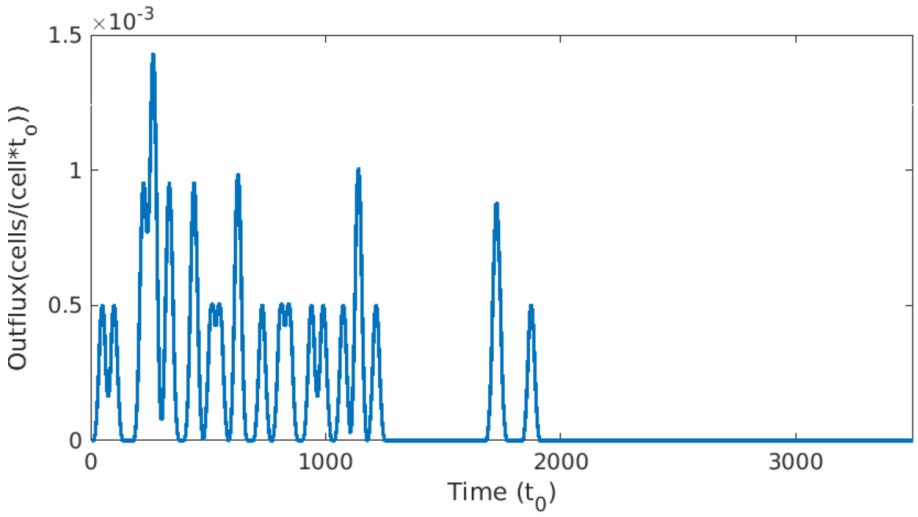


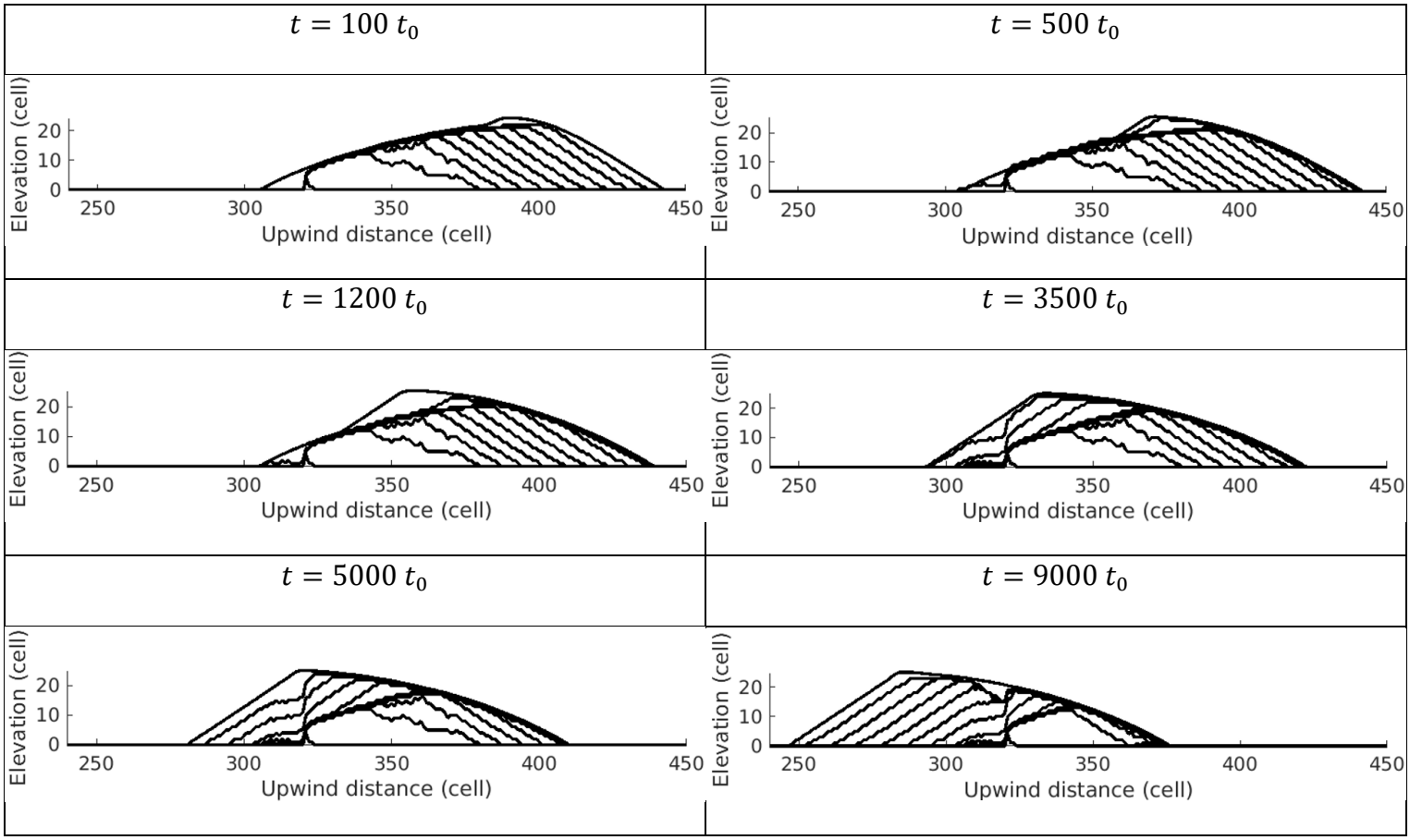
Figure 5-4. Sand E-W flux computed at a distance (white dashed line labelled in the second image of Figure 5-1 (A)) from the lee (west) slope plinth. The magnitude of sand outflux is shown to decrease over time as the dune re-orientates to the E-W wind.

5.1.2 Internal sedimentary structure

The internal structures of the dune at the four time steps shown (Figure 5-1) are presented in Figure 5-5, as well as two later times when the sedimentary structure is further adapted to the reversed wind (t=5000 t_0 and 9000 t_0). Figure 5-5 (A) provides bedding patterns visualized with buried dune surfaces for each 1000 t_0 time interval. Figure 5-5 (B) shows age-depth profiles drilled through the dune crest. The two key stratigraphic components (e.g. Kocurek, 2009; Bristow, 2008), main grain flow strata and low angle (reactivation) truncation are well reflected in Figure 5-5. These stratigraphy features were previously demonstrated by GPR data. For example, Bristow, et al. (2010 a) surveyed reversing dunes in Antarctica. The GPR images show combinations of grain flow strata and reactivation surfaces at a higher complexity. Also, in barchan dunes surveyed by Bristow (2019), the GPR images demonstrate erosional surfaces near dune crests. The main grain flow strata at the

angle of repose are truncated by the lower angle surfaces, partially attributed to burial of the erosional surfaces (i.e. active stoss slope) during the short reversed wind period. In Bristow (2019), the low angle surfaces are at similar stages to the active stoss slope at time steps t=100 t_0 t=500 t_0 where they did not significantly replace the strata of the original wind.

(A)



(B)

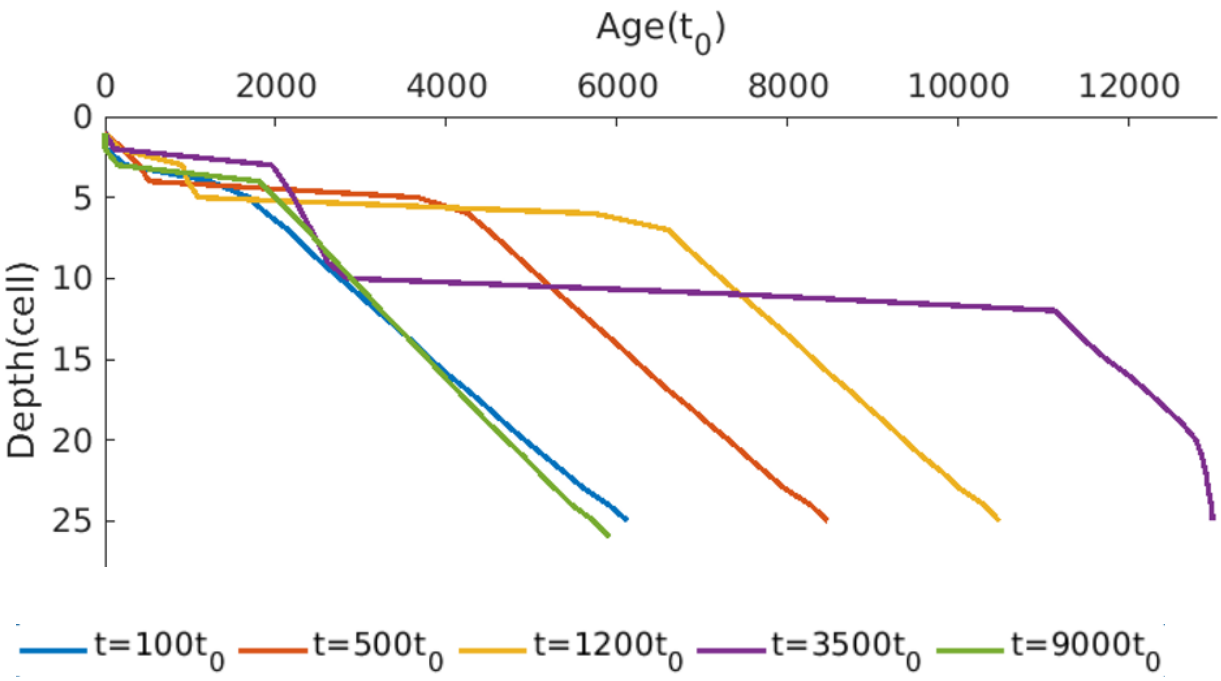


Figure 5-5. Evolution of the internal sedimentary structure of the dune enforced with a reversed wind. (A) Beddings visualized with buried dune surfaces with an interval of 1000 t_0 (B) Age-depth profiles through the dune crest.

The strata of the initial dune (Section 4.1) dips towards the east with the original wind (W-E). Under the reversed wind (E-W), strata develop towards the west with extension of the slip face through the whole west slope, as indicated by Figure 5-5 (A). With the slip face extension, the original stoss (west) slope gets buried as a low angle surface under the newly developed strata dipping westwards. Below the surface are strata dipping eastwards that remain not reactivated by the E-W wind at the time specified. In Figure 5-5 (A), when $t = 100\ t_0$, $500\ t_0$ and $1200\ t_0$, the original stoss (west) slope is still partially exposed on the surface as the slip face formed under the E-W wind has not reached the plinth. From time step $t = 3500\ t_0$ onwards, the west slope has been fully buried as the low angle surface that separates opposite sequences of strata above and below.

Correspondingly in Figure 5-5 (B), above chronology gaps at depth 3-cell, 4-cell, 5-cell and 12-cell $t = 100\ t_0$, $500\ t_0$, $1200\ t_0$ and $3500\ t_0$ indicate accumulation of the newly developed dips under E-W wind. Below the gaps the age-depth columns still pass through the initial dune that remains dipping eastwards (not activated). In comparison, for the latest time $t = 9000\ t_0$, although initial strata dipping to the east still remains in the corner (stoss stope base, Figure 5-5 (A)), the age-depth profile fully (Figure 5-5 (B)) show the E-W wind accumulation. The vertical profile here does not pass through the bounding surface or bottom strata sequences, so the chronology is continuous.

Previous work also demonstrates the combined sedimentary structure produced by reversed winds. For example, Bristow, et al. (2000) shows cross sections mapped with GPR through an elongating linear dune. The wind regime can be approximated to seasonally bimodal at the time of data collection in 2000. This wind regime was applied to reconstruction of the dune evolution in the past via the radar facies. In GPR images, it is a common feature where grain flow strata dip to opposite directions, separated with a low angle surface. Additionally, in Bristow, et al. (2000), at varying locations, the strata formed by the reversed wind is differently weighted in the combined stratigraphy. Older (smaller, close to dune termination) cross sections tend to show that the reversed wind left more dominant strata, similarly to $t = 9000\ t_0$ (Figure 5-5 (A)), whilst in younger sections, more original (before wind reversed) strata remain, like in $t = 3500\ t_0$ and $5000\ t_0$ (Figure 5-5 (A)).

5.1.3 Summary of Section 5.1

This section had an initial exploration of the reverse wind control on flow pattern, sand movement, dune dynamic and the internal sedimentary structure of the dune. Downwind extension of a slip face in the lee was found to be the key feature of the

topography development. Before the slip face reached the plinth, the lee slope base was at a lower gradient, over which the wind reaccelerated to a maximum strength and decelerated for a second time. This reacceleration enabled the wind to erode sand on the lee slope, in which case the extension of the slip face weakened the sand carrying capability of the wind.

Enforcing the reversed wind was able to generate the two key features of aeolian dune stratigraphy. On the one hand, the dune had two sequences of grain flow strata dipping to the opposite directions and they respectively show constant accumulation rate in age-depth profiles. On the other hand, the initial low gradient lee slope got buried as a low angle (reactivation) surface separating the two opposite sequences of strata. In age-depth profiles, the low angle surface was reflected by a chronology gap, above which was the accumulation newly developed by the reversed wind and below which was the remaining sediments before the opposing wind occurs. These stratigraphic features have been well documented by previous fieldwork. In particular, linear dunes surveyed with GPR (e.g. Bristow, et al., 2000) show opposite dips taking varying portions in the sedimentary structure at varying elongation stages of the dunes. With combination of OSL dating, Bristow, et al. (2005 and 2007) also demonstrated forming of chronology gaps where GPR beddings shows a low gradient surface.

5.2 Lateral migration of individual linear dunes

5.2.1 Lateral migration cases in response to varying wind angles

This section explores the lateral migration cases of an individual linear dune under an asymmetrical bimodal wind regime. The initial topography and the wind condition

are schematized in Figure 5-6 (A). Here the domain is set as 200 cells in width (N-S) and 400 cells in length (W-E). All simulations initiate with the linear dune located in the middle of the domain with both slopes at the angle of repose 35°.

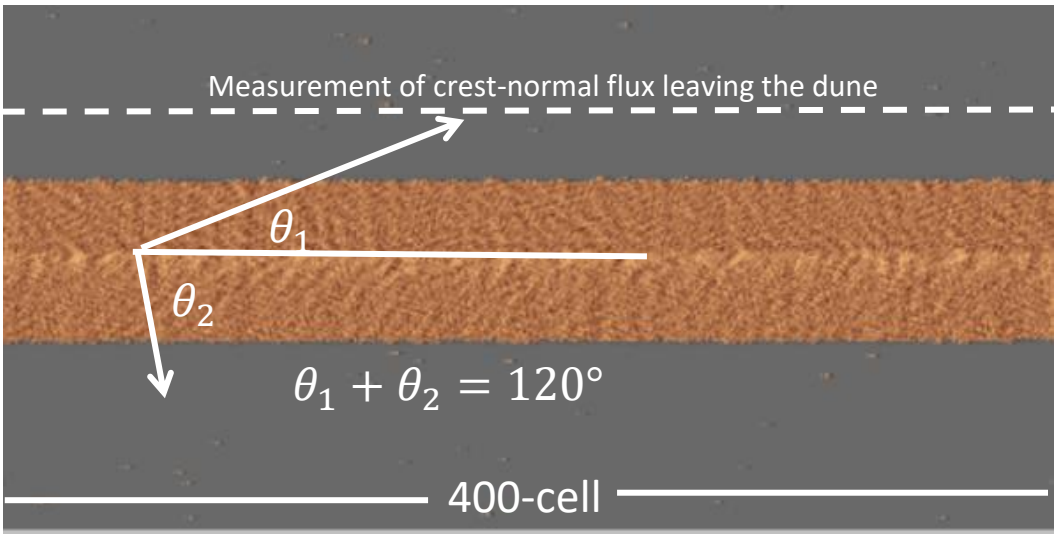
The wind regime has a fixed cycle duration length of $T = 2400\ t_0$, fixed duration of the two winds where $T_1 = 1600\ t_0$, $T_2 = 800\ t_0$ and fixed wind-wind angle $\theta = 120^{\circ}$. The only wind parameter varied is combinations between the two dune crest angles θ_1 and θ_2 (i.e. varying θ_1 and θ_2 combinations with fixed sum $\theta = \theta_1 + \theta_2 = 120^{\circ}$). Periodical boundaries are enforced to the whole domain to keep the total mass of sand as well as avoid generating dune terminations (to simplify the scenario). This ensures influences of elongation are excluded so that lateral migration is studied in the simplified scenario.

In these wind condition settings, the wind cycle duration $T = 2400\ t_0$ ensures that the dune does not break as a result of transverse instability (i.e. Parteli, et al., 2011; Yizhaq, et al., 2012). Also, when $T = 2400\ t_0$, the crest oscillation distance is not so short that the slip face cannot reach dune plinth, but the dune base together with the whole dune has a net displacement. For the setting of $\theta = 120^{\circ}$, the consideration is to select an angle greater than 90°, which is typically thought as the minimum wind angle threshold that can generate or maintain linear dunes (e.g. Rubin, et al., 1990; Werner, 1995; Parteli, et al, 2009 and 2014). Additionally, durations of the two winds $T_1 = 1600\ t_0$, $T_2 = 800\ t_0$ are for the consideration of selecting a typical asymmetry ratio $N = T_1/T_2$ (rather than symmetrical regime where $T_1 = T_2$, which is rarely natural). Testing of θ_1 and θ_2 combinations is around the 'fingering mode' (e.g. Correch du Pont, et al., 2014) that orientates the dune to the resultant sand transport direction. Here for *N=2*, and $\theta = 120^{\circ}$, Rozier, et al.

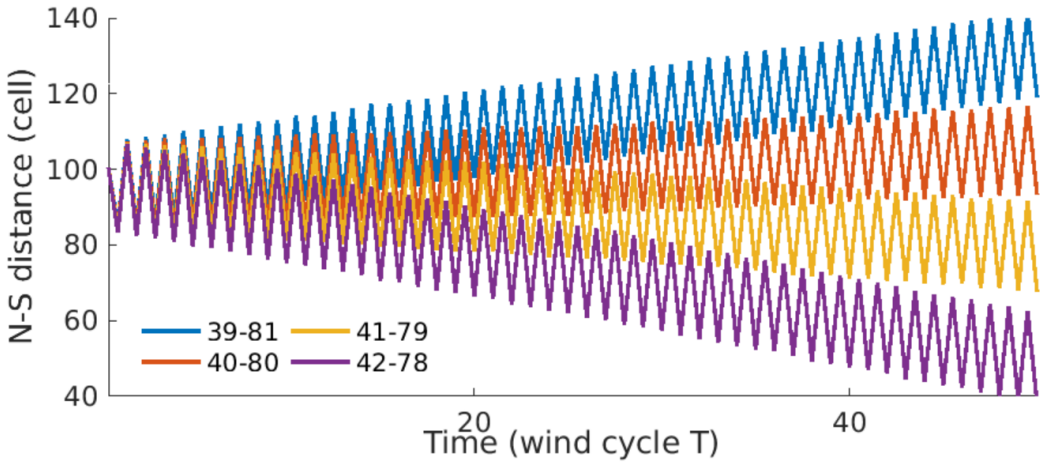
(2019) used the combination of $\theta_1 = 40^\circ$ and $\theta_2 = 80^\circ$. The wind angle tests here, therefore, is around this setting.

Figure 5-6 (B) plots a time series of the N-S distance of the dune crest location, taking four θ_1 & θ_2 combination examples. The N-S location data are collected at the end of each wind period, so the dune crest oscillation is also shown by the four N-S distance-time profiles. Figure 5-6 (C) provides the N-S migration rate (to time) with respect to the wind angle θ_1 (also $\theta_2 = 120^\circ - \theta_1$) with the unit cells/t_0, computed for an extended time scale longer than 200 wind cycles. The rate is computed with the crest location after each full wind cycle (i.e. after θ_2 wind period), which is the southmost location of the dune crest. In Figure 5-6 (C), positive rates mean the dune migrates southwards and negative rates mean the dune migrates northwards.

(A)



(B)



(C)

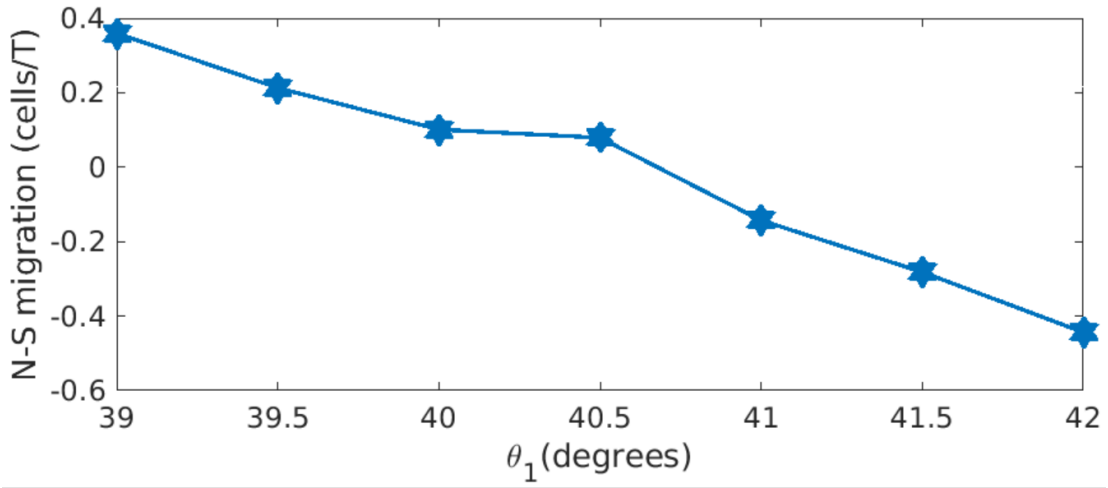


Figure 5-6. Lateral migration of the linear dune (by tracking dune crest locations) at varying combination of wind-crest angles θ_1 and θ_2, with the wind-wind angle fixed to $\theta = 120°$ ($\theta_1 + \theta_2 = \theta$ fixed with varying combinations of θ_1 and θ_2), wind cycle duration fixed *T=2400* t_0 and durations of the two winds fixed where $T_1 = 1600\ t_0$ and $T_2 = 800\ t_0$. The 200-cell (N-S) by 400-cell (E-W) domain is enforced with periodical boundaries. (A) Topography image of the linear dune at initial condition. (B) Crest-normal (N-S) distance of the dune crest location with respect to time, taking four lateral migration examples. (C) Southward lateral migration rate (cells $/t_0$) with

respect to a set of combination of θ_1 and θ_2. In (C), positive rates mean the dune has a net migration to the south and negative rates mean the dune migrates to the north.

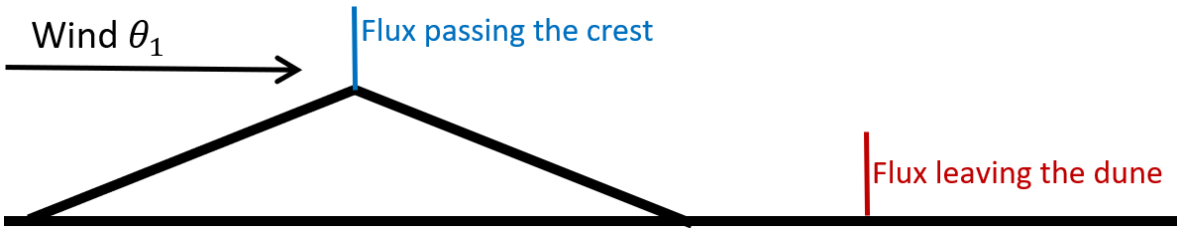
The four examples of Figure 5-6 (B) indicate that the linear dune lateral migration rate is constant to time, with crest oscillation of approximately 20 cells during each cycle. A greater angle θ_1 leads to greater northwards and less southwards migration component. For example, during the earliest 50 T (i.e. wind cycles) shown by Figure 5-6 (B) from the initial condition, there is a net displacement to the north of 42 cells under $\theta_1 = 42^{\circ}$, while the total migration distance is reduced to 20 cells when θ_1 is reduced by one degree to 41°. This output is also demonstrated by more data points of Figure 5-6 (C).

In addition to the general relationship between sideways movement and the two wind crest angles, another key information indicated by Figure 5-6 (B) and (C) is the high sensitivity of the lateral migration in response to tiny changes of the wind angles. As discussed above, one degree reduction of θ_1 (42 to 41) and increase of θ_1 (78 to 79) leads to 50% change of the distance displaced, while further one degree reduction of θ_1 from 41° to 40° leads to opposing migrating direction. This high sensitivity is particularly demonstrated by data points of Figure 5-6 (C) around a migration rate ($\theta_1 = 40.5^{\circ}$, $\theta_2 = 79.5^{\circ}$). Half degree of θ_1 increase and decrease lead to opposite sideways displacements.

To understand the direct drivers behind the lateral migration scenarios shown in Figure 5-6, the crest normal (i.e. N-S) sand flux data is computed on the surface of each cell. Figure 5-7 (A) schematizes the two locations directly relating to the sideways movement: one is measured at the dune crest ($Q_{crest\perp}$), labelled as 'Flux

passing the crest', the other ($Q_{out\perp}$) is measured at a distance away from the wind at the narrower angle, labelled as 'Flux leaving the dune'. Both $Q_{crest\perp}$ and $Q_{out\perp}$ are crest-normal. The site of $Q_{out\perp}$ measurement taken in the domain is labelled on the topography image of Figure 5-6 (A) with a white dashed line. The flux $Q_{crest\perp}$ describes the amount of sand that (instantaneously) passes over the crest from the north slope to the south slope. The flux $Q_{out\perp}$ results from wind carrying away sand on the north slope (which is the lee slope of wind θ_1) of the whole wind regime, either by eroding the slope or by directly transporting sand away from the slope. The outflux of the other wind θ_2 is at a much smaller order than θ_1 (see Figure 4-13, Chapter 4) where wind only carries a tiny amount of sand at wind-crest angle 80-degree. As periodical boundaries are enforced, the two interdune areas in the domain are equivalent regarding the $Q_{out\perp}$ measurements. The profiles of $Q_{out\perp}$ and $Q_{crest\perp}$ with respect to the wind angles θ_1 & θ_2 are provided in Figure 5-7 (B). For each data point, the $Q_{crest\perp}$ computes the southward flux at the instantaneous dune crest for each 5 t_0 and the sum of the whole cycle (with 480 units of 5 t_0) is taken for each specified θ_1 point.

(A)



(B)

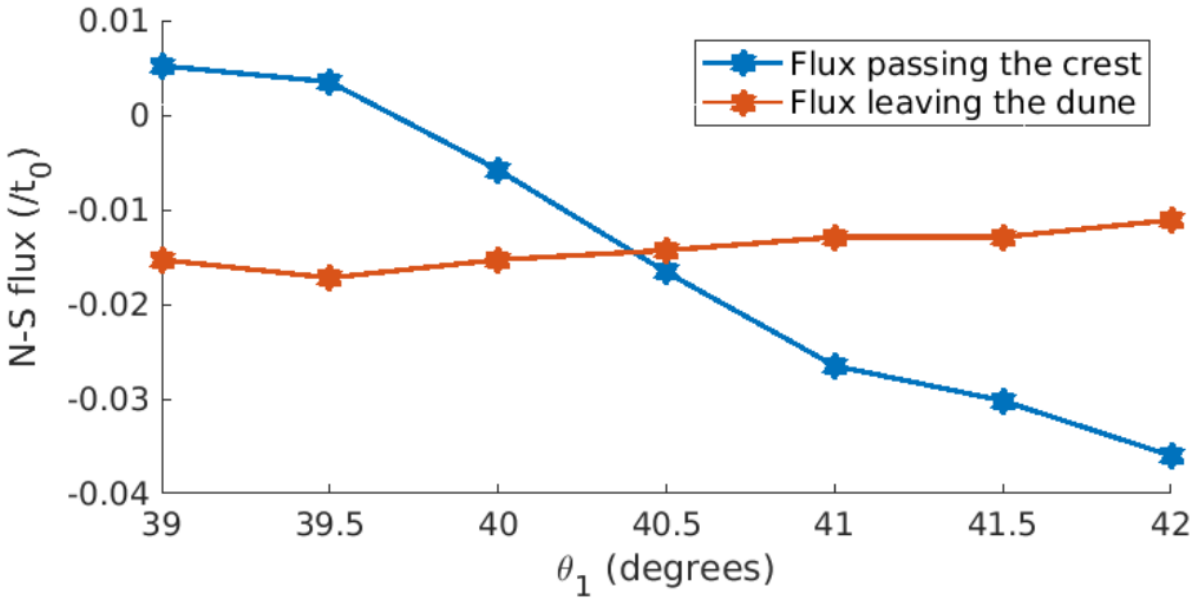


Figure 5-7. Crest-normal (N to S) sand flux (averaging a full wind cycle T=2400 t_0) from north to south measured at the dune crest (Q_{crest}) and over a distance (Q_{out}) from the primary wind (duration T_1, angle θ_1) lee slope base (measurement location is labelled with a white dashed line in the topography image of Figure 5-6 (A)) with respect to the wind angles θ_1 and θ_2 ($\theta_2 = 120° - \theta_1$) for the set of angles shown in Figure 5-6. (A) Schematic of locations of the flux measurement (B) Flux-θ_1 profiles. Positive values mean the resultant flux is to the south and negative values mean the resultant flux is to the north.

In Figure 5-7, $Q_{out\perp}$ is negative as a result of sand lost by the wind θ_1 deducted with the loss of θ_2. When Figure 5-7 (B) was made, it was first assumed that the N-S crest-normal flux $Q_{crest\perp}$ corresponded to the lateral migration shown in Figure 5-6 (C). In this assumption, for example, if the overall $Q_{crest\perp}$ is towards the north (i.e. negative data points of Figure 5-7 (B)), the crest location would migrate northwards, hence the whole linear dune would migrate northward where Figure 5-6 (C) should show a negative N-S migration. However, for the two points $\theta_1 = 39.5°$ and $\theta_1 = 40°$,

the overall $Q_{crest\perp}$ is northward, while the overall lateral migration is southward, being opposite to the resultant flux $Q_{crest\perp}$. This means the dune migrates to the opposite direction to the resultant sand moving at the crest. In other words, the dune laterally moves 'opposite' to the migration of the crest. Therefore the initial assumption of lateral migration-$Q_{crest\perp}$ dependence does not fit all scenarios. This is where $Q_{out\perp}$ is supplemented to further elucidate where the sand goes after passing the crest. In Figure 5-7, $Q_{crest\perp}$ determines how much sand is gained by the lee slope (i.e. north), while $Q_{out\perp}$ determines how much sand is lost (i.e. not trapped by grain flow) by the lee slope

The key information indicated by Figure 5-7 is that the difference $Q_{crest\perp}-Q_{out\perp}$ corresponds to the lateral migration shown in Figure 5-6 (C). The dune migrates southwards where $Q_{crest\perp}-Q_{out\perp}$ is positive (i.e. southwards) and the dune migrates northwards where the difference is negative. Based on the control of $Q_{crest\perp}$ and $Q_{out\perp}$, the lateral migration shown by Figure 5-7 is classed as below:

Type (1) --- For the point $\theta_1 = 39°$, the lateral migration is directly driven by avalanche in the lee of the wind enforced with angle θ_2. The southward $Q_{crest\perp}$ is adequate for making the south slope have a net sand gained by grain flow and driving the dune migrating to the same direction.

Type (2) --- For the two points $\theta_1 = 39.5°$ and $\theta_1 = 40°$, the overall $Q_{crest\perp}$ means a net northward amount of sand passes the crest, but a $Q_{out\perp}$ leads to a larger amount of sand taken away from the north slope. This means the $Q_{crest\perp}$ is too small to supply the $Q_{out\perp}$. The scenario is equivalent to the $Q_{out\perp}$ exceeds the $Q_{crest\perp}$ supplied to the dune lee, resulting in a net erosion (sand loss) from the lee slope.

Therefore, the lateral migration is actually resulted from a net loss of sand from the north slope.

Type (3) --- For the point $\theta_1 = 40.5°$, it can be approximated to zero net lateral migration (Figure 5-6 (C)). The scenario is equivalent to where $Q_{crest\perp}$ that passes over the dune crest is fully moved away by the wind, leading to the $Q_{out\perp}$ equal to $Q_{crest\perp}$ (Figure 5-7 (B)).

Type (4) --- For points θ_1 is greater than $40.5°$, the lateral migration is directly driven by the primary wind enforced with angle θ_1. The northward $Q_{crest\perp}$ is large enough to make the north slope gain sand and the whole dune moves to the north.

Generally speaking, types (1) and (4) are lateral migration directly driven by avalanche and the whole dune moves forward with the crest. In comparison, the direct driver of type (2) is net erosion of the lee slope of the more crest-parallel wind, this lee slope and the whole dune moves backward (to the crest).

5.2.2 Internal structure in response to the lateral migration cases

To clarify the sand deposition and preservation corresponding to Figure 5-7, sand deposition time within a wind cycle is computed. Figure 5-8 shows the accumulative distribution. In preserved grain cells (i.e. excluding active sand of the ongoing wind cycle) since a simulation initiates, for all t_0 units within a 2400 t_0 wind cycle, the grain cell number is counted if the remainder of the absolute deposition time divided by T (t/T) is equal to the time step (x axis of Figure 5-8). The sum of total portion up to this time is plotted on Figure 5-8. Therefore, in Figure 5-8, increasing parts of the curve indicate a net deposition and preservation into the stratigraphy, while flat parts indicate no sand is preserved at that time step. The seven sets of θ_1 and θ_2

combinations shown in Figure 5-6 and Figure 5-7 are included in Figure 5-8 and labelled on the legend.

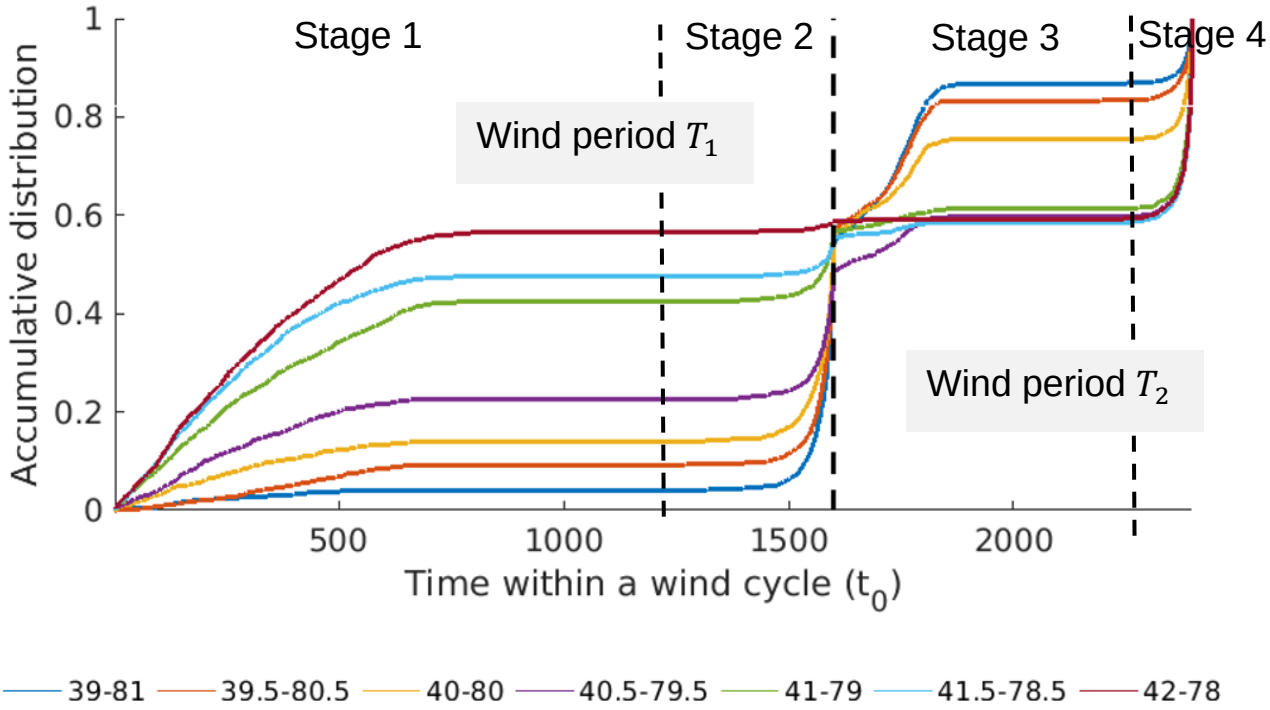


Figure 5-8. Accumulative distribution of deposition time of preserved sand within a wind cycle duration T=2400 t_0 ($T_1 + T_2$). The four stages of preserved deposition are labelled on the plot: Stage 1---beginning of the primary wind period T_1 at angle θ_1, Stage 2---end of the primary wind period T_1 at angle θ_1, Stage 3---beginning of the secondary wind period T_2 at angle θ_2, Stage 4---end of the secondary wind period T_2 at angle θ_2.

Similarly to lateral migration cases, the component of preserved sand is highly sensitive to tiny changes of the wind angle. According to Figure 5-8, the deposition time component within cycles is concentrated on four stages (labelled on the figure with black dashed lines): the two beginnings and two ends of each wind period.

In general, with increase of the wind angle θ_1, more sand is incorporated into the stratigraphy during θ_1 period T_1. Therefore between time steps 0 and 1600 t_0 the

(preserved) deposition rates shows a positive correlation to θ_1. For the angle θ_2 wind period, the three scenarios where $\theta_1 = 39°, 39.5°$ and 40° show a decreasing trend between time steps 1600 t_0 and 2400 t_0, while the trend is less clear for the four greater angles

To further clarify the forming process of this deposition pattern, Figure 5-9 is provided to show the spatial distribution of the four stages identified in Figure 5-8. Practically, the cell numbers preserved after the last past cycle are counted after the ongoing cycle. Dune topography (2D cross sections) at the ends (also beginnings) of the wind cycle are labelled with black lines. The intercepting areas of the topography lines are the preserved body of this studied wind cycle and the cell number curves of Figure 5-9 are indicative of distribution over this preserved body. In general, under each wind condition (i.e. θ_1 and θ_2 combination) the common feature of the four stages distribution is

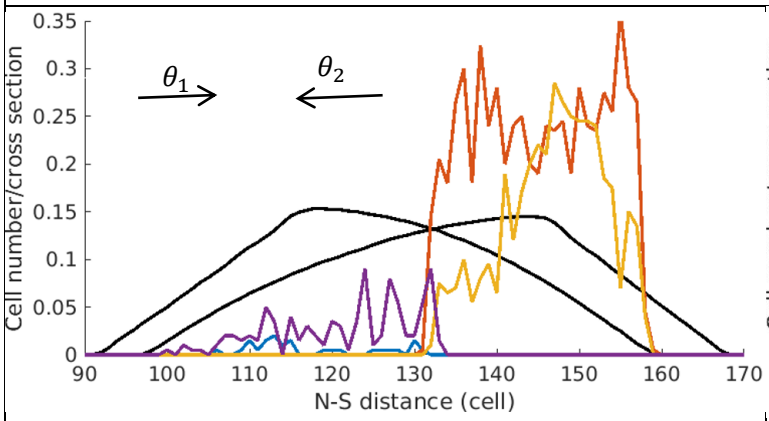
---Stage 1: Sand deposited in early primary T_1 wind (θ_1) period is preserved on the north slope, which is the lee slope of wind θ_1.

---Stage 2: Sand deposited in late T_1 wind period is preserved on the south slope, which is the stoss slope of wind θ_1 and lee slope of wind θ_2.

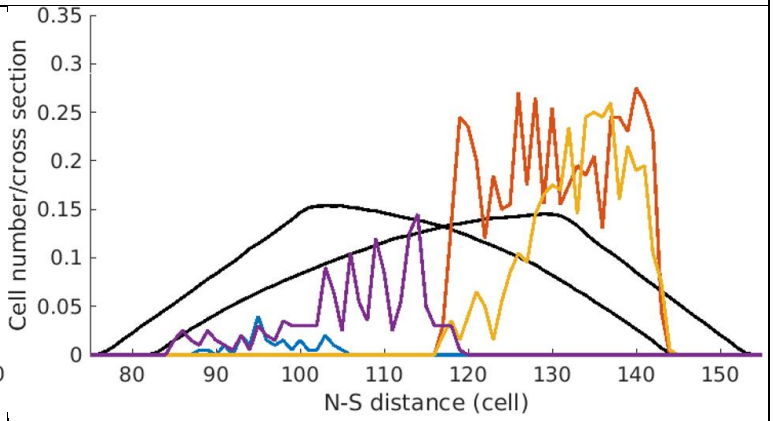
---Stage 3: Sand deposited in early secondary T_2 wind (θ_2) period is preserved on the south slope, which is the lee slope of θ_2 and stoss slope of wind θ_1.

---Stage 4: Sand deposited in late T_2 wind (θ_2) period is preserved on the north slope, which is the stoss slope of wind θ_2 and lee slope of wind θ_1.

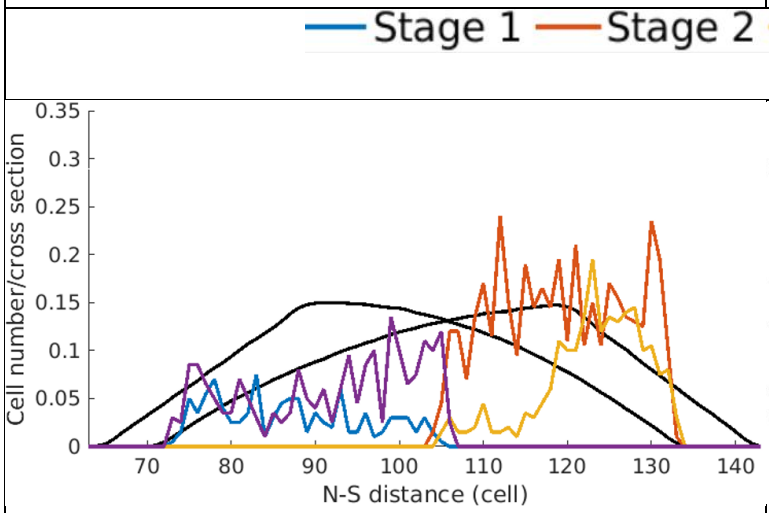
$\theta_1 = 39^\circ, \theta_2 = 81^\circ$



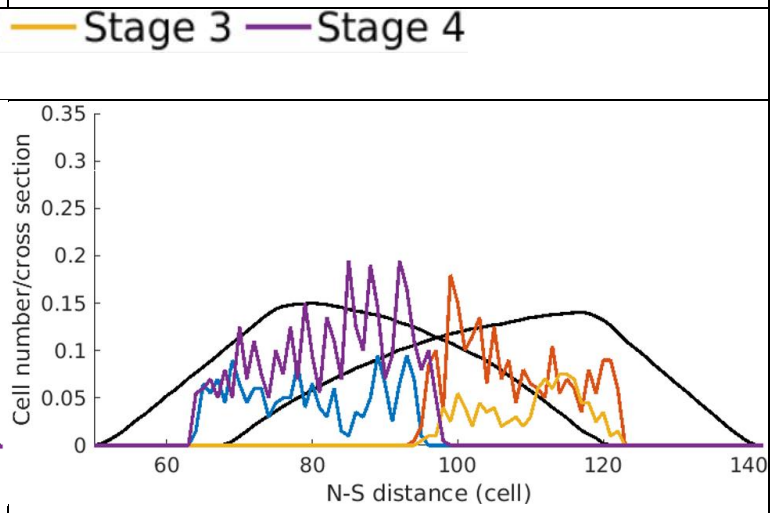
$\theta_1 = 39.5^\circ, \theta_2 = 80.5^\circ$



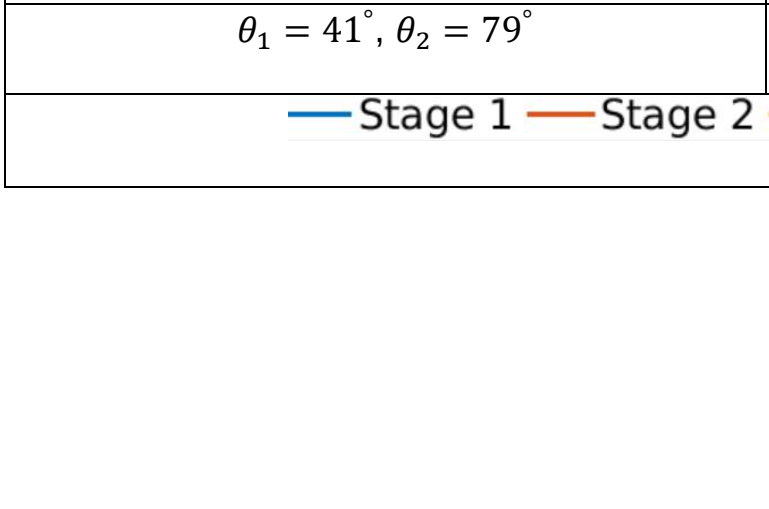
$\theta_1 = 40^\circ, \theta_2 = 80^\circ$



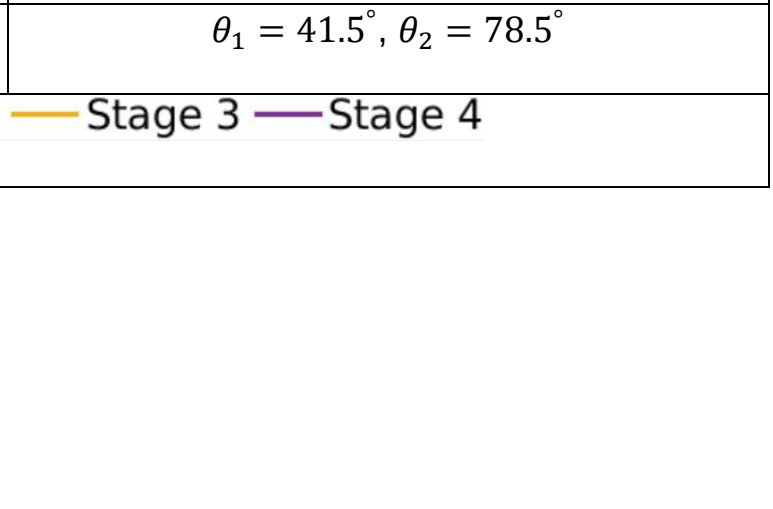
$\theta_1 = 40.5^\circ, \theta_2 = 79.5^\circ$



$\theta_1 = 41^\circ, \theta_2 = 79^\circ$



$\theta_1 = 41.5^\circ, \theta_2 = 78.5^\circ$



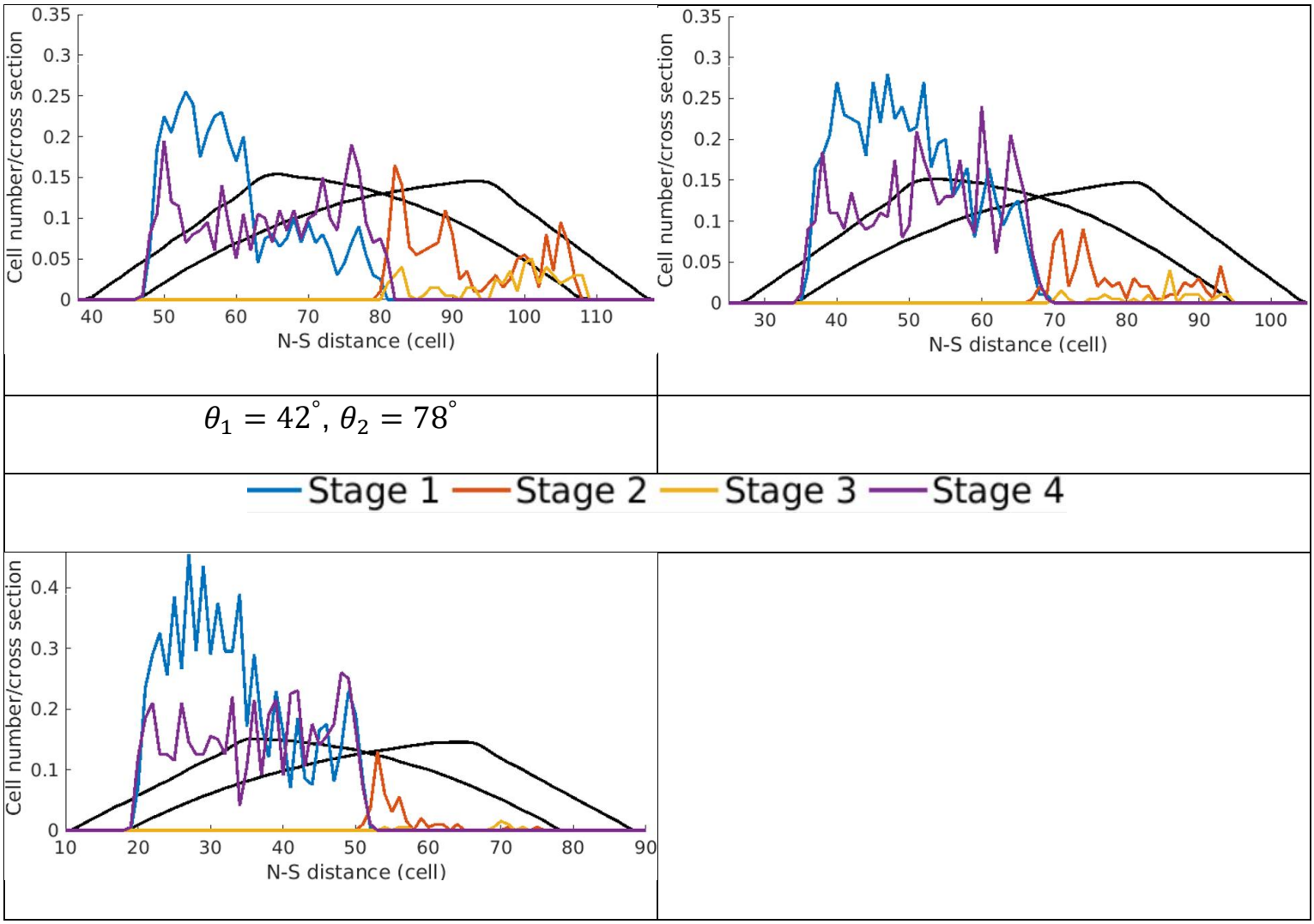


Figure 5-9. Distribution of the four sand deposition stages (labelled in Figure 5-8) within a wind cycle over dune topography, under fixed wind cycle duration T=2400 t_0 ($T_1 + T_2 = T$), fixed $T_1 = 1600\, t_0$ and $T_2 = 800\, t_0$, fixed wind-wind angle $\theta = \theta_1 + \theta_2 = 120°$ with varying combinations θ_1 and θ_2, The distribution is described by the number of cells deposited in a wind cycle and remaining preserved after the subsequent cycle. The topography at the end of T_1 and T_2 are labelled (black curves) on each diagram and their interacting area is the preserved part.

In Figure 5-9, sand of Stage 1 and Stage 3 is deposited in the form of avalanche in the corresponding lee side of the ongoing wind period. They deposit at the early

time, forming the earliest deposited portion of the two wind periods. Erosion on the stoss slope of the subsequent wind period cannot reach and reactivate them, thus they are preserved. For Stage 2 and Stage 4, sand is deposited on the stoss slope of the ongoing wind and does not continue moving to the lee slope due to shifting to the other wind. This stoss slope becomes the lee slope of the reversed wind, forming grain flow strata to preserve Stage 2 and Stage 4 sand. In this general feature:

---Stage 3 grain flow preserves sand remaining on the stoss (south) slope during Stage 2. Similarly, Stage 1 grain flow preserves sand remining on the stoss (north) slope during Stage 4.

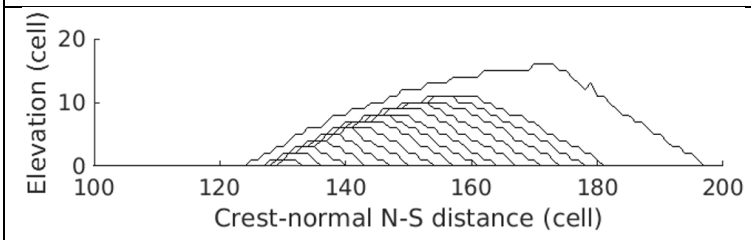
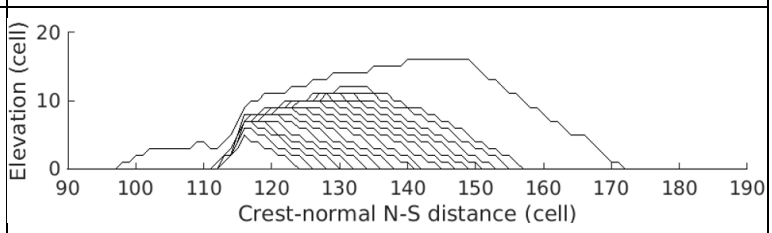
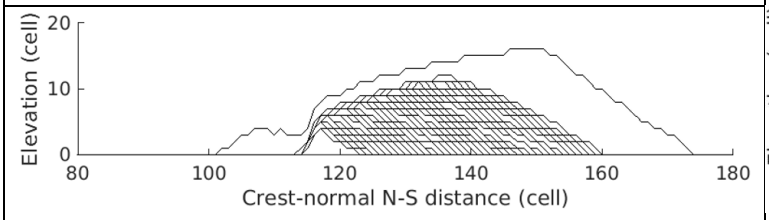
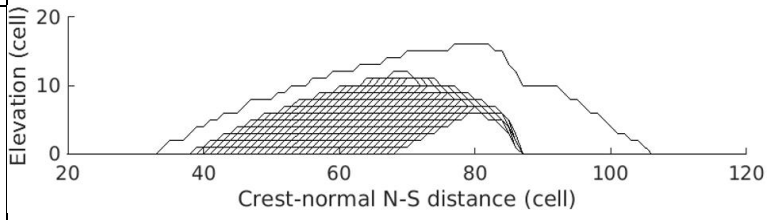
---Stage 1 grain flow strata are remaining sand after stoss slope erosion during Stage 3. Similarly, Stage 3 grain flow strata are remaining sand after stoss slope erosion during Stage 1.

Under the control of deposition and preservation processes described above, with Wind 1 getting more perpendicular (i.e. increase of θ_1), this wind generates more grain flow strata for Stage 1 and preserves more sand remaining on the stoss slope of Wind 2 during Stage 4. Therefore, cell numbers preserved during Stage 1 and Stage 4 increase together as a result of increasing θ_1. This corresponds to the fundamental wind angle effect identified in Chapter 4: more perpendicular wind, greater grain flow magnitude and higher sand volume incorporated into the avalanche deposition.

The internal sedimentary structure resulted from the sideways moving cases are presented in Figure 5-10 below. Buried surface lines are visualized for each 5 T. For all images of Figure 5-10, the time interval between temporally adjacent surface lines is same, hence the density of the surfaces is indicative of ages and migration

rates of the dunes. Higher density of the surface lines indicates slower migration of the dune. Similarly to lateral migration in response to tiny angle changes, the surfaces density and dune ages are highly sensitive as well. For example, when $\theta_1 = 40^{\circ}$, the surfaces density is higher than double of that in $\theta_1 = 39^{\circ}$, so is the dune age.

In Type (1) and (4) (see the classification labelled on page 143 and page 144), the stratigraphy is characterized by grain flow strata preserved during avalanche processes, as usually considered as the lateral migration evidences (e.g. Bristow, et al., 2000, 2005 and 2007). To compare, in Type (2), the stratigraphy also shows unidirectional layers, but the layers are actually accumulation of stoss slope (erosional) surfaces. Some previous field observed linear dunes have also been thought as erosional processes-based linear dunes (e.g. Rubin and Hunter, 1985).

$\theta_1 = 39^{\circ}, \theta_2 = 81^{\circ}$	$\theta_1 = 39.5^{\circ}, \theta_2 = 80.5^{\circ}$
	
$\theta_1 = 40^{\circ}, \theta_2 = 80^{\circ}$	$\theta_1 = 40.5^{\circ}, \theta_2 = 79.5^{\circ}$
	
$\theta_1 = 41^{\circ}, \theta_2 = 79^{\circ}$	$\theta_1 = 41.5^{\circ}, \theta_2 = 78.5^{\circ}$

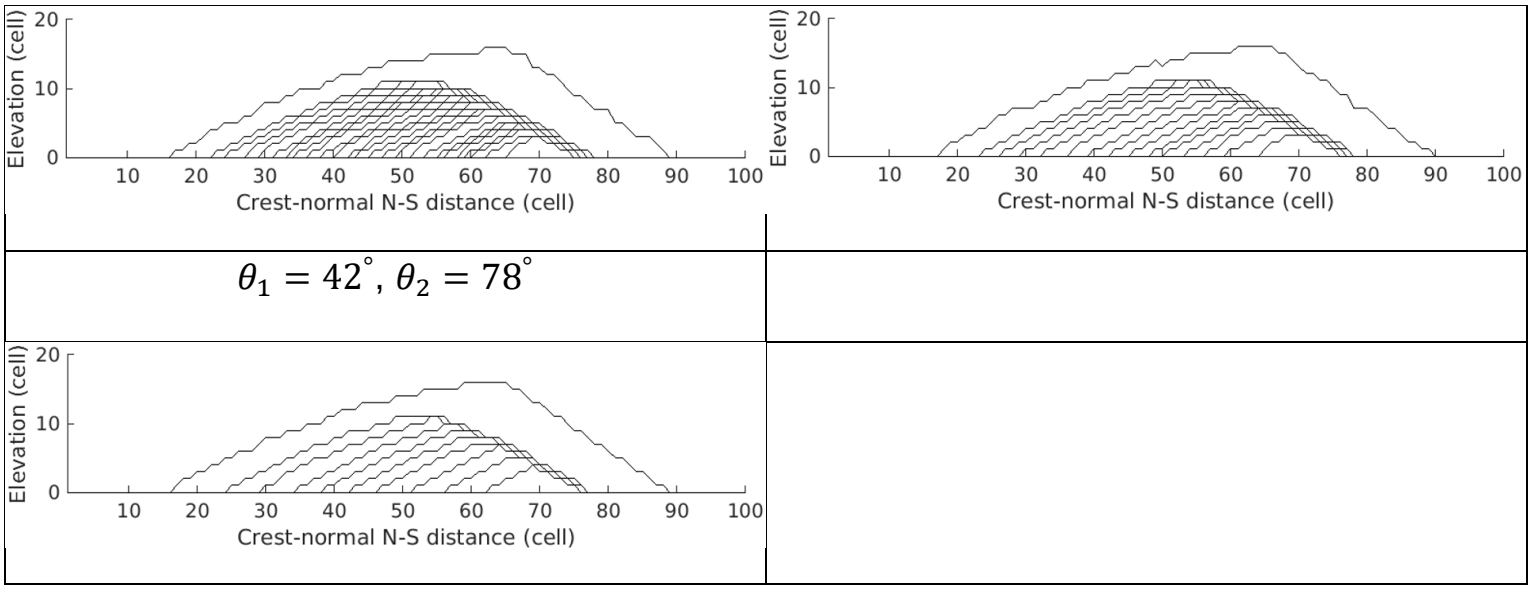


Figure 5-10. Bedding patterns of linear sand dunes under varying lateral migration scenarios indicated by Figure 5-6 (C), visualized with buried surface lines with the time interval of per *5 T.*

5.2.3 Summary of Section 5.2

To summarize Section 5.2, the lateral migration of linear sand dunes is very sensitive to wind angles. Tiny changes (i.e. less than one degree) of wind angles leads to significant changes of the migration speed or opposite migration of the linear dune. Lateral migration of linear dunes can be categorized as (1) avalanche driven, forming grain flow strata at angle of repose (2) erosion driven, forming sequences of preserved erosional surface.

5.3 Lateral migration of multiple linear dunes

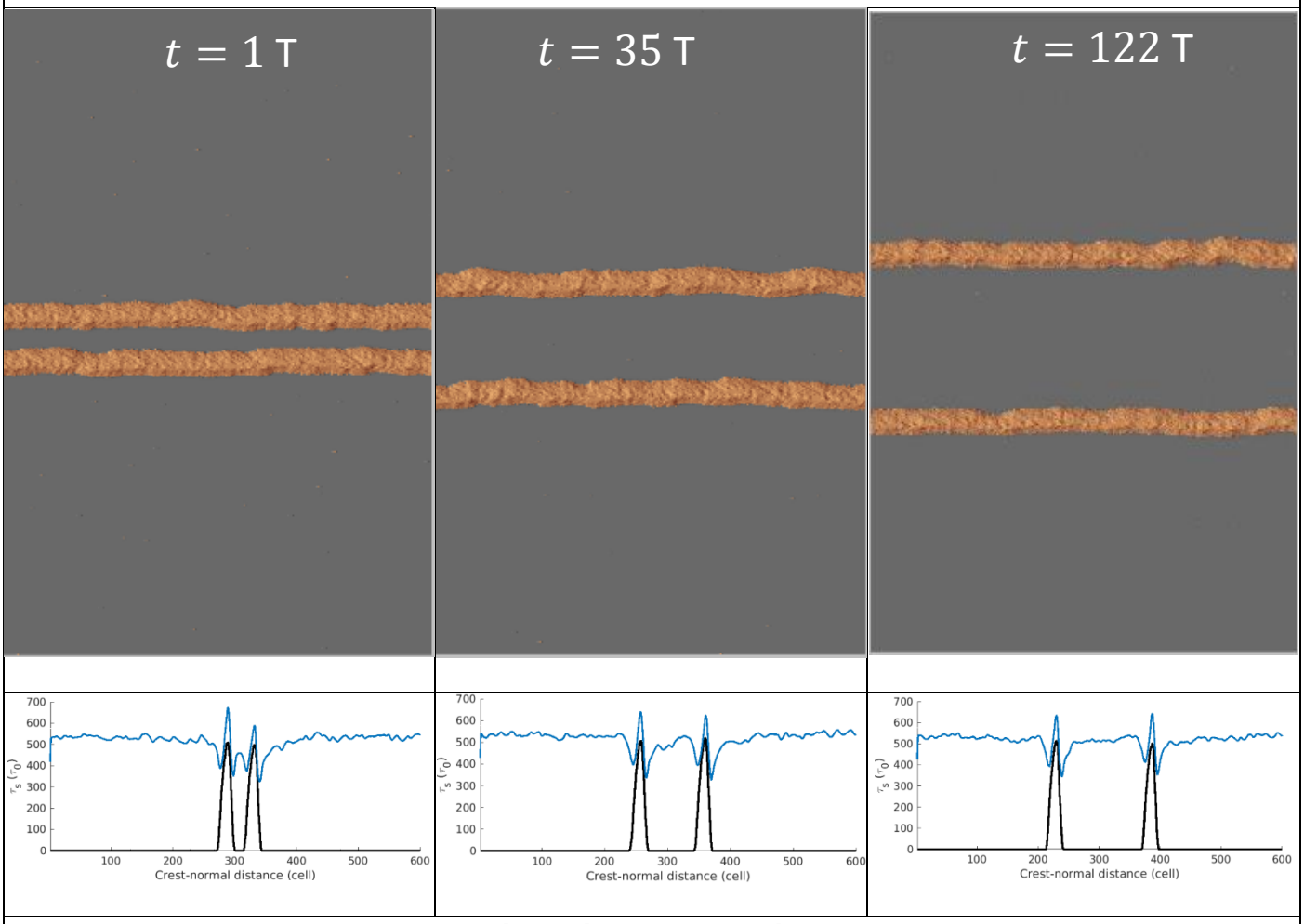
In Section 5.2, lateral migration cases discussed only takes into account the sand movement processes of one individual linear dune that does not receive external sand influx or have interaction with adjacent dunes. However, most natural dune fields are aligned with multiple linear dunes, interacting with each other and forming patterns (e.g. Thomas, 1986; Ewing and Kocurek, 2005; Day and Kocurek, 2018; Gunn, et al., 2021), such as regarding the dune size and spacing (e.g. Wasson and

Hyde, 1983; Thomas, 1986; Pelletier, 2009; Gadal, et al., 2019). Alignment of multiple linear dunes further complicates dynamics of linear dunes. For example, within one dune field, they may migrate towards different directions (e.g. Bristow, et al., 2000, 2005 and 2007). Also, under the control of same wind conditions, differently coarsened field patterns may appear (e.g. Telfer, et al., 2017).

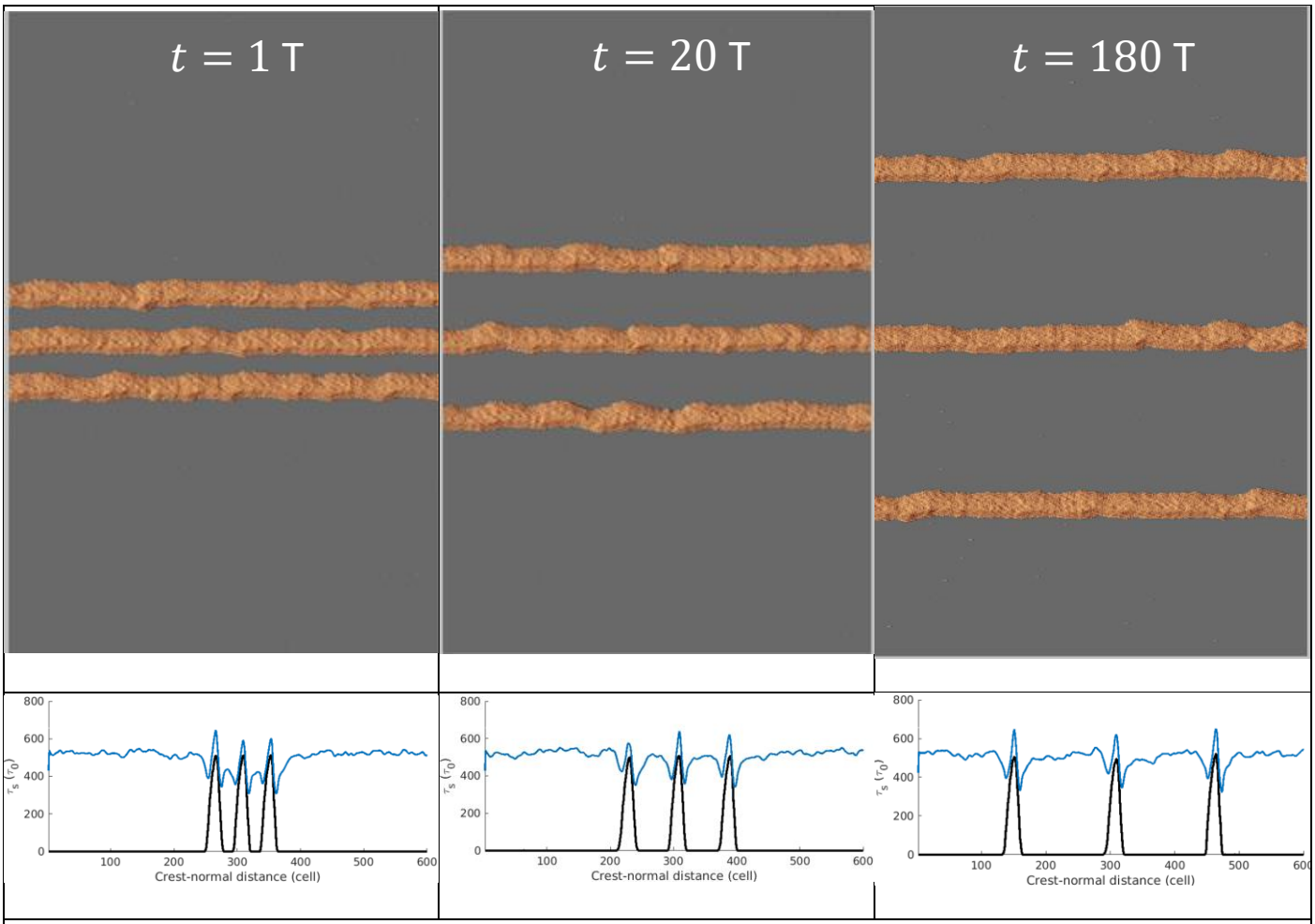
Therefore, this section here has a purpose to explore whether or not the lateral migration of linear dunes may be influenced by alignment of multiple dunes. Again, the starting point is kept as simple as possible: linear dunes with the same size are accommodated on a 400-cell (W-E) by 600-cell (N-S) domain. The vertical depth of the domain is 300 cells, ensuring that the LG modelled flow is not affected by the thickness of the boundary layer. Figure 5-11 (A) presents topography images of three simulations respectively with 2, 3 and 4 dunes aligned. Selection of these three sequences takes into account that the two-dune represents the simplest scenario where the dune migration can be resulted from the close spacing. The other two sequences are selected to show that a whole dune field may display a same or similar dune-spacing (as in the two-dune case), because the periodicity of this pattern is driven by the flow interaction distance. They are associated with the wind shear stress profiles over the cross sections of the whole domain, computed at the beginning of the wind period T_1. The crest-crest distance of adjacent dunes is 40 cells. Figure 5-11 (B) presents lateral moving of the dune, described by taking the sum of grain cell number of each N-S column at each time step specified. A symmetrical bimodal wind regimes are enforced with $T = 2400t_0$ (i.e. $T_1 = 1200\ t_0$ and $T_2 = 1200\ t_0$) and $\theta = 120^{\circ}$ (i.e. $\theta_1 = 60^{\circ}$ and $\theta_2 = 60^{\circ}$).

(A)

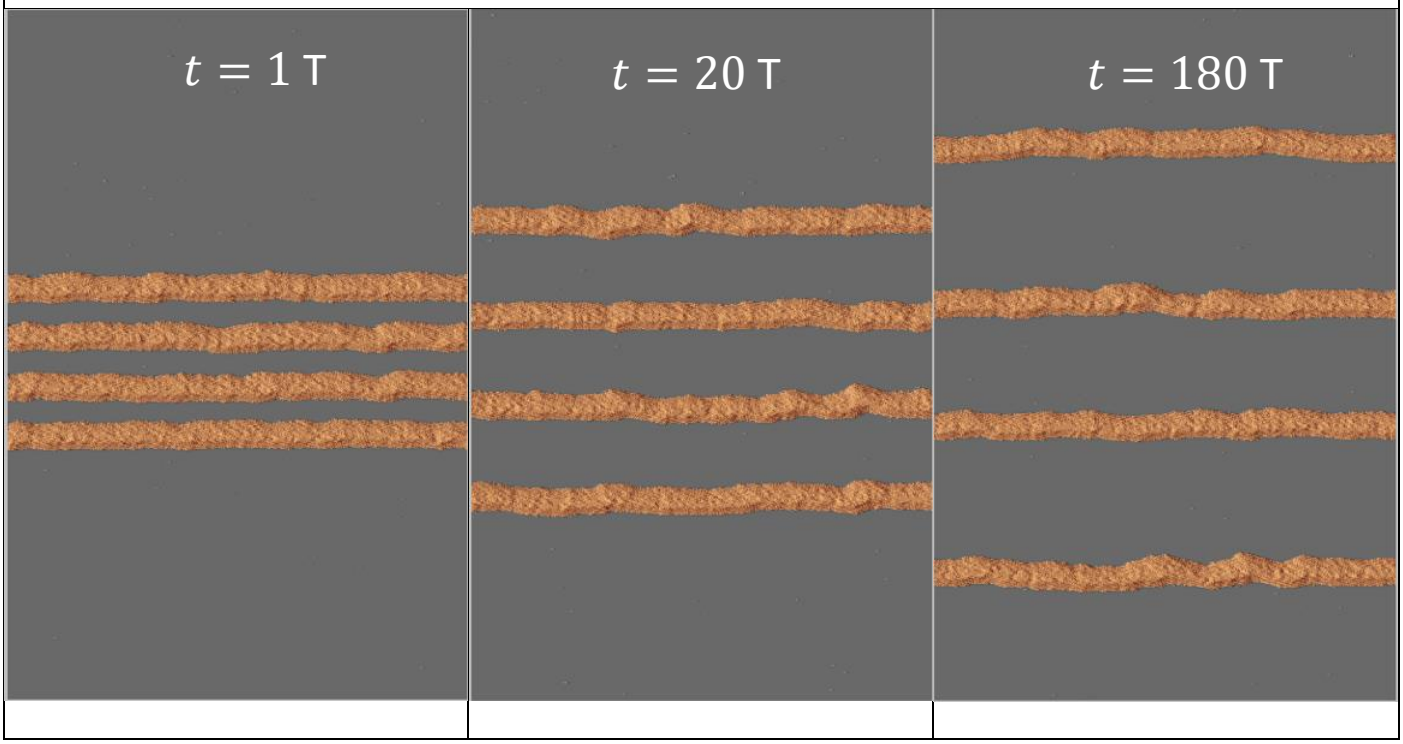
Two dunes separation

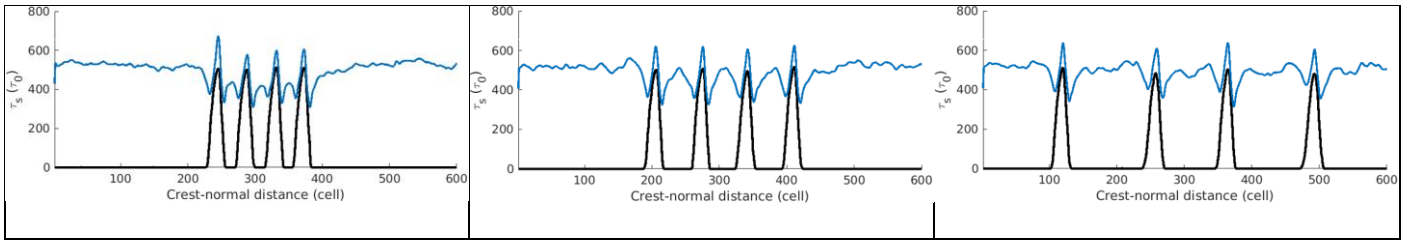


Three dunes separation

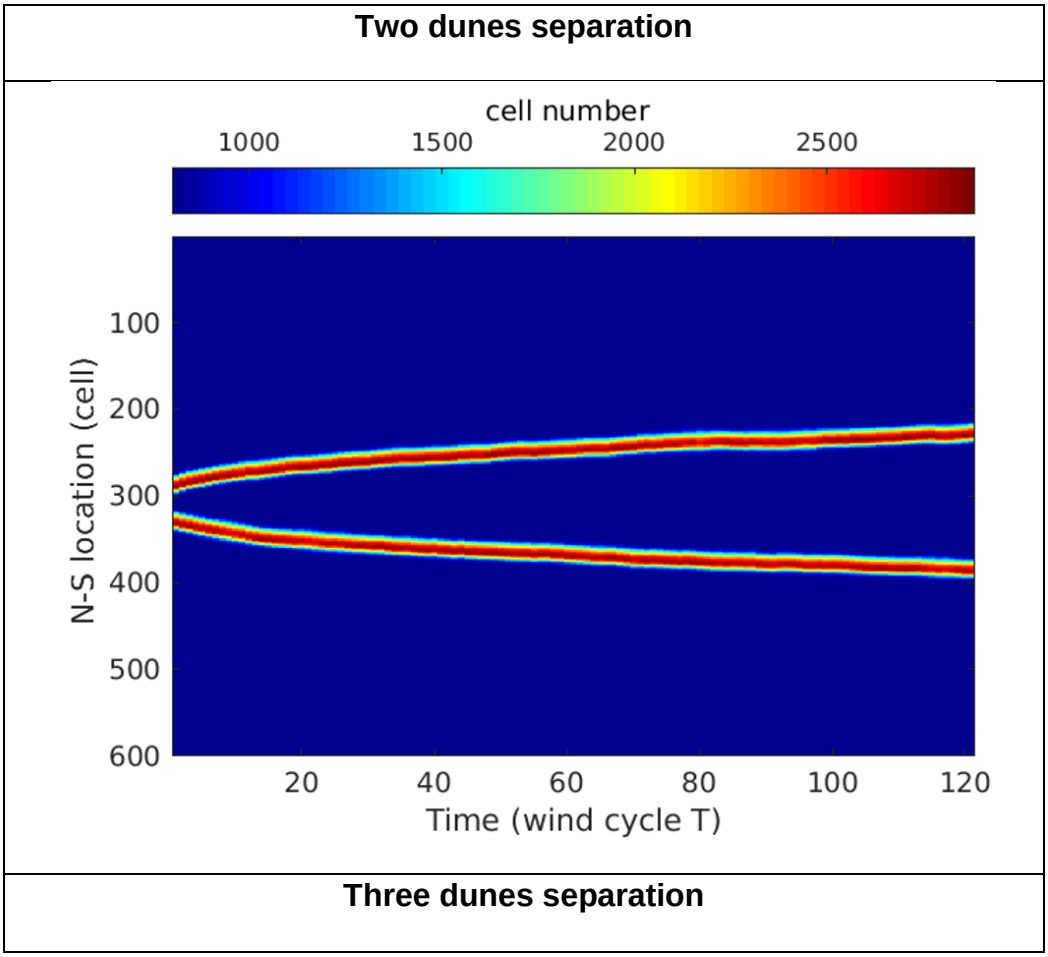


Four dunes separation




800
600
400
200
0
100
200
300
400
500
600
Crest-normal distance (cell)

(B)


Two dunes separation
cell number
1000
1500
2000
2500
N-S location (cell)
100
200
300
400
500
600
20
40
60
80
100
120
Time (wind cycle T)
Three dunes separation

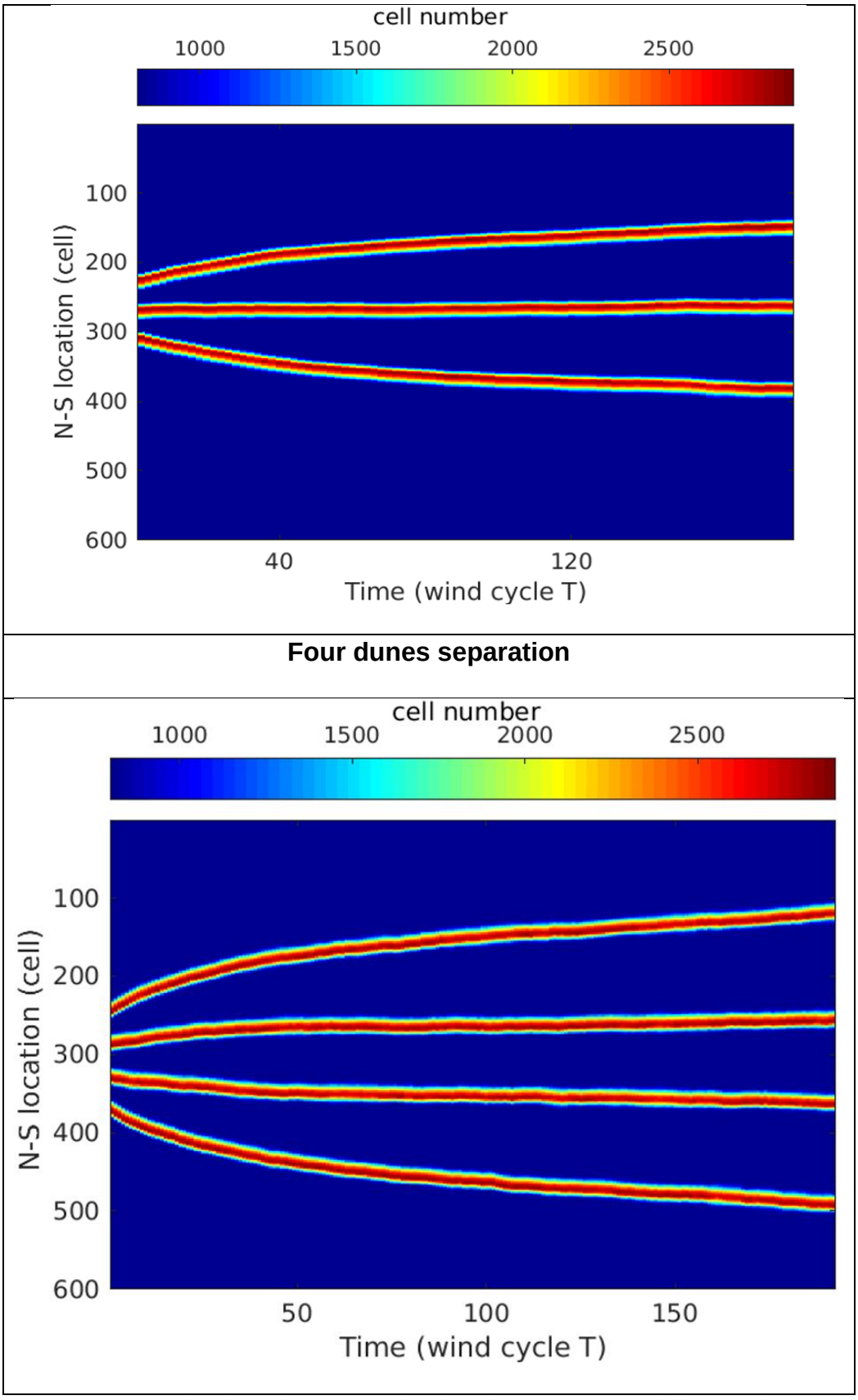


Figure 5-11. Lateral migration of multiple closely spaced linear dunes under symmetrical bimodal wind regimes where wind cycle duration T=2400 t_0,

within which each of the wind period $T_1 = T_2 = 1200\, t_0$ and the angle (with dune crest) of the two wind $\theta_1 = \theta_2 = 60^{\circ}$. The initial distance between adjacent dunes is 40 cells and all dunes have the same size 10 cells high. (A) Topography images and wind shear stress (modelled with LG) profiles. Time steps from the initial condition are labelled on each topography image. (B) Dune migration with respect to time described by taking the total mass of sand per cross section of the whole domain,

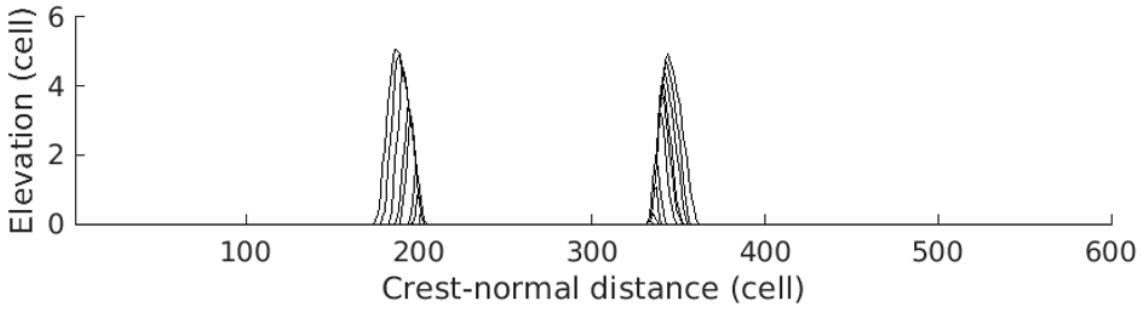
For the three simulations, in Figure 5-11 (A) within one domain there are linear dunes laterally migrating towards opposing directions. For the scenario aligned with three dunes, there is also the middle dune remaining static, having no net sideways displacement. The overall evolution pattern of multiple linear dunes controlled by symmetrical winds is that they separate or spread from the middle of the domain. Temporally, the separation starts with the highest speeds where t=0 and gradually slows down. For example, in the two-dune scenario (Figure 5-11 (A)), during the earliest 15 T each dune has a net displacement of 40 cells from the initial location. In comparison, for the same duration between *t=105 T* and *t=120 T*, the displacement if less than 15 cells. Spatially, dunes further away from the domain centre migrates faster. The example is offered by the four-dune scenario of Figure 5-11 (A), the northmost and southmost dune migrate faster than the two adjacent dunes between.

The key information demonstrated by Figure 5-11 (A) shear stress profiles is that when two dunes are closely spaced, even though they do not have direct body contact, the airflow patterns over the two dunes can interact. Generally speaking, during a specified wind period, the (LG modelled) wind is stronger over the downwind dune than over the upwind dune. In the three scenarios shown, the

northmost dune interacts with the strongest northward wind. Therefore, the downwind dune migrates faster during this wind period. During the period of the opposite wind, the previous slower upwind dune migrates faster. Gradually the variation of wind strengths between two dunes in wind alteration leads to separating of the two dunes. The separating process slows down with increase of the dune spacing and ends until the distance between them is so far that the wind flow over the two dunes does not interact and two winds experience the same wind strength.

The internal sedimentary structure of linear dunes in the separation scenarios is presented in Figure 5-12, giving examples of the two-dune and four-dune scenarios. Selection of these two snapshots mainly concerns the snapshots that best reflect the depositional structure through the dune field. Beddings are mapped with buried dune surfaces at a time interval of per 100T.

(A)



(B)

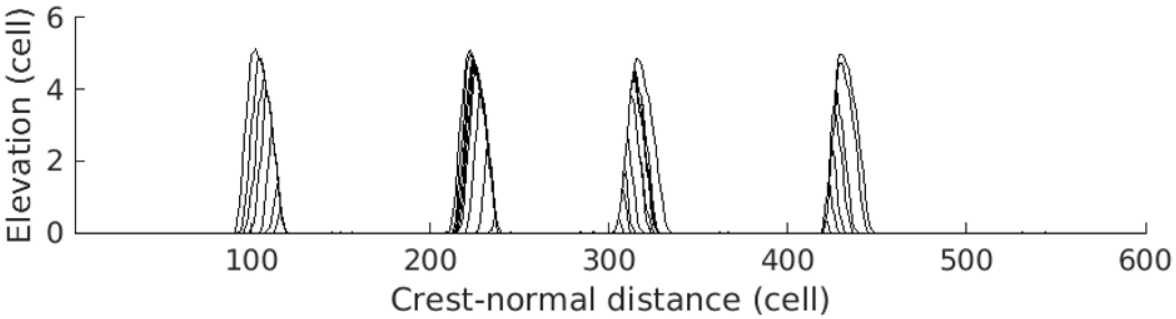


Figure 5-12. Bedding patterns of the dune separation scenarios shown in Figure 5-11, mapped with buried surface lines per 100 T. (A) Two dune separation (B) Four dune separation

The internal structure shown in Figure 5-12 corresponds to sideways moving scenarios of Figure 5-11. Strata dip to the same direction as the lateral displacement. Therefore in both Figure 5-12 (A) and (B) the dune field accommodates two dipping directions. In Figure 5-12 (B), the two central dunes (i.e. between 200-cell and 350-cell distance) show the tendency caused by the migration speed with time: the surface lines get denser in later times when the dune migration gets slower.

The modelled cases where linear dunes separate may provide solution to the recently proposed question: whether a coarser dune field is older or a finer dune field is older (e.g. Telfer, et al., 2017; Day and Kocurek, 2018). Telfer, et al, (2017) hypothesized that under the same wind condition, the coarser dune fields with larger dunes are older than the adjacent finer dune field with smaller dunes. In other words, smaller dunes were assumed to preserve more recent records. The OSL dating outputs of Telfer, et al. (2017) eventually do not support the initial hypothesis. Here the linear dune separating scenarios modelled with the CA may provide an answer that the age has a dependence on sampling location. In dune fields with separating dunes, the middle of the field is usually buried with oldest sediments when the dune system started to develop. In this case sampling locations may affect the outputs when investigating the age of a dune field.

5.4 Summary of Chapter 5

This chapter investigated dynamics of an existing linear dune. Key findings include:

Firstly Section 5.1 investigated the control of wind reversal on evolution of the dune wind structure, sand movement and internal sedimentary structure over an extended time scale. Slip face extension together with development of the opposing grain flow strata were found to be key features in the dune evolution, forming the chronology gap in sand age-depth profiles. The previous stoss slope was eventually buried as a low angle erosional surface in the wind reversing process.

Secondly Section 5.2 investigated sideways moving possibilities of an individual linear dune, suggesting that tiny changes (i.e. order of less than one degree) of wind angles makes significant influence on lateral migration direction of a linear dune. The most direct driver of the net sideways displacement was found to be the crest-normal flux at the dune crest deducted with the sand moved off from the lee slope. Lateral migration of in individual linear dunes can be either driven by avalanche (moving forward with the crest) or driven by erosion (scouring) of the lee slope (simultaneously with sand supplying the stoss slope). Respectively, they form stratigraphy occupied by unidirectional grain flow strata (e.g. Bristow, et al., 2000, 2005 and 2007) or by unidirectional erosional surface (e.g. Rubin and Hunter, 1985). Field surveyed linear dunes were mostly classed as the first type of migration (i.e. avalanche driven).

Thirdly, Section 5.3 explores lateral migration that may occur in closely spaced multiple dunes. Under the same environmental wind, when dunes are closely spaced, the downwind dune interacts with stronger wind than the upwind dune, hence migrates faster. Two dunes separate, laterally migrating towards opposite directions. Correspondingly, for the internal stratigraphy, the dune separation pattern results in cross strata dipping to opposite directions and central dunes burying the oldest sediments among the whole dune field.

Section 5.2 and 5.3 both potentially drive dunes migrating towards varying directions within one same dune field under the same environmental wind. Either small variation of wind angles or airflow interaction between dunes can be the driver of varying lateral migration scenarios.

Chapter 6 Bimodal wind regime controls on initiation and elongation of linear dunes

Following the study of developed linear dunes in Chapter 5, Chapter 6 moves on to the dynamic processes controlling the initiation and longitudinal extension of linear dunes under the operation of bimodal wind regimes. The influence of lateral migration is excluded here to simplify the simulations and ensure clarity in discerning the mechanisms of longitudinal extension. Firstly, Section 6.1 starts with detailing the condition settings employed in the simulations, including domain dimensions, wind condition and sand supply. Following this there is a detailed analysis of the elongation dynamics of a linear dune under a specified bimodal wind regime. Secondly, Sections 6.2 to 6.4 explore how the elongation dynamics, and corresponding internal structures, of linear dunes are influenced by varying properties of a bimodal wind regime, including wind angles, wind cycle durations, and duration ratios between the two winds.

This chapter has a goal to fill in the knowledge gap identified in Section 2.3 of Chapter 2 and resolve the previously proposed question (e.g. Rubin and Ikeda, 1990; Parteli, et al., 2009 and 2014): what controls the formation of linear sand dunes and how is the internal architecture built? Previous work has identified that directionality of bimodal wind regimes (e.g. Parteli, et al., 2009 and 2014) is one of the key determinants of dune elongation where dunes form under wind-wind angles greater than 90-degree (e.g. Bagnold, 1941; McKee and Tibbitts, 1964; Rubin and Hunter, 1987; Kocurek and Ewing, 2005; Rubin and Hesp, 2009). The role of other controlling factors, such as sand influx conditions, wind signal frequencies and wind strength ratios, however, remain not completely clear. To exclude the influence of bedform interaction and transverse growth, linear dunes discussed in this chapter are generated with the ‘fingering mode’ termed by Correch du Pont, et al. (2014). In

this case, the linear dune is solely orientated along the direction of the resultant sand flux.

6.1 Elongation dynamics of linear dunes

This section analyses a typical elongation process of a linear dune simulated with ReSCAL, from the initial condition (detailed below in 6.1.1) to a steady state of the domain shown. Figure 6-1 presents a series of images showing the topography evolution throughout the extended time scale with domain, wind and sediment supply conditions described below.

6.1.1 Simulation settings

The first topography image of Figure 6-1 schematizes settings of bidirectional wind conditions and sand supply. In this chapter, all simulations are run in a 200-cell (N-S) by 1600-cell (W-E) domain. The vertical depth of the 3D domain is 100 cells, ensuring that the boundary layer thickness does not impact on the dune development. Each simulation initiates from a non-erodible bedrock and the two winds are adjusted to the angles that ensure the dune longitudinally extends along the W-E direction. One wind is enforced at angle θ_1 (with the dune orientation) for a duration of T_1, while the other wind approaches the dune at angle θ_2 (with the dune orientation) for a duration of T_2, where the wind-wind angle is $\theta = \theta_1 + \theta_2$ and the duration of a full wind cycle is $T = T_1$+T_2. For a symmetrical wind regime, $\theta_1 = \theta_2$ and $T_1 = T_2$. For an asymmetrical wind regime, a duration ratio $N = T_1 / T_2$ is introduced and θ_1 and θ_2 are adjusted with the dune orientation accordingly (i.e. longer T_1, smaller θ_1). Under the wind regime enforced, sand is supplied from a circular source with radius r installed on the top of the 3D domain, above the upwind termination of the dune (location labelled with a red dot in Figure 6-1). Grain cells

are introduced to the land surface directly under the circular source at a constant rate R_{in} through each full simulation. Practically, in each minimal time unit t_0, a probability equal to R_{in} is enforced on each cell within the circular source, determining whether or not the land surface below receives a grain (i.e. an air flow cell transform into the immobile grain type). With this algorithm enforced for an extended time, on average $R_{in}\pi r^2$ grain cells are supplied by the source per t_0.

This sand supply condition mimics the scenario documented by Tsoar (1989) and was deployed by Rozier, et al. (2019) in longitudinal dune modelling. In this thesis the N-S domain boundaries are periodical boundaries, simulating lateral mass exchange with adjacent dunes where sand moved out of the domain is supplied back from the same location of the other side. Under this boundary setting, the system modelled is equivalent to an infinitely wide (i.e. crest-normal direction) dune field with exactly the same linear dune copied and pasted at the fixed crest-to-crest spacing (equal to the domain width 200-cell here) for infinite times.

This sand supply condition ensures that the linear dune (if it forms under specified wind conditions) is attached to the upwind source, not only disabled from a net lateral (N-S direction) migration, but also prevented from migrating longitudinally out of the domain at the east boundary. Some previous work (e.g. Parteli, et al., 2009, 2014; Gao, et al., 2016; Liu and Baas, 2020) reported scenarios where the linear dune only evolved with sand supplied at the initial condition (e.g. piles or blocks), without extra injection once a simulation starts. In these scenarios, the longitudinal extension is largely restricted, because the dune soon moves out of the domain without sufficient elongation. Enforcing constant sand supply throughout the full simulation time solves this limitation and allows sufficient space and time for dune elongation to evolve.

In the scenario presented in Figure 6-1 and discussed in 6.1.2 below, selection criteria of the wind condition was similar to what was described in Chapter 5.2. First, the wind cycle T=2400 t_0 is not so long that the elongating dune would break into barchans during a wind period due to a 'transverse instability' effect (Parteli, et al., 2011; Niiya, et al., 2012 and 2013; Yizhaq, et al., 2012). Additionally, the duration ratio N=T_1/T_1=2 (where T_1=1600 t_0 and T_1=800 t_0) is representative of a typical asymmetry of a bimodal wind regime (Rozier, et al., 2019) and again, not so large that the dune would split into barchans during the primary wind (T_1) period. Further the wind-wind angle $\theta = \theta_1 + \theta_2 = 120^{\circ}$ is a typical setting for linear dune generation as θ is greater than 90° (e.g. Bagnold, 1941; McKee and Tibbitts, 1964; Parteli, et al., 2009 and 2014; Rubin and Hunter, 1987; Rubin and Hesp, 2009). The upwind injection rate R_{in} from the circular source is 0.05. With the R_{in} setting, 4.1 grain cells are supplied by the upwind source per t_0 and 9840 grain cells are supplied during each full wind cycle T. Below, in Section 6.1.2, are detailed discussion surrounding the elongation of the linear dune.

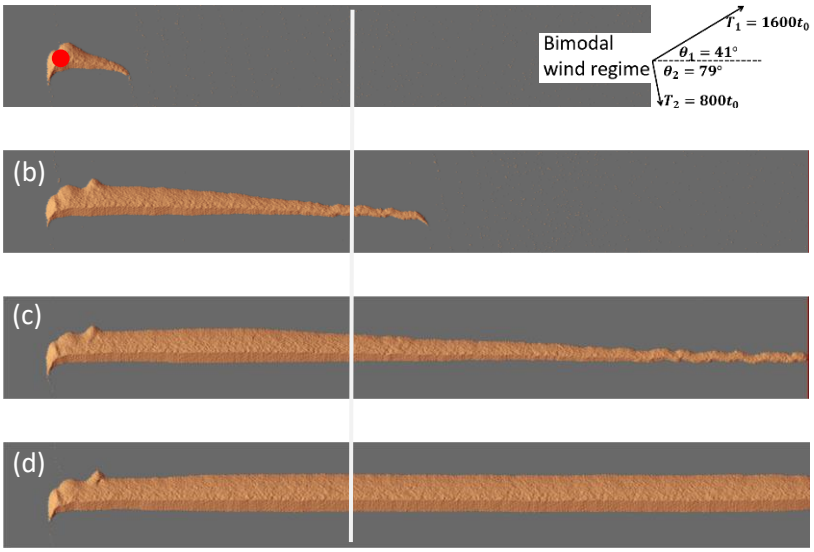


Figure 6-1. Topographic evolution of an elongating linear dune modelled with ReSCAL from the early stage to a steady state (i.e. all cross sections have

finished growing) applying a circular sand source from the upwind (location labelled with the red dot in (a)). The wind condition is schematized in the first image: *T=2400 t_0, θ=120°* and *N=2 (T_1 =1600 t_0, T_2 =800 t_0, $\theta_1 = 41^\circ$, $\theta_2 = 79^\circ$).* N-S domain boundaries are periodical boundaries. Four images are the snapshot at the end of the wind cycle at *t=3 T, 20 T, 30 T* and 408 T from the initial condition.

6.1.2 Evolution of a cross section

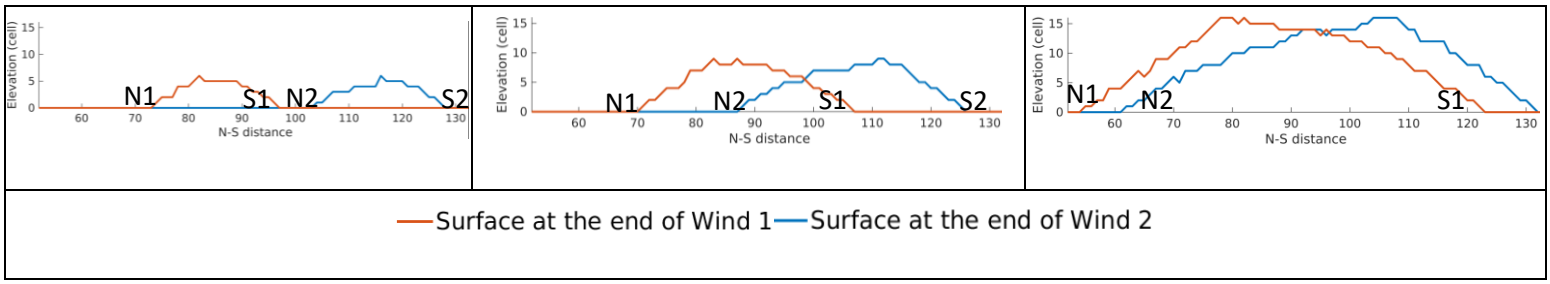
Topographic evolution of the cross section

According to Figure 6-1, as soon as the simulation starts, an asymmetric barchan accumulates (t=3 T) under the circular source at the ceiling. One arm of the barchan elongates towards the east, forming the linear ridge (t=20 T) and eventually the downwind tip of the dune reaches the east boundary of the domain (t=30T). During the elongation process, each crest-normal section gets wider until a steady width is reached (t=600 T). Figure 6-2 below presents the evolution of a cross section (location labelled with a white line in Figure 6-1) at the three time steps t=20T, 30T and 408. Shown in Figure 6-2 (A) are the dune topographies at the end of the two wind periods T_1 and T_2 (i.e. northmost and southmost migration distances). Figure 6-2 (B) tracks the location (in N-S distance) of the dune crest and two base lines (location of points N1, N2, S1 and S2 marked in Figure 6-2 (A)) and the corresponding dune width from t=0 to the stage where the section has reached the steady width and stopped widening.

(A)

(a) 20th wind cycle T	(b) 30th wind cycle T	(c) 408th wind cycle T

S2



(B)

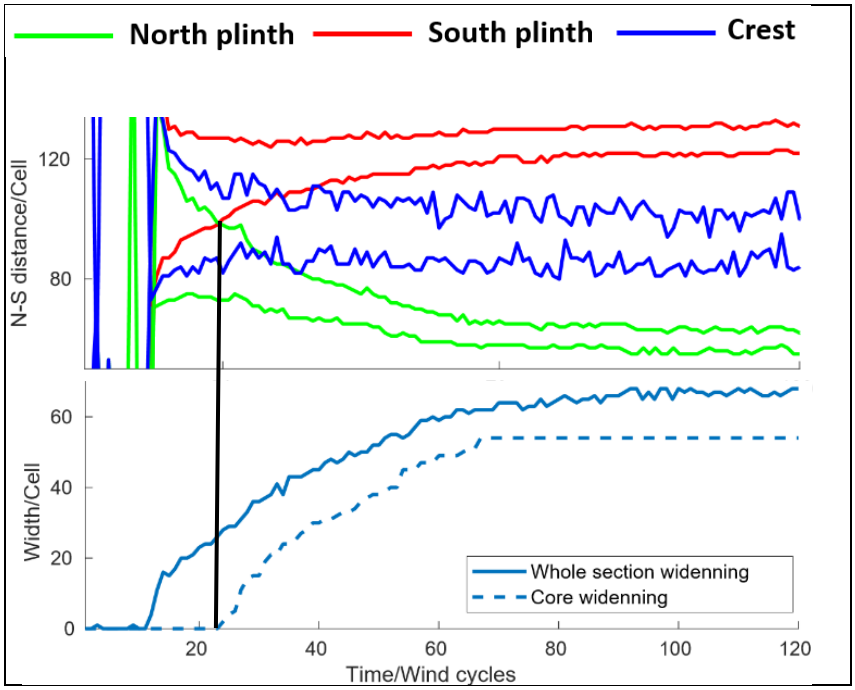


Figure 6-2. Dynamics of a linear dune cross section (labelled with a white line in Figure 6-1) modelled with ReSCAL under the bimodal wind regime T=2400t_0, θ=120° and N=2 (T_1 =1600t_0, T_2 =800t_0, $\theta_1 = 41^{\circ}$, $\theta_2 = 79^{\circ}$) enforced with N-S periodical boundaries (A) 2D topography transects at the specified time steps (a) stratigraphy preservation not started (b) a preserved core started growing (c) steady state. (B) Dune width and core width evolution with time from beginning of the simulation to the steady state, associated with tracks of dune crest and north (N1&N2) and south (S1&S2) plinths at ends of two wind

periods, see points labelled in (A), core initiating time labelled with a vertical black line.

In Figure 6-2 (A), at the earliest time t=20 T, the cross section is so narrow that net lateral displacement during a wind period exceeds the section width and no sediment remains preserved after each wind period. Figure 6-2 (B), therefore, shows that the dune footprints do not intercept. At the later time t=30, the section width has exceeded the lateral migration distance within a wind period. Here sediments buried in the intercepting areas of the two baselines are preserved and incorporated into the stratigraphy, forming a 'core' of the dune. Correspondingly, the core growth begins (Figure 6-2 (B)) from t=22 T. At the last time-step of t=408 T, both the preserved core and the dune have reached the steady (i.e. maximum can be grown to) width and stopped growing. Through the time shown, the dune crest oscillation starts from the longest distance (blue curve in the upper panel of Figure 6-2 (B)), gradually slowing down with size growth of the cross section, afterwards getting stabilized when core building starts.

The width increase of the whole dune section and the core section are the fastest at the beginning when the growth starts, gradually slowing down with growth of the cross section. On the one hand, with extension of the linear dune ridge, the fixed amount of sand supplied distributes to a greater number of cross sections, hence each cross section receives less. On the other hand, for the same change of width δW_{dune}, assuming the same geometric ratio h/W_{dune} (where h is the dune height), a greater amount of sand is needed when W_{dune} is larger. The two factors both lead to the trend a decrease in the rate of dune widening as time progresses.

Drivers of the steady state

According to Figure 6-2, the cross section does not grow infinitely, but stops at a maximum width. Both the whole dune and the stratigraphy core reach this steady state. To clarify the origin of the steady state, Figure 6-3 (A) shows sand flux (averaging the sum of a wind cycle T) evolution with time from the initial condition to the steady state (i.e. the dune width has reached the maximum). Figure 6.3 shows the time series of both the longitudinal (W-E) flux over the entire surface $Q_{mean||}$ (take the mean of Q_{we} over the whole cross section surface) and inter-dune flux outside of the dune $Q_{out||}$. Here $Q_{out||}$ results from lee slope sand erosion and transport. In the bimodal wind regime presented in this section, the sand flux not trapped by the dune $Q_{out||}$ mainly derives from the wind at angle $\theta_1 = 41°$ for the duration $T_1 = 1600t_0$, because the lee (north) slope flow is strong.

Figure 6-3 (A) indicates that in response to the width increase of the cross section, $Q_{out||}$ remains fairly constant, not influenced by the dune width, whilst $Q_{mean||}$ has a positive correlation with growth of the cross section. At the steady state, the W-E flux slightly fluctuates around the sand influx supplied by the upstream source around 9840 grain cells per full wind cycle, as labelled with the horizontal dashed line in Figure 6-3 (A).

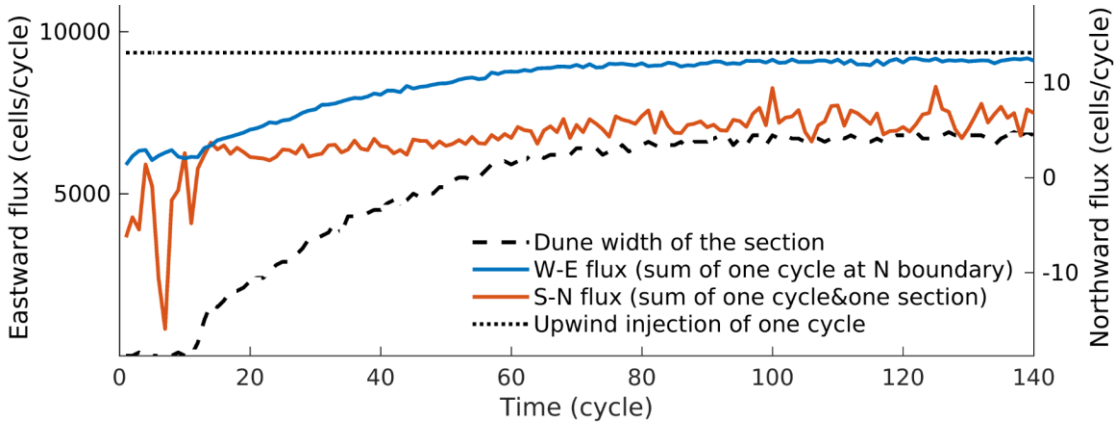
To further clarify the $Q_{mean||}$ dependence on dune width, Figure 6-3 (B) provides the $Q_{mean||}$ profile with respect to the width of the cross section. A linear correlation is indicated between the dune width W_{dune} and the mean crest-parallel sand flux over the surface $Q_{mean||}$. Owing to mass balance kept by the periodical boundaries, regarding the whole 3D model domain, there is no net mass influx or outflux in the crest-normal (N-S) direction. Instead, the crest-parallel (W-E) flux through the east boundary is the only path sand can leave the domain with the circular source supply

being the only origin of sand origin. As a result, for the full model domain, at the steady state, the sand influx supplied by R_{in} from the upwind tip equals to the sand outflux leaving the domain from the east domain boundary. This mass balance applies to all cross sections reaching their steady state. Therefore for each cross section, there exists a relationship between $Q_{mean||}$ and $Q_{out||}$, dune width W_{dune} and inter-dune spacing width W_{out} (domain N-S width deducted by W_{dune} at the steady state) and sand influx supplied from the upwind source Q_{in}. In scenarios with a circular source of radius r in this chapter, $Q_{in} = R_{in}\pi r^2/(W_{dune} + W_{out})$ where W_{dune}+W_{out} is the N-S width of the domain 200-cell.

$$Q_{in} * (W_{dune} + W_{out}) = Q_{mean||} * W_{dune} + Q_{out||} * W_{out} \quad \text{Equation 6.1}$$

This relationship enforces a limitation for further growth in size of linear dunes under the specified environmental condition, restricting the dune ridge width balancing with the sand influx. This may be one of the mechanisms that drive the constant ratio between linear dune width and inter-dune distance found by some previous study (e.g. Thomas, 1986; Lancaster, 1988). For most linear dune and transverse dune simulations presented in this thesis, Equation 6.1 may be approximated to $Q_{in}(W_{dune} + W_{out}) = Q_{mean||} * W_{dune}$, because the volume and flux of sand distributed on flat inter-dune surfaces ($Q_{out} * W_{spacing}$) is on a far smaller order than the dune sand volume (see Figure 4-13 of Chapter 4 and Figure 6-3 (A)).

(A)



(B)

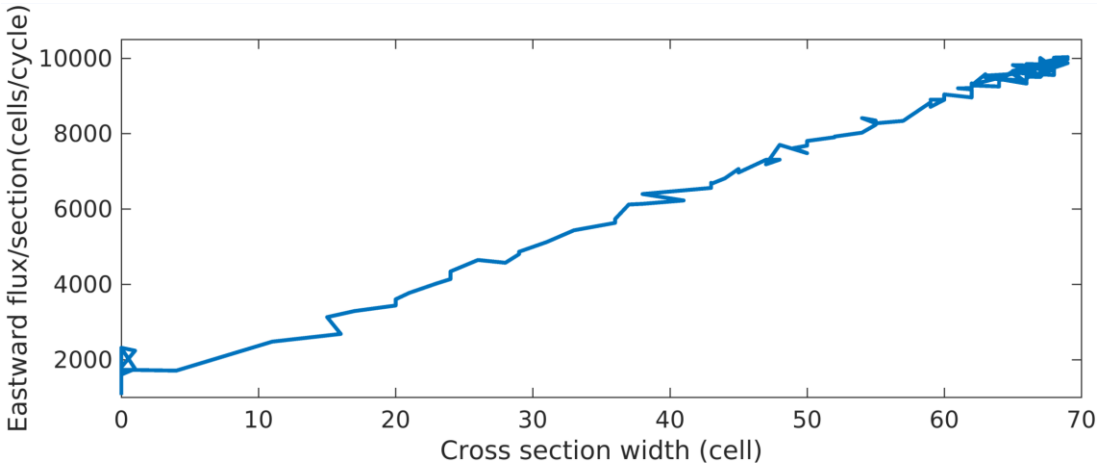


Figure 6-3. Sand flux profiles driving the dune cross section (labelled in Figure 6-1) reaching a steady state, taking sum of flux data of a full wind cycle (A) Crest-parallel (W-E) sand flux evolution with time, including the flux over the whole dune surface and outflux measured at the inter-dune surface (north domain boundary). The influx supplied by the upwind circular source and the dune width evolution with time both are labelled. (B) Dune surface W-E flux with respect to the cross section width up to the maximum width reached.

Stratigraphy and chronology of the cross section

Regarding the internal structure of the cross section analysed above, Figure 6-4 shows the stratigraphy visualized with dune topography at the end of each of the wind periods T_1 and T_2. Figure 6-5 presents the associated chronological structures. Considering the clearness of the preserved core age and visualising multiple age-distance profiles within one diagram, the chronology is described by the absolute deposition time from the initial condition, instead of the often used (e.g. Munyikwa, 2005; Telfer, et al., 2007 and 2011; Stone and Thomas, 2008) age between the last exposure time to the sampling time, because this age depends on sampling times. Figure 6-5 (A) are time profiles with respect to the vertical depth from the top of the core (practically taking the maximum elevation of the long preserved body), sampled at varying crest-normal (N-S) distances. Figure 6-5 (B) shows chronology profiles with respect to crest-normal distances sampled at varying elevations along the cross section. These two sets of profiles, therefore respectively indicate the vertical accumulation of each specified column and transverse extension of each shown horizontal line. Both Figure 6-4 and Figure 6-5 are mapped after the cross section has reached the steady state where the width and height have stopped growing and the core is no longer active.

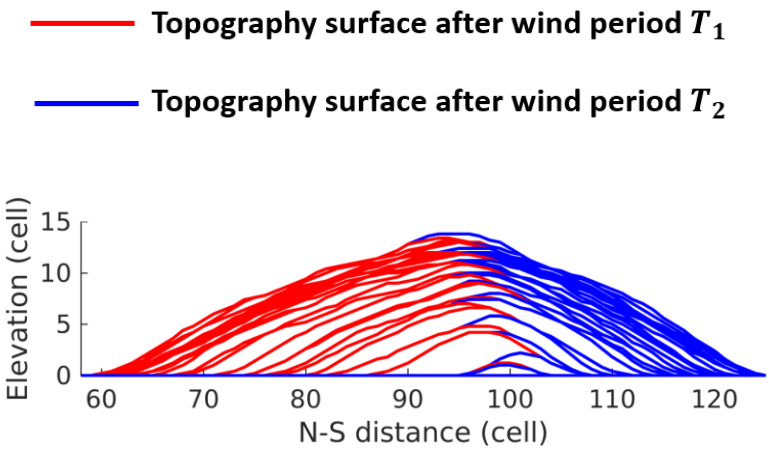
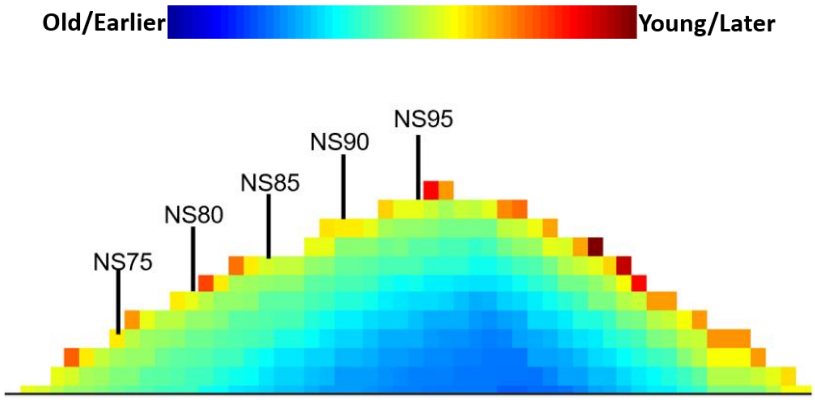


Figure 6-4. Beddings of an elongating dune cross section (labelled in Figure 6-5) under a bimodal wind regime, visualized by topography surfaces after each wind period.

Figure 6-4 indicates that the sedimentary records contain sand deposited by both winds. Firstly, grain flow strata are formed on the corresponding lee slope of each wind. Sand deposited during one wind period not only gets preserved in the lee, but also overlaps a few cells on the windward side of the crest. This is attributed to the stoss slope preservation described in Section 5.2 where some sand has not passed the dune crest before a wind period ends, and afterwards gets preserved by the grain flow strata of the reversed wind. As shown in Figure 5-8 and Figure 5-9, this deposited sand is preserved near the dune crest, which corresponds to the overlapping portion indicated by Figure 6-4.

(A)



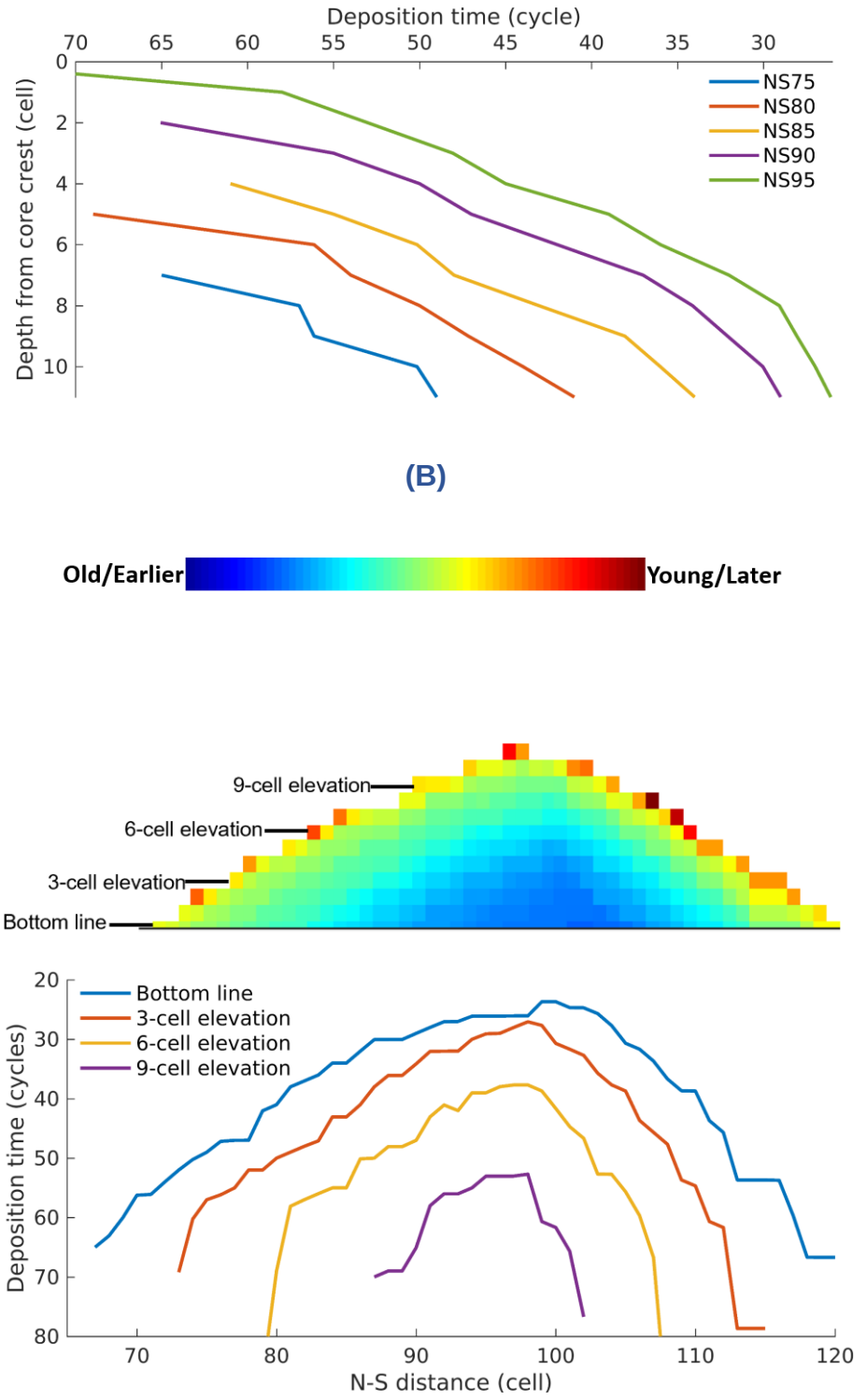


Figure 6-5. Chronology profiles of the preserved core (visualized with coloured images) of the cross section labelled in Figure 6-1, sampled when the cross section is at the steady state (i.e. has reached the maximum width and stopped widening further). The chronology is described by the absolute

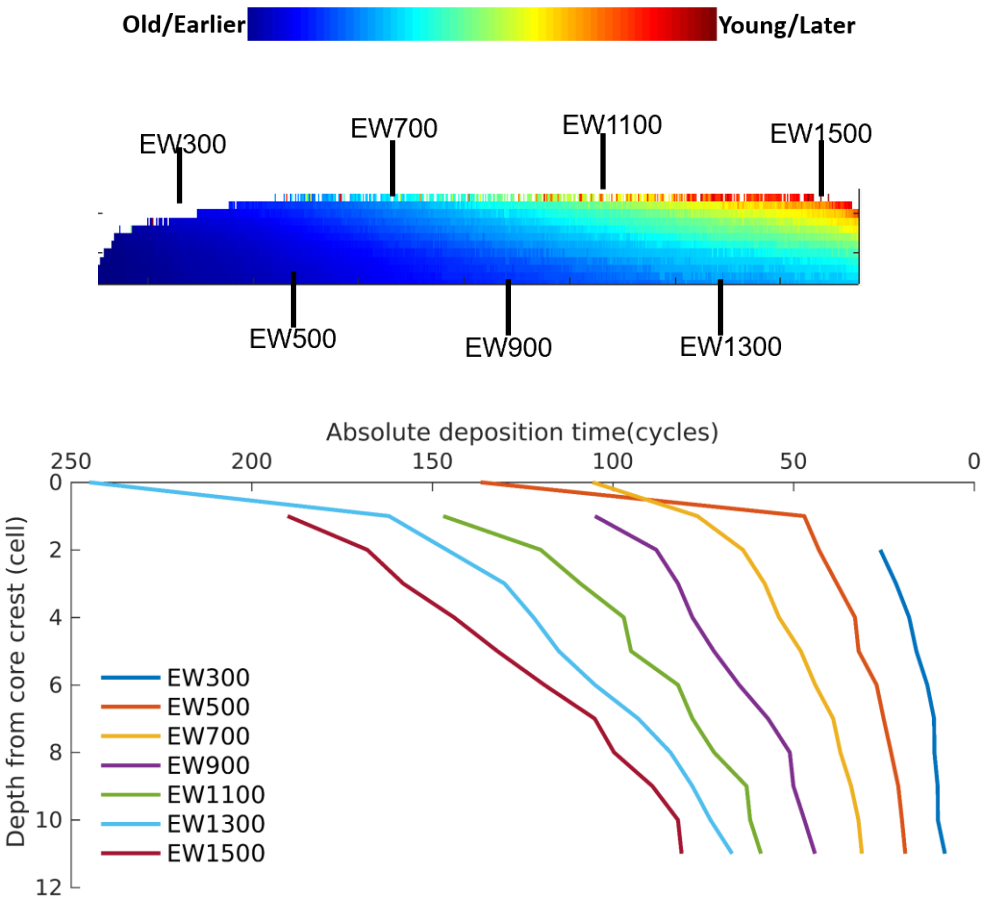
deposition time (since the initial condition of a simulation run). (A) Chronology with respect to vertical distance (from the highest elevation of the preserved core) sampled at varying transverse (N-S) locations labelled. (B) Chronology with respect to transverse (N-S) distance sampled at varying elevations as labelled.

A key interpretation from the data shown in Figure 6-5 is that chronology profiles of vertical accumulation and horizontal lateral (N-S, crest-normal) extension have the same trend: they start with the fastest rate (to time) at the beginning but slow down with as the dune grows in size. For example, in Figure 6-5 (A) the central location labelled with NS95, the growth of the initial two-cell height (between depth 8-cell and 10-cell) only takes 3 wind cycles, whilst the youngest part of the core takes 15 cycles to accumulate from depth 2-cell to 0-cell.

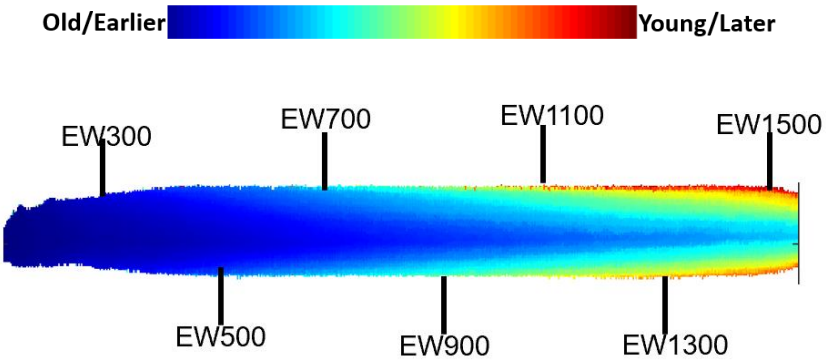
6.1.3 Stratigraphy and chronology of the whole dune

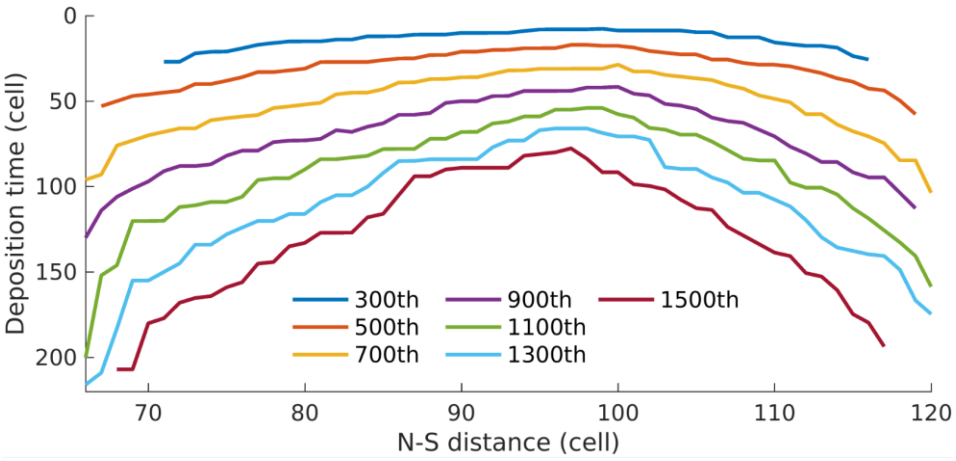
Chronological structures of the entire linear dune are provided in Figure 6-6. They are sampled from each cross section after the model domain has reached the steady state (i.e. maximum width and height of the enforced wind and sand supply condition). Figure 6-6 (A) shows the temporal profiles with respect to vertical distances from the crest of the core drilled through the crest at a set of longitudinal (W-E) locations. Following are time-transverse (N-S) distance profiles (Figure 6-6 (B)) of these W-E locations extracted from the bottom layer of sand. Also, Figure 6-6 (C) shows the time-longitudinal (W-E) structures at varying transverse (N-S) locations.

(A)


Old/Earlier
Young/Later
EW300
EW700
EW1100
EW1500
EW500
EW900
EW1300
Absolute deposition time(cycles)
250
200
150
100
50
0
Depth from core crest (cell)
0
2
4
6
8
10
12
EW300
EW500
EW700
EW900
EW1100
EW1300
EW1500

(B)


Old/Earlier
Young/Later
EW300
EW700
EW1100
EW1500
EW500
EW900
EW1300



(C)

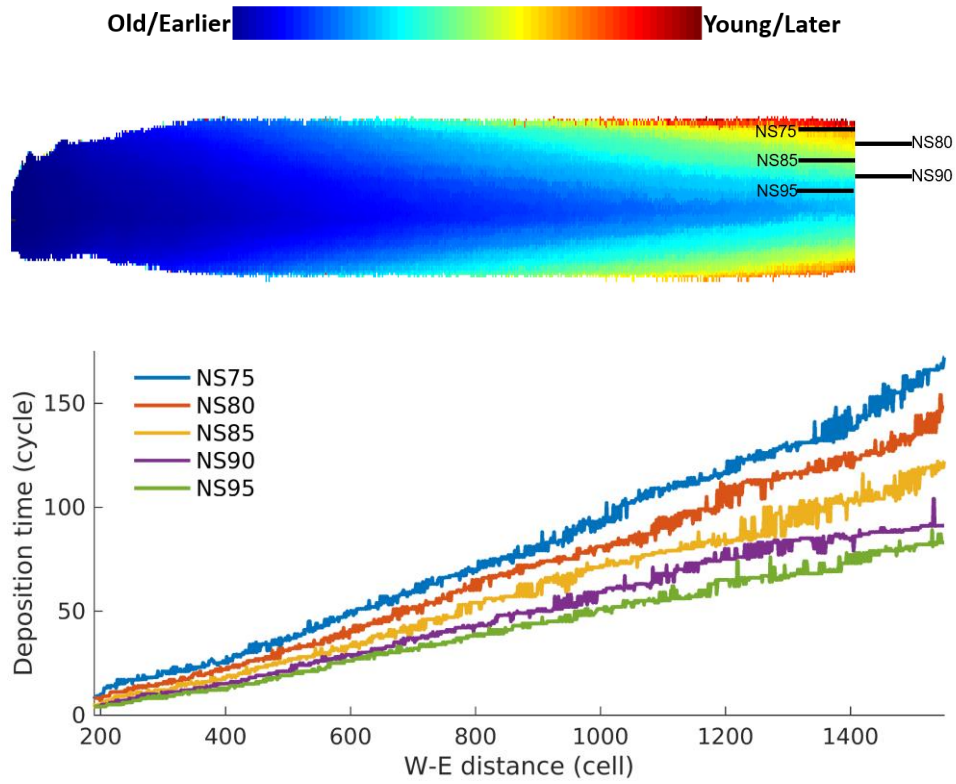


Figure 6-6. Chronological profiles of the preserved core (visualized with coloured images) of the elongating linear dune shown in Figure 6-1, sampled when the whole dune within the model domain has reached the steady state (i.e. each cross section has reached the steady width). The chronology is described by the absolute deposition time since the initial condition. (A) Chronology with respect to vertical distance sampled at varying longitudinal

(W-E) locations labelled. (B) Chronology with respect to transverse (N-S) distance sampled at same W-E locations of (A), labelled (C) Chronology with respect to W-E distance sampled at varying N-S locations labelled.

For cross sections of the elongating dune, the key information indicated by Figure 6-6 (A) and (B) is that the closer to the upwind source, the faster the cross section grow in height (Figure 6-6 (A)) and width (Figure 6-6 (B)). The most (longitudinally) upwind core section (labelled with EW300) spends less than 15 T wind cycles to reach a steady state. In comparison, it takes longer than 100 T for the most downwind section (labelled with EW1500) to reach the steady state. For each chronological profile, the core building is fastest when it starts to grow and gets slower as the core size increases. Correspondingly, Figure 6-6 (C) indicates slower elongation for the longitudinal sections further from the (transverse) middle of the core.

In general, in terms of chronology built by dune elongation and once the dune has reached a steady state, older sediments are preserved further (longitudinally) upwind, while longer range of more recent dune ages are buried further downwind. Additionally, if the linear dune develops solely in the longitudinal extension mode (e.g. Correch du Pont, et al., 2014), for each cross section generally the preserved core starts building directly beneath the top of the core, hence the oldest sand can be found beneath the core crest once the core topography has been identified. For the whole dune, the oldest sand location depends on when the dune is surveyed because the dune has an oscillating layer on the surface and the relative location of the core changes accordingly.

6.1.4 Key findings from Section 6.1

Section 6.1 introduced fundamental criteria considered for parameter setting of Chapter 6, including the model domain dimensions, bimodal wind conditions and sand supply conditions. Theses settings were for the purpose of studying the elongation manner of linear sand dunes, ensuring the lateral and longitudinal migration both were disabled so that the dynamic of elongation was studied alone. The dune scenarios explored in this section simulated the sand supply conditions described by Tsoar, 1989 and deployed by previous ReSCAL work undertaken by Rozier, et al. (2019).

---The analysis started with tracking the topography evolution of a specified cross section, progressing to the long term internal stratigraphy and chronology structure. The cross section started growing at the fastest rate (to time), gradually slowing down with the increasing size and eventually reaching a steady state (i.e. maximum size).

---With enforcing crest-normal periodical boundaries, reaching the steady state was driven by the dune surface crest-parallel sand flux (net outflux of a cross section) getting balanced with the upwind sand supply (net influx of a cross section).

---Once a cross section width has exceeded a certain threshold, the dune width exceeded annual sideways oscillation distance and the long preserved stratigraphy started to be incorporated into a core buried. The sedimentary structure of the core was mainly characterized by bidirectional dips formed by avalanche during each wind period. In response to the topography evolution trend (i.e. slowing down / logarithmical growth rate with time), the chronology buried indicated the vertical profile drilled through the core crest had the oldest sand and shortest period of

reaching a steady state. Further vertical profiles consisted of younger sand whilst more abundant of chronology (i.e. longer range of sand ages).

---Based on understanding about a cross section, the chronology analysis was extended to the whole dune ridge within the model domain. All cross sections eventually reached the maximum width balancing with the upwind sand flux. For the chronology, more upwind cross sections were buried with older sand spanning shorter historical times, whilst more downwind cross sections were the opposite, containing sand ranging for a longer and more recent time.

Following 6.1 is detailed analysis regarding dynamics of an elongating linear dune generated by a typical bimodal wind regime.

6.2 Wind condition control on linear dune formation

Based on discussion of the longitudinal extension dynamic of a specific bimodal wind regime in 6.1, this section has a primary goal to elucidate how the dune development is influenced by varying the properties of the bimodal wind regime. Figure 6-7 schematizes the relationship of a resultant linear dune with the wind regime enforced. The exploration surrounds the wind cycle duration T, wind-wind angle θ, as well as the extent of asymmetry of a wind regime as described by the duration ratio between the two winds $N = T_1/T_2$. All simulations are enforced with the same injection rate $R_{in} = 0.05$ from the upwind circular source and N-S periodical boundaries. Each set of experiments starts with a presentation of topographic images of dune evolution under each tested wind regime, identifying a range of parameters resulting in the production of elongating linear dunes. The dynamics of this elongation are then analysed with respect to the preservation of sediment and dune internal structure.

For the internal structure shown in Section 6.1 where a (triangular) core is preserved, Table 6-1 summarizes the threshold (minimum) dune width for core development for the wind conditions tested. Simulated outputs presented in this section are compared with previous work on linear dune formation controlled by bidirectional winds (i.e. Rubin and Ikeda, 1990; Parteli, et al., 2009 and 2014; Gao, et al., 2016).

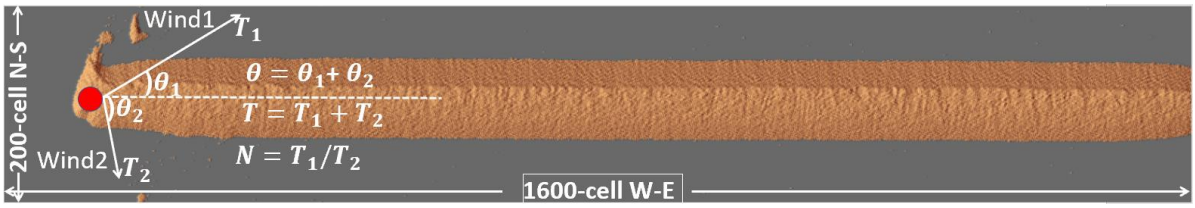


Figure 6-7. Bimodal wind regime and sand supply settings schematized on an elongating dune. The upwind sand supply source is labelled with a red dot, a 10 cells diameter circle installed on the ceiling of the 3D domain, enforced with an injection rate of 0.05 (i.e. probability of injecting a grain on the surface per t_0), dropping sand on the land surface directly under it.

6.2.1 Wind angle

Figure 6-8 shows topographic images of dunes at the steady state responding to bimodal wind regimes at varying wind-wind angles, θ. Symmetrical wind regimes are enforced where $T_1 = T_2$ and two sequences of wind cycle durations T are included as they show varying topography patterns. The range of wind angles takes into account the previously recognized threshold of 90° for linear dune formation (e.g. Bagnold, 1941; Rubin and Ikeda, 1989; Parteli, et al., 2009 and 2014). In Figure 6.8 wind angles are shown both above and below this threshold. Applying angles smaller than 90° is for the purpose of testing whether linear dune dunes can be produced with the constant upwind sediments supply rather than the traditionally

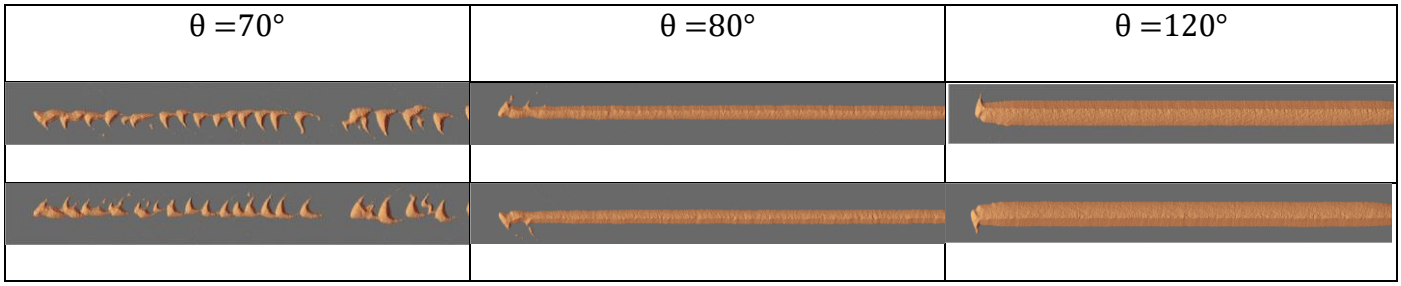
used piles or blocks in previous numerical studies (e.g. Parteli, et al., 2009 and 2014; Liu and Baas, 2020).

Under the longer wind cycle T=2400 t_0 ($T_1 = T_2 = 1200\ t_0$, Figure 6-8 (A)), when θ =80° ($\theta_1 = \theta_2 = 40^{\circ}$) and θ =120° ($\theta_1 = \theta_2 = 60^{\circ}$) linear dunes are generated in the mode of infinite elongation, similar to the scenario analysed in Section 6.1. These dunes are characterized by infinite dune length and the same dune width through the linear ridge. At the steady state shown, the dune size (i.e. width and height) is larger with the greater angle θ =120° than where θ =60° . This is explained by the relationship $Q_{in} * (W_{dune} + W_{out}) = Q_{mean||} * W_{dune}$, where a greater θ results in a smaller longitudinal component for sand transport, and so $Q_{mean||}$ is smaller. Therefore, with the same sand supply condition, the steady state W_{dune} is larger for larger values of θ. For the smallest bimodal angle shown here of ***θ =70°*** ($\theta_1 = \theta_2 = 35^{\circ}$), a linear dune does not form. Instead, barchans showing size similarity are emitted from the upwind source, aligned in a corridor pattern (Hersen, 2004). These barchans are seen to periodically reorientate in response to wind reversal.

Under the shorter wind cycle T=100 t_0 ($T_1 = T_2 = 50\ t_0$, Figure 6-8 (B)), three angles below 90° are tested. The largest angle tested of θ =70° ($\theta_1 = \theta_2 = 35^{\circ}$) is able to generate a linear dune in an infinite elongated mode, differing from the barchan pattern formed under T=2400 t_0 (the influence of T is discussed in the subsequent section 6.2.2). With the two smaller angles of ***θ =50°*** and ***θ =60°,*** both scenarios show a linear ridge extending from the upwind source, narrowing to the east and terminating before reaching the downwind boundary. Barchans are ejected from the east termination with slight reorientation in wind reversal. The linear ridge is approximately 820 cells long where ***θ =60°*** and shorter at 310 cells where ***θ =50°.***

According to Figure 6-8, with the controlled upwind sand supply, smaller wind-wind angle θ tends to form narrower linear dunes due to a larger longitudinal sand flux. Barchans are generated where the linear ridge is too narrow to be maintained. The outputs of Figure 6-8 indicate formation of linear dunes where the wind-wind angle θ is smaller than 90°, differing from previous work (e.g. Parteli, et al., 2009 and 2014; Liu and baas, 2020) using sand piles or blocks as the initial condition. Here the subsequent (within this section) analysis regarding elongation linear dunes only considers the 'simpler' scenario where the infinite elongation occurs.

(A) T=$2400t_0$, T_1 =$1200t_0$, T_2 =$1200t_0$, N=1



(B) T=$100t_0$, $50t_0$-$50t_0$, N=1

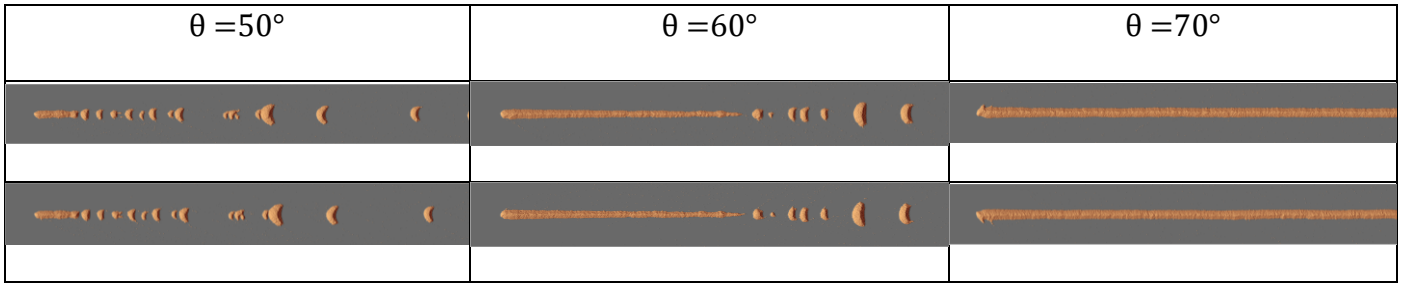


Figure 6-8. Topographic images of dunes under symmetrical (N=1) bimodal wind regimes influenced by the wind-wind angle θ, taking snapshots at the ends of the two wind periods at steady state. (A) T=2400 t_0 (B) T=100 t_0. The two wind cycle durations T are set to cover a full range of θ from 50° to 120°, identifying the full linear dune initiation potentials driven by wind directionality, as previously raised (Parteli, et al., 2009 and 2014).

With influence of wind-wind angle (θ) on dune evolution identified, the dynamics of (infinitely) elongating linear dunes are investigated under symmetrical wind regimes with varying wind angle and consistent wind cycle duration, where $T_1 = T_2 = 1200\ t_0$. Figure 6-9 provides data on evolution of the width of the persistently preserved core over time with the analysed cross section as labelled in Figure 6-1. Figure 6-10 is supplemented to show the longitudinal extension described by the downwind (east) dune tip location. Owing to the stronger crest-parallel sand transport capability, the linear dune and the preserved core both elongate faster under smaller values of θ (Figure 6-10). Correspondingly the tracked cross section starts to grow faster.

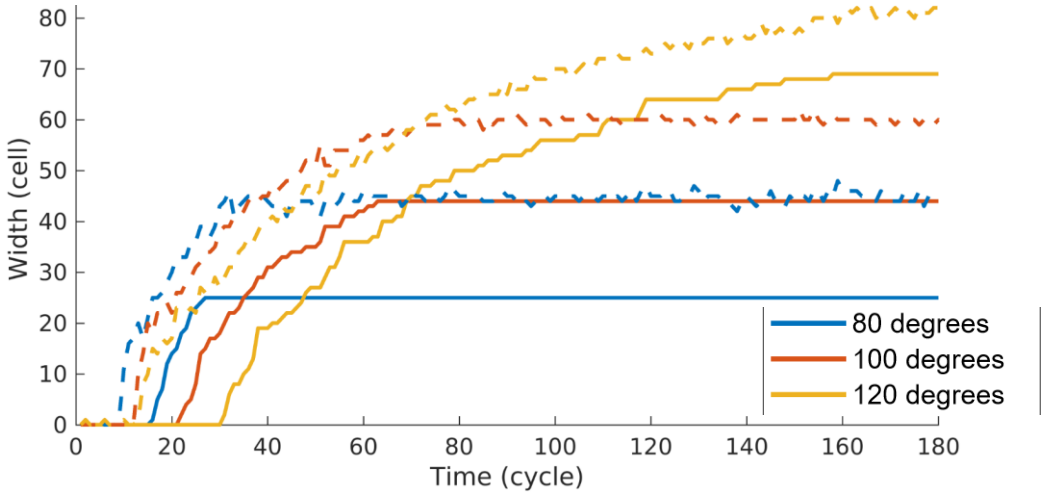


Figure 6-9. Cross section (same location as labelled in Figure 6.1) width evolution with time, including whole dune width (dashed line) and preserved core (solid line), at varying wind-wind angles, θ, in bimodal wind regimes. Symmetrical bimodal wind regimes are enforced with a consistent wind cycle duration, T=2400 t_0 with a constant upwind sand supply.

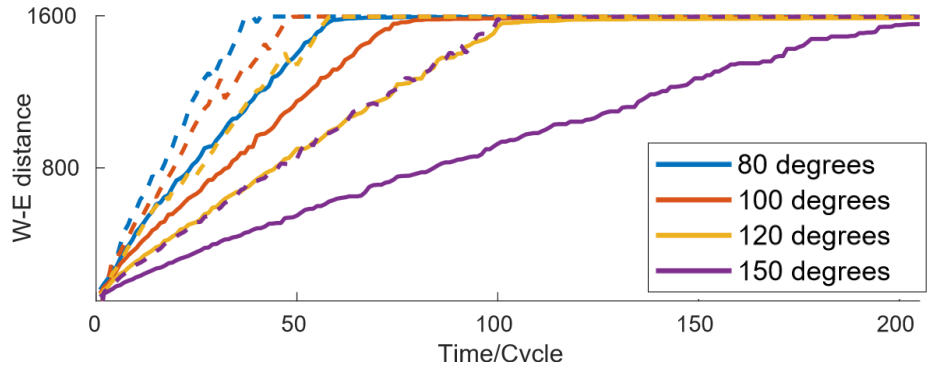


Figure 6-10. Linear dune longitudinal extension (described with downwind dune termination location in W-E distance) with time of the whole dune (dashed line) and the preserved core (solid line), at varying wind-wind angle θ in bimodal wind regimes. Symmetrical bimodal wind regimes are enforced with wind cycle duration T=2400 t_0 with a constant upwind sand supply.

Figure 6-9 indicates that under greater angle θ, the preserved core dominates a higher portion of the whole dune. At the steady state where the cross section has stopped widening, the core width and dune width ratio W_{core}/W_{dune} is only 63.4% when θ =80° (Table 6-1). In comparison, the ratio is 87.3% when θ =120°. Additionally, greater θ means a longer delay between the dune starting to grow and the core starting to develop (Figure 6-9). Also, with a greater θ, due to the stronger crest-normal (N-S) sand transport oscillating laterally, a larger dune width is required (Table 6-1) to initiate core preservation. Figure 6-10 shows that the dune tip elongation is approximately linear with time, partially contributing to the (roughly) logarithmic trend in width growth. Both the dune and the core elongates faster when the dune is enforced with a smaller θ.

Regarding the impact of varying θ on sediment preservation, for the analysed cross section, the narrowest dune produced by the smallest θ (θ =80°) buries the oldest sand because the core building starts earlier, after only 17 T from the initial condition

(Figure 6-9). The sedimentation history recorded by the core, however, is the shortest as the core spends the shortest time to reach the steady state at *t = 23 T* (Figure 6-9). The preserved sediment therefore only spans a total of 6 T. In contrast, the widest dune produced with $\theta = 120°$ preserves the youngest core, which starts building after 32 T from the initial condition, and the sedimentary record is much wider in time span, spanning 125 T before the dune reaches a steady state at 157 T. Figure 6-10 indicates a similar control of θ on the chronological structure; smaller θ results in older sediments but a narrower time span of preserved records.

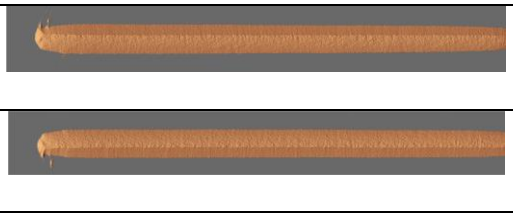
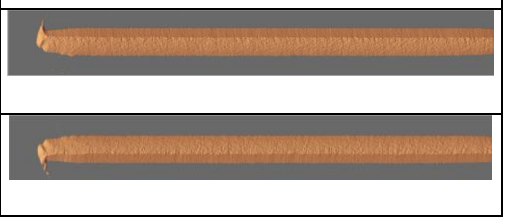
The variation in dune dimensions and chronological structure resulting from a varying wind-wind angle (θ) is related to previously proposed issues. For example, the wind angle may partially determine the dune width and spacing (e.g. Wasson and Hyde, 1983; Thomas, 1986; Lancaster, 1988; Mills, et al., 2013) driven by the mass balance equation $Q_{in} * (W_{dune} + W_{out}) = Q_{mean||} * W_{dune}$. Also, the chronology structure identified above may provide numerical solutions to the recently proposed scientific question about dune age and dune field pattern coarseness (e.g. Telfer, et al., 2017; Day and Kocurek, 2018). With the environmental conditions applied here, more acute wind-wind angles tend to bury older sediments and produce narrower dune ridges (finer dune field pattern), while more obtuse angles tend to bury longer range of more recent ages and produce wider dune ridges (coarser dune field pattern).

6.2.2 Wind duration length

Shown in Figure 6-11 are topographic images at the steady state of dunes simulated at varying wind cycle durations, T, using symmetrical bimodal winds. The

topographies shown in Figure 6.11 are snapshots at the end of the appropriate wind cycle encompassing both wind periods. Two sequences of wind-wind angle (*θ*) are presented; θ =120° and 70°.

(A) N=1, θ=120°

$T = 100t_0,\ T_1 = T_2 = 50t_0$	$T = 1200t_0,\ T_1 = T_2 = 600t_0$	$T = 2400t_0,\ T_1 = T_2 = 1200t_0$
		

(B) N=1, θ=70°

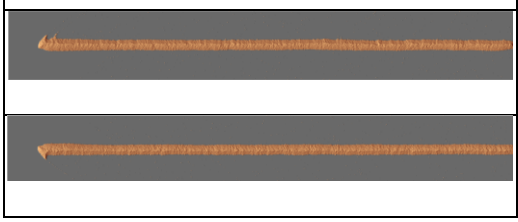
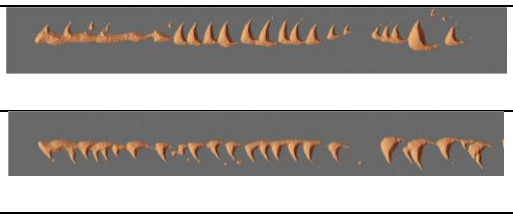
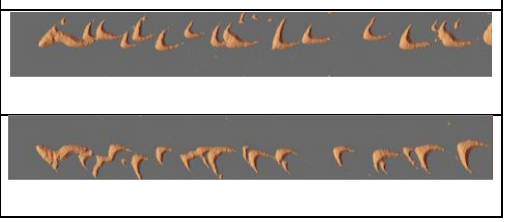
$T = 800t_0,\ T_1 = T_2 = 400t_0$	$T = 2400t_0,\ T_1 = T_2 = 1200t_0$	$T = 4800t_0,\ T_1 = T_2 = 2400t_0$
		

Figure 6-11. Topographic images of dunes under symmetrical bimodal wind regimes influenced by the wind cycle duration, T. Snapshots are at the end of the two wind periods at steady state. (A) θ=120°, to show the T impact on linear dune dimension (B) θ=70°, to show the T impact on linear dune formation.

Under the greater wind angle of θ=120° (Figure 6-11 (A)), linear dunes are formed under the three different wind cycles in the infinite elongation mode, and the resulting linear ridge is narrower with longer wind cycles . For the two scenarios T=2400 t_0 and T=1200 t_0, during each wind period T_1 and T_2, the slip face for the simulations at θ=120° reach the plinth of the lee slope. For the shortest wind cycle of T=100 t_0, the dune crest oscillates on an annual basis and the slip face is unable

to reach plinth of the lee slope. In these cases, the dune base remains static and so forms part of the preserved core of the dune.

Under the smaller wind angle, θ=70° (Figure 6-11 (B)) results in three varying topographic patterns. An infinitively elongating linear dune is formed when the wind cycle duration is short, i.e. T=800 t_0. However, at larger values of T (T=2400 t_0 and 4800 t_0) size-similar barchans develop along a corridor are formed when T=2400 t_0. With further increase of the wind cycle duration to T=4800 t_0, this corridor looking alignment is destroyed and the barchans migrate over longer distances off the central location.

The overall trend reflected by Figure 6-11 (B) is that a longer wind cycle duration leads to more 'discrete' topography. This is attributed to the 'transverse instability' (e.g. Parteli, et al., 2012; Niiya, et al., 2012 and 2013), suggesting that the rarity of transverse dune on planetary bodies is because the dunes are transversely broken into barchans when the corresponding wind direction lasts for a long time. Here the transverse instability is demonstrated in the ReSCAL outputs, showing the dune field pattern appears as broken barchans rather than an integrated linear dune. Further, according to Figure 6-11 (A), longer wind cycle duration T also results in narrower width where linear dunes can be generated under the certain wind condition. The dependence of dune dimensions on T is attributed to fundamental analysis regarding sand outflux (Figure 5-4) driven by the lee slope gradient and the mass balance Equation 6.1 $Q_{in} * (W_{dune} + W_{out}) = Q_{mean||} * W_{dune} + Q_{out||} * W_{out}$. Where T is smaller, for example, in $T = 100\ t_0$, Figure 6-11, the slip face cannot reach the plinth at the end of either wind period. Therefore in the early time of the subsequent wind period, the reversed wind interacts with a steep lee slope (after 1300 t_0 part of the flux profile, Figure 5-4, Chapter 5) and less sand is lost by the

lee slope where Q_{out} is small. As a result, with the controlled sand influx (R_{in}) from the upwind, the elongating dune incorporates more sand and grows to larger size where T is shorter.

Below are discussion surrounding the 'simple' scenarios where linear dunes can elongate in the infinite mode, extending to the east boundary and all cross section reaching the same width eventually.

The elongation with time is presented in Figure 6-12 by tracking the W-E distance of the downwind (east) termination of the dune and the core. Figure 6-13 provides data on evolution of the core width of the dune over time with the analysed cross section (location as labelled in Figure 6-1). The simulations here use symmetrical wind regimes where θ=120° ($\theta_1 = 60^{\circ}$, $\theta_2 = 60^{\circ}$).

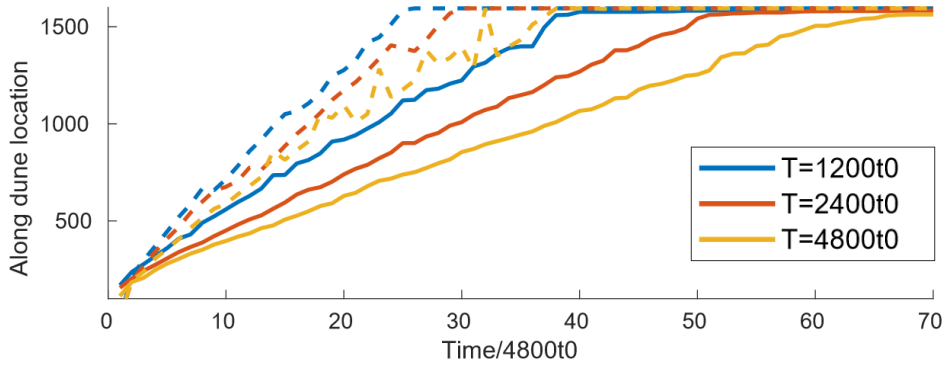


Figure 6-12. Linear dune longitudinal extension (described with downwind dune termination location in W-E distance) with time of the whole dune (dashed line) and the preserved core (solid line), at varying wind cycle durations T in symmetrical wind regimes where the wind-wind angle θ=120° with a constant sand supply from the upwind.

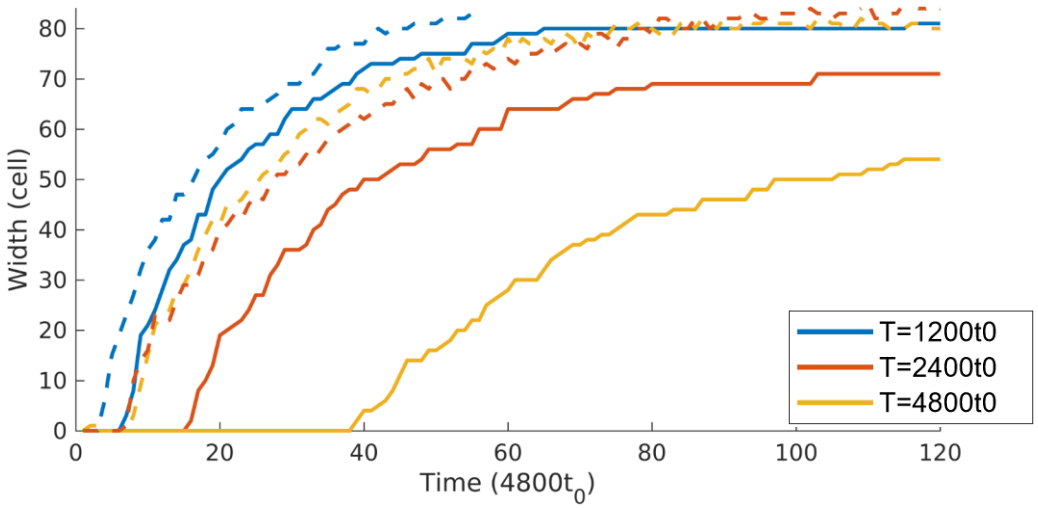


Figure 6-13. Width evolution with time of the elongating linear dune cross section labelled, including the whole dune (dashed line) and the preserved core (solid line), at varying wind cycle durations T in symmetrical wind regimes where the wind-wind angle θ=120° with a constant sand supply from the upwind

In general, a shorter wind cycle duration (T) leads to a more rapid elongation of both the whole dune and the preserved core (Figure 6-12). When T=1200 t_0 the dune tip has reached the east boundary of the domain after only 24 T from the initial condition. In contrast, it takes 37 T for the same condition to be reached when T=4800 t_0. Correspondingly, the analysed cross section width starts to grow (Figure 6-13). For the stratigraphy preservation, the tracked cross section starts to preserve a core at a smaller width (Table 6-1) because the dune width can faster exceeds the oscillating distance within a wind period.

In terms of the internal structure, the core dynamics indicate that higher frequency (shorter T) bimodal winds result in the preservation of older sediments (see the starting time of core building in Figure 6-13). However, such high frequency winds also tend to preserve a shorter time range of sediment preservation. In contrast,

lower frequency bimodal winds (longer T) result in the preservation of younger sediments, but over a longer duration of time. For example, in Figure 6-13, the oldest sand preserved where T=1200 t_0 is deposited at 6T since the initial condition, while for T=4800 t_0, sand starts to be preserved 32 T later. Similarly in Figure 6-12, where T=1200 t_0, the preserved chronology span across 37 T, whilst at T=4800 t_0 the core record spans 68 T. The outputs modelled here using ReSCAL indicate that variations in dune dimensions and ages may be attributed to the contribution of varying wind cycle frequencies, over daily, seasonal and annual scales.

6.2.3 Wind asymmetry (duration ratio between two winds)

Figure 6-14 shows topographic images at the steady state of dunes simulated at varying strengths of asymmetry in bimodal wind regimes. In all the examples shown, the wind cycle duration was set at T=$2400t_0$ and the wind-wind angle $\theta = 120°$. The strength of bimodal asymmetry was implemented by changing the duration ratio N between the two winds where $N = T_1/T_2$.

The general trend shown by Figure 6-14 is that greater asymmetry ($N = T_1/T_2$) tends to build narrower linear ridges and, where the ridge width is too narrow to be maintained, asymmetrical barchans are formed. For the four smaller scenarios of asymmetry (where N=1, 1.4, 2, 2.4), linear dunes develop in the infinite elongation mode and increases in N lead to a narrowing of the linear ridge. The influence of N on dune width corresponds to the relationship of Equation 6.1. Firstly, greater asymmetry in the wind regime (i.e. greater N) results in longer wind cycle duration, T_1, and narrower θ_1, both of which increase $Q_{out||}$ (see the Q_{out} profile with respect to wind-crest angle in Figure 4-13, Chapter 4). As a result, less sand is preserved by the linear dune. Secondly, there is a slight increasing trend of the crest-parallel flux over dune surfaces $Q_{mean||}$ with increasing N (Table 6-1). Here both $Q_{mean||}$ and

Q_{out} lead to narrower dune width under more asymmetrical winds. In summary, greater asymmetry in bimodal wind regime leads to narrower linear dunes.

With greater wind asymmetry (e.g. N=3, Figure 6-14), the dune elongates towards the middle of the domain, but then the ridge breaks down into asymmetric barchanoid forms. A discrete asymmetric barchan dune field is produced with the most asymmetrical wind where N=3.5, where the barchan arms are narrower than those simulated where N=3. In both cases, the longer arm of the barchan has a crest that oscillates with shifting between the two winds. The discussion below has a focus on the four 'simple' scenarios with infinite linear dune elongation and equal width among all cross sections at the steady state.

$T=2400t_0, \theta=120°$

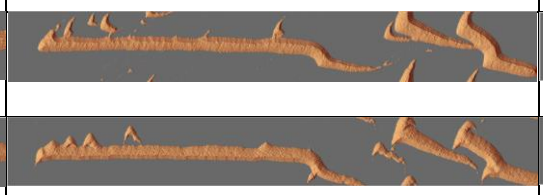
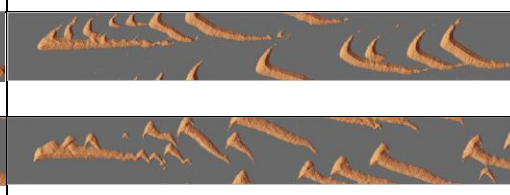
$N=1, T_1=1200t_0, T_2=1200t_0$	$N=1.4, T_1=1400t_0, T_2=1000t_0$	$N=2, T_1=1600t_0, T_2=800t_0$
$\theta_1 = 60^{\circ}, \theta_2 = 60^{\circ}$	$\theta_1 = 50^{\circ}, \theta_2 = 70^{\circ}$	$\theta_1 = 41^{\circ}, \theta_2 = 79^{\circ}$
		
$N=2.4, T_1=1700t_0, T_2=700t_0$	$N=3, T_1=1800t_0, T_2=600t_0$	$N=3.5, T_1=1900t_0, T_2=500t_0$
$\theta_1 = 37^{\circ}, \theta_2 = 83^{\circ}$	$\theta_1 = 31.5^{\circ}, \theta_2 = 89.5^{\circ}$	Not applicable
		

Figure 6-14. Topographic images of dunes under simulated using asymmetrical bimodal wind regimes described by the duration ratios $N = T_1/T_2$, with a constant sand supply from the upwind.

Figure 6-15 shows the dune elongation with time by tracking the location of the east tip of the dune and the preserved core. Figure 6-16 provides data on evolution of the core width of the dune over time with the analysed cross section as labelled in Figure 6-1.

Figure 6-15 indicates that the rate of the tip of the whole dune elongation does not vary significantly between the differing simulations shown, but the preserved core elongation shows a clear trend that larger N leads to faster elongation of the core. Correspondingly in Figure 6-16, in all N scenarios, the cross section of the whole dune approximately starts growing at the same time around 10 T since the initial condition, while core building starts from different times (starting time of core building is the time when the core tip reaches this cross section). Under the most asymmetrical wind shown where N=2.4, the core stats building is the earliest amount the four N cases at 20 T, while the starting time is over 10 T later for the symmetrical regime N=1. As shown in Table 6-1, the minimum dune width required for core preservation does not show a significant dependence on N. Therefore, the varying speed of core elongation is attributed to the growth rate of dune width. The analysed cross section widens more rapidly (Figure 6-16) in response to greater N (i.e. greater bimodal asymmetry). This more faster widening means that a state of sediment preservation is reached more quickly.

In terms of preservation of the chronology (i.e. indicated by the core elongation and width evolution with time), the simulated outputs of Figure 6-15 and Figure 6-16 indicate that more a more asymmetrical wind results in older sediments, but over a shorter overall range of time. For example, in Figure 6-16, where N=2.4, the core of the cross section buries the oldest sand (among the four N scenarios) that deposits at 20 T, whilst the total length of the core records only spans 24T. In contrast, under

the symmetrical regime N=1, the oldest sand (Figure 6-16) preserved deposits at 30 T from the initial condition, while the cross section preserves the sedimentary records of 154 T long in age, which is over six times of that in N=2.4. Additionally in Figure 6-16, by tracking the oldest sediments of all cross sections, whole linear dune within the domain, records of 80 T are preserved by the wind N=2.4, while the wind N=1 covers 100 T.

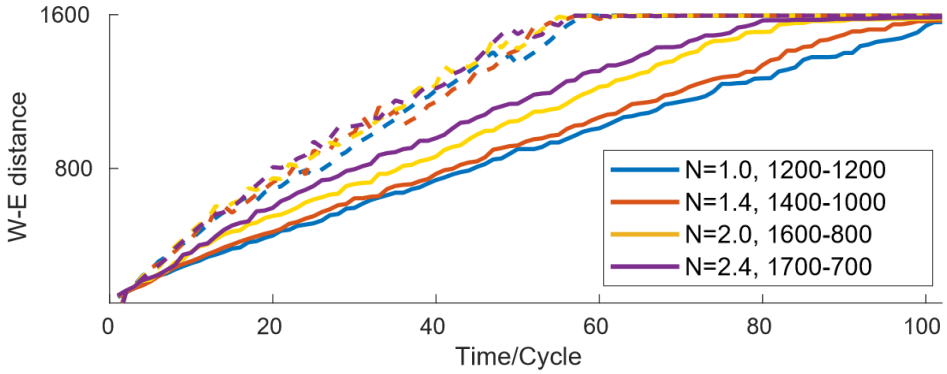


Figure 6-15. Linear dune longitudinal extension (described with downwind dune termination location in W-E distance) with time of the whole dune (dashed line) and the preserved core (solid line), at varying duration ratios of the two winds $N = T_1/T_2$ in bimodal wind regimes with a constant sand supply from the upwind.

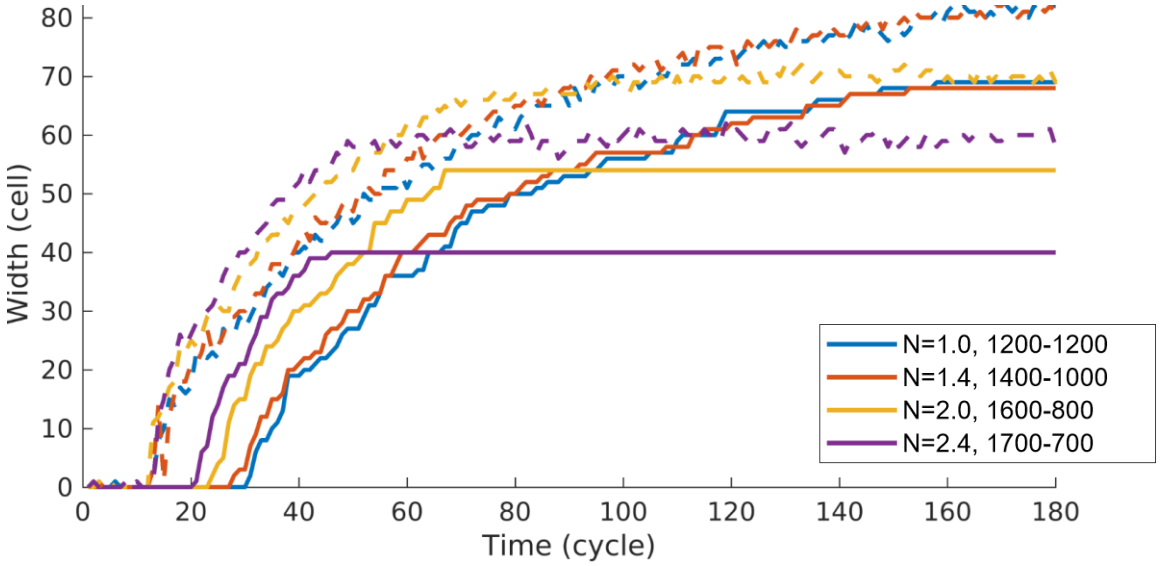


Figure 6-16. Width evolution with time of the elongating linear dune cross section labelled, including the whole dune (dashed line) and the preserved core (solid line), at varying duration ratios of the two winds $N = T_1/T_2$ in bimodal wind regimes. In the bimodal wind enforced, duration of a full wind cycle T=$2400\ t_0$, wind-wind angle $\theta = 120°$ with constant sand supply from the upwind.

Table 6-1. Summary of quantified features of linear dunes with simulations at steady state, infinite elongation and constant upwind sand supply. The dune width and height data are measured at the end of each wind cycle. (A) At varying wind-wind angle, θ (B) At varying wind cycle duration ratio, T (C) At varying bimodal wind asymmetry, duration ratio N=T_1/T_2.

(A)

N=1, T_1 =$1200t_0$, T_2 =$1200t_0$

	θ=80°	θ=100°	θ=120°

Minimum dune width for core building(cell)	24.2	26.9	29.8
Core width(cell)	28.3167	46.2475	73.7864
Dune width(cell)	44.6527	60.5691	84.5241
Core width ratio(cell)	63.4%	76.4%	87.3%
$Q_{mean\|\|}$(/(cell*t_0))	0.2486	0.2078	0.1525
$Q_{out\|\|}$(/(cell*t_0))	$5.87 * 10^{-3}$	$1.52 * 10^{-3}$	$3.64 * 10^{-5}$
Trend: greater θ, larger dune, larger core, larger core ratio			

(B)

	T_1 =600t_0, T_2 =600t_0	T_1 =1200t_0, T_2 =1200t_0	T_1 =2400t0, T_2 =2400t_0
Minimum dune width for core building (cell)	23.1	29.8	42.1
Core width (cell)	82.1	73.8	58.0
Dune width (cell)	87.8	84.5	80.2
Core width ratio	93.5%	87.3%	72.3%
$Q_{mean\|\|}$(/(cell*t_0))	0.1522	0.1525	0.1519
$Q_{out\|\|}$(/(cell*t_0))	$3.15 * 10^{-5}$	$3.64 * 10^{-5}$	$4.07 * 10^{-5}$
Trend: larger T---smaller dune, smaller core and smaller core ratio			

(C)

T =1200t_0, θ=120°

	$T_1 = 1200t_0$, $T_2 = 1200t_0$	$T_1 = 1400t_0$, $T_2 = 1000t_0$	$T_1 = 1600t_0$, $T_2 = 800t_0$	$T_1 = 1700t_0$, $T_2 = 700t_0$
θ_1	60°	50°	41°	37°
θ_2	60°	70°	79°	83°
Minimum dune width for core building(cell)	29.8	30.5	28.3	26.7
Core width (cell)	73.17	70.1	55.3	42.5
Dune width (cell)	84.5	82.7	69.8	59.3
Core width ratio	86.6%	84.7%	79.1%	71.7%
$Q_{mean\|\|}$(/(cell*t_0))	0.1525	0.1389	0.1497	0.1209
$Q_{out\|\|}$(/(cell*t_0))	$3.64 * 10^{-5}$	$8.81 * 10^{-4}$	$2.78 * 10^{-3}$	$3.92 * 10^{-3}$
Trend: larger N(T_1/T_2), smaller dune , smaller core and smaller core ratio				

6.2.4 Key findings of Section 6.2

This section fully explored how linear dune formation and elongation are controlled by properties of a bimodal wind regime. All simulations were based on a constant upwind sand supply. For a bimodal wind regime, wind-wind angle (θ), wind cycle duration (T) and the duration ratio (N) were all seen to impact on the dynamics of linear dunes and their patterns of morphology and sediment preservation. Key findings include:

---The wind-wind angles smaller than 90° were able to initiate elongating linear dunes. The variation from the threshold 90° commonly recognized by previous work (e.g. Bagnold, 1941; Rubin and Ikeda, 1990; Werner, 1995; Rubin and Hesp, 2009

Parteli, et al., 2009 and 2014; Liu and Baas, 2012) was attributed to the sand supply from the (longitudinally) upwind throughout an extended time since dune initiation.

---For the internal structure, older sediments were more likely to be preserved where the wind-wind angles were smaller, the wind was at higher frequencies (i.e. shorter cycle durations) or the bimodal wind regime was in greater symmetry. In these cases with older sand preservation, the range of sand ages was shorter. On the contrary, with opposite trends of these wind properties (i.e. greater wind angles, lower frequencies, higher asymmetry), the dune was less capable of preserving older / earlier sand deposition, but it was better preservable of longer ranges of more recent sand ages.

---There were delays between the dune growth and preserved core growth with time. Therefore dune dynamics reconstructed from the final chronology snapshot is only indicative of the core preservation process, instead of dynamics of the whole dune.

6.3 Summary of Chapter 6

This Chapter explored the longitudinal extension dynamic of linear sand dunes. Simulation results were presented with ascending dimensions and complexity, spatially from 2D transects to full 3D domains and extended to sets of varying wind properties. For linear dunes initiated in an elongation manner, several findings were involved in the chapter:

---Elongating linear dunes were found to be characterized by the structure of a persistently buried core beneath an activate sand layer that oscillates with wind shifting. The internal stratigraphy of the core was featured by bidirectional cross strata deposited by avalanche of each wind. The core started to grow once the dune cross section width exceeded its oscillation distance.

---Spatially through a linear dune, more upwind cross sections were found to preserve older (i.e. deposited in earlier times of dune initiating) sand, spanning shorter range of sand ages. In contrast, more downwind cross sections preserved younger (i.e. deposited in later times of dune initiation) sand, whilst longer ranges of more recent sand ages were spanned.

---Regarding linear dune initiation and elongation, greater wind-wind angles, high wind signal frequencies (shorter cycle durations) or greater bimodal wind symmetry were found to facilitate initiation of elongating linear dunes (instead of breaking them) and lead to larger dimensions where the dune formed.

---Regarding the internal sedimentary structure, smaller wind-wind angles, high wind signal frequencies (shorter cycle durations) or more asymmetrical regime were found to be better capable of preserving older sediments, spanning shorter ranges of the earlier deposition time in the dune initiation history. In contrast, the opposite trend of the three regime properties was found to have better preservation of longer ranges of more recent chronology records.

Chapter 7 Conclusion

This thesis had a primary aim to investigate the internal sedimentary structure and depositional chronology of aeolian sand dunes using a numerical model. Under this overall aim, two research questions were raised:

Research Question (1):

What is the internal sedimentary structure of sand dunes of different types and in differing environmental wind conditions?

Research Question (2):

What are the controlling processes that lead to the development and preservation of such internal sedimentary structures?

Surrounding the two key questions, this thesis explored the two 'simplest' wind regimes controlling dune dynamics with specific objectives of identifying the impact of both unidirectional (Objective 1) and bidirectional (Objective 2) winds on aeolian dune evolution and structure.

7.1 Key findings

Simulation steps were designed to address each objective in order of ascending complexity. In general, the cellular automaton (CA) numerical modelling approach (based on that of Nishimori and Ouchi, 1993, Werner, 1995, Narteau, et al., 2009) was found to be more appropriate than continuous modelling approaches to fulfil the thesis aims. This is because CAs are capable of tracking the activation time of all individual cell units so that the full chronological record of the dune was identifiable. A Real Space Cellular Automaton model (ReSCAL, Rozier, et al., 2014) was selected over the CAs of Nishimori and Ouchi (1993) and Werner (1995) because it enabled the simulation of relatively realistic wind flow over the instantaneous

topography where a ‘naturally’ generated wind was necessary. The lattice gas (LG) wind component of ReSCAL was coupled to sediment transport and dune morphology, allowing a dynamic computation of sediment erosion on dune surfaces. This was in positive contrast to what was possible with the empirical aerodynamic algorithms employed in the CAs of Nishimori and Ouchi (1993), Werner (1995), Momiji, et al., (2000) and so forth.

7.1.1 Investigation and key findings for Objective 1

Objective 1: To identify the impact of unidirectional wind regimes on aeolian dune evolution and sedimentary structure

There are two simulation steps involved in fulfilling this objective, testing the impact of both wind angle variability and wind speed variability on transverse dune dynamics and sediment preservation. Exploration and results of Objective 1 are presented in Chapter 4. Before the two steps are investigated in the chapter, Section 4.1 firstly presents the simplest scenario with a crest-normal wind enforced on a transverse dune at a fixed strength. This is for the purpose of validation of the LG wind coupled in ReSCAL, comparing the modelled wind flow structure over the topography with the literature.

Summary of key findings of Step 1.1

---Step 1.1: Testing the impact of wind speed variability on transverse dune dynamics and sediment preservation

This step was investigated in Section 4.2. The key findings are summarized below

(a) With respect to wind speeds, higher wind speeds tend to build steeper dunes (i.e. higher ratios between dune height and horizontal length of the windward slope, h/L), in good agreement with previous field data (e.g. Lancaster, 1985; Neuman, et

al., 2000; Walker and Hesp, 2013) and modelled data (e.g. Zhang, et al., 2012). Also, for a fixed dune topography, lower speed winds triggered lower avalanche magnitudes, as demonstrated by previous high resolution field surveys on transverse dunes (Nield, et al., 2017; Cornwall, et al., 2018), as well as wind tunnel experiments in the laboratory (Sutton, et al., 2003 a and b).

(b) As a result of the relationship found between wind speed and magnitude of grain flow on dune lee slope surfaces, it was discovered that under lower wind speeds, a lower volume of sand was subsequently preserved in the stratigraphy. Therefore, in ReSCAL outputs here, over an extended time scale, low wind speeds form thinner grain flow strata for a fixed range of sediment age. This tendency has long been interpreted by sedimentologists where the thickness of the strata is considered as an indicator of wind strength at the burial time of the sediments (e.g. Tanner, 1965; Parrish and Peterson, 1988; Mountney and Jagger, 2004; Rowe et al., 2007; Eastwood, et al., 2012).

(c) It was found that in lower wind speeds preserved sediments are reactivated more slowly. As a result, once buried in a low wind speed environment, sediments remain preserved in the dune body for a longer time and the dune is capable of holding chronological records for a longer period of time. In contrast, in high wind speed environments, the greater avalanche magnitude forms thicker sedimentary strata which is based on faster reactivation of the older sediments and the overall age of the dune is younger.

Summary of key findings of Step 1.2

---Step 1.2: To identify the impact of wind angle variability on transverse dune dynamics and sediment preservation

This simulation step was investigated in Section 4.3. For the internal sedimentary structure, this step was mainly concerned with dunes that were not orientated to the transverse direction of the unimodal wind. An example is offered by linear dunes driven by two winds at very acute angles (e.g. Rubin and Hesp, 2009) or by unidirectional winds (e.g. Bagnold, 1941; Fryberger and Dean, 1979; Hesp, 1981; Schatz, et al., 2006; Herrmann, et al., 2008; Rubin and Hesp, 2009; Craddock, et al., 2015). Key findings of Step 2 are summarized below. For the short-term aerodynamic and sand moving processes on dune surfaces, this step was concerned with any scenarios where the wind is incident at oblique angles and the linear dunes are controlled by bidirectional winds (Hanna, 1969; McKee and Tibbitt, 1964; Tsoar, 1983; Livingstone, 1986; Wiggs, et al., 1996b; Bristow, et al., 2000) are also involved.

(d) With smaller incidence angles (i.e. more crest-normal wind), there is a greater degree of wind flow acceleration along the stoss slope (in agreement with Lancaster, 1985; Sweet and Kocurek, 1990; Walker and Hesp, 2009), greater deceleration in the lee, and a longer distance required for downwind flow recovery. The findings of this thesis show that the general wind structure is in agreement with previously measured wind profiles on linear dunes (e.g. Tsoar, 1983; Livingstone, 1986; Sweet and Kocurek, 1990; Wiggs, et al., 1996b) where sand transport and erosion is possible on the lee slope. More perpendicular winds result in stronger erosivity on the windward slope and weaker erosivity on the lee slope. Correspondingly, more crest-parallel winds lead to larger flow velocity on the lee and the potential for lee slope erosion and sand transport into the downwind interdune. This tendency has been demonstrated by previous qualitative description (e.g. Lancaster, 1985; Tsoar, et al., 1985, 2004; Sweet and Kocurek, 1990).

(e) Simulations show that winds that are more crest-normal have a similar effect to higher wind speeds, triggering larger magnitude avalanche events and so forming thicker preserved strata on the lee slope. This results in a steeper age-depth profile. In contrast, more crest-parallel winds have a similar effect to lower wind speeds, triggering weaker avalanche events and so forming thinner preserved strata on the lee slope. This results in a flatter age-depth profile.

(f) A threshold wind angle exists (≈30º in ReSCAL, from the crest-parallel direction) which, if exceeded, results in bed instability (Correch du Pont, et al., 2014) where linear dunes collapse into barchans with perpendicular orientation.

7.1.2 Investigation and key findings for Objective 2

Objective 2: To identify the impact of bimodal wind regimes on the geomorphological dynamics and sedimentary structure of aeolian dunes.

Under bimodal wind regimes, linear dunes are the most common resulting dune type (e.g. Bagnold, 1941; McKee and Tibbits, 1964; Tsoar, 1983; Rubin and Hunter, 1985; Rubin and Ikeda, 1900; Rubin and Hesp, 2009). This objective was resolved in Chapters 5 and 6 involving the three simulation steps required to understand linear dune dynamics. First, (Step 2.1) the impact of wind reversal was identified, including the fundamental wind flow structure, evolution of the topography and internal stratigraphy. Secondly (Step 2.2), dynamics and depositional patterns of established linear dunes were explored, with a focus on identifying the lateral migration potentials (e.g. Tsoar, 1983; Rubin, 1987; Hesp, et al., 1989; Wiggs, 2001; Rubin, et al., 2005; Tsoar, et al., 2004; Livingstone, 2007), for both individual and multiple dunes. Thirdly (Step 2.3), the initiating stage of linear dunes were investigated, with a focus on the elongation manner with upwind sand supplies (e.g.

Bagnold, 1941; Fryberger and Dean, 1979; Tsoar, 1983; Rubin and Hunter, 1985; Rubin and Ikeda, 1990; Tsoar, et al., 2004; Parteli, et al., 2009, 2014).

Summary of key findings of Step 2.1

---Step 2.1: To identify the fundamental wind, topography and stratigraphy features in wind reversal.

This simulation step is investigated in Section 5.1. This step partially plays the role of validation of ReSCAL model, particularly for the general wind flow pattern modelled with the LG in the wind reversal process.

(g) Once an opposing wind starts, a slip face begins to develop at the dune crest and extends downward through the lee slope (previous stoss slope). During this stage, the lee slope has an upper portion at the angle of repose and a lower portion of reduced gradient. The wind structure described with shear stress τ_s is characterized by a 'bump', a secondary flow reacceleration and deceleration where the lee slope gradient shifts from the high gradient slip face to the flat base. This finding accords with field measured structures (e.g. Tsoar, et al., 1983; Livingstone, 1986; Wiggs, et al., 1996b) which describe wind reacceleration starting from the middle of the lee slope. In particular, the flow modelled with LG is in good agreement with the wind profile measured by Livingstone (1986) which was based on a similar topography feature, consisting of a slip face and a flat base portion.

(h) During the development of the slip face, the low gradient portion of the lee slope (i.e. the previous stoss slope) gets progressively buried by the developing slip face. Correspondingly, the internal stratigraphy built under the opposing wind has two key features (1) bidirectional dips / strikes / grain flow strata, with the newly developing sequences overlapping the original dips preserved from the original winds (2) a low

angle surface truncating the two sequences of opposing strata, forming chronological unconformities in age-depth profiles. Wind reversal has been commonly found as one of the origins of bounding surfaces and chronological unconformities in aeolian dunes (e.g. Brookfield, 1977; Talbolt, 1985; Havholm and Kocurek, 1994; Bristow, et al., 2000, 2005, 2007 2010a; Bristow, 2019). The numerical simulation run in this thesis has constructed the full evolution from the topography to the internal stratigraphy.

(i) When the slip face reached the dune plinth, the low angle base was fully buried as the low angle truncation. From this time, the whole lee slope (and dune) started migrating downwind and allowed the preservation of unidirectional dip strata. Eventually, if the opposing wind lasted long enough, the unidirectional dips occupied the whole dune. Therefore, the internal sedimentary structure of a specific dune cross section largely depends on the duration of the reversed wind and the size of the dune cross section. In smaller dunes, the strata remaining from the previous wind is less persistent than in larger dunes. An example is offered by the linear dune surveyed by Bristow, et al. (2000). Cross sections taken from varying locations of the linear ridge involve stratigraphy that ranges from unidirectional (two opposite directions) to varying degrees of bidirectional.

Summary of key findings of Step 2.2

---Step 2.2: To investigate the lateral migration possibilities of existing dunes

This simulation step was investigated in Sections 5.2 and 5.3, respectively for individual (Step 2.2.1) linear dunes and closely spaced multiple dunes (Step 2.2.2). Key findings are summarized below.

Step 2.2.1 Individual dunes (presented in Section 5.2)

(j) For linear sand dunes that have net sideways migration, the internal stratigraphy is characterised by (1) grain flow strata (lee slope preservation) or (2) erosional surfaces (stoss slope preservation), both of which are unidirectional and corresponding to the direction of the lateral migration of the linear dune. The grain flow strata feature (1) has long been used as an indicator to identify the lateral migration of linear dunes in the past (e.g. Bristow, et al., 2000, 2005 and 2007; Tsoar, et al., 2004; Livingstone, et al., 2007; Wiggs, et al., 2021). For the other possibility (2), the erosional surface driven stratigraphy is newly identified with the numerical model. The origin of this deposition pattern is sediments remaining on the stoss slope at the end of a wind period (no time to pass the crest) exceeding the amount of sand carried away from the lee slope, leading to a net erosion of the lee slope and net accumulation of the windward slope.

The type (2) migration occurred where one wind was enforced at a very narrow angle (long duration) with the dune crest while the other wind was close to crest-normal (short duration). Under the narrow angle, the wind erosivity was so weak over the stoss slope that sand could not easily pass the crest as the wind direction changed. This contributed to accumulation of sand on the windward slope in addition to the deposition of grain flow strata as a result of avalanching in response to the more perpendicular wind. Similarly, during the more crest-parallel wind, the erosion of the lee slope was strong, contributing to overall sand loss in addition to the stoss slope erosion resulting from the perpendicular wind. The direct driver of the lateral migration in these circumstances was found to be the crest-normal sand flux $Q_{crest\perp} - Q_{out\perp}$ where $Q_{crest\perp}$ is the flux gained by a slope and $Q_{out\perp}$ is the flux lost by the lee slope.

(k) The lateral migration of a linear dune is highly sensitive to tiny variations of wind directions. Less than one degree change of a wind angle may lead to opposing migration direction or significantly changed migration speed.

Step 2.2.2 Multiple dunes (presented in Section 5.3)

(l) During a given wind period, where multiple dunes were closely spaced and the dune sizes were close, it was found that the wind was stronger over the more downwind dunes. This flow feature has started to be noted by some recent work (e.g. Bristow, et al., 2018 and 2019). Therefore dunes at more downwind locations migrated more rapidly during the ongoing wind period. With two winds enforced, side dunes are in the downwind location of each wind, so they moved laterally faster than central dunes, gradually separating. As a result, their grain flow strata dipped towards opposite directions and central dune preserved the oldest sediments of the dune field as it was less capable of migration.

This newly discovered flow interaction control may provide explanations for varying migration directions observed within one dune field as reported, for example, by Bristow, et al. (2005, 2007). Additionally, the separation of multiple dunes as a result of variation in migration potential may provide further explanation regarding dune field age coarsening (e.g. Telfer, et al., 2016; Day and Kocurek, 2018), and dune width and spacing (e.g. Wasson and Hyde, 1983; Lancaster, 1985; Thomas, 1986). In the dune separating scenario, dunes closer to the central location preserve older sediments. In the width and spacing issue, the stable inter-dune spacing may be resulted from the distance at which adjacent dunes are not impacted by the flow pattern of each other.

Summary of key findings of Step 2.3

---Step 2.3: To identify controls of bidirectional wind properties on dune initiation and elongation

This step was investigated in Chapter 6, mimicking scenarios with a constant supply from upwind, as previously found in field observations (e.g. Tsoar, 1989) and employed in previous modelling work (e.g. Rozier, et al., 2019). The investigation started with detailed analysis of an example of dune elongation under a specified wind regime, progressing to testing controls on dune development under varying bimodal wind regimes observed in previous studies (e.g. Rubin and Ikeda, 1990; Rubin and Hesp, 2009; Parteli, et al., 2009 and 2014; Telfer, et al., 2017).

Step 2.3.1 General evolution dynamic of an elongating linear dune

(m) Linear dunes forming in the elongation dynamic were characterized by a preserved core beneath a sand layer that was activated during each wind period. With a constant upwind sand supply, the longitudinal extension with time was found to be approximately linear. As a result, for each cross section, both the whole dune and the core grew in width and height logarithmically with time, because more sand was needed for the same growth in height and width but less sand was available because of the elongation of the dune. The preserved core of the dune developed once the dune width exceeded the lateral oscillation distance during a wind cycle. This cross section width and height growth pattern is in agreement with some OSL data (e.g. Stone and Thomas, 2008; Srivastava, et al., 2019).

(n) Under the mechanism of dune elongation and width widening, it was found that the upwind portions of the dune preserved older sediments. However, whilst the

downwind dune sections were younger in age, they were found to preserve more abundant of chronology information relating to recent periods.

(o) In agreement with literature (e.g. Bagnold, 1941; Hanna, 1969; McKee and Tibbit, 1964; Rubin and Hunter, 1985; Tsoar, et al., 2004) it was found that the core of a linear dune was characterized by the preservation of bidirectional grain flow strata.

Step 2.3.2 Controls of bimodal wind properties

(p) In general, greater wind angles, shorter cycle durations (higher frequency wind), and less asymmetrical regimes were found to be more capable of generating integrated elongating linear dunes (rather than splitting into barchans) and resulted in wider dune ridges. Correspondingly such wind regimes lead to preservation of a longer history of dune deposition. This general trend, where narrower wind angles tend to generate asymmetric barchans rather than linear dunes corresponds to previous findings (e.g. Rubin and Hesp, 2009; Parteli, et al., 2009 and 2014).

(q) The tendency with respect to the wind regime geometries in (p) is controlled by a 'simple' mass balance relationship with the upwind sand supply: $R_{in} = Q_{mean||} * W_{dune} + Q_{out||} * W_{spacing}$ (Equation 6.1 of Section 6.1.2). In this relationship, sand supplied from upwind at a rate R_{in} distributes either through the dune width W_{dune}, forming the longitudinal flux $Q_{mean||}$, or distributes over the inter-dune width $W_{spacing}$, forming the flux $Q_{out||}$. For the wind-wind angles, smaller θ generates greater $Q_{mean||}$ so the dune width stopped growing at a smaller W_{dune}. For the wind cycle duration, shorter T generated less Q_{out}, leading to larger dune width. For the wind asymmetry (described by wind period duration ration N=T_1/T_2), more asymmetrical wind regimes generated slightly higher $Q_{mean||}$ and significantly higher $Q_{out||}$

(contributed by the narrower wind), leading to less sand distribution for the dune and resulting in a smaller dune size.

7.2 Overall conclusion

Surrounding the internal sedimentary structure of sand dunes, this thesis explored the control of the two ‘simplest’ wind regimes, unimodal and bimodal, on the internal stratigraphy of aeolian sand dunes. A ReSCAL model was deployed as the key approach for simulating the internal sedimentary structure associated with the dune building process. Several wind-related factors were identified as having a major impact on the preservation of sedimentary structure:

(1) Wind directionality.

(2) Wind strength (either in varying durations or speeds).

(3) Wind flow interaction between closely spaced dunes.

(4) For bimodal wind regimes, wind directionality, wind cycle duration, and asymmetry between the two winds.

For dunes driven by unimodal winds, it was found that (1) and (2) control the thickness of preserved cross strata by directly affecting the grain flow magnitude occurring on dune slip faces. If a dune experienced a wind opposing to the previous wind, opposing sets of cross strata associated with the previous low angle stoss slope may be found buried in the dune body. This low angle surface is reflected by a chronology gap in age-depth profiles if the drilled vertical column intercepts the surface.

For bimodal winds, where linear dunes are the major type, (3) and (4) both contribute to the variation of dune sizes, geometric features, lateral migration (directions and speeds), elongation potential and, correspondingly, preservation of internal stratigraphy. In general, the formation of the internal sedimentary structure of sand dunes is controlled by the overall environmental wind and the wind flow pattern over each individual dune, that may vary between dunes.

To summarize, this thesis deployed a CA dune model coupled with a LG wind flow generator to study how unidirectional winds and bidirectional winds drive the evolution and initiation of sand dunes.

7.3 Future work

During the writing of this thesis, some difficulties and limitations of the research process, including in the use of the ReSCAL model, were identified. Below is a summary of the key limitations and identification of potential future esearch requirements:

(1) For the ReSCAL model, the general wind flow structure modelled with LG was in agreement with the literature in terms of wind directions (e.g. Lancaster, 1985; Tsoar, et al., 1985; Livingstone, 1986; Wiggs, et al, 1996b). However, it was found that the LG has sacrificed quantitative accuracies to ensure increased computing speed. The modelled wind clearly showed features that are not representative. For example, the modelled lee-side flow recirculation zone was much shorter than the commonly agreed four dune heights (e.g. Parsons, et al., 2004; Baddock, et al., 2007; Schatz and Herrmann, 2010). For future work, there may be a potential to apply a more accurate CFD model coupled with a simpler dune model (rather than the complicated doublet transition basis employed by the ReSCAL model). The

results of this thesis were not significantly affected by the inaccuracy of the wind as it is mainly focused on individual dunes. For explorations involving dune interaction, a more dedicated and coupled wind model is required.

(2) Chapter 4 investigated the grain flow magnitude and strata formation in response to wind angles where the dune was not reorientated to the wind. Although many geologists have been reconstructing the palaeo winds by exploring the strata direction (e.g. Tanner, 1965; Mountney and Jagger, 2004; Rowe, et al., 2007; Eastwood, et al., 2012), it is unclear under what conditions the preserved strata fails to reflect the wind direction at the time of burial. In other words, it remains unclear under what conditions the cross strata may not be orientated in accordance with the ongoing wind direction. In addition to the strata, a more fundamental issue is under what conditions a dune may be reorientated to the ongoing wind direction.

For example, in some longitudinal dune fields (Bagnold, 1941; Fryberger and Dean, 1979; Hesp, 1981; Rubin and Hesp, 2009; Craddock, et al., 2015), the dunes interact with winds at oblique angles, rather than reorientating in response to the wind. Further, in these dune fields, the internal sedimentary structure remains unclear.

(3) In Chapter 4, superimposing dune ridges were found to arise near the lee slope base where the wind is sufficiently oblique to the dune crest (i.e. equal or lower than 20-degrees). This secondary dune ridges alignment was also documented by field observations (e.g. Walker and Shugar, 2013) in the dune lee. Additionally, superimposing bedforms were also found in the windward side of dune crests (e.g. Narteau, et al., 2009). This type of pattern evolution is characterized by decrease of dune sizes and the crest to crest spacing, opposing to the more commonly found

pattern coarsening (e.g. Ewing, et al., 2006; Ewing and Kocurek, 2010; Gao, et al., 2015). So far the pattern finning processes have been less often studied and future work could fully explore flow (either geomorphological or environmental) conditions that may lead to finning or coarsening of the pattern. For example, the previous work (e.g. Walker and Shugar, 2013; Gao, et al., 2015) and Section 4.3 here tended to show that the secondary dune ridges occur where the flow locally accelerates.

(4) Chapter 5 identified lateral migration structures and Chapter 6 independently explored elongation structures formed by wind reversal. Future work could expand on our understanding of these controls on internal sedimentary structure by considering their operation in combination, rather than independently (e.g. lateral migration and longitudinal extension).

(5) Chapter 6 demonstrated the influence of the wind cycle duration on dune development. In realistic wind environments, there are wind signals at multiple scales (e.g. daily, monthly, annually). There remains potential to fully explore how the internal stratigraphy of dunes is preserved under multiple frequencies, further interrogating the influence of signal shredding in high frequency events (Jerolmack and Paula, 2014) on dune sediment preservation.

(6) For the whole thesis where linear dunes were involved, all discussions avoided generating sinuous dunes for simplification. Future work could specifically investigate wind bimodality controls on the sinuosity of linear dunes. For example, some ReSCAL outputs have shown that linear dunes might get sinuous due to the transverse instability (e.g. Parteli, et al., 2011) when the wind periods are long enough.

Reference List

Allen, J. (1968) 'The nature and origin of bed-form hierarchies', *Sedimentology,* 10(3), pp. 161-182.

Anderson, R. S. (1990) 'Eolian ripples as examples of self-organization in geomorphological systems', *Earth-Science Reviews,* 29(1-4), pp. 77-96.

Anderson, R. S. and Bunas, K. L. (1993) 'Grain size segregation and stratigraphy in aeolian ripples modelled with a cellular automaton', *Nature,* 365(6448), pp. 740-743.

Andreotti, B., Claudin, P. and Douady, S. (2002) 'Selection of dune shapes and velocities Part 1: Dynamics of sand, wind and barchans', *The European Physical Journal B-Condensed Matter and Complex Systems,* 28(3), pp. 321-339.

Araújo, A. D., Parteli, E. J., Pöschel, T., Andrade, J. S. and Herrmann, H. J. (2013) 'Numerical modeling of the wind flow over a transverse dune', *Scientific reports,* 3(1), pp. 1-9.

Ashkenazy, Y., Yizhaq, H. and Tsoar, H. (2012) 'Sand dune mobility under climate change in the Kalahari and Australian deserts', *Climatic Change,* 112(3), pp. 901-923.

Assis, W. R. and Franklin, E. d. M. (2020) 'A comprehensive picture for binary interactions of subaqueous barchans', *Geophysical Research Letters,* 47(18), pp. e2020GL089464.

Baas, A. C. (2002) 'Chaos, fractals and self-organization in coastal geomorphology: simulating dune landscapes in vegetated environments', *Geomorphology,* 48(1-3), pp. 309-328.

Baas, A. C. (2007) 'Complex systems in aeolian geomorphology', *Geomorphology,* 91(3-4), pp. 311-331.

Baas, A. C. and Nield, J. (2007) 'Modelling vegetated dune landscapes', *Geophysical Research Letters,* 34(6).

Baddock, M., Livingstone, I. and Wiggs, G. F. (2007) 'The geomorphological significance of airflow patterns in transverse dune interdunes', *Geomorphology,* 87(4), pp. 322-336.

Baddock, M. C., Wiggs, G. F. and Livingstone, I. (2011) 'A field study of mean and turbulent flow characteristics upwind, over and downwind of barchan dunes', *Earth Surface Processes and Landforms,* 36(11), pp. 1435-1448.

Baird, T., Bristow, C., Lou, W., Du, E., Bryant, R., Mitchell, T. and Vermeesch, P. (2021) 'Blowout morphometrics and mass balances', *Frontiers in Earth Science*. 9. 669440. 2296-6463

Besler, H. (2002) 'Complex barchans in the Libyan Desert: dune traps or overtaking solitons?', *Zeitschrift für Geomorphologie. Supplementband,* (126), pp. 59-74.

Bishop, S. R., Momiji, H., Carretero-González, R. and Warren, A. (2002) 'Modelling desert dune fields based on discrete dynamics', *Discrete Dynamics in Nature and Society,* 7(1), pp. 7-17.

Bo, T.-L. and Zheng, X.-J. (2013) 'Wind speed-up process on the windward slope of dunes in dune fields', *Computers & Fluids,* 71, pp. 400-405.

Bourke, M. C., Ewing, R. C., Finnegan, D. and McGowan, H. A. (2009) 'Sand dune movement in the Victoria Valley, Antarctica', *Geomorphology,* 109(3-4), pp. 148-160.

Bourke, M. C. and Goudie, A. S. (2009) 'Varieties of barchan form in the Namib Desert and on Mars', *Aeolian Research,* 1(1-2), pp. 45-54.

Breed, C. S., Grolier, M. J. and McCauley, J. F. (1979) 'Morphology and distribution of common 'sand'dunes on Mars: Comparison with the Earth', *Journal of Geophysical Research: Solid Earth,* 84(B14), pp. 8183-8204.

Bristow, C., Pugh, J. and Goodall, T. (1996) 'Internal structure of aeolian dunes in Abu Dhabi determined using ground-penetrating radar', *Sedimentology,* 43(6), pp. 995-1003.

Bristow, C. S. (2019) 'Bounding surfaces in a barchan dune: Annual cycles of deposition? Seasonality or erosion by superimposed bedforms?', *Remote Sensing,* 11(8), pp. 965.

Bristow, C. S., Augustinus, P. C., Wallis, I., Jol, H. and Rhodes, E. (2010a) 'Investigation of the age and migration of reversing dunes in Antarctica using GPR and OSL, with implications for GPR on Mars', *Earth and Planetary Science Letters,* 289(1-2), pp. 30-42.

Bristow, C. S., Bailey, S. and Lancaster, N. (2000) 'The sedimentary structure of linear sand dunes', *Nature,* 406(6791), pp. 56-59.

Bristow, C. S., Duller, G. and Lancaster, N. (2007) 'Age and dynamics of linear dunes in the Namib Desert', *Geology,* 35(6), pp. 555-558.

Bristow, C. S., Jol, H., Augustinus, P. and Wallis, I. (2010b) 'Slipfaceless 'whaleback'dunes in a polar desert, Victoria Valley, Antarctica: Insights from ground penetrating radar', *Geomorphology,* 114(3), pp. 361-372.

Bristow, C. S. and Jol, H. M. (2003) 'An introduction to ground penetrating radar (GPR) in sediments', *Geological Society, London, Special Publications,* 211(1), pp. 1-7.

Bristow, C. S., Lancaster, N. and Duller, G. (2005) 'Combining ground penetrating radar surveys and optical dating to determine dune migration in Namibia', *Journal of the Geological Society,* 162(2), pp. 315-321.

Bristow, N., Blois, G., Best, J. and Christensen, K. (2018) 'Turbulent flow structure associated with collision between laterally offset, fixed-bed barchan dunes', *Journal of Geophysical Research: Earth Surface,* 123(9), pp. 2157-2188.

Bristow, N., Blois, G., Best, J. and Christensen, K. (2019) 'Spatial scales of turbulent flow structures associated with interacting barchan dunes', *Journal of Geophysical Research: Earth Surface,* 124(5), pp. 1175-1200.

Brookfield, M. (1977) 'The origin of bounding surfaces in ancient aeolian sandstones', *Sedimentology,* 24(3), pp. 303-332.

Brothers, S. C., Kocurek, G., Brothers, T. C. and Buynevich, I. V. (2017) 'Stratigraphic architecture resulting from dune interactions: white sands dune field, New Mexico', *Sedimentology,* 64(3), pp. 686-713.

Buckland, C. E., Bailey, R. M. and Thomas, D. S. (2019) 'Using post-IR IRSL and OSL to date young (< 200 yrs) dryland aeolian dune deposits', *Radiation Measurements,* 126, pp. 106131.

Bullard, J., Thomas, D., Livingstone, I. and Wiggs, G. (1995) 'Analysis of linear sand dune morphological variability, southwestern Kalahari Desert', *Geomorphology,* 11(3), pp. 189-203.

Bullard, J. E. and Nash, D. J. (1998) 'Linear dune pattern variability in the vicinity of dry valleys in the southwest Kalahari', *Geomorphology,* 23(1), pp. 35-54.

Burkinshaw, J. R., Illenberger, W. K. and Rust, I. C. (1993) 'Wind-speed profiles over a reversing transverse dune', *Geological Society, London, Special Publications,* 72(1), pp. 25-36.

Chopard, B. and Droz, M. (1988) 'Cellular automata approach to non-equilibrium phase transitions in a surface reaction model: static and dynamic properties', *Journal of Physics A: Mathematical and General,* 21(1), pp. 205.

Chopard, B. and Droz, M. (1998) *Cellular automata.* Springer.

Claudin, P. and Andreotti, B. (2006) 'A scaling law for aeolian dunes on Mars, Venus, Earth, and for subaqueous ripples', *Earth and Planetary Science Letters,* 252(1-2), pp. 30-44.

Clemmensen, L. (1989) 'Preservation of interdraa and plinth deposits by the lateral migration of large linear draas (Lower Permian Yellow Sands, northeast England)', *Sedimentary Geology,* 65(1-2), pp. 139-151.

Cornwall, C., Jackson, D. W., Bourke, M. C. and Cooper, J. A. G. (2018) 'Morphometric analysis of slipface processes of an aeolian dune: Implications for grain-flow dynamics', *Sedimentology,* 65(6), pp. 2034-2054.

Courrech du Pont, S., Narteau, C. and Gao, X. (2014) 'Two modes for dune orientation', *Geology,* 42(9), pp. 743-746.

Craddock, R. A. (2012) 'Aeolian processes on the terrestrial planets: Recent observations and future focus', *Progress in Physical Geography,* 36(1), pp. 110-124.

Craddock, R. A., Hutchinson, M. and Stein, J. (2010) 'Topographic data reveal a buried fluvial landscape in the Simpson Desert, Australia', *Australian Journal of Earth Sciences,* 57(1), pp. 141-149.

Craddock, R. A., Tooth, S., Zimbelman, J. R., Wilson, S. A., Maxwell, T. A. and Kling, C. (2015) 'Temporal observations of a linear sand dune in the Simpson Desert, central Australia: Testing models for dune formation on planetary surfaces', *Journal of Geophysical Research: Planets,* 120(10), pp. 1736-1750.

Davis, J. M., Banham, S. G., Grindrod, P. M., Boazman, S. J., Balme, M. R. and Bristow, C. S. (2020) 'Morphology, development, and sediment dynamics of elongating linear dunes on Mars', *Geophysical Research Letters,* 47(12), pp. e2020GL088456.

Day, M. and Kocurek, G. (2017) 'Aeolian dune interactions preserved in the ancient rock record', *Sedimentary Geology,* 358, pp. 187-196.

Day, M. and Kocurek, G. (2018) 'Pattern similarity across planetary dune fields', *Geology,* 46(11), pp. 999-1002.

De Winter, R. and Ruessink, B. (2017) 'Sensitivity analysis of climate change impacts on dune erosion: case study for the Dutch Holland coast', *Climatic Change,* 141(4), pp. 685-701.

Duller, G. and Augustinus, P. (1997) 'Luminescence studies of dunes from north-eastern Tasmania', *Quaternary Science Reviews,* 16(3-5), pp. 357-365.

Durán, O., Schwämmle, V. and Herrmann, H. (2005) 'Breeding and solitary wave behavior of dunes', *Physical Review E,* 72(2), pp. 021308.

Durán, O., Schwämmle, V. and Herrmann, H. (2007) 'Barchan dune's size distribution induced by collisions', *arXiv preprint cond-mat/0701370*.

Durán, O., Schwämmle, V., Lind, P. G. and Herrmann, H. J. (2009) 'The dune size distribution and scaling relations of barchan dune fields', *Granular Matter,* 11(1), pp. 7-11.

Durán, O., Schwämmle, V., Lind, P. G. and Herrmann, H. J. (2011) 'Size distribution and structure of Barchan dune fields', *Nonlinear Processes in Geophysics,* 18(4), pp. 455-467.

Eastwood, E., Nield, J., Baas, A. and Kocurek, G. (2011) 'Modelling controls on aeolian dune-field pattern evolution', *Sedimentology,* 58(6), pp. 1391-1406.

Eastwood, E. N., Kocurek, G., Mohrig, D. and Swanson, T. (2012) 'Methodology for reconstructing wind direction, wind speed and duration of wind events from aeolian cross-strata', *Journal of Geophysical Research: Earth Surface,* 117(F3).

Edgett, K. S. and Blumberg, D. G. (1994) 'Star and linear dunes on Mars', *Icarus,* 112(2), pp. 448-464.

Elbelrhiti, H., Andreotti, B. and Claudin, P. (2008) 'Barchan dune corridors: field characterization and investigation of control parameters', *Journal of Geophysical Research: Earth Surface,* 113(F2).

Elbelrhiti, H., Claudin, P. and Andreotti, B. (2005) 'Field evidence for surface-wave-induced instability of sand dunes', *Nature,* 437(7059), pp. 720-723.

Endo, N., Kubo, H. and Sunamura, T. (2004) 'Barchan-shaped ripple marks in a wave flume', *Earth Surface Processes and Landforms: The Journal of the British Geomorphological Research Group,* 29(1), pp. 31-42.

Endo, N., Sunamura, T. and Takimoto, H. (2005) 'Barchan ripples under unidirectional water flows in the laboratory: formation and planar morphology', *Earth Surface Processes and Landforms,* 30(13), pp. 1675-1682.

Ewing, R. C. and Kocurek, G. (2010a) 'Aeolian dune-field pattern boundary conditions', *Geomorphology,* 114(3), pp. 175-187.

Ewing, R. C., Kocurek, G. and Lake, L. W. (2006) 'Pattern analysis of dune-field parameters', *Earth Surface Processes and Landforms: The Journal of the British Geomorphological Research Group,* 31(9), pp. 1176-1191.

Ewing, R. C. and Kocurek, G. A. (2010b) 'Aeolian dune interactions and dune-field pattern formation: White Sands Dune Field, New Mexico', *Sedimentology,* 57(5), pp. 1199-1219.

Ewing, R. C., McDonald, G. D. and Hayes, A. G. (2015) 'Multi-spatial analysis of aeolian dune-field patterns', *Geomorphology,* 240, pp. 44-53.

Fenton, L. K. (2005) 'Potential sand sources for the dune fields in Noachis Terra, Mars', *Journal of Geophysical Research: Planets,* 110(E11).

Fitzsimmons, K. E., Rhodes, E. J., Magee, J. W. and Barrows, T. T. (2007) 'The timing of linear dune activity in the Strzelecki and Tirari Deserts, Australia', *Quaternary Science Reviews,* 26(19-21), pp. 2598-2616.

Forrest, S. B. and Haff, P. K. (1992) 'Mechanics of wind ripple stratigraphy', *Science,* 255(5049), pp. 1240-1243.

Frank, A. and Kocurek, G. (1996) 'Airflow up the stoss slope of sand dunes: limitations of current understanding', *Geomorphology,* 17(1-3), pp. 47-54.

Frisch, U., Hasslacher, B. and Pomeau, Y. (1986) 'Lattice-gas automata for the Navier-Stokes equation', *Physical review letters,* 56(14), pp. 1505.

Fryberger, S. G., Ahlbrandt, T. S. and Andrews, S. (1979) 'Origin, sedimentary features, and significance of low-angle eolian" sand sheet" deposits, Great Sand Dunes National Monument and vicinity, Colorado', *Journal of Sedimentary Research,* 49(3), pp. 733-746.

Fryberger, S. G. and Dean, G. (1979) 'Dune forms and wind regime', *A study of global sand seas*: US Government Printing Office Washington, pp. 137-169.

Gadal, C., Narteau, C., du Pont, S. C., Rozier, O. and Claudin, P. (2020) 'Periodicity in fields of elongating dunes', *Geology,* 48(4), pp. 343-347.

Gao, X., Gadal, C., Rozier, O. and Narteau, C. (2018) 'Morphodynamics of barchan and dome dunes under variable wind regimes', *Geology,* 46(9), pp. 743-746.

Gao, X., Narteau, C. and Gadal, C. (2021) 'Migration of Reversing Dunes Against the Sand Flow Path as a Singular Expression of the Speed-Up Effect', *Journal of Geophysical Research: Earth Surface,* 126(5), pp. e2020JF005913.

Gao, X., Narteau, C. and Rozier, O. (2015) 'Development and steady states of transverse dunes: A numerical analysis of dune pattern coarsening and giant dunes', *Journal of Geophysical Research: Earth Surface,* 120(10), pp. 2200-2219.

Gao, X., Narteau, C., Rozier, O. and Du Pont, S. C. (2015) 'Phase diagrams of dune shape and orientation depending on sand availability', *Scientific reports,* 5(1), pp. 1-12.

Giudice, A. L. and Preziosi, L. (2020) 'A fully Eulerian multiphase model of windblown sand coupled with morphodynamic evolution: Erosion, transport, deposition, and avalanching', *Applied Mathematical Modelling,* 79, pp. 68-84.

Haff, P. K. (1994) 'Discrete mechanics', *Granular Matter*: Springer, pp. 141-160.

Hanna, S. R. (1969) 'The formation of longitudinal sand dunes by large helical eddies in the atmosphere', *Journal of Applied Meteorology and Climatology,* 8(6), pp. 874-883.

Hardy, J., De Pazzis, O. and Pomeau, Y. (1976) 'Molecular dynamics of a classical lattice gas: Transport properties and time correlation functions', *Physical review A,* 13(5), pp. 1949.

Hatano, Y., Kanda, Y., Udo, K., Takewaka, S., Ueki, R., Hatano, N., Mouri, H., Chiba, M., Kurihara, K. and Nishimura, H. (2004) 'A wind tunnel experiment of sand transport and its comparison with the Werner model', *Journal of Geophysical Research: Earth Surface,* 109(F1).

Havholm, K. and Kocurek, G. (1994) 'Factors controlling aeolian sequence stratigraphy: clues from super bounding surface features in the Middle Jurassic Page Sandstone', *Sedimentology,* 41(5), pp. 913-934.

Herrmann, H. J., Durán, O., Parteli, E. J. and Schatz, V. (2008) 'Vegetation and induration as sand dunes stabilizators', *Journal of Coastal Research,* 24(6), pp. 1357-1368.

Hersen, P. (2004) 'On the crescentic shape of barchan dunes', *The European Physical Journal B-Condensed Matter and Complex Systems,* 37(4), pp. 507-514.

Hersen, P., Andersen, K. H., Elbelrhiti, H., Andreotti, B., Claudin, P. and Douady, S. (2004) 'Corridors of barchan dunes: Stability and size selection', *Physical Review E,* 69(1), pp. 011304.

Hersen, P. and Douady, S. (2005) 'Collision of barchan dunes as a mechanism of size regulation', *Geophysical Research Letters,* 32(21).

Hersen, P., Douady, S. and Andreotti, B. (2002) 'Relevant length scale of barchan dunes', *Physical Review Letters,* 89(26), pp. 264301.

Hesp, P. (1981) 'The formation of shadow dunes', *Journal of Sedimentary Research,* 51(1), pp. 101-112.

Hesp, P., Hyde, R., Hesp, V. and Zhengyu, Q. (1989) 'Longitudinal dunes can move sideways', *Earth Surface Processes and Landforms,* 14(5), pp. 447-451.

Hesp, P. A. and Hastings, K. (1998) 'Width, height and slope relationships and aerodynamic maintenance of barchans', *Geomorphology,* 22(2), pp. 193-204.

Hugenholtz, C., Moorman, B. and Wolfe, S. (2007) 'Ground penetrating radar (GPR) imaging of the internal structure of an active parabolic sand dune', *Special Papers-geological Society of America*, 432, pp. 35.

Hugenholtz, C. H. and Barchyn, T. E. (2012) 'Real barchan dune collisions and ejections', *Geophysical Research Letters,* 39(2).

Hunter, R. E., Richmond, B. M. and Rho Alpha, T. (1983) 'Storm-controlled oblique dunes of the Oregon coast', *Geological Society of America Bulletin,* 94(12), pp. 1450-1465.

Iverson, J., Greeley, R., Marshall, J., Leach, R. and White, B. 'Effect of Density Ratio: Threshold Speeds on Venus'. *Lunar and Planetary Science Conference*, 388-389.

Jackson, D. W., Bourke, M. C. and Smyth, T. A. (2015) 'The dune effect on sand-transporting winds on Mars', *Nature Communications,* 6(1), pp. 1-5.

Jackson, D. W., Cooper, A., Green, A., Beyers, M., Guisado-Pintado, E., Wiles, E., Benallack, K. and Balme, M. (2020) 'Reversing transverse dunes: Modelling of airflow switching using 3D computational fluid dynamics', *Earth and Planetary Science Letters,* 544, pp. 116363.

Jackson, P. and Hunt, J. (1975) 'Turbulent wind flow over a low hill', *Quarterly Journal of the Royal Meteorological Society,* 101(430), pp. 929-955.

Jerolmack, D. J. and Paola, C. (2007) 'Complexity in a cellular model of river avulsion', *Geomorphology,* 91(3-4), pp. 259-270.

Jerolmack, D. J. and Paola, C. (2010) 'Shredding of environmental signals by sediment transport', *Geophysical Research Letters,* 37(19).

Katsuki, A., Kikuchi, M., Nishimori, H., Endo, N. and Taniguchi, K. (2011) 'Cellular model for sand dunes with saltation, avalanche and strong erosion: collisional simulation of barchans', *Earth Surface Processes and Landforms,* 36(3), pp. 372-382.

Katsuki, A., Nishimori, H., Endo, N. and Taniguchi, K. (2005) 'Collision dynamics of two barchan dunes simulated using a simple model', *Journal of the Physical Society of Japan,* 74(2), pp. 538-541.

Kerr, R. C. and Nigra, J. O. (1952) 'Eolian sand control', *AAPG Bulletin,* 36(8), pp. 1541-1573.

Kocurek, G. (1981) 'Significance of interdune deposits and bounding surfaces in aeolian dune sands', *Sedimentology,* 28(6), pp. 753-780.

Kocurek, G. (2009), 'Desert aeolian systems', in Reading, H. G. *Sedimentary environments: processes, facies and stratigraphy.* John Wiley & Sons.

Kocurek, G. and Ewing, R. C. (2005) 'Aeolian dune field self-organization–implications for the formation of simple versus complex dune-field patterns', *Geomorphology,* 72(1-4), pp. 94-105.

Kocurek, G., Ewing, R. C., Grotzinger, J. P. and Milliken, R. E. (2012) 'Source-to-Sink: An Earth/Mars Comparison of Boundary Conditions for Eolian Dune Systems', *Sedimentary Geology of Mars*: SEPM Society for Sedimentary Geology, pp. 0.

Kocurek, G., Ewing, R. C. and Mohrig, D. (2010) 'How do bedform patterns arise? New views on the role of bedform interactions within a set of boundary conditions', *Earth surface processes and landforms,* 35(1), pp. 51-63.

Kocurek, G., Robinson, N. and Sharp Jr, J. (2001) 'The response of the water table in coastal aeolian systems to changes in sea level', *Sedimentary Geology,* 139(1), pp. 1-13.

Kroy, K., Fischer, S. and Obermayer, B. (2005) 'The shape of barchan dunes', *Journal of Physics: Condensed Matter,* 17(14), pp. S1229.

Kroy, K., Sauermann, G. and Herrmann, H. J. (2002) 'Minimal model for sand dunes', *Physical Review Letters,* 88(5), pp. 054301.

Lancaster, N. (1985) 'Variations in wind velocity and sand transport on the windward flanks of desert sand dunes', *Sedimentology,* 32(4), pp. 581-593.

Lancaster, N. (1988) 'Controls of eolian dune size and spacing', *Geology,* 16(11), pp. 972-975.

Lancaster, N. (2008) 'Desert dune dynamics and development: insights from luminescence dating', *Boreas,* 37(4), pp. 559-573.

Lancaster, N. (2013) *Geomorphology of desert dunes.* Routledge.

Lancaster, N., Nickling, W., Neuman, C. M. and Wyatt, V. (1996) 'Sediment flux and airflow on the stoss slope of a barchan dune', *Geomorphology,* 17(1-3), pp. 55-62.

Landry, W. and Werner, B. (1994) 'Computer simulations of self-organized wind ripple patterns', *Physica D: Nonlinear Phenomena,* 77(1-3), pp. 238-260.

Liu, B. and Coulthard, T. J. (2015) 'Mapping the interactions between rivers and sand dunes: implications for fluvial and aeolian geomorphology', *Geomorphology,* 231, pp. 246-257.

Liu, B. and Coulthard, T. J. (2017) 'Modelling the interaction of aeolian and fluvial processes with a combined cellular model of sand dunes and river systems', *Computers & Geosciences,* 106, pp. 1-9.

Liu, Y. and Baas, A. C. (2020) 'Internal sedimentary structure of linear dunes modelled with a cellular automaton', *Sedimentology,* 67(7), pp. 3718-3734.

Livingstone, I. (1988) 'New models for the formation of linear sand dunes', *Geography*, pp. 105-115.

Livingstone, I. (1989) 'Monitoring surface change on a Namib linear dune', *Earth Surface Processes and Landforms,* 14(4), pp. 317-332.

Livingstone, I. (1993) 'A decade of surface change on a Namib linear dune', *Earth Surface Processes and Landforms,* 18(7), pp. 661-664.

Livingstone, I. (2003) 'A twenty-one-year record of surface change on a Namib linear dune', *Earth Surface Processes and Landforms,* 28(9), pp. 1025-1031.

Livingstone, I. and Nickling, W. (1986) *Geomorphological significance of wind flow patterns over a Namib linear dune.* In *Aeolian geomorphology (pp. 97-112).* Routledge.

Livingstone, I., Wiggs, G. F. and Baddock, M. (2005) 'Barchan dunes: why they cannot be treated as ‘solitons’ or ‘solitary waves’', *Earth Surface Processes and Landforms: The Journal of the British Geomorphological Research Group,* 30(2), pp. 255-257.

Long, J. T. and Sharp, R. P. (1964) 'Barchan-dune movement in imperial valley, California', *Geological Society of America Bulletin,* 75(2), pp. 149-156.

Lucas, A., Narteau, C., Rodriguez, S., Rozier, O., Callot, Y., Garcia, A. and Courrech du Pont, S. (2015) 'Sediment flux from the morphodynamics of elongating linear dunes', *Geology,* 43(11), pp. 1027-1030.

Lucas, A., Rodriguez, S., Narteau, C., Charnay, B., Du Pont, S. C., Tokano, T., Garcia, A., Thiriet, M., Hayes, A. G. and Lorenz, R. D. (2014) 'Growth mechanisms and dune orientation on Titan', *Geophysical Research Letters,* 41(17), pp. 6093-6100.

Lü, P., Narteau, C., Dong, Z., Rozier, O. and Courrech du Pont, S. (2017) 'Unravelling raked linear dunes to explain the coexistence of bedforms in complex dunefields', *Nature communications,* 8(1), pp. 1-9.

Mayaud, J. R., Bailey, R. M. and Wiggs, G. F. (2017) 'A coupled vegetation/sediment transport model for dryland environments', *Journal of Geophysical Research: Earth Surface,* 122(4), pp. 875-900.

Michelsen, B., Strobl, S., Parteli, E. J. and Pöschel, T. (2015) 'Two-dimensional airflow modeling underpredicts the wind velocity over dunes', *Scientific reports,* 5(1), pp. 1-8.

Mills, N., Radebaugh, J. and Le Gall, A. 'Ongoing measurements of dune width and spacing on Titan reveal dune field properties'. *44th Lunar and Planetary Science Conference*, LPI Contribution No. 1719, p. 2305.

Momiji, H., Carretero-González, R., Bishop, S. R. and Warren, A. (2000) 'Simulation of the effect of wind speedup in the formation of transverse dune fields', *Earth Surface Processes and Landforms,* 25(8), pp. 905-918.

Mountney, N. P. and Jagger, A. (2004) 'Stratigraphic evolution of an aeolian erg margin system: the Permian Cedar Mesa Sandstone, SE Utah, USA', *Sedimentology,* 51(4), pp. 713-743.

Mountney, N. P. and Thompson, D. B. (2002) 'Stratigraphic evolution and preservation of aeolian dune and damp/wet interdune strata: an example from the Triassic Helsby Sandstone Formation, Cheshire Basin, UK', *Sedimentology,* 49(4), pp. 805-833.

Mulligan, K. R. (1988) 'Velocity profiles measured on the windward slope of a transverse dune', *Earth surface processes and Landforms,* 13(7), pp. 573-582.

Munyikwa, K. (2005) 'Synchrony of Southern Hemisphere Late Pleistocene arid episodes: A review of luminescence chronologies from arid aeolian landscapes south of the Equator', *Quaternary Science Reviews,* 24(23-24), pp. 2555-2583.

Narteau, C., Lajeunesse, E., Métivier, F. and Rozier, O. (2006) 'Modelling of dune patterns by short range interactions', *River, Coastal and Estuarine Morphodynamics,* 2, pp. 1035-1046.

Narteau, C., Zhang, D., Rozier, O. and Claudin, P. (2009) 'Setting the length and time scales of a cellular automaton dune model from the analysis of superimposed bed forms', *Journal of Geophysical Research: Earth Surface,* 114(F3).

Neuman, C. M., Lancaster, N. and Nickling, W. (2000) 'The effect of unsteady winds on sediment transport on the stoss slope of a transverse dune, Silver Peak, NV, USA', *Sedimentology,* 47(1), pp. 211-226.

Nickling, W., Neuman, C. M. and Lancaster, N. (2002) 'Grainfall processes in the lee of transverse dunes, Silver Peak, Nevada', *Sedimentology,* 49(1), pp. 191-209.

Nield, J. M. and Baas, A. C. (2008) 'Investigating parabolic and nebkha dune formation using a cellular automaton modelling approach', *Earth Surface Processes and Landforms,* 33(5), pp. 724-740.

Nield, J. M., Wiggs, G. F., Baddock, M. C. and Hipondoka, M. H. (2017) 'Coupling leeside grainfall to avalanche characteristics in aeolian dune dynamics', *Geology,* 45(3), pp. 271-274.

Niiya, H., Awazu, A. and Nishimori, H. (2012) 'Bifurcation analysis of the transition of dune shapes under a unidirectional wind', *Physical review letters,* 108(15), pp. 158001.

Niiya, H., Awazu, A. and Nishimori, H. (2013) 'Stability of transverse dunes against perturbations: A theoretical study using dune skeleton model', *Aeolian Research,* 9, pp. 63-68.

Nishimori, H., Katsuki, A. and Sakamoto, H. (2009) 'Coupled Odes model for the collision process of barchan dunes', *Theoretical and Applied Mechanics Japan,* 57, pp. 179-184.

Nishimori, H. and Ouchi, N. (1993a) 'Computational models for sand ripple and sand dune formation', *International Journal of Modern Physics B,* 7(09n10), pp. 2025-2034.

Nishimori, H. and Ouchi, N. (1993b) 'Formation of ripple patterns and dunes by wind-blown sand', *Physical Review Letters,* 71(1), pp. 197.

Nishimori, H., Yamasaki, M. and Andersen, K. H. (1998) 'A simple model for the various pattern dynamics of dunes', *International Journal of Modern Physics B,* 12(03), pp. 257-272.

Parsons, D. R., Walker, I. J. and Wiggs, G. F. (2004) 'Numerical modelling of flow structures over idealized transverse aeolian dunes of varying geometry', *Geomorphology,* 59(1-4), pp. 149-164.

Parteli, E., Schwämmle, V., Herrmann, H. J., Monteiro, L. and Maia, L. (2006) 'Profile measurement and simulation of a transverse dune field in the Lençóis Maranhenses', *Geomorphology,* 81(1-2), pp. 29-42.

Parteli, E. J., Andrade Jr, J. S. and Herrmann, H. J. (2011) 'Transverse instability of dunes', *Physical review letters,* 107(18), pp. 188001.

Parteli, E. J., Durán, O., Bourke, M. C., Tsoar, H., Pöschel, T. and Herrmann, H. (2014) 'Origins of barchan dune asymmetry: Insights from numerical simulations', *Aeolian Research,* 12, pp. 121-133.

Parteli, E. J., Durán, O., Tsoar, H., Schwämmle, V. and Herrmann, H. J. (2009) 'Dune formation under bimodal winds', *Proceedings of the National Academy of Sciences,* 106(52), pp. 22085-22089.

Pelletier, J. D. (2009) 'Controls on the height and spacing of eolian ripples and transverse dunes: A numerical modeling investigation', *Geomorphology,* 105(3-4), pp. 322-333.

Ping, L., Narteau, C., Dong, Z., Zhang, Z. and Courrech du Pont, S. (2014) 'Emergence of oblique dunes in a landscape-scale experiment', *Nature Geoscience,* 7(2), pp. 99-103.

Pye, K. and Tsoar, H. (2008) *Aeolian sand and sand dunes.* Springer Science & Business Media.

Reffet, E., Courrech du Pont, S., Hersen, P. and Douady, S. (2010) 'Formation and stability of transverse and longitudinal sand dunes', *Geology,* 38(6), pp. 491-494.

Roskin, J., Tsoar, H., Porat, N. and Blumberg, D. G. (2011) 'Palaeoclimate interpretations of Late Pleistocene vegetated linear dune mobilization episodes: evidence from the northwestern Negev dunefield, Israel', *Quaternary Science Reviews,* 30(23-24), pp. 3364-3380.

Rozier, O. and Narteau, C. (2014) 'A real-space cellular automaton laboratory', *Earth Surface Processes and Landforms,* 39(1), pp. 98-109.

Rozier, O., Narteau, C., Gadal, C., Claudin, P. and Courrech du Pont, S. (2019) 'Elongation and stability of a linear dune', *Geophysical Research Letters,* 46(24), pp. 14521-14530.

Rubin, D. M. (1990) 'Lateral migration of linear dunes in the Strzelecki Desert, Australia', *Earth Surface Processes and Landforms,* 15(1), pp. 1-14.

Rubin, D. M. (2012) 'A unifying model for planform straightness of ripples and dunes in air and water', *Earth-science reviews,* 113(3-4), pp. 176-185.

Rubin, D. M. and Carter, C. L. (1987) *Cross-bedding, bedforms, and paleocurrents.* Society of Economic Paleontologists and Mineralogists Tulsa, Oklahoma.

Rubin, D. M. and Hesp, P. A. (2009) 'Multiple origins of linear dunes on Earth and Titan', *Nature Geoscience,* 2(9), pp. 653-658.

Rubin, D. M. and Hunter, R. E. (1982) 'Bedform climbing in theory and nature', *Sedimentology,* 29(1), pp. 121-138.

Rubin, D. M. and Hunter, R. E. (1985) 'Why deposits of longitudinal dunes are rarely recognized in the geologic record', *Sedimentology,* 32(1), pp. 147-157.

Rubin, D. M. and Hunter, R. E. (1987) 'Bedform alignment in directionally varying flows', *Science,* 237(4812), pp. 276-278.

Rubin, D. M. and Ikeda, H. (1990) 'Flume experiments on the alignment of transverse, oblique, and longitudinal dunes in directionally varying flows', *Sedimentology,* 37(4), pp. 673-684.

Rubin, D. M., Tsoar, H. and Blumberg, D. G. (2008) 'A second look at western Sinai seif dunes and their lateral migration', *Geomorphology,* 93(3-4), pp. 335-342.

Sagan, C. and Bagnold, R. (1975) 'Fluid transport on Earth and aeolian transport on Mars', *Icarus,* 26(2), pp. 209-218.

Sauermann, G., Rognon, P., Poliakov, A. and Herrmann, H. J. (2000) 'The shape of the barchan dunes of Southern Morocco', *Geomorphology,* 36(1-2), pp. 47-62.

Schatz, V. and Herrmann, H. J. (2006) 'Flow separation in the lee side of transverse dunes: a numerical investigation', *Geomorphology,* 81(1-2), pp. 207-216.

Schatz, V., Tsoar, H., Edgett, K. S., Parteli, E. J. and Herrmann, H. J. (2006) 'Evidence for indurated sand dunes in the Martian north polar region', *Journal of Geophysical Research: Planets,* 111(E4).

Schwämmle, V. and Herrmann, H. (2005) 'Reply to the discussion on ‘Barchan Dunes: why they cannot be treated as “solitons” or “solitary waves”'', *Earth Surface Processes and Landforms: The Journal of the British Geomorphological Research Group,* 30(4), pp. 517-517.

Schwämmle, V. and Herrmann, H. J. (2003) 'Solitary wave behaviour of sand dunes', *Nature,* 426(6967), pp. 619-620.

Srivastava, A., Durcan, J. A. and Thomas, D. S. (2019) 'Analysis of late Quaternary linear dune development in the Thar Desert, India', *Geomorphology,* 344, pp. 90-98.

Stokes, S. and Gaylord, D. R. (1993) 'Optical dating of Holocene dune sands in the Ferris Dune Field, Wyoming', *Quaternary Research,* 39(3), pp. 274-281.

Stone, A. and Thomas, D. (2008) 'Linear dune accumulation chronologies from the southwest Kalahari, Namibia: challenges of reconstructing late Quaternary palaeoenvironments from aeolian landforms', *Quaternary Science Reviews,* 27(17-18), pp. 1667-1681.

Sutton, S., McKenna Neuman, C. and Nickling, W. (2013) 'Avalanche grainflow on a simulated aeolian dune', *Journal of Geophysical Research: Earth Surface,* 118(3), pp. 1767-1776.

Swanson, T., Mohrig, D., Kocurek, G., Cardenas, B. T. and Wolinsky, M. A. (2019) 'Preservation of autogenic processes and allogenic forcings in set-scale aeolian architecture I: numerical experiments', *Journal of Sedimentary Research,* 89(8), pp. 728-740.

Swanson, T., Mohrig, D., Kocurek, G. and Liang, M. (2017) 'A surface model for aeolian dune topography', *Mathematical Geosciences,* 49(5), pp. 635-655.

Sweet, M. (1992) 'Lee-face airflow, surface processes, and stratification types: their significance for refining the use of eolian cross-strata as paleocurrent indicators', *Geological Society of America Bulletin,* 104(11), pp. 1528-1538.

Talbot, M. (1985) 'Major bounding surfaces in aeolian sandstones—a climatic model', *Sedimentology,* 32(2), pp. 257-265.

Telfer, M., Bailey, R., Burrough, S., Stone, A., Thomas, D. and Wiggs, G. (2010) 'Understanding linear dune chronologies: insights from a simple accumulation model', *Geomorphology,* 120(3-4), pp. 195-208.

Telfer, M. and Hesse, P. (2013) 'Palaeoenvironmental reconstructions from linear dunefields: recent progress, current challenges and future directions', *Quaternary Science Reviews,* 78, pp. 1-21.

Telfer, M. and Thomas, D. (2007) 'Late Quaternary linear dune accumulation and chronostratigraphy of the southwestern Kalahari: implications for aeolian palaeoclimatic reconstructions and predictions of future dynamics', *Quaternary Science Reviews,* 26(19-21), pp. 2617-2630.

Telfer, M., Thomas, D., Parker, A., Walkington, H. and Finch, A. (2009) 'Optically Stimulated Luminescence (OSL) dating and palaeoenvironmental studies of pan (playa) sediment from Witpan, South Africa', *Palaeogeography, Palaeoclimatology, Palaeoecology,* 273(1-2), pp. 50-60.

Telfer, M. W. (2011) 'Growth by extension, and reworking, of a south-western Kalahari linear dune', *Earth Surface Processes and Landforms,* 36(8), pp. 1125-1135.

Thomas, D. S., Knight, M. and Wiggs, G. F. (2005) 'Remobilization of southern African desert dune systems by twenty-first century global warming', *Nature,* 435(7046), pp. 1218-1221.

Toby, S. C., Duller, R. A., De Angelis, S. and Straub, K. M. (2019) 'A stratigraphic framework for the preservation and shredding of environmental signals', *Geophysical Research Letters,* 46(11), pp. 5837-5845.

Tsoar, H. (1983) 'Dynamic processes acting on a longitudinal (seif) sand dune', *Sedimentology,* 30(4), pp. 567-578.

Tsoar, H. (1989) 'Linear dunes-forms and formation', *Progress in Physical Geography,* 13(4), pp. 507-528.

Tsoar, H. (2001) 'Types of aeolian sand dunes and their formation', *Geomorphological fluid mechanics*: Springer, pp. 403-429.

Tsoar, H. (2005) 'Sand dunes mobility and stability in relation to climate', *Physica A: Statistical Mechanics and its Applications,* 357(1), pp. 50-56.

Tsoar, H., Blumberg, D. G. and Stoler, Y. (2004) 'Elongation and migration of sand dunes', *Geomorphology,* 57(3-4), pp. 293-302.

Tsoar, H., Rasmussen, K., Sørensen, M. and Willetts, B. 'Laboratory studies of flow over dunes'. *Proceedings of international workshop on the physics of blown sand*: University of Aarhus Aarhus, Denmark, 327-350.

Tsoar, H. and Yaalon, D. H. (1983) 'Deflection of sand movement on a sinuous longitudinal (seif) dune: use of fluorescent dye as tracer', *Sedimentary Geology,* 36(1), pp. 25-39.

Vermeesch, P. (2011) 'Solitary wave behavior in sand dunes observed from space', *Geophysical Research Letters,* 38(22).

Vermeesch, P. and Drake, N. (2008) 'Remotely sensed dune celerity and sand flux measurements of the world's fastest barchans (Bodele, Chad)', *Geophysical Research Letters,* 35(24).

Vriend, N. M., Hunt, M. L., Clayton, R. W., Brennen, C. E., Brantley, K. S. and Ruiz-Angulo, A. (2007) 'Solving the mystery of booming sand dunes', *Geophysical Research Letters,* 34(16).

Walker, I. J. (1999) 'Secondary airflow and sediment transport in the lee of a reversing dune', *Earth Surface Processes and Landforms: The Journal of the British Geomorphological Research Group,* 24(5), pp. 437-448.

Walker, I. J., Hesp, P. A., Davidson-Arnott, R. G., Bauer, B. O., Namikas, S. L. and Ollerhead, J. (2009) 'Responses of three-dimensional flow to variations in the angle of incident wind and profile form of dunes: Greenwich Dunes, Prince Edward Island, Canada', *Geomorphology,* 105(1-2), pp. 127-138.

Walker, I. J. and Shugar, D. H. (2013) 'Secondary flow deflection in the lee of transverse dunes with implications for dune morphodynamics and migration', *Earth surface processes and landforms,* 38(14), pp. 1642-1654.

Warren, A. and Allison, D. (1998) 'The palaeoenvironmental significance of dune size hierarchies', *Palaeogeography, Palaeoclimatology, Palaeoecology,* 137(3-4), pp. 289-303.

Warren, A. and Kay, S. (1987) 'Dune networks', *Geological Society, London, Special Publications,* 35(1), pp. 205-212.

Webb, P. and McKelvey, B. (1959) 'Geological investigations in South Victoria Land, Antarctica: Part 1—Geology of Victoria Dry Valley', *New Zealand Journal of Geology and Geophysics,* 2(1), pp. 120-136.

Werner, B. (1995) 'Eolian dunes: computer simulations and attractor interpretation', *Geology,* 23(12), pp. 1107-1110.

Werner, B. and Gillespie, D. (1993) 'Fundamentally discrete stochastic model for wind ripple dynamics', *Physical review letters,* 71(19), pp. 3230.

Werner, B. and Kocurek, G. (1997) 'Bed-form dynamics: Does the tail wag the dog?', *Geology,* 25(9), pp. 771-774.

Werner, B. and Kocurek, G. (1999) 'Bedform spacing from defect dynamics', *Geology,* 27(8), pp. 727-730.

Wiggs, G. F. (2001) 'Desert dune processes and dynamics', *Progress in physical geography,* 25(1), pp. 53-79.

Wiggs, G. F., Livingstone, I., Thomas, D. S. and Bullard, J. E. (1996) 'Airflow and roughness characteristics over partially vegetated linear dunes in the southwest Kalahari Desert', *Earth Surface Processes and Landforms,* 21(1), pp. 19-34.

Wiggs, G. F., Livingstone, I. and Warren, A. (1996) 'The role of streamline curvature in sand dune dynamics: evidence from field and wind tunnel measurements', *Geomorphology,* 17(1-3), pp. 29-46.

Wiggs, G. F., Thomas, D. S., Bullard, J. E. and Livingstone, I. (1995) 'Dune mobility and vegetation cover in the southwest Kalahari Desert', *Earth surface processes and landforms,* 20(6), pp. 515-529.

Wiggs, G. F. and Weaver, C. (2012) 'Turbulent flow structures and aeolian sediment transport over a barchan sand dune', *Geophysical research letters,* 39(5).

Wolf-Gladrow, D. A. (2004) *Lattice-gas cellular automata and lattice Boltzmann models: an introduction.* Springer.

Yan, N. and Baas, A. C. (2017) 'Environmental controls, morphodynamic processes, and ecogeomorphic interactions of barchan to parabolic dune transformations', *Geomorphology,* 278, pp. 209-237.

Yan, N. and Baas, A. C. (2018) 'Transformation of parabolic dunes into mobile barchans triggered by environmental change and anthropogenic disturbance', *Earth Surface Processes and Landforms,* 43(5), pp. 1001-1018.

Yizhaq, H., Ashkenazy, Y. and Tsoar, H. (2009) 'Sand dune dynamics and climate change: A modeling approach', *Journal of Geophysical Research: Earth Surface,* 114(F1).

Yizhaq, H., Katra, I., Kok, J. F. and Isenberg, O. (2012) 'Transverse instability of megaripples', *Geology,* 40(5), pp. 459-462.

Zhang, D., Narteau, C. and Rozier, O. (2010) 'Morphodynamics of barchan and transverse dunes using a cellular automaton model', *Journal of Geophysical Research: Earth Surface,* 115(F3).

Zhang, D., Narteau, C., Rozier, O. and Courrech du Pont, S. (2012) 'Morphology and dynamics of star dunes from numerical modelling', *Nature Geoscience,* 5(7), pp. 463-467.